Nuclear Science ISBN 978-92-64-99006-7

Speciation Techniques and Facilities for Radioactive Materials at Synchrotron Light Sources

Workshop Proceedings
Karlsruhe, Germany
18-20 September 2006

NEA No. 6288

NUCLEAR ENERGY AGENCY
ORGANISATION FOR ECONOMIC CO-OPERATION AND DEVELOPMENT

ORGANISATION FOR ECONOMIC CO-OPERATION AND DEVELOPMENT

The OECD is a unique forum where the governments of 30 democracies work together to address the economic, social and environmental challenges of globalisation. The OECD is also at the forefront of efforts to understand and to help governments respond to new developments and concerns, such as corporate governance, the information economy and the challenges of an ageing population. The Organisation provides a setting where governments can compare policy experiences, seek answers to common problems, identify good practice and work to co-ordinate domestic and international policies.

The OECD member countries are: Australia, Austria, Belgium, Canada, the Czech Republic, Denmark, Finland, France, Germany, Greece, Hungary, Iceland, Ireland, Italy, Japan, Korea, Luxembourg, Mexico, the Netherlands, New Zealand, Norway, Poland, Portugal, the Slovak Republic, Spain, Sweden, Switzerland, Turkey, the United Kingdom and the United States. The Commission of the European Communities takes part in the work of the OECD.

OECD Publishing disseminates widely the results of the Organisation's statistics gathering and research on economic, social and environmental issues, as well as the conventions, guidelines and standards agreed by its members.

* * *

This work is published on the responsibility of the Secretary-General of the OECD. The opinions expressed and arguments employed herein do not necessarily reflect the official views of the Organisation or of the governments of its member countries.

NUCLEAR ENERGY AGENCY

The OECD Nuclear Energy Agency (NEA) was established on 1st February 1958 under the name of the OEEC European Nuclear Energy Agency. It received its present designation on 20th April 1972, when Japan became its first non-European full member. NEA membership today consists of 28 OECD member countries: Australia, Austria, Belgium, Canada, the Czech Republic, Denmark, Finland, France, Germany, Greece, Hungary, Iceland, Ireland, Italy, Japan, Luxembourg, Mexico, the Netherlands, Norway, Portugal, Republic of Korea, the Slovak Republic, Spain, Sweden, Switzerland, Turkey, the United Kingdom and the United States. The Commission of the European Communities also takes part in the work of the Agency.

The mission of the NEA is:

- to assist its member countries in maintaining and further developing, through international co-operation, the scientific, technological and legal bases required for a safe, environmentally friendly and economical use of nuclear energy for peaceful purposes, as well as
- to provide authoritative assessments and to forge common understandings on key issues, as input to government decisions on nuclear energy policy and to broader OECD policy analyses in areas such as energy and sustainable development.

Specific areas of competence of the NEA include safety and regulation of nuclear activities, radioactive waste management, radiological protection, nuclear science, economic and technical analyses of the nuclear fuel cycle, nuclear law and liability, and public information. The NEA Data Bank provides nuclear data and computer program services for participating countries.

In these and related tasks, the NEA works in close collaboration with the International Atomic Energy Agency in Vienna, with which it has a Co-operation Agreement, as well as with other international organisations in the nuclear field.

Cover credits: FZK, Germany.

FOREWORD

by Melissa A. Denecke (INE-FZK)

The 4th Workshop on Speciation Techniques and Facilities for Radioactive Materials at Synchrotron Light Sources "Actinide-XAS-2006" was held at the *Forschungszentrum Karlsruhe* (FZK), Germany, on 18-20 September 2006. Actinide-XAS-2006 addressed the specialised field of synchrotron techniques for investigating radioactive materials. The workshop was organised by the FZK Institute for Nuclear Waste Disposal (INE), with support from the Institute for Synchrotron Radiation (ISS), the European Commission Joint Research Center Institute of Transuranium Elements (ITU), and the Johannes Gutenberg University of Mainz, Germany. This workshop was hosted for the first time in Germany, highlighting Europe's capability for performing work in this field. European synchrotron facilities for investigations on radioactive materials are available at two dedicated beamlines (the INE-Beamline at the ANKA facility in full user operation since October 2005, and the Rossendorf Beamline at the European Synchrotron Radiation Facility). Furthermore, another beamline is under construction at SOLEIL (*Matière radioactive à Soleil MARS*) in France and there are planned capabilities at the Swiss Light Source (microXAS).

Actinide-XAS-2006, as its predecessors in Grenoble, France (2000 and 2002) and Berkeley, California, USA (2004), provided a forum for learning and scientific discussion, thereby strengthening existing and establishing new transnational co-operative scientific networks. Financial support by the FZK Nuclear Safety Research Program (NUKLEAR), the European Network of Excellence for Actinide Sciences (ACTINET), ITU, and the infrastructure initiative "Integrating Activity on Synchrotron and Free Electron Laser Science" enabled the invitation of young researchers to participate in the workshop.

Six topical sessions (Solution and Co-ordination Chemistry of the Actinides; Solid State Chemistry and Physics of the Actinides; Actinides in Environmental and Life Sciences; Upcoming Techniques; Theoretical and Modelling Tools; and Facilities Reports) were held during the three-day workshop. The latest results on the application of highly brilliant synchrotron radiation in radionuclide and actinide sciences were presented in roughly 60 contributed talks and poster contributions.

In his opening address of the workshop, Dr. Joachim Knebel, head of the NUKLEAR programme at FZK, welcomed nearly 70 participants from seven European countries, Japan and the United States. This was followed by the sessions on Solution and Co-ordination Chemistry of the Actinides and Solid State Chemistry and Physics of the Actinides, with presentations ranging from themes associated with partitioning and transmutation strategies to reduce the long-term radiotoxicity of radioactive waste to the application of synchrotron radiation techniques in nuclear fuel research and development. An evening poster session was held near the INE-Beamline in the ANKA experimental hall, and participants were given the opportunity to tour the facility.

The second day covered sessions on: Actinides in Environmental and Life Sciences, including presentations of the behaviour of actinides in radioactive waste repositories and the interactions of actinides and microbial populations; Upcoming Techniques, with an emphasis on spatially as well as time-resolved techniques; and Theoretical and Modelling Tools. It is worth noting that during this

fourth workshop a number of contributions linked experimental results to quantum chemical calculations, leading to novel synergy effects in the field of radionuclide research. An evening reception on site was used for intense scientific discussion and to plan future co-operation between the participating research groups.

The third day began with a session on existing or planned facilities at synchrotron light sources allowing the investigation of radioactive materials and concluded with a discussion led by Steve Conradson about the current interest in actinides, challenges in actinide sciences and possible future directions. At the close of the workshop, an invitation was extended to hold Actinide-XAS-2008 at the new synchrotron source SOLEIL near Paris.

In these proceedings, the contributions which were not available as reviewed manuscripts at the time of publication appear only as original abstracts, as printed in the workshop programme in September. All other contributions have been peer-reviewed.

A word of gratitude goes to all those involved in making Actinide-XAS-2006 an interesting and worthwhile endeavour: the funding institutions for support, the members of the Scientific Organising Committee, members of the Local Organising Committee, and especially those attending and making contributions. Thank you all!

Participants at the Actinide-XAS-2006 gathered outside lecture hall

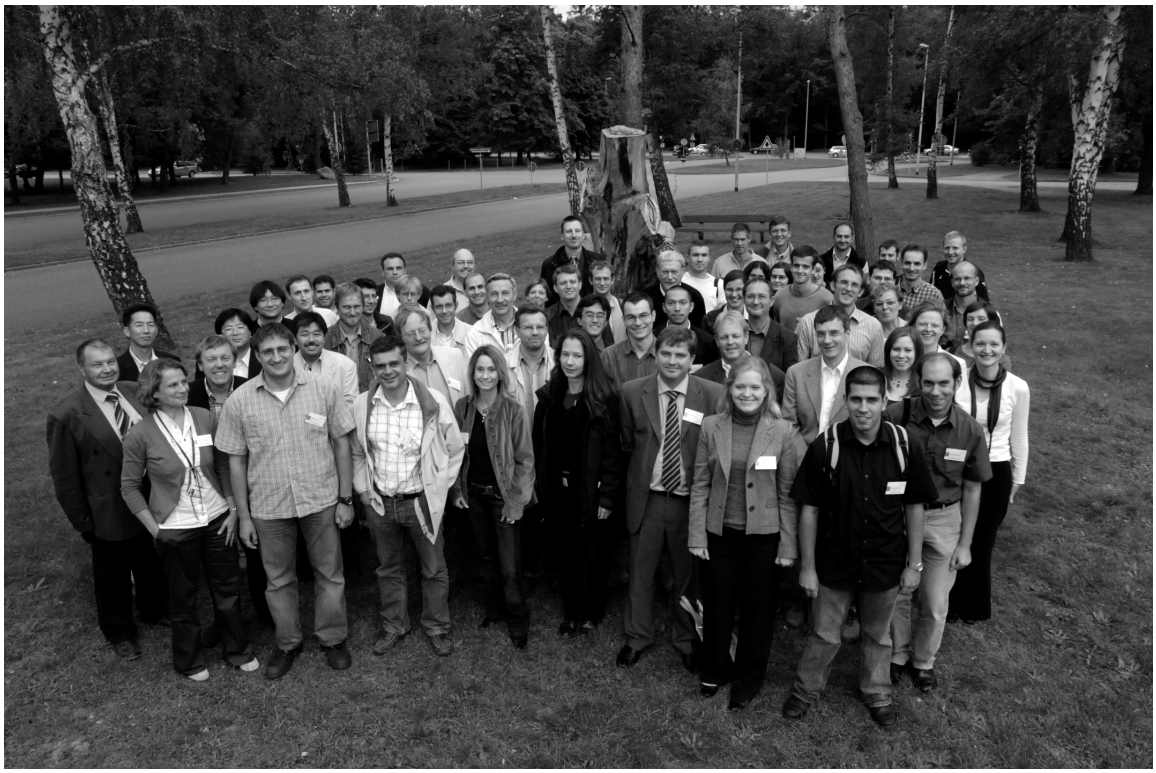

TABLE OF CONTENTS

SESSION I

SOLUTION AND CO-ORDINATION CHEMISTRY OF THE ACTINIDES

Chair: Christiane Görrler-Walrand

COMBINED TECHNIQUES FOR STUDYING ACTINIDE COMPLEXES IN ROOM TEMPERATURE IONIC LIQUIDS

Clotilde Gaillard, Isabelle Billard, Soufiane Mekki, Ali Ouadi
Institut Pluridiciplinaire Hubert Curien (IPHC), DRS, Strasbourg, France
Christoph Hennig
Forschungszentrum Rossendorf, Dresden, Germany
Melissa A. Denecke
Forschungszentrum Karlsruhe, INE, Karlsruhe, Germany

Abstract

Room temperature ionic liquids (RTILs) are a new class of solvents. Their main interest is related to their "green" properties (non-volatile, non-flammable, etc.), but also from the variability of their physico-chemical properties (stability, hydrophobicity, viscosity) as a function of the RTIL cationic and anionic components. In the frame of the nuclear fuel reprocessing, RTILs are particularly attractive in order to improve existing processes or to develop new ones for actinide and lanthanide partitioning, in replacement of toxic solvents used nowadays, for metal electrodeposition or for liquid/liquid extraction by the use of task specific ionic liquids. However, despite the increasing number of publications devoted to ionic liquids, the solvation effects, the solute-solvent and solvent-solvent interactions are still hardly known. These fundamental aspects are of tremendous importance to the understanding of the solvating properties of these new solvents.

In this frame, we have undertaken studies on the solvation and complexation of lanthanides (III) and actinides in RTILs, by the use of spectroscopic techniques. Experiments were led in various ionic liquids in order to highlight the role of the anionic part of the RTILs on the reactivity of the studied cations. Results have clearly shown that solvation phenomena in RTILs are not as "simple" as in classical solvents. The dissolution of a Ln/An salt, even if complete, does not imply dissociation and solvation of the metal cation by the RTILs anions only. The nature of first co-ordination sphere of Ln/An depends on the competition between its counter-anions and the RTIL anions, which, in turn, influence the complexation reaction with other added anions such as chlorides.

Introduction

Room temperature ionic liquids (RTILs) are a class of solvents generally composed of organic cations associated with inorganic anions, which are liquids below 100°C. In the most studied RTILs (see Figure 1), cations are derivative from imidazolium, tetraalkylammonium or pyridinium. Common anions are halogens, PF_6^-, BF_4^-, $CF_3SO_3^-$ and $(CF_3SO_2)_2N^-$. Due to their ionic nature, RTILs exhibit unique properties. They have negligible vapour pressure, are air and water stable, non flammable and thus, are often considered as "green" solvents, i.e. safe for the environment. Their physico-chemical properties strongly depend on their cationic and anionic moieties, so that even small changes in the RTIL anion or cation can entail huge variation on their properties. As a general rule, anions are responsible for the viscosity and miscibility of RTIL with water, while the low meting point and hydrophobicity are controlled by the cationic part [1]. This tunability offers large opportunities for the design of RTILs-based systems. As a matter of fact, those solvents are studied in all fields of chemistry, for catalysis, electrochemistry or separation. Their use for nuclear wastes reprocessing is also possible since these liquids are as resistant to radiations than organic solvents used nowadays [2-4].

Figure 1: Cations and anions composing the most widely used RTILs. (a) N-alkylpyridinium, (b) N,N'-dialkylimidazolium, (c) alkylammonium.

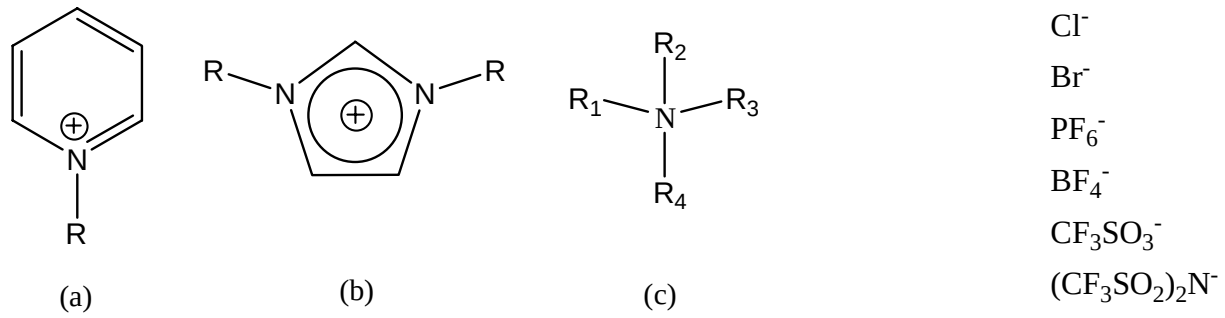

(a) (b) (c)

RTILs are conducting materials and exhibit a wide electrochemical window compared to regular solvents [5], their use can thus be envisioned for direct electrodeposition of actinides and lanthanides [6]. Electrochemical behaviour of lanthanides (Eu, Sm, La) [7] and of $AnCl_6^-$ with An = U, Np, Pu was investigated [8, 9], and recently, reduction of Th(IV) to Th(0) could be achieved in tetraalkyl-based RTILs more easily that in other nonaqueous solvents [10]. RTILs are also studied in view to their use for liquid-liquid separation of actinides and lanthanides. Many studies have shown their possible use in replacement of the toxic and flammable organic solvents used nowadays [11-15]. But whereas Ln/An are extracted in traditional organic solvents as neutral complexes, the nature of the extracted species was found to be dependant on the RTIL composition. The cationic moieties which have a direct influence on the RTILs hydrophobicity play a major role in the extraction mechanism and according to the nature of the cations, Ln and An are extracted as neutral species in very hydrophobic RTILs or as charged complexes in less hydrophobic RTILs [16-19]. The flexibility of RTIL structure also makes possible the use of task-specific ionic-liquids (TSILs) for liquid-liquid extraction. These compounds are made by grafting the extracting moieties on the RTIL skeleton (in general the cation) and thus, they combine the properties of ionic liquids (e.g., nonvolatility, nonflammability) with those of classical extracting compounds. TSILs behave both as the organic phase and the extracting agent, suppressing the problems encountered through extractant/solvent miscibility and facilitating species extraction and solvent recovery. For the moment, few studies have shown the synthesis and efficiency

of TSIL for extraction [20, 21], but americium(III) could be successfully extracted by hydroxyl-benzylamine-functionalised imidazolium TSIL [22].

Those studies show that the ionic nature of RTILs gives them fundamental properties which are very different from traditional molecular solvents. As a slight change in RTIL structure can strongly influence the chemical processes, the main problem is to find the good RTIL for the good application. To that aim, it is necessary to understand the fundamental interactions occurring in RTILs, in particular solute-solvent interactions. The aim of our work is to get insight into those fundamental interactions. We have chosen to work on imidazolium-based RTILs (1-methyl-3-butyl imidazolium cation, hereafter noted "Bumim") and to look at the solvation and complexation mechanisms of Eu(III) and U(VI) in RTILs as a function of the RTIL anionic part and the dissolved salt.

Experimental

The RTILs $BumimTf_2N$, $BumimPF_6$ (purity > 99 %) and BumimCl (purity > 98%) were purchased at Solvionic. After dissolution of the salts, drying of the RTIL solutions was achieved by heating them under vacuum (e.g., at 70°C and 1.8 mBar for 2 hours) [23]. The remaining water content after drying was measured by the Karl-Fischer technique (detection limit = 4.10^{-3} M). EXAFS and TRES experiments are performed at room temperature.

TRES experiments were performed with an excitation wavelength of 266 nm (Nd:YAG laser, 10 Hz, 6 ns pulse duration). The laser intensity is monitored with a powermeter (Scientech). The luminescence intensity as a function of time after excitation is selected via a monochromator and directed to a photomultiplier, connected to a fast oscilloscope. The laser setup is not corrected for light collection efficiency in the wavelength range investigated. The raw luminescence intensity at a given wavelength is obtained by integrating all corresponding counts. This data, plotted as a function of the emission wavelength in the range 585-630 nm, corresponds to the raw emission spectrum of the sample. The wavelength precision of the monochromator is ± 0.25 nm, with a resolution on the order of ± 0.3 nm, but the emission spectra are recorded with 1 nm steps.

For XAS measurement, the liquid samples were placed in polyethylene vials. Eu L_{III}-edge EXAFS measurements were carried out at ANKA (Karlsruhe-Germany) on the XAS station and at the INE-beamline under normal storage ring conditions (2.5 GeV, 200 – 100 mA). Spectra were recorded using a Si<311> water-cooled double-crystal monochromator at the XAS station and a Si<111> water-cooled double-crystal monochromator at the INE station. Both are calibrated in energy using the first inflection point in the K-edge of a Fe foil, defined as 7.112 keV. All RTILs samples were measured in fluorescence mode at room temperature using a 5 element solid state germanium detector (Canberra). Uranium L_{III} edge measurements were carried out at ESRF on the ROBL beamline. Spectra were recorded in transmission mode using a double crystal Si<111> monochromator. An Yttrium foil was used for calibration in energy at 17038 eV. XAFS data reduction was carried out using the IFEFFIT code [24], and their analysis was made using the FEFFIT code [25], with phase and backscattering amplitude functions generated with the FEFF 8.1 code [26]. Fits of the Fourier transform (FT) k^3-weighted EXAFS data to the EXAFS equation was performed in R-space between 1 and 3 Å for europium samples, and between 1 and 4 Å for uranium samples. The k-range used was 1.5-11.1 $Å^{-1}$ for Eu samples and 3.5-16 $Å^{-1}$ for U samples. The amplitude reduction factor (S_0^2) was held constant to 1 for all fits. The shift in the threshold energy (E_0) was allowed to vary as a global parameter for all atoms in each of the fits. Estimated errors for co-ordination number (N) are ± 20 %, for radial distance (R) ± 0.02 Å and for the Debye-Waller factors (σ^2) ± 0.001-0.002 $Å^2$.

Results

Complexation of Eu(III) with chlorides

The aim of this study is to evidence the influence of the RTIL composition on the complexation of Eu(III) with chlorides. We have chosen europium(III) because this homologue of actinides (III) can be characterised by Time Resolved Emission Spectroscopy (TRES). Trivalent europium was dissolved in a wet $BumimTf_2N$ ($[H_2O]$ = 0.4 M) as its triflate salt at a concentration of 5.10^{-3} M. As we have shown previously that water could be a competitive ligand to solutes in RTILs [27], caution must be paid to its presence in RTIL solution. Therefore, water was removed by drying the solution under vacuum, its final concentration was found below 4.10^{-3} M. Another solution was made in the same way, in which chloride ions were also introduced at a ratio [Cl]/[Eu] = 6. Figure 2 exhibits the emission spectra as a function of the chloride content in $BumimTf_2N$ solutions.

Figure 2: Emission spectra of the Eu(III) triflate salt 5.10^{-3} M in $BumimTf_2N$ as a function of chloride concentration. — : $[Cl^-] = 0$; × : $[Cl^-] = 3.10^{-2}$ M.

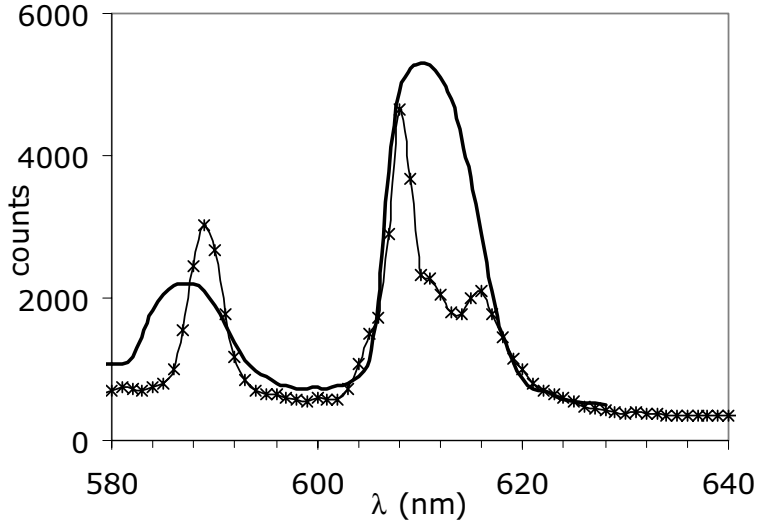

The strong changes observed, in particular on the hypersensitive band at 613 nm, are correlated to a change in the co-ordination sphere of europium. After dissolution of $EuTf_3$, two lifetimes are measured: 1596 µs – 81% and 643 µs-19%. The major species probably correspond to Eu solvated only by Tf_2N^- anions, while the minor species may correspond to a Eu solvation sphere formed by Tf_2N^- and 1 or 2 water molecules. Indeed, although the water concentration in the dried sample is very low (4.10^{-3} M), it still correspond to the presence of one water molecule per Eu.

After introduction of chloride ions, we see the apparition of a well-defined structure on the band at 613 nm. Only one lifetime is measured in this solution (2560 µs), as a sign of the introduction of chloride ions in Eu co-ordination sphere. Nevertheless, TRES could not allow us to know the exact composition of Eu co-ordination sphere. Therefore, we have analysed the 2 solutions (without and with chloride) by X-ray absorption spectroscopy. EXAFS spectra and their corresponding Fourier Transforms are shown in Figure 3. As observed by TRES, the addition of Cl^- entails strong changes in the EXAFS spectra, as a sign of Eu complexation with Cl. In particular, a shift in the FT main peak to higher distances is observed. Table 1 displays EXAFS fit results. Upon dissolution of $EuTf_3$ salt in $BumimTf_2N$, the co-ordination sphere of Eu is composed of ~9 oxygen atoms at 2.43 Å. The structure

of the triflate ($CF_3SO_3^-$) and bistriflimide ($(CF_3SO_2)_2N^-$) anions are very similar, and they both coordinate through their SO group. So we can not conclude from those EXAFS experiments on the relative contribution of Tf^- and Tf_2N^- anions in europium co-ordination sphere. After chloride addition, the whole Eu co-ordination sphere is composed of Cl atoms: ~6 Cl at 2.69 Å. We evidence here the total complexation of Cl ions, with the formation of the hexachloro-complex of Eu.

Figure 3: EXAFS and corresponding Fourier Transform of europium triflate 0.02 M in RTILs. Solid line = experimental data; •: $BumimTf_2N$, without chloride; □: $BumimTf_2N$, with chloride $[Cl^-] = 0.12$ M; ∗: $BumimPF_6$ with chloride $[Cl^-] = 0.12$ M.

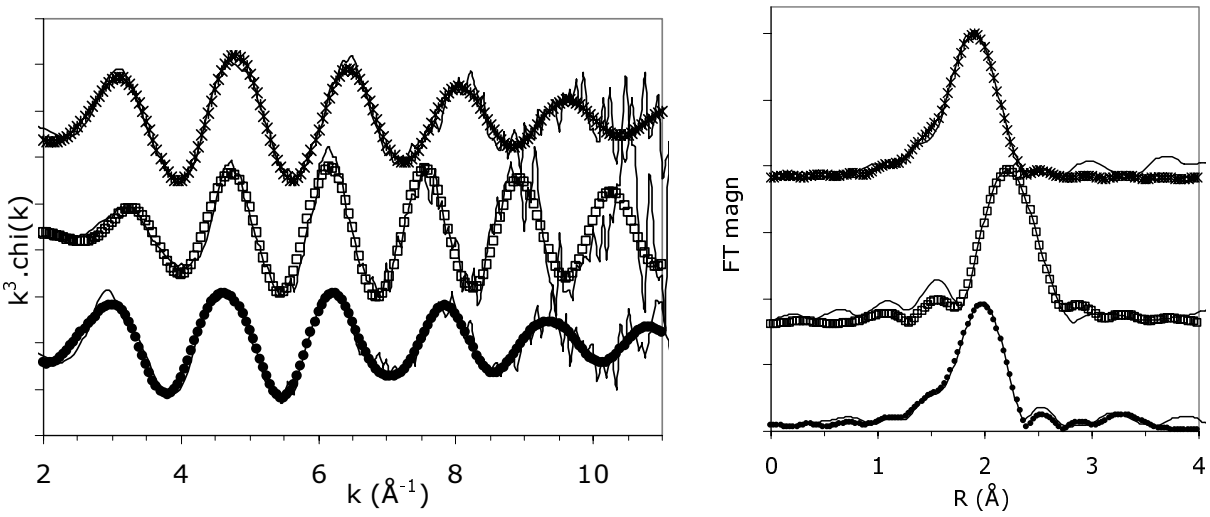

Table 1: EXAFS structural parameters for Eu(III) and U(VI) RTILs solutions.

Sample composition	shell	N	R (Å)	σ^2 (Å²)	E_0 (eV)	R factor
$EuTf_3$ 0.02 M in $BumimTf_2N$	Eu-O	9.8	2.43	0.008	0.03	0.013
$EuTf_3$ 0.06 M + BumimCl 0.35 M in $BumimTf_2N$	Eu-Cl	6.9	2.69	0.006	-6.2	0.031
$EuTf_3$ 0.02 M + BumimCl 0.12 M in $BumimPF_6$	Eu-F	10	2.36	0.009	-3.3	0.007
$UO_2(NO_3)_2.6H_2O$ 0.02 M in $BumimTf_2N$	$U\text{-}O_{ax}$ $U\text{-}O_{eq}$ $U\text{-}O_N$ U-N	2* 1.1 4 2#	1.76 2.47 2.50 2.92	0.002 0.004 0.008 0.003	-0.9	0.02
$UO_2(NO_3)_2.6H_2O$ 0.02 M + BumimCl 0.08 M in $BumimTf_2N$	$U\text{-}O_{ax}$ U-Cl	2* 3.5	1.77 2.69	0.002 0.005*	6.0	0.05

* held constant during the fit
\# linked to N

Thus, in BumimTf$_2$N, chloride ions are the strongest complexant to europium. In particular, they have a better affinity to Eu than Tf$_2$N$^-$ anions, since the latter are totally removed from Eu solvation sphere upon addition of Cl. In order to look at the influence of the RTIL composition on the Eu properties, we have made the same experiment in BumimPF$_6$: europium triflate and BumimCl were dissolved in this RTIL, the solution was then dried and analysed by EXAFS. The spectrum is displayed on Figure 3. While in BumimTf$_2$N the addition of chloride entails a strong shift of the main peak on the FT towards larger distance, no marked evolution is seen in BumimPF$_6$. Fit results (see Table 1) show that in this RTIL, no chloride has complexed to europium. Thus, by changing the RTIL anion from Tf$_2$N$^-$ to PF$_6^-$, we have change the reactivity of chlorides towards europium from a total complexation to no complexation at all. This illustrates the important role of the RTIL composition on complexation phenomena.

Effect of the dissolved salts on the co-ordination sphere: an example with U(VI)

Previous experiments have shown the influence of RTIL composition on the reactivity of europium. Next is an example which illustrates another specific feature of solvation phenomena in RTILs. Uranyl species were dissolved in BumimTf$_2$N as their nitrate salt [U] = 0.02 M, the solution was then dried in order to remove the water contained initially in the RTIL and the water added with the uranyl nitrate salt. The remaining water in solution was found below 4.10^{-3} M. EXAFS analysis of this solution (see Figure 4 and Table 1) clearly shows that nitrate ions remain in uranyl co-ordination sphere, although the salt is fully dissolved. Structural parameters obtained by the fit indicate that uranyl is coordinated by 2 bidentate nitrate groups, the co-ordination sphere being completed by ~1 oxygen atom from the RTIL anion and/or the remaining water. This shows that in BumimTf$_2$N, nitrates are strong ligands to uranyl, which is not the case in water [28]. Also, we evidence here that in RTIL, dissolution of a salt does not necessary mean dissociation of this salt.

Figure 4: EXAFS and corresponding Fourier Transform of uranyl samples in BumimTf$_2$N. ■: uranyl nitrate; — : uranyl nitrate + BumimCl

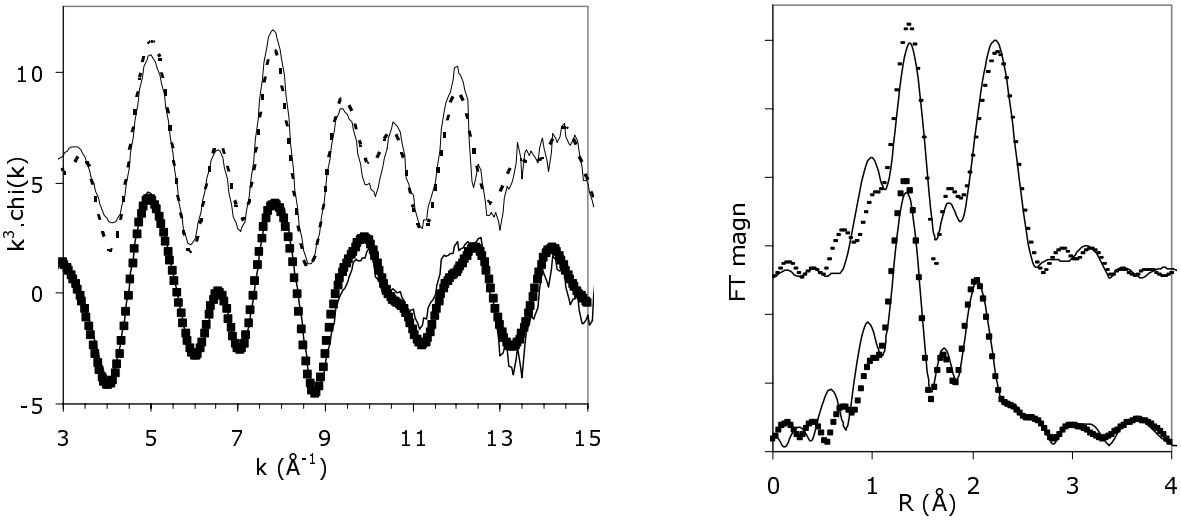

We then added chloride ions in solution, with a [Cl]/[U] = 4. This entails strong changes in the EXAFS and FT spectra (Figure 4), in particular a shift of the peak originally centred at 2 Å towards larger distances. Fit shows that nitrate ions are removed from the co-ordination sphere and chloride

ions are totally complexed to uranyl, with the formation of the tetra-chloro-complex. Thus, despite the presence of strong nitrate ligands, chlorides remain, as observed for europium, the strongest complexant.

Conclusion

Those studies illustrate that solvation and complexation phenomena are not as “simple” in RTILs as those in classical solvents. Changing the anionic part of RTIL entails a different reactivity of cationic species like europium. Also, the dissolution of a salt, although completed, does not always imply dissociation and solvation of the metal cation by RTIL anions. Thus, the co-ordination properties of a cation in RTILs markedly depend on the chemical form under which it is introduced in solution, on the composition of the RTIL and on the presence of any additional anions like chlorides.

Acknowledgements

The authors acknowledge the ANKA Angstroemquelle Karlsruhe and ESRF for beamtime allocation. This work was supported by ACTINET and the French GdR PARIS.

References

[1] J.G. Huddleston, A.E. Visser, W.M. Reichert, H.D. Willauer, G.A. Broker and R.D. Rogers, *Green Chem.* **2001**, *3*, 156.

[2] L. Berthon, S. Nikitenko, I. Bisel, C. Berthon, M. Faucon, B. Saucerotte, N. Zorz and P. Moisy, *Dalton Trans.* **2006**, 2526.

[3] D. Allen, G.M. Baston, A.E. Bradley, T. Gorman, A. Haile, I. Hamblett, J.E. Hatter, M.J. Healey, B. Hodgston, R. Lewin, K.V. Lovell, B. Newton, W.R. Pitner, D.W. Rooney, D. Sanders, K.R. Seddon, H. E. Sims and R. C. Thied, *Green Chem.* **2002**, *4*, 152.

[4] G.M. Baston and A.E. Bradley in R.D. Rogers and K.R. Seddon, ACS Publishing Series, San Diego, California, **2002**, *Vol.*

[5] P.A. Suarez, S. Einloft, J.E. Dullius, R.F. De Suza and J. Dupont, *J. Chem. Phys.* **1998**, *95*, 1626.

[6] A.I. Bhatt, I. May, V.A. Volkovich, M.E. Hetherington, B. Lewin, R.C. Thied and N. Ertok, *J. Chem. Soc., Dalton Trans.* **2002**, 4532.

[7] A.I. Bhatt, I. May, V.A. Volkovich, D. Collison, M. Helliwell, I. B. Polovov and R. Lewin, *Inorg. Chem.* **2005**, *44*, 4934.

[8] S. Nikitenko and P. Moisy, *Inorg. Chem.* **2006**, *45*, 1235.

[9] S. Nikitenko, C. Cannes, C. Le Naour, P. Moisy and D. Trubert, *Inorg. Chem.* **2005**, *44*, 9497.

[10] A.I. Bhatt, N.W. Duffy, D. Collison, I. May and R.G. Lewin, *Inorg. Chem.* **2006**, *45*, 1677.

[11] A.E. Visser, R.P. Swatloski, W.M. Reichert, S.T. Griffin and R.D. Rogers, *Ind. Eng. Chem. Res.* **2000**, *39*, 3596.

[12] T. Guoxin, Z. Yongjun, X. Jingming and Z. Ping, *Inorg. Chem.* **2003**, *42*, 735.

[13] M.P. Jensen, J.A. Dzielawa, P. Rickert and M.L. Dietz, *J. Am. Chem. Soc.* **2002**, *124*, 10664.

[14] V.A. Cocalia, M.P. Jensen, J.D. Holbrey, S.K. Spear, D.C. Stepinski and R.D. Rogers, *Dalton Trans.* **2005**, 1966.

[15] C. Gaillard, G. Moutiers, C. Mariet, T. Antoun, B. Gadenne, P. Hesemann, J.J.E. Moreau, A. Ouadi, A. Labet and I. Billard in *Potentialities of RTILs for the nuclear fuel cycle: electrodeposition and extraction*, R.D. Rogers and K.R. Seddon, Oxford University Press, **2005**, *Vol.* p. 19.

[16] M.L. Dietz, J.A. Dzielawa, I. Laszak, B.A. young and M.P. Jensen, *Green Chem.* **2003**, *5*, 682.

[17] M.P. Jensen, J. Neuefeind, J.V. Beitz, S. Skanthakumar and L. Soderholm, *J. Am. Chem. Soc.* **2003**, *125*, 15466.

[18] M.L. Dietz and J.A. Dzielawa, *Chem. Commun.* **2001**, 2124.

[19] M.L. Dietz and D.C. Stepinski, *Green Chem.* **2005**, *7*, 747.

[20] A.E. Visser, R.P. Swatloski, W.M. Reichert, R. Mayton, S. Sheff, A. Wierzbicki, J.H. Davis and R.D. Rogers, *Chem. Commun.* **2001**, 135.

[21] A.E. Visser, R.P. Swatloski, W.M. Reichert, R. Mayton, S. Sheff, A. Wierzbicki and R.D. Rogers, *Environ. Sci. Technol.* **2002**, *36*, 2523.

[22] A. Ouadi, B. Gadenne, P. Hesemann, J.J.E. Moreau, I. Billard, C. Gaillard, S. Mekki and G. Moutiers, *Chem. Eur. J.* **2006**, *12*, 3074.

[23] C. Gaillard, I. Billard, A. Chaumont, S. Mekki, A. Ouadi, M.A. Denecke, G. Moutiers and G. Wipff, *Inorg. Chem.* **2005**, *44*, 8355.

[24] M. Newville, *J. Synchrotron Rad.* **2001**, *8*, 322.

[25] M. Newville, B. Ravel, D. Haskel, J.J. Rehr, A. Stern and Y. Yacoby, *Physica B* **1995**, *208-209*, 154.

[26] A. Ankudinov and J.J. Rehr, *Phys. Rev. B* **2000**, *62*, 2437.

[27] I. Billard, S. Mekki, C. Gaillard, P. Hesemann, G. Moutiers, C. Mariet, A. Labet and J.C. Bünzli, *Eur. J. Inorg. Chem.* **2004**, 1190.

[28] L. Couston, D. Pouyat, C. Moulin and P. Decambox, *Appl. Spectr.* **1995**, *49*, 349.

COMBINED TRLFS, EXAFS AND THEORETICAL INVESTIGATIONS ON ACTINIDE/LANTHANIDE COMPLEXED WITH PARTITIONING RELEVANT LIGANDS

Petra J. Panak, Melissa A. Denecke, Michael Weigl, Andreas Geist, Bernd Schimmelpfennig
Institut für Nukleare Entsorgung, Forschungszentrum Karlsruhe, Karlsruhe, Germany

Abstract

In the context of advanced treatment of nuclear waste, organic ligands have been developed, which separate An(III) from Ln(III) elements in liquid-liquid extraction with high separation factor. One of these ligands is 2,6-di(5,6-dipropyl-1,2,4-triazin-3-yl)pyridine (BTP). We studied the Cm(III) and Eu(III) complexes of this ligand in organic solution by extended x-ray absorption fine structure **(**EXAFS) and time-resolved laser fluorescence spectroscopy (TRLFS). The goal is to understand the chemical interactions responsible for the high selectivity of BTP. We found that the co-ordination sphere of Cm(III) and Eu(III) complexes are very similar. EXAFS investigations showed that the cations are coordinated to nine nitrogen atoms, exhibiting that three BTP ligands are bound. We observed no significant interatomic distance differences in both systems. Quantum chemical calculations performed at different levels support this finding. In contrast, trends in their TRLFS spectra are different. $Cm(BTP)_3$ is formed at much lower ligand/metal concentration ratio, than $Eu(BTP)_3$. For [BTP]/[Eu] ratios between 8 and 630, Eu(III) forms two different complexes with n-C_3H_7-BTP, the Eu-BTP (1:1) complex at low ligand concentration, which is transformed to $Eu(BTP)_3$ with increasing BTP concentration. Contrary to the results obtained for Eu(III), $Cm(BTP)_3$ is exclusively formed at all [ligand/metal ion] ratios > 3.3. This indicates a significantly higher affinity of the BTP toward Cm(III). In addition, significant differences were observed in the kinetic behavior. Whereas $Cm(BTP)_3$ is formed instantaneously, the transformation of the Eu(III)-(1:1)- to the Eu(III)-(1:3)-complex occurs within several days. This is in good agreement with n-C_3H_7-BTP's high selectivity for trivalent actinides over lanthanides in liquid-liquid extraction.

CHARACTERISATION OF HEAVY CATIONS FROM DYSPROSIUM TO PLUTONIUM

C. Den Auwer[1], P. Guilbaud[1], D. Guillaumont[1], P. Moisy[1], C. Fillaux[1], C. Le Naour[2], D. Trubert[2], E. Simoni[2], V. DiGiandomenico[2], C. Hennig[3], A. Scheinost[3], S.D. Conradson[4]

[1]CEA Marcoule DEN/DRCP/SCPS, 30207 Bagnols sur Cèze, France
[2]IPN Orsay, 91405 Orsay, France
[3]FZR, ROBL at ESRF, 38043 Grenoble, France
[4]LANL, Los Alamos, NM87545, NM, USA

Abstract

For industrial, environmental and public health purposes, actinide chemistry has been the subject of considerable efforts since the 50s. Aqueous redox chemistry, ionic selective recognition, uptake by specific biomolecules or compartments of the geosphere are some of the major fields of investigation. The physical-chemical properties of the actinide and lanthanide elements strongly depend on the frontier orbital electronic configuration.

This paper is divided in two parts. In the first one, coupling XAS with molecular dynamics allows to take into account solvent and disorder effects while fitting the EXAFS data of aqueous uranyl and dysprosium cations. In the second one EXAFS structural parameters of oxocations from protactinium to plutonium are compared to quantum chemical calculations.

Introduction

Actinide molecular chemistry is surprisingly rich compared to lanthanide chemistry because the "5f" orbital extent is rather large compared to the lanthanide family and consequently, their “5f” valence electrons are relatively available. For industrial, environmental and public health purposes, this chemistry has been the subject of considerable efforts since the 50s. Aqueous redox chemistry, ionic selective recognition, uptake by specific biomolecules or compartments of the geosphere are some of the major fields of investigation. The physical-chemical properties of the actinide elements strongly depend on the 5f/6d electronic configuration. These properties can also be compared to the lanthanide “analogues”. Some actinides (U, Np, Pu and Am) can form AnO_2^{n+} (n= 1, 2) oxocations, so-called actinyls, with two strong An-O covalent bonds. Overall, the actinide co-ordination spheres are characterised by large and flexible ligand polyhedra.

Protactinium, as the first actinide with 5f-electrons involved in bonding, occupies a key position in the actinide series. At formal oxidation state V (its most stable oxidation state in solution as well as in the solid state) Pa(V) corresponds to the formal $5f^0$ electronic configuration. U(VI) also corresponds to the formal oxidation state $5f^0$ and is in most cases encountered as the stable oxocationic form UO_2^{2+}. The first stable form of actinide at formal oxidation state (V) under atmospheric conditions is NpO_2^+ with formal $5f^2$ electronic configuration. U(V) is highly unstable under atmospheric conditions and Pu(V) disproportionates into Pu(IV) and Pu(VI). On the other hand, the existence of the PaO_2^+ form in solution and in solid state has never been reported.

Several spectroscopic tools have been technically adapted to actinide chemistry, as Infrared Spectroscopy and Spectrophotometry. In solution, combined XANES and EXAFS data at the actinide L_{III} edge is a structural probe of the cation co-ordination sphere. Coupling the XAFS data analysis with molecular dynamics calculations leads to a better description of the cation-solvent interactions. It also allows to account for effective global disorder around the central atom using statistically meaningful time spaced snapshots. This is particularly important when large disordered polyhedra are composed of similar ligands as water molecules. Further comparison of the XAFS data with quantum chemical calculations provides complementary structural and electronic models from *ab initio* techniques. Structural comparison between Pa, U, Np and Pu oxocations in aqueous solution at formal oxidation states (V) and (VI) is corroborated by quantum chemical calculations.

This contribution is divided in two paragraphs. At first, coupling EXAFS data analysis with molecular dynamic calculation has been carried out for two model co-ordination polyhedra, aqueous dysprosium and aqueous uranyl. The first cation exhibits a pseudo spherical co-ordination sphere (considered spherical with respect to the spectrum resolution) and the second cation exhibits the well known pentagonal bipyramidal co-ordination sphere of the actinyl species.

Experimental

The following complexes have been investigated: **Pa(V)/HF_C** (Pa(V) in [HF]=0.5M); **Pa(V)/HF_d** (Pa(V) in [HF]=0.05M); **U(VI)/$HClO_4$** (U(VI) in [$HClO_4$]=0.5M); **Np(V)/$HClO_4$** (Np(V) in [$HClO_4$]=0.05M) **Pu(V)/$HClO_4$** (Pu(V) in [$HClO_4$]=0.05M); **Dy(III)/HCl** (Dy(III) in [HCl]=0.1M) Experimental details are described elsewhere [1, 2].

XAS measurements were performed in 600 µL cells specifically designed for radioactive samples. All data were acquired at the cation L_{III} edge. XAS measurements of dysprosium, protactinium and plutonium were carried out on the Rossendorf beam line (ROBL) at ESRF (6.0 GeV at 200 mA) in fluorescence mode, at room temperature, with a Si(111) water cooled monochromator in a channel cut mode. XAS measurements of uranium and neptunium were carried out on the 11-2 beam line at SSRL (3.0 GeV at 100 mA) in fluorescence mode at room temperature, with a Si(220) nitrogen cooled monochromator in a channel cut mode. Energy calibration was carried out with a Y

foil (17052 eV at the absorption maximum), Zr foil (18014 eV at the absorption maximum) and Fe foil (7112 eV at the absorption maximum). Data were extracted with Athena code [3] and fitted in R-space ($k^3\chi(k)$ Kaiser Fourier transformed) between 1 and 4 Å. Phases, amplitude and inelastic losses were calculated with Feff82 [4].

Molecular dynamics simulations were performed using the AMBER6 [5] and PMEMD [6] software programs with explicit polarization. Water molecules are described using the POL3 model [7].

Quantum chemistry calculations were performed using the Amsterdam Density Functional (ADF) program package [8]. Relativistic effects were considered through the zeroth-order regular approximation (ZORA). Uncontracted triple-ζ Slater type valence orbitals with one set of polarization functions were used for all atoms. The frozen-core approximation was used. The density functional consists of a local density part using the parameterization of Vosko, Wilk, and Nusair and exchange-correlation gradient corrected parts of Becke. All the results have been obtained using the conductor-like solvation model (COSMO) to take into account solvent effects.

Results

Coupling XAS with molecular dynamics: the dysprosium and uranyl case

A crucial issue of XAS analysis is to obtain reliable electronic model parameters (phase $\Phi(\theta, k, R) = 2kR + \phi$, amplitude $f(\theta, k, R)$, electron mean free path $\lambda(k)$ and inelastic losses S_0^2). These electronic parameters are obtained either by calculation or by extraction from a model compound of known structure (*i. e.* the absorber to neighbor distance *R* and the number of neighbors *N* are known and chemically close to the material under investigation). However, the difficulty to obtain 3-dimensional structures from single crystal diffraction that are applicable to solution studies is often responsible for the scarcity of adequate model compounds. On the other hand, XAS simulation codes have become accessible to heavy elements and can be used to calculate the electronic parameters on the basis of assumed atomic coordinates of model clusters. For instance, for the past few years, the Feff code has been extensively tested for heavy elements.

More recently, model clusters based on molecular dynamics calculations have been used in order to provide more reliable model clusters for solution studies. Such clusters can then be used in XAS simulation codes in order to calculate *ad hoc* electronic parameters. This procedure presents several advantages: i) first it allows to account for solvent effects in the calculation of the atomic potentials and avoids an arbitrary truncation of the cluster when it is based on solid state X-ray diffraction pattern. The solvent is treated explicitly up to a sphere radius of c.a. 6–10 Å, depending on the size of the co-ordination polyhedron; ii) it accounts for structural stereochemical relaxation, dielectric effects and solvent effects that can dramatically influence the cation co-ordination sphere in solution in comparison with solid state structures; iii) it allows to partially account for disorder effects, such as residence time of the ligands in the cation first co-ordination sphere or dynamical fluctuations of the geometry of the cation co-ordination sphere. These effects can often be accounted for by statistical disorder through the EXAFS Debye-Waller factor.

Two typical model actinide polyhedra have been investigated: bipyramidal type (uranyl(VI) aquo ion) and pseudo spherical type (dysprosium(III) aquo ion). 10 snapshots of the uranyl cluster and 17 snapshots of the dysprosium cluster (issued from molecular dynamics simulations) were necessary in order to obtain a satisfactory fit of the experimental EXAFS data. In the fitting procedure, the structural parameters from each equivalent ligand (path) were linked together and no Debye Waller factor was introduced in the fitting equation. Figure 1a shows the fitted EXAFS data of **U(VI)/HClO$_4$** and **Dy(III)/HCl**. Best fit parameters of **U(VI)/HClO$_4$** : 2 oxygen atoms (fixed) at 1.76(1) Å and 5 water molecules (fixed) at 2.42(2) Å, (R_f = 5.0%, S_0^2 = 0.8, Δe_0 = 9.7). These values compare

satisfactorily with best fit parameters presented in Table 1 obtained from a "classical" path by path fit. Figure 1b shows the radial distribution function around uranium atoms in aqueous uranyl solution calculated from the 10 snapshots. The square of the standard deviation of the axial oxygen distribution (0.0006 $Å^2$) and of the equatorial oxygen distribution (0.0046 $Å^2$) is to be compared with fitted Debye Waller factors of Table 1. The value corresponding to the axial oxygen atoms is underestimated by the molecular dynamics while the value corresponding to the equatorial water molecules compares very well. Best fit parameters of **Dy(III)/HCl** : 8 oxygen atoms (fixed) at 2.37(1) Å (R_f = 7.1%, S_0^2 = 0.7, Δe_0 = 8.8). The square of the standard deviation of the 8 oxygen distribution is equal to 0.0053 $Å^2$. These values compare very well to reported parameters for Dy(III) in acidic solution (Dy-O = 2.38 Å and σ^2 = 0.0043 $Å^2$) (2).

Table 1: Best fit parameters of the experimental $k^3\chi(k)$ data at the actinide L_{III} edge. Figures in italics have been fixed. Uncertainties are in parentheses.

Pa(V)/HF_C : *7* F/O at 2.16(1) Å σ^2 = 0.0050 $Å^2$
S_0^2 = 0.8, Δe_0 = 3.6, R_f = 2.6 %

U(VI)/$HClO_4$: *2* 0 at 1.76(1) Å σ^2 = 0.0031 $Å^2$
4.6(6) 0 at 2.43(2) Å σ^2 = 0.0055 $Å^2$
S_0^2 = 1.1, Δe_0 = 9.3, R_f = 2.7 %

Np(V)/$HClO_4$: *2* 0 at 1.82(1) Å σ^2 = 0.0008 $Å^2$
4.4(9*)* 0 at 2.49(2) Å σ^2 = 0.0043 $Å^2$
S_0^2 = 0.9, Δe_0 = 8.4, R_f = 5.5 %

Pu(V)/$HClO_4$: *2* 0 at 1.81(1) Å σ^2 = 0.0020 $Å^2$
3.5(8) 0 at 2.47(2) Å σ^2 = 0.0044 $Å^2$
S_0^2 = 0.7, Δe_0 = 6.6, R_f = 5.1 %

Figure 1a: Experimental (solid line) and fitted (dotted line) EXAFS spectra of U(VI)/$HClO_4$ and Dy(III)/HCl

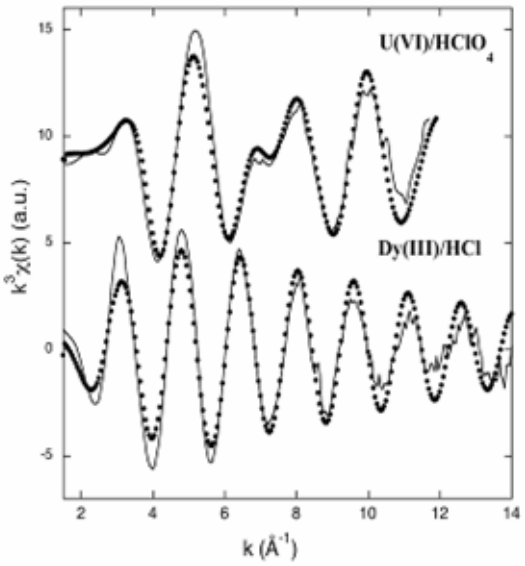

Figure 1b: Radial distribution function calculated from molecular dynamics.

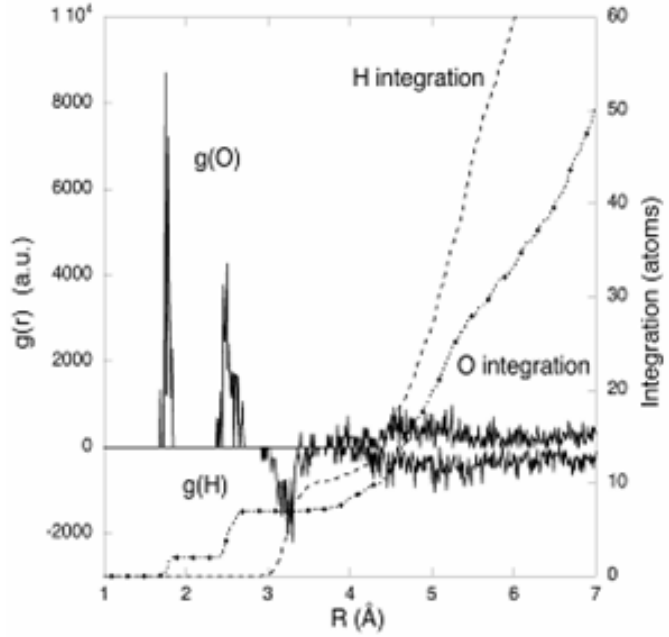

These two examples involving two characteristic model co-ordination spheres of heavy cations underline the importance of generating reliable model clusters for EXAFS fitting. For higly disordered systems, Debye Waller factors are always difficult to estimate and can become a misleading adjustable parameter. Coupling molecular dynamics with EXAFS data fitting might be therefore a promising approach.

From protactinium to plutonium oxocations

Figure 2a presents the L_{III} edge XANES spectra and fist derivative of **Pa(V)/HF_C**, **Pa(V)/HF_d**, **U(VI)/$HClO_4$**, **Np(V)/$HClO_4$** and **Pu(V)/$HClO_4$**. All spectra with the exception of those derived for protactinium exhibit the well known multiple scattering feature around 15 eV above the edge [9, 10] that is attributed to the trans dioxo unit of the actinyl species. This is also clearly visible in the absorption derivative of Figure 2b. Qualitatively, these values suggest that none of the two protactinium complexes is a trans dioxo cation. Furthermore, XANES simulations with FDMNES [11] based on model clusters have shown that due to the intrinsic width of the actinide L_{III} edges, the presence or absence of a mono oxo unit does not significantly modify the shape of the edge. This suggests that **Pa(V)/HF_C** and **Pa(V)/HF_d** are either in the form of PaO^{3+} or Pa^{5+}.

Figure 2a: L_{III} edge XANES spectra of Pa(V)/HF_C (—), Pa(V)/HF_d (—•—), U(VI)/$HClO_4$, Np(V)/$HClO_4$ and Pu(V)/$HClO_4$.

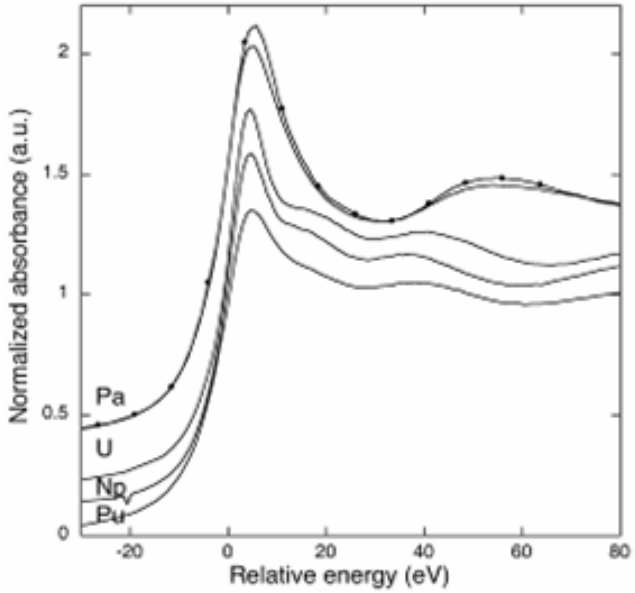

Figure 2b: Derivative of the L_{III} edge XANES spectra of Pa(V)/HF_C (—), Pa(V)/HF_d (—•—), U(VI)/$HClO_4$, Np(V)/$HClO_4$ and Pu(V)/$HClO_4$.

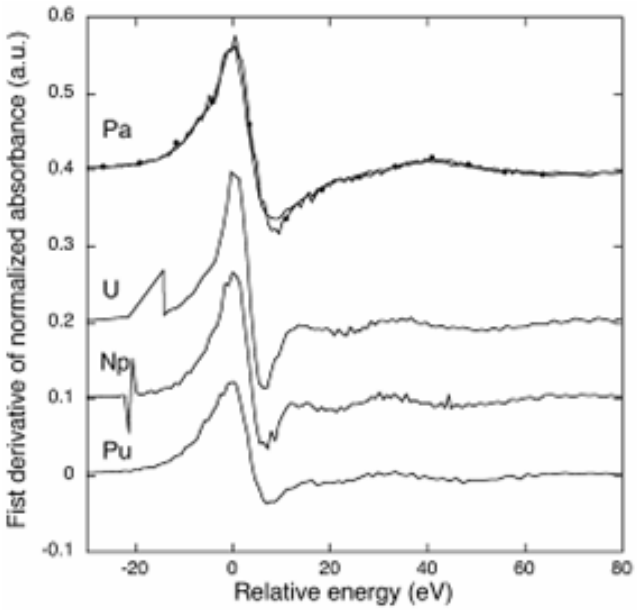

Table 1 presents the best fit parameters obtained from the EXAFS data at the actinide L_{III} edge (Figure 3). Analysis of the EXAFS spectrum of **Pa(V)/HF_d** is in progress. The structural data obtained for **U(VI)/$HClO_4$**, **Np(V)/$HClO_4$** and **Pu(V)/$HClO_4$** are in agreement with the literature [12, 13]. The shortening of the oxygen axial and equatorial distances from Np(V) to Pu(V) (0.02 Å), although close

to the uncertainty, is in agreement with the expected actinides contraction from Z to Z+1. Protactinium(V) is known to behave differently from its neighbors. Indeed, in concentrated HF it is present as a fluoro cation with no evidence of short dioxo bond, as suggested by the XANES spectrum. In contrast, Pa(V) has been shown to occur as a mono oxo cation in concentrated sulfuric acid, with mixed bidentate and monodentate sulfate ions (1). Wether **Pa(V)/HF$_d$** occurs as a PaO^{3+} or Pa^{5+} cation is still under investigation.

Figure 3: $k^3\chi(k)$ experimental (solid line) and fitted (dots) EXAFS curves of Pa(V)/HF$_c$, U(VI)/HClO$_4$, Np(V)/HClO$_4$ and Pu(V)/HClO$_4$.

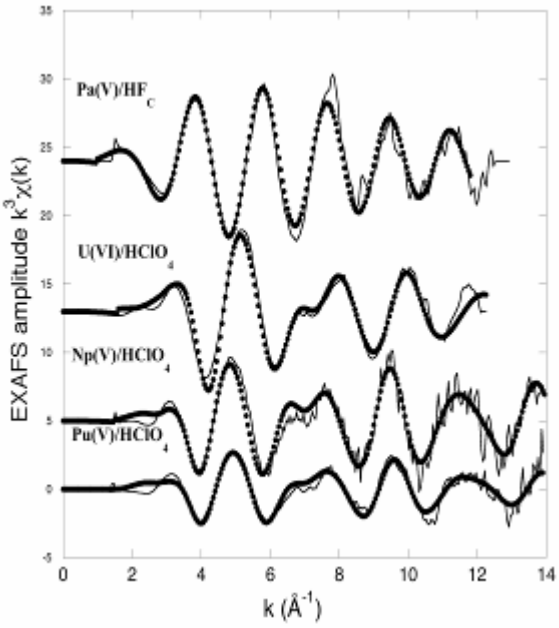

Quantum chemistry calculations have also been performed on the actinyl cation bound to four or five water molecules. Comparison of the EXAFS data with distances obtained from calculations is very satisfactory if we consider five water molecules coordinated to U(VI) and Np(V) and four water molecules bound to Pu(V) : **U(VI)** (2 O at 1.80 Å and 5 O at 2.43 Å) **Np(V)** (2 O at 1.83 Å and 5 O at 2.51 Å) and **Pu(V)** (2 O at 1.82 Å and 4 O at 2.46 Å). These results are an indication of a change in the number of coordinated water from **Np(V)** to **Pu(V)** from five to four, as already reported.

Calculations performed on $[PaF_7]^{3-}$ result in a Pa-F distance of 2.18 Å, in very good agreement with EXAFS data. It should be mentioned that the variation of the number of fluorides in the inner co-ordination sphere of Pa(V) induces only a minor change of 0.06 Å in Pa-F distances (2.12 Å in $[PaF_6]^{2-}$ and 2.24 Å in $[PaF_8]^{4-}$). In absence of any Pa model compound for EXAFS data analysis, the number of 7 F atoms suggested by quantum chemical calculations has been fixed in the fitting porcedure.

Conclusion

Although the L_{III} X-ray absorption edges of actinyl compounds have been investigated recently, understanding of the underlying co-ordination mechanisms is still incomprehensive.

We present first a combination of XAFS data analysis with molecular dynamics calculation for two distinct large co-ordination polyhedra: pentagonal bipyramid and pseudo sphere. Combination of these two techniques allows to better account for solvent effects as well as structural and thermal

disorder. This is a particularly promising approach for large intricate systems where disorder parameters are difficult to estimate.

In a second step, the series of actinide(V) cations has been investigated in acidic medium, from protactinium to plutonium. Protactinium exhibits specific behavior and differs from its Z+1 neighbor by not forming a trans dioxo species. EXAFS structural parameters have been further compared to quantum chemical data.

Acknowledgment

Support for this research was provided by CEA/DEN, the ACTINET program (JRP-02-19), a European network for actinide sciences and Groupement de Recherche PARIS, France. XAS measurements were carried out at ESRF, a European user facility and at Stanford Synchrotron Radiation Laboratory, a national user facility operated by Stanford University on behalf of the U.S. Department of Energy, Office of Basic Energy Sciences. The authors would like to thank for their help J. Bargar and J. Rogers (SSRL/11-2).

References

1. C. Le Naour, D. Trubert, M. Di Giandomenico, C. Fillaux, C. Den Auwer, P. Moisy and C. Hennig, *Inorg. Chem.* **44**, 9542-9546 (2005).
2. A. Ruas, P. Guilbaud, C. Den Auwer, C. Moulin, J-P. Simonin, P. Turq, P. Moisy *J. Phys. Chem.* Accepted for publication.
3. B. Ravel, M. Newville, *J. Synch. Rad.* **12**, 537-541 (2005).
4. J.J. Rehr, R. C. Albers, *Rev. Mod. Phys*. **72**, 621-654 (2000).
5. D.A. Case, D.A. Pearlman, J.W. Caldwell, T.E. Cheatham III, W.S. Ross, C.L. Simmerling, T.A. Darden, K.M. Merz, R.V. Stanton, A.L. Cheng, J.J. Vincent, M. Crowley, V. Tsui, R.J. Radmer, Y. Duan, J. Pitera, I. Massova, G.L. Seibel, U.C. Singh, P.K. Weiner, P.A. Kollman, *AMBER 6*, University of California: San Francisco, **1999**. / T.E. Cheatham III, P. Cieplak, P.A. Kollman; *J. Biomol. Struct. Dyn.* **1999,** 16, 845-861.
6. R.E. Duke, L.G. Pedersen, *PMEMD 3.1*, University of North Carolina: Chapel Hill, **2003**.
7. J.W. Caldwell, P.A. Kollman., J. Phys. Chem. **1995**, 99, 6208-6219 / E.C. Meng, P.A. Kollman; J. Phys. Chem. **1996**, 100, (27), 11460-11470.
8. ADF2005.01, SCM, Theoretical Chemistry, Vrije Universiteit, Amsterdam, The Netherlands, *http://www.scm.com*.
9. E.A. Hudson, J.J. Rehr, J.J. Bucher, *Phys. Rev. B* **52**, 13815-13826 (1995).
10. C. Den Auwer, D. Guillaumont, P. Guilbaud, S.D. Conradson, J.J. Rehr, A. Ankudinov, E. Simoni, *New. J. Chem.* **28**, 929-939 (2004).
11. Y. Joly, *Phys. Rev. B* **63**, 125120-125129 (2001)
12. S.D. Conradson, *Appl. Spect.* **52**, 252A-279A (1998).
13. M.R. Antonio, L. Soderholm, C. W. Williams, J-P. Blaudeau, B.E. Bursten, *Radiochim. Acta* **89**, 17-25 (2001).

EXAFS STUDIES OF THE SOLUTION STRUCTURE OF TRIVALENT ACTINIDE AND LANTHANIDE COMPLEXES OF N-DONOR EXTRACTING AGENTS FOR An(III)/Ln(III) PARTITIONING

Fabien Burdet[1)], Melissa A. Denecke[2)], Michael Weigl[2)], Marinella Mazzanti[1)]

1)Commissariat à l'Énergie Atomique (CEA)-Grenoble, Département de Recherche Fondamentale sur la Matière Condensée (DRFMC), 38054 Grenoble, Cedex 09, France
2) Forschungszentrum Karlsruhe GmbH, Institut für Nukleare Entsorgung, P.O. Box 3640, D-76021 Karlsruhe, Germany

Abstract

The design of selective extractants for the separation of An(III) from Ln(III) is one of the key point in the partitioning/transmutation strategy for the reprocessing of used nuclear fuel. This separation is particularly difficult due to the chemical similarity of An(III) and Ln(III). However, some ligands bearing soft nitrogens have been reported to complex An(III) more strongly than Ln(III), owing to a greater covalent contribution to the metal-nitrogen bonding.

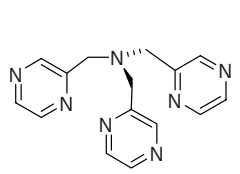

TPZA

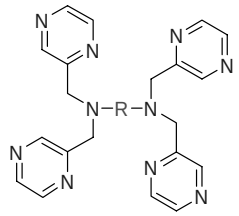

R = CH_2-CH_2 : TPZEN

R = *trans*-1,2-Cyclohexyl : TPZCN

The Grenoble laboratory has previously showed that the good separation factor ($SF_{Am/Eu}$=25) of the tripodal ligand TPZA, is correlated with a significant difference ($\Delta d_{La/U\text{-}Npyrazine}$=0.047Å) in the metal-nitrogen bond length in the crystal structure for two isostructural La(III) and U(III) complexes. However, this correlation was not observed for the tetrapodal ligands TPZEN and TPZCN: Although significant structural differences ($\Delta d_{La/U\text{-}Npyrazine}$=0.054Å) were observed in the solid state structure of TPZCN complexes this ligand has a poor separation factor ($SF_{Am/Eu}$=2). On the other hand, no structural differences were found for the complexes of TPZEN witch shows a good selectivity in the An(III)/Ln(III) separation ($SF_{Am/Eu}$=70).

Here we report EXAFS studies carried out to relate the solution co-ordination structure to liquid-liquid extraction performance for the three ligands TPZA, TPZEN and TPZCN.

EXAFS INVESTIGATION OF U(VI), U(IV) AND Th(IV) SULFATO COMPLEXES IN AQUEOUS SOLUTION

Christoph Hennig , Katja Schmeide, Vinzenz Brendler, Henry Moll, Satoru Tsushima, and Andreas C. Scheinost
Forschungszentrum Rossendorf, Institute of Radiochemistry, 01314 Dresden, Germany

Abstract

The structures of aqueous U(VI), U(IV) and Th(IV) sulfato complexes were investigated by L_{III} edge EXAFS spectroscopy in solutions with total sulfate concentrations ranging from 0.05 to 3 M. U(VI), U(IV) and Th(IV) sulfate samples comprises both, sulfate in monodentate and bidentate co-ordination. In equimolar $[SO_4^{2-}]_{total}$/U(VI) solutions, the species distribution is dominated by monodentate sulfate co-ordination with a U-S_{mon} distance of 3.57±0.02 Å. With increasing $[SO_4^{2-}]_{total}$/U(VI) ratio, bidentate co-ordination becomes dominant with a U-S_{bid} distance of 3.11±0.02 Å. In general, in all systems the bidentate co-ordination becomes dominant with increasing sulfate co-ordination. An exclusively bidentate co-ordination was observed only for U(VI) with high total sulfate concentration. The aqueous Th(IV) sulfate comprises both, monodentate and bidentate co-ordination with Th-S distances of 3.14±0.02 and 3.81±0.02 Å, respectively. A similar co-ordination is obtained for U(IV) sulfato complexes at pH 1 with U-S distances of 3.08±0.02 Å and 3.67±0.02 Å. These parameters were used to identify the structure of some corresponding thermodynamic species. The EXAFS data suffer from double-electron resonances that will be discussed in a second contribution.

RECENT STATUS OF XAFS WORK ON MOLTEN SALT SYSTEMS IN THE SPRING-8

Yoshihiro Okamoto, Tsuyoshi Yaita, Hideaki Shiwaku, Shinichi Suzuki
Japan Atomic Energy Agency, Kouto 1-1-1, Sayo-cho, Hyogo 679-5148, Japan

Paul A.Madden
University of Edinburgh, The King's Building, West Mains Road, Edinburgh EH9 3JJ, United Kingdom

Abstract

The local structure and structural change of trivalent metal chlorides $RECl_3$ (RE=Gd, Tb and Dy) and UCl_3 by mixing with LiCl-KCl eutectic were investigated by a high-temperature XAFS and a molecular dynamics (MD) techniques. In both of molten pure $DyCl_3$ and its mixture with LiCl-KCl, the local structure was predominantly the octahedral 6-fold co-ordination $(DyCl_6)^{3-}$. Co-ordination numbers (CN) of the 1st neighbour correlation in molten pure $GdCl_3$ and $TbCl_3$ were slightly larger than 6. By the mixing, however, they decreased to 6. It seems that the local structure of molten $RECl_3$ diluted in LiCl-KCl solvent is commonly the octahedral co-ordination. On the other hand, the local structure of molten pure UCl_3 , which has a larger cation than Gd^{3+} ion, was an 8-fold and its mixture with LiCl-KCl was not a stable 6-fold co-ordination. The molecular dynamics simulation of the mixture systems clarified that the mixing behaviour is completely different between with LiCl and with KCl. It is estimated that a stable octahedral 6-fold co-ordination structure is not formed in "a binary mixture of MCl_3 having a large metal ion with LiCl" like UCl_3-LiCl system.

Introduction

We have investigated the local structure of many molten salt systems [1-5] by using the high-temperature XAFS technique [6]. Most significant feature of the XAFS technique is a selectivity of element. The local structure around small amount of metal ion in solvent can be investigated with high quality. This attractive feature is not or is difficult in other experimental techniques such as diffraction. We have observed some interesting structural changes of molten trivalent metal chlorides by mixing with alkali chlorides. For example, the octahedral co-ordination structure $(YCl_6)^{3-}$ in pure YCl_3 was stabilized by mixing with alkali chlorides [1]. We found that molten pure $BiCl_3$, which shows molecular nature, changed to ionic melt by mixing with alkali chlorides [5].

Recently, we start to use high-energy (beyond 38keV) XAFS for studying molten salt at SPring-8. Energetic range available in the BL11XU covers K-absorption edge of all lanthanide elements. Generally, a sample vessel such as glass or metal is used in the molten salt XAFS measurement [6]. In our XAFS measurement system, for example, the lowest energy is automatically limited around 10keV because of an X-ray absorption effect by the quartz glass. It means that L_3-edge of lanthanides cannot be selected for XAFS measurements, since the highest L_3 energy is 9.244keV for lutetium. Oppositely, the absorption effect by the cell can be essentially ignored in the K-edge XAFS of lanthanides. It is a great advantage in the XAFS measurement of high-temperature molten salts. In the present study, recent activities of molten salt XAFS study including simulation results in JAEA were reported.

Experiment and Simulation

XAFS Experiment

Molten salt XAFS measurements were performed in a transmission geometry at the BL11XU beamline in the SPring-8, Harima, Japan and the BL-27B (X-rays ranging from 5 to 20keV are available) beamline in the Photon Factory, Tsukuba. High-energy XAFS measurements beyond 38keV were performed at the BL11XU beamline. The radiation monochromatized by double Si(311) crystals with liquid nitrogen cooled system was used in the BL11XU beamline The optic and XAFS measurement systems in the beamline were described in ref. [7]. We measured lanthanide K-edge XAFS of some molten $RECl_3$ (RE=La, Gd, Tb and Dy) and their mixture with LiCl-KCl eutectic. In the BL-27B beamline [8], radioactive materials such as uranium, thorium and some minor actinides can be used. We measured U L_3-edge XAFS of 5% and 17%UCl_3 in LiCl-KCl eutectic melt to investigate the local structure around U^{3+} ion.

Details of high-temperature XAFS measurement system such as the electric furnace and sample vessels and the XAFS data analysis procedure is described in ref.[6]. We have used the quartz cell having a beam window. The XAFS measurement was performed by using fixed time scan (typically 1-3 s for each step). The XAFS data analysis was performed by using WinXAS ver.3.1 developed by Ressler [9]. The FEFF8 code [10] was used to simulate a XAFS function $\chi(k)$. The backscattering amplitude and the phase shift functions used in the curve fitting were also calculated from the FEFF8. Structural parameters were obtained by using a following equation,

$$\chi(k) = \sum_j N_j S_j^{\,2}(k) F_j(k) \exp(-2\sigma_j^2 k^2) \exp(-2r_j/\lambda) \exp(\frac{2}{3} C4_j k^4) \sin(2kr_j + \phi_j(k) - \frac{4}{3} C3_j k^3) / (kr_j^{\,2})$$

where

N_j - co-ordination number(CN) of ion **j** around central ion **i**
$S_j(k)$ – amplitude reduction factor mainly due to many-body effect
$F_j(k)$ – backscattering amplitude for each neighbouring atom

σ_j^2 – Debye-Waller factor corresponding to thermal vibration
Λ Å electron free mean path
$\phi_{ij}(k)$ – total phase shift experienced by photoelectron
r_j – average distance of ion **j** from the central ion **i**
C3,C4 – 3rd and 4th cumulants

Molecular Dynamics and XAFS Simulations

In addition to the XAFS analysis with the curve fitting, the XAFS simulation technique [11] was used to examine the XAFS data. We have used a molecular dynamics (MD) technique for investigating the structure and physical properties of molten chlorides [12,13]. In these simulations, the effect of the induced dipoles caused by polarization of the Cl^- ions are considered. It is so called the polarizable ionic model (PIM) [14]. The structure of molten lanthanide trichlorides was successfully examined by the PIM simulation [15]. The MD simulation of molten UCl_3 and its mixtures with LiCl-KCl were performed in the present work. We used pair potentials of UCl_3 proposed by our group [13] and MCl_3-LiCl-KCl mixtures used by Brooks *et al.*[16]. Four kinds of compositions; 5, 17, 50 and 100% UCl_3 were calculated using a total of 336 ions.

In the XAFS simulation, a small cluster around the absorber (M^{3+} ion) was at first extracted from the MD simulation. Cartesian coordinates of each ion in the cluster were used as input information in the FEFF calculation. In the FEFF, "Debye" parameter was not used. It means that a XAFS function without dynamical and fluctuation factors like Debye-Waller factor is obtained in each FEFF calculation. We assumed that the fluctuation factor is compensated by averaging FEFF outputs ("frozen" XAFS function) from many clusters. Then, the above procedure was repeated many times to obtain a stationary value in the averaged XAFS function. The XAFS function converges generally after 20000 times FEFF calculations [11].

Results and discussion

Molten $RECl_3$ (RE=Gd, Tb and Dy) and their mixture with LiCl-KCl eutectic

XAFS functions $k^3\chi(k)$ of solid and molten $GdCl_3$, $TbCl_3$ and $DyCl_3$ are shown in Figure 1. A phase shift was observed for $GdCl_3$ and $TbCl_3$, while there is no phase shift in $DyCl_3$. Especially, the phase shift is remarkable in $GdCl_3$. Oscillation of the XAFS curve decreased by melting in all melts. XAFS functions $k^3\chi(k)$ of molten pure $RECl_3$ (RE=Gd, Tb and Dy) and their mixture with LiCl-KCl are shown in Figure 2. Composition of $RECl_3$ is 10% for $GdCl_3$, 1.5% for $TbCl_3$ and 1.0% for $DyCl_3$, respectively. A small phase shift to higher k direction was observed in $GdCl_3$ system. Curve fitting results of all systems above are listed in Table 1(a)-(c).

Solid $GdCl_3$ has a UCl_3-type crystal structure at room temperature [17]. In this crystal, Gd^{3+} ion is surrounded by 9 Cl^- ions (six Cl^- ions with distance r=2.820Å and three Cl^- ions with r=2.911Å). In the XAFS measurement at room temperature, these two kinds of correlations were not separated. Thus, these were treated as single correlation in the fit. The separation distance of the 1st Gd^{3+}-Cl^- correlation decreased from 2.84Å to 2.74Å by the melting. The large phase shift in the XAFS function (Figure 1) is assigned to the difference of 0.1Å. The CN also decreased from 8.7 to 6.5 by melting. It suggests that the octahedral co-ordination $(GdCl_6)^{3-}$ is formed in the melt, though the CN is slightly larger than 6. By the mixing with LiCl-KCl, these structural parameters changed to 2.69Å and 6.1, respectively. The small phase shift shown in the Figure 2 is due to the change of 0.05Å. The results imply that formation and stabilization of the octahedral $(GdCl_6)^{3-}$ co-ordination were promoted by the melting and the mixing.

Figure 1 XAFS function $k^3\chi(k)$ of solid and molten $RECl_3$ (RE=Gd, Tb and Dy)

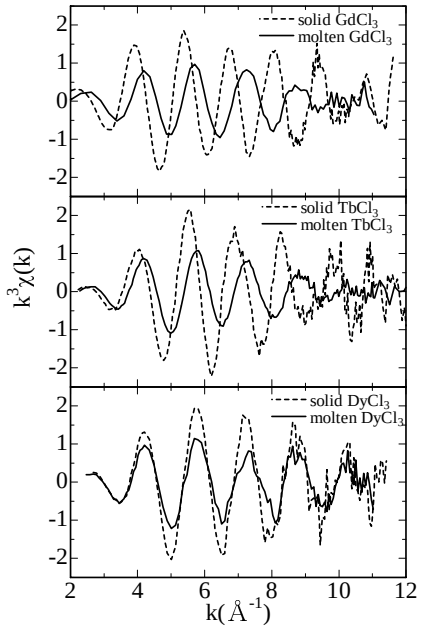

Figure 2 XAFS function $k^3\chi(k)$ of molten $RECl_3$ (RE=Gd, Tb and Dy) and their mixtures with LiCl-KCl eutectic

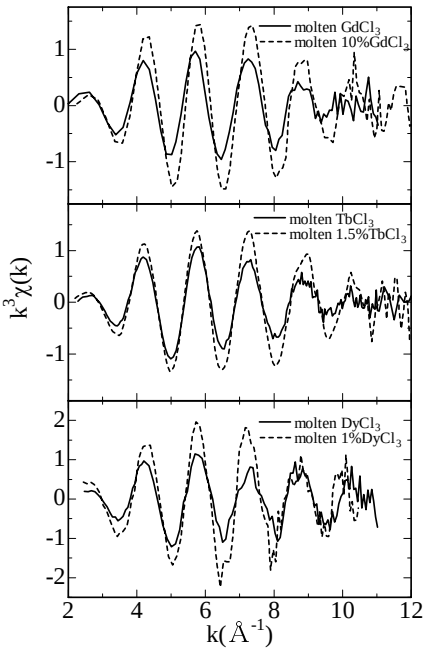

Solid $TbCl_3$ has a $PuBr_3$-type crystal structure at room temperature [18]. In this crystal, Tb^{3+} ion is surrounded by 8 Cl^- ions. By the melting, the CN and separation distance of the 1st Tb^{3+}-Cl^- correlation decreased from 7.9 and 2.73Å to 6.8 and 2.69Å, respectively. The 1st Tb^{3+}-Cl^- distance in

the present work is close to 2.68Å from the neutron diffraction [19]. The small phase shift observed in the XAFS function (Figure 1) is attributed to the difference of 0.04Å, as shown in the Table 1(b). As well as $GdCl_3$, the CN decreased to 6.1 by mixing with LiCl-KCl eutectic. On the other hand, the Tb^{3+}-Cl^- distance did not change. Therefore, there is no phase shift in the Figure 2. What we should pay attention here is high similarity of fitting parameters between 10%$GdCl_3$ (Table 1(a)) and 1.5%$TbCl_3$ (Table 1(c)) mixture melts. Both mixture melts show almost the same parameter in spite of their different crystal structure (UCl_3-type in $GdCl_3$ and $PuBr_3$-type in $TbCl_3$) at room temperature. It can be concluded that the stabilized octahedral co-ordination structure is predominant in both mixtures.

It is well known that YCl_3 shows very small volume change at melting [20]. We reported from the systematic XAFS analysis [1] that the 1st Y^{3+}-Cl^- distance and its CN did not change by mixing with LiCl-KCl. Similar results are expected for $DyCl_3$, since crystal structure of $DyCl_3$ is almost the same as that of YCl_3. The XAFS measurements of molten $NdCl_3$ and $DyCl_3$ using L_3-edge were carried out by Matsuura *et al.*[21]. They also reported that the change by melting for $DyCl_3$ was smaller than that for $NdCl_3$. As can be seen in the Table 1(c), the CN and the 1st Dy^{3+}-Cl^- distance did not change either by melting or by mixing. It is interesting behaviour, since the two previous systems show more contrasted results by melting and/or mixing. Parameters in the pure melt are close to those of mixtures of $GdCl_3$ and $TbCl_3$. It means that the octahedral co-ordination structure is already formed in the pure $DyCl_3$ melt. Only Debye-Waller factor and cumulants changed by the mixing. It suggests that the octahedral $(DyCl_6)^{3-}$ co-ordination is further stabilized by the mixing.

Table 1 Curve fitting results of solid and molten $RECl_3$ and their mixture with LiCl-KCl eutectic. "Residual" parameters are defined as $R = \sum_{i=1}^{N} \left| k^3 \chi_{\exp}(k) - k^3 \chi_{cal}(k) \right| / \sum_{i=1}^{N} \left| k^3 \chi_{\exp}(k) \right|$.

(a)$GdCl_3$

	T(K)	$S_j^2(k)$	N_j	r_{ij}(Å)	σ_j^2(Å^2)	C3(10^3Å^3)	C4(10^4Å^4)	residual
solid $GdCl_3$	R.T.	0.871	8.7	2.84	0.0127			4.83
molten $GdCl_3$	923	0.830	6.5	2.74	0.0178	1.884	0.409	2.83
molten 10%$GdCl_3$ in LiCl-KCl	853	0.884	6.1	2.69	0.0110	1.114	0.495	1.92

(b)$TbCl_3$

	T(K)	$S_j^2(k)$	N_j	r_{ij}(Å)	σ_j^2(Å^2)	C3(10^3Å^3)	C4(10^4Å^4)	residual
solid $TbCl_3$	R.T.	0.866	7.9	2.73	0.0116			5.88
molten $TbCl_3$	950	0.834	6.8	2.69	0.0160	1.256	0.672	3.94
molten 1.5%$TbCl_3$ in LiCl-KCl	823	0.848	6.1	2.68	0.0113	1.232	0.285	3.63

(c)$DyCl_3$

	T(K)	$S_j^2(k)$	N_j	r_{ij}(Å)	σ_j^2(Å^2)	C3(10^3Å^3)	C4(10^4Å^4)	residual
solid $DyCl_3$	R.T.	0.911	6.2	2.67	0.0035			4.48
molten $DyCl_3$	1000	0.900	6.0	2.67	0.0098	0.561	0.064	4.00
molten 1%$DyCl_3$ in LiCl-KCl	800	0.923	6.1	2.68	0.0059	0.344	0.020	3.99

Molten UCl_3 in LiCl-KCl eutectic

XAFS functions $k^3\chi(k)$ of molten 5% and 17%UCl_3 in LiCl-KCl eutectic at 823K are shown in Figure 3. The XAFS functions are very noisy in comparison with $RECl_3$ systems in the Figure 1 and the Figure 2. It is due to a strong X-ray absorption by the quartz cell. We used the cell with 1.0mm thick windows for safety reasons. Therefore, only 4% of the incident X-ray beam passes through the cell at 17.167keV (energy of the U L_3-edge). Fourier transforms $|FT(k^3\chi(k))|$ of the XAFS function are shown in Figure 4, together with curve fitting results. Structural parameters obtained from the fitting are listed in Table 2. The nearest U^{3+}-Cl^- distance is 2.79Å for 17%UCl_3 and 2.77Å for 5%UCl_3, respectively. These values are shorter than 2.84Å in the pure UCl_3 melt obtained by the X-ray diffraction analysis [13]. The CN of Cl^- ion around U^{3+} is 6.9 for 17%UCl_3 and 6.6 for 5%UCl_3. The obtained CN values are slightly larger than 6, though they are smaller than CN=8.0 in the pure melt. Also in the previous work [22], we obtained the CN of 7.3 for 15%UCl_3. These results suggest that molten UCl_3 does not change to the stabilized octahedral co-ordination structure by the mixing with LiCl-KCl, in contrast with molten $RECl_3$ (RE=Gd, Tb and Dy).

Table 2 Curve fitting results and MD simulation results of UCl_3 systems.

	T(K)	$S_j^2(k)$	N_j	r_{ij}(Å)	σ_j^2(Å^2)	C3(10^3Å^3)	C4(10^4Å^4)	method
(Exp.)								
5%UCl_3	823	0.726	6.6	2.77	0.0192	0.534	1.398	This work
17%UCl_3	823	0.711	6.9	2.79	0.0201	1.316	1.946	This work
15%UCl_3	823	0.736	7.3	2.82	0.0270	0.922	------	XAFS [22]
UCl_3	1200		8.0	2.84				XRD [13]
(MD)								
5%UCl_3	823		6.8	2.79				MD
17%UCl_3	823		7.2	2.80				MD
50%UCl_3	973		7.6	2.81				MD
UCl_3	1173		7.9	2.81				MD

Figure 3 XAFS function $k^3\chi(k)$ of molten 17% and 5%UCl_3 in LiCl-KCl eutectic (solid line: experimental, circle: simulation)

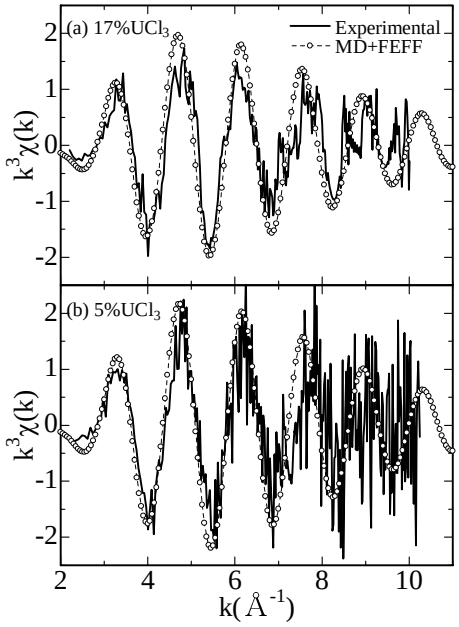

Figure 4 Fourier transform magnitudes |FT($k^3\chi(k)$)| of molten 17% and 5%UCl_3 in LiCl-KCl eutectic (solid line : experimental, dashed line : fitting curve)

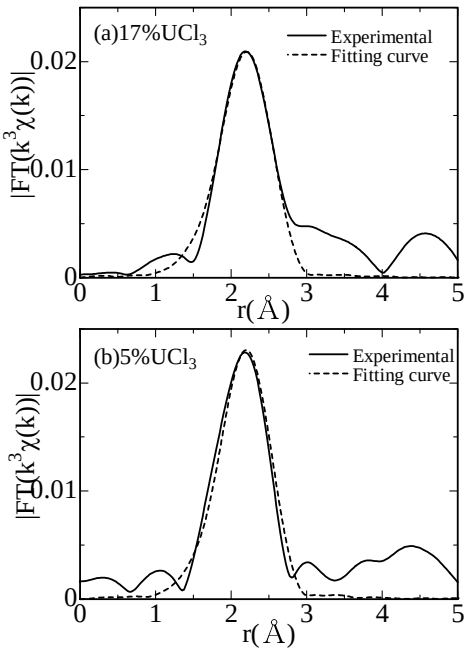

XAFS curves simulated by the combinational use of MD and FEFF8 are shown in the Figure 3 as circles. They were obtained by averaging 25000 FEFF calculations. It means that 25000 clusters of 200000 MD steps calculations were used in these XAFS simulations. Simulated XAFS functions are in good agreement with experimental ones. Structural parameters obtained from the simulation are listed in the Table 2. The CN and interionic distance of the 1st U^{3+}-Cl^- correlation in the experimental and the simulated results are plotted in Figure 5. In the simulation, the 1st U^{3+}-Cl^- distance showed very small change. On the other hand, the simulation resulted in decreases of the CN by the mixing as the XAFS analysis shows. The simulated CN for the pure UCl_3 melt is 7.9. It is almost the same as that in the XRD. On the other hand, the simulated CN for 5%UCl_3 mixture melt is 6.8. The simulated CN of the 1st U^{3+}-Cl^- correlation is still larger than 6, though it is clearly smaller than that of the pure melt. It is similar to the experimental result.

Figure 5 The separation distance and the CN of the 1st U^{3+}-Cl^- correlation for UCl_3-(LiCl-KCl eutectic) system obtained from the XAFS analysis and the MD simulation

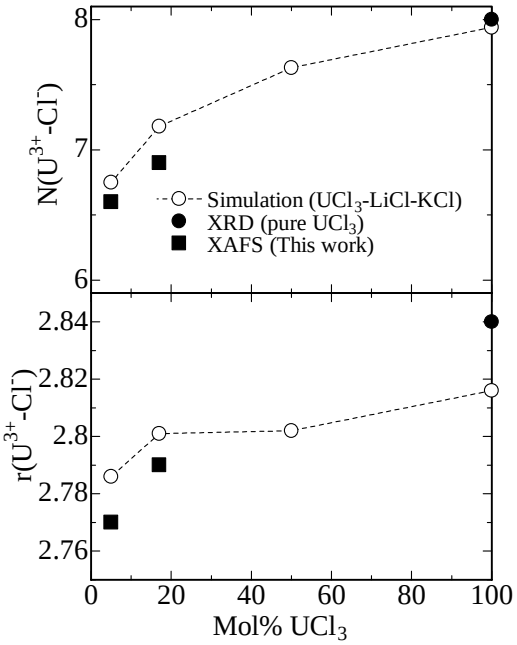

Figure 6 (a) shows distribution ratio of the CN for each composition of UCl_3. It can be seen that the CN is mainly 8 for the pure melt and the mixture with 50%UCl_3 composition. On the other hand, most predominant CN was 7 in 17% and 5%UCl_3 mixture melts. Similar analysis was reported by Glover and Madden [23] for molten $LaCl_3$ in NaCl and CsCl solvents. According to their report, the averaged CN is 6.48 for 5%$LaCl_3$-NaCl and 6.01 for 5%$LaCl_3$-CsCl. Thus, we had expected that the CN decreased to about 6 by the mixing. In other words, the octahedral 6-fold co-ordination is formed and stabilized by the mixing with alkali chlorides. However, the averaged CN in the 5%UCl_3 mixture melt was about 7. Also in the XAFS data analysis, the CN was clearly larger than 6 as shown in the Table 2. Figure 6 (b) shows the CN distribution ratio for 5%UCl_3-LiCl and 5%UCl_3-KCl binary mixtures. It is clear that the solvent effect is completely different between LiCl and KCl. Mixing with KCl, U^{3+} shows very stable the 6-fold $(UCl_6)^{3-}$ co-ordination structure, since ratio of the CN=6 was beyond 95%. On the other hand, the CN was mainly 8 for 5%UCl_3-LiCl system. It is similar to the result of pure melt. Formation and stabilization of the 8-fold $(UCl_8)^{5-}$ structure in place of the octahedral structure is not likely in UCl_3-LiCl system, since the ratio of the CN=8 did not change by

the mixing. Mixing with LiCl does not affect the co-ordination structure. The result shows that the mixture of UCl_3 with LiCl-KCl eutectic melt has intermediate value between them.

Figure 6 The distribution ratio of the CN in (a) 5%UCl_3 in LiCl-KCl and (b) 5%UCl_3 in LiCl and KCl

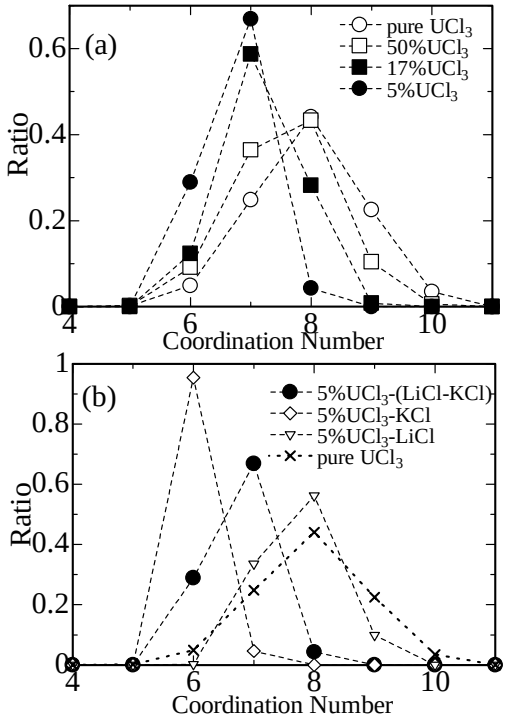

Conclusion

The XAFS analysis and the MD simulation of molten $RECl_3$ (RE=Gd, Tb and Dy) and UCl_3 in LiCl-KCl were performed to elucidate structural changes by the mixing. In both of $GdCl_3$ and $TbCl_3$, the 1st RE^{3+}-Cl^- distances and their CNs decreased by the melting and/or by the mixing. In the mixture state, they have similar structural parameters corresponding to the stable octahedral co-ordination structure $(RECl_6)^{3-}$. On the other hand, the analyzed result implies that molten pure $DyCl_3$ has the stable $(DyCl_6)^{3-}$ structure. By the mixing, it is further stabilized. The Dy in $DyCl_3$ adopts the octahedral co-ordination already by melting, whereas $GdCl_3$ and $TbCl_3$ need to be mixed with the LiCl-KCl eutectic to form $(RECl_6)^{3-}$. Although the $RECl_3$ systems have different crystal structure, all three adopt in the mixture system with LiCl-KCl eutectic the octahedral co-ordination $(RECl_6)^{3-}$ with similar structural parameters except for the Debye-Waller factor.

In molten UCl_3 systems having a larger cation, the CN decreased from 8 in the pure melt to 6.9 in 17%UCl_3 and 6.6 in 5%UCl_3 mixtures. However, they are still larger than 6. It can be seen from the MD simulation of binary UCl_3-LiCl and UCl_3-KCl systems that a mixing effect is different between LiCl and KCl. Molten UCl_3 forms the stabilized $(UCl_6)^{3-}$ co-ordination by the mixing with KCl. On the other hand, the mixing with LiCl does not give any stable co-ordination structures. It can be estimated from the XAFS and the MD results that a stable octahedral co-ordination structure like $(UCl_6)^{3-}$ is not formed in UCl_3-LiCl binary system. The XAFS result showing the CN larger than 6 may be assigned to the mixing effect by LiCl.

Acknowledgements

The authors gratefully acknowledge the interest and encouragement of Dr.J.Mizuki and Dr.K.Aoki (JAEA/SPring-8). The MD simulations in the present work were performed by using the Altix3700Bx2 and the PC cluster-A in the Center of Computational Science & E-systems (CCSE) of the JAEA.

References

[1] Y. Okamoto, M. Akabori, H. Motohashi, H. Shiwaku, T. Ogawa, J. Synchrotron Rad., **8**(2001)1191.

[2] Y. Okamoto, H. Shiwaku, T. Yaita, H. Narita, H. Tanida, J. Mol. Struct., **641**(2002)71.

[3] Y. Okamoto, H. Motohashi, Z. Naturforsch., **57a**(2002)277.

[4] Y. Okamoto, T. Yaita, K. Minato, Electrochemistry, **73**(2005)745.

[5] Y. Okamoto, T. Yaita, K. Minato, J.Mol.Struct., **749**(2005)70.

[6] Y. Okamoto, M. Akabori, H. Motohashi, A. Itoh, T. Ogawa, Nucl.Instr.Meth.Phys.Res. A, **487**(2002)605.

[7] H. Shiwaku, T. Mitsui, K. Tozawa, K. Kiriyama, T. Harami, T. Mochizuki, 8th International Conference on Synchrotron Radiation Instrumentation, AIP Conference Proceedings, **705**(2004)659.

[8] H. konishi, A. Yokoya, H. Shiwaku, H. Motohashi, T. Makita, Y. Kashihara, S. Hashimoto, T. Harami, T.A. Sasaki, H. Maeta, H. Ohno, H. Maezawa, S. Asaoka, N. Kanaya, K. Itoh, N. Usami, K. Kobayashi, Nucl. Instr. Meth. Phys. Res.A, **372**(1996)322.

[9] T. Ressler, J. Synchrotron Rad., **5**(1998)118.

[10] A.L. Ankudinov, J.J. Rehr, Phys. Rev. **B56**(1997)R1712.

[11] Y. Okamoto, Nucl. Instr. Meth. Phys. Res. A, **526**(2004)572.

[12] Y. Okamoto, P.A. Madden, J. Phys. Chem. Sol., **66**(2005)448.

[13] Y. Okamoto, P. Madden, K. Minato, J. Nucl. Mater., **344**(2005)109.

[14] P.A. Madden, M. Wilson, J. Phys.; Condens. Matter, **12**(2000)A95.

[15] F. Hutchinson, M. Wilson, P.A. Madden, Mol. Phys., **99**(2001)811.

[16] R. Brooks, A. Davis, G. Ketwaroo, P.A. Madden, J. Phys. Chem. B, **109**(2005)6485.

[17] C. Au, R. Au, Acta. Cryst., **23**(1967)1112.

[18] J.D. Forrester, A. Zalkin, D.H. Templeton, J.C.Wallmann, Inorg. Chem. **3**(1964)185.

[19] J.C. Wasse, P.S. Salmon, J. Phys.: Condens. Matter, **14**(2002) L703.

[20] J. Mochinaga, K. Irisawa, Bull. Chem. Soc. Japan, **47**(1974)364.

[21] H, Matsuura, A.K. Adya, D.T. Bowron, J. Synchrotron Rad., **8**(2001)779.

[22] Y. Okamoto, M. Akabori, A. Itoh, T. Ogawa, J. Nucl. Sci. Technol. Suppl., **3**(2002) 638.

[23] W. Glover, P.A. Madden, J. Chem. Phys., **121**(2004)7293.

SESSION II

SOLID STATE CHEMISTRY AND PHYSICS OF THE ACTINIDES

Chair: David K. Shuh

RESONANT X-RAY SCATTERING AND MULTIPOLAR ORDER IN ACTINIDE DIOXIDES

R. Caciuffo
European Commission, Joint Research Centre, Institute for Transuranium Elements, Postfach 2340, Karlsruhe, D-76125 Germany

Abstract

The discovery in 2002 [1] of electric quadrupole ordering in the NpO_2 opened a new chapter in the understanding of the low-temperature ground states of actinide dioxides, insulating compounds with the simple cubic CaF_2 crystal structure and general formula $U_{1-x}Np_xO_2$ ($0 \leq x \leq 1$). The phenomenon found at 25 K in NpO_2 is that the 5*f* charge distribution develops an anisotropic component, with long-range ordering of the charge quadrupoles driven by a primary magnetic octupolar order parameter belonging to the totally symmetric irreducible representation of L = 3 in D_{3d} symmetry ($\Box_1$). The experiments consist of tuning the photon energy to the actinide *M* absorption edge (at which photon energy core 3*d* electrons are promoted to the partially occupied 5*f* valence states), and then, once the repeat of the anisotropic charge distribution is known, to measure the azimuthal distribution of the scattered resonant x-ray intensity. This intensity distribution is related to the symmetry of the 5*f* anisotropic charge distribution. The experiments were performed at the European Synchrotron Radiation Facility (ESRF) in Grenoble, France, with the single crystals mounted in ITU.

NpO_2 shows no measurable magnetic dipole component. In 2003 experiments were performed [2] on a single crystal with $x = 0.25$. Dipole ordering was found on both the U and Np ions, and quadrupolar ordering was also found associated with both ions. However, these were different from those in pure NpO_2. Whereas a longitudinal (L) 3-k configuration was found for NpO_2, the $x = 0.25$ sample was found to have a transverse (T) 3-k configuration. The understanding of these different configurations then allowed an experiment to be performed in 2005 on a single crystal of UO_2. The azimuthal dependence of the intensity from non-specular reflections reveals 3-k T antiferro-electric-quadrupolar order also UO_2 [3]. The complication in UO_2 is that both dipole ordering and an internal distortion of the oxygen atoms due to the quadrupole ordering are present; these have contrived to make it difficult to observe directly the quadrupole ordering in UO_2, although such ordering was predicted almost 40 years ago [4], and the oxygen displacements reported 30 years ago [5]. These experiments also suggest a qualitative explanation of the unusual behaviour [5] of the mixed oxides with $0.40 < x < 0.80$. In this region there is competition between the L and T quadrupole ordering, resulting in quadrupolar frustration and only short-range dipole and quadrupole ordering.

References:

[1] J.A. Paixão *et al.*, Phys. Rev. Lett. **89**, 187202 (2002).
[2] S.B. Wilkins *et al.*, Phys. Rev. B **70**, 214402 (2004).
[3] S.B. Wilkins *et al.*, Phys. Rev. B Rapid Comm. **73** , 060406 (2006).
[4] S.J. Allen, Phys. Rev **167**, 492 (1968).
[5] J.Faber *et al.*, Phys. Rev. Lett. **35**, 1770 (1975).

SPECTRAL STUDY OF THE CHEMICAL BOND NATURE IN URANIUM COMPOUNDS USING X-RAY AND SYNCHROTRON RADIATION

Yury Teterin
RRC "Kurchatov Institute", Moscow, Russia

Abstract

The chemical bond nature in the uranium compounds UO_3, UO_2, UF_4, UO_2F_2 was studied on the basis of the X-ray photoelectron, conversion, resonant and non-resonant emission, and Auger spectral structure parameters of the outer (OVMO, 0-13 eV binding energy) and inner (IVMO, 13-40 eV binding energy) valence molecular orbitals taking into account the relativistic Xα-discrete variation calculation results reflecting the uranium environment in these compounds. On the basis of the experimental and theoretical results the MO diagrams were built. They reflect an up-to-date view point on the nature of the chemical bond in uranium compounds. The U5f electrons were shown to be able to participate directly in the chemical bond. The U5f electrons weakly participating in the chemical bond in UO_2 and UF_4 were shown to be strongly localized on the ions. The experimental evaluation of the contribution of the U6p electronic states to several MOs was done. As a result the U6p electrons were found to participate significantly in the formation of the IVMO, as well as the OVMO. The composition and the sequence order of the IVMO in the binding energy range 13-40 eV was determined. It has to be noted that the IVMO (13-40 eV) formation is typical for compounds of several elements in the periodic Table and it is very important in chemistry, biology and physics.

Introduction

While studying uranium compounds with the X-ray photoelectron spectroscopy (XPS) method it was traditionally suggested that only low binding energy incompletely filled electronic shells (~0-13 eV BE) participate in the chemical bond formation. To a certain degree, it was because of the wide use of visible and ultraviolet excitation sources in the atomic and molecular spectroscopy. X-ray emission studies were also pointed to these electron energies. Despite the fact that quantum mechanics does not forbid relatively deep (~13-40 eV BE) filled electronic shells to participate in the inner valence molecular orbitals (IVMO) formation, their influence on the interatomic binding in compounds comparing to the outer valence molecular orbitals (OVMO, ~0-13 eV BE) influence was neglected. However, during the last few years it was shown theoretically for uranium oxides [1-3] and experimentally for other elements [4] that under certain conditions the IVMOs can form in compounds of any element of the periodic Table. This is a novel and extremely important fact in solid-state physics and chemistry.

This work considers the new data on the nature of the chemical bond using UO_2, γ-UO_3, UF_4 and UO_2F_2 as examples. These data were obtained using the modern X-ray spectral methods, such as: X-ray photoelectron, conversion electron, non-resonant and resonant X-ray $O_{4,5}$(U) emission, near $O_{4,5}$(U) edge absorption, resonant photoelectron and oxygen Auger spectroscopies; as well as the relativistic electronic structure calculation for the UO_8^{12-} (O_h), $[(UO_2)O_4]^{6-}$ (D_{4h}), $[(UO_2)F_6]^{4-}$ (D_{6h}) and UF_8^{4-} (C_{4v}) clusters reflecting the uranium environments in these compounds. Since the IVMO formation is general, the data for uranium dioxide can be used for the study of the chemical bond nature not only in actinide compounds, but also in compounds of other elements.

Experimental

XPS and OKLL Auger spectra of the studied compounds [5] were measured with an electrostatic spectrometer HP 5950A Hewlett-Packard using monochromatized $AlK_{\alpha 1,2}$ ($h\nu$=1486.6 eV) radiation in a vacuum of $1.3 \cdot 10^{-7}$ Pa at room temperature. The device resolution measured as full width at the half-maximum (FWHM) of the $Au4f_{7/2}$ line on the standard rectangular golden plate was 0.8 eV. The binding energies (eV) were measured relative to the binding energy of the C1s electrons from hydrocarbons adsorbed on the sample surface accepted to be equal to 285.0 eV. The FWHM were measured relative to the width of the C1s line of hydrocarbons accepted to be equal to 1.3 eV. The error in determination of electron binding energies and the line widths did not exceed 0.1 eV and that of the relative line intensities was less than 10%. The conversion electron spectra (CES) were measured with the same spectrometer using an extra accelerating electronic system and widened up to ~2500 eV energy range without any significant changes of the device parameters. The sample preparation was described in [5].

X-ray $O_{4,5}$(U) emission spectra (XES) of UO_2 were measured with a spectrometer RSM-500 with an energy resolution of 0.3 eV. The spectra were recorded at the X-ray tube voltage 1 KV (15 mA) and 3 KV (5 mA). The samples were settled on a silver plate which served as an X-ray tube anode [6].

Resonant X-ray $O_{4,5}$(U) emission spectra (RXES) were collected at the undulator Beamline 7.0.1 of the Advanced Light Source (ALS) at the Lawrence Berkeley National Laboratory [7]. Experiments were done in the XES branchline chamber at approximately 5×10^{-9} Torr. The RXES spectra were measured with the beam incident at ~75° to the substrate normal. The beam size was less than 1 mm^2. The grazing-incidence fluorescence grating spectrometer with a two-dimensional position sensitive detector was used to measure the RXES spectra. The energies were calibrated using the elastic scattering features. The total electron yield NEXAFS spectra were measured with the beam incident normal to the substrate in current mode. Resonant photoelectron (RXPES) and total electron yield

spectra of UO_2 were measured at the Russian-German Beamline BESSY II in Berlin. A thin UO_2 film on metallic uranium foil was used as a sample [8].

The self-consistent field relativistic X_α discrete variation (SCF X_α-DV) calculation results for the UO_8^{12-} (O_h) cluster at R_{U-O}=2.37 Å (see for example [5]), were used for interpretation of the XPS and other spectral data.

Results and discussion

X-ray photoelectron spectroscopy (XPS).

The low binding energy (0-40 eV) XPS from uranium compounds can be conditionally subdivided into the two ranges (Figure 1). The first between 0–13 eV shows the structure attributed to the OVMOs built mostly from the incompletely filled outer U5f,6d,7s and O2p AOs. The second from 13-40 eV shows the IVMO related fine structure. These IVMOs are built mostly from the completely filled inner valence U6p and O2s AOs. The IVMO spectral range exhibits pronounced peaks and can be subdivided into the six components. The OVMO XPS structure has typical features and can be subdivided into the four components (Figure 1). Taking into account the MO compositions and photoionization cross-sections [9] the theoretical spectral intensities for some energy ranges were determined [10]. Despite the approximation imperfections, there is a good qualitative agreement between the theoretical and experimental data. The similar considerations can be done for the spectra of the valence electrons of γ-UO_3 [11], UO_2F_2 [12], UF_4 (Figure 2) [5].

Figure 1: XPS (a) and CES (b) from UO_2. Theoretical data are given under the spectra as vertical bars. The subtracted background and spectra decomposition are shown. Experimental intensities are given in arbitrary units and the theoretical intensities are normalized in %.

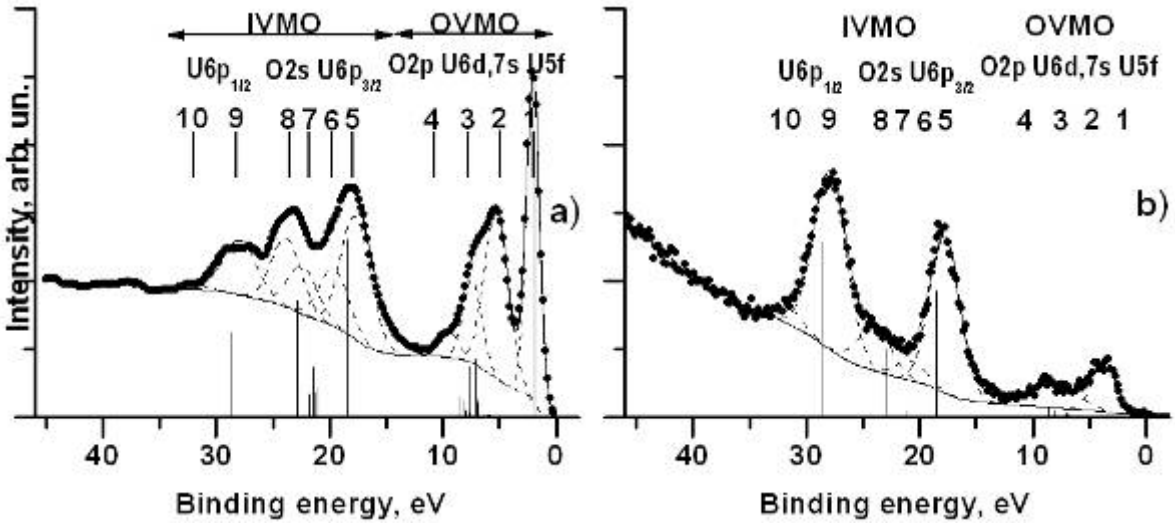

Figure 2. XPS (a) and CES (b) from UF_4. Theoretical data are given under the spectra as vertical bars. The subtracted background and spectra decomposition are shown. Experimental intensities are given in arbitrary units and the theoretical intensities are normalized in %.

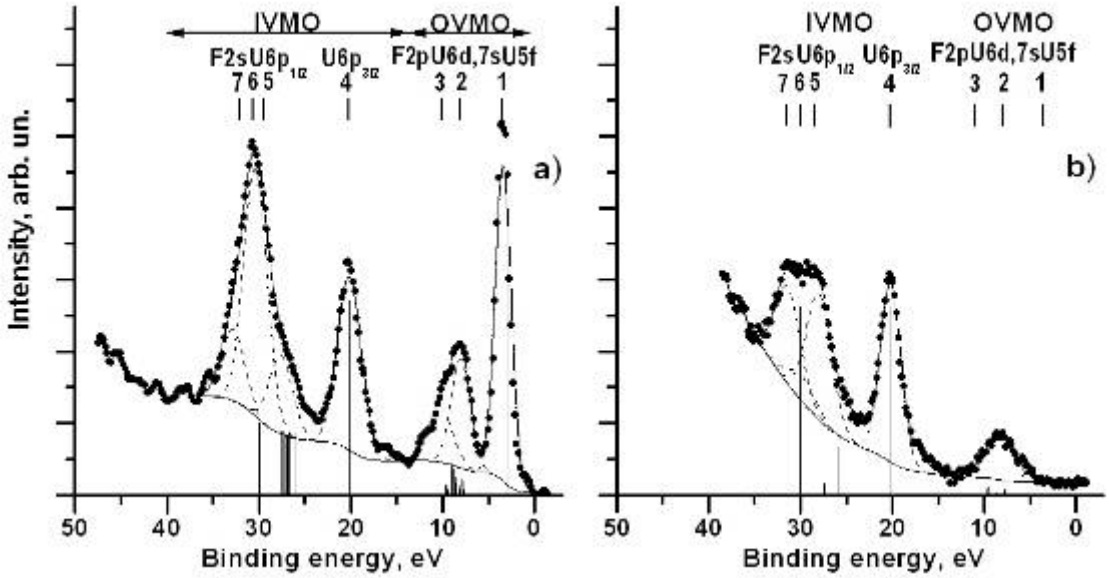

Taking into account the relativistic calculations for the UO_8^{12-} (O_h), $[(UO_2)O_4]^{6-}$ (D_{4h}), $[(UO_2)F_6]^{4-}$ (D_{6h}), UF_8^{4-} (C_{4v}) clusters in the MO LCAO (molecular orbitals as linear combinations of atomic orbitals) approximation a schematic diagram of the MOs can be built (Figures 3-4). This diagram enables the understanding of the real XPS structure of the studied compounds. For example, in this approximation for UO_2 one can formally separate the antibonding $9\gamma_8^-(5)$, $8\gamma_6^-(6)$ and corresponding bonding $8\gamma_8^-(8)$, $7\gamma_6^-(9)$ IVMOs, as well as the quasiatomic (in a certain approximation) $4\gamma_7^-$, $5\gamma_7^+(6)$, $8\gamma_8^+$, $8\gamma_6^+(7)$, $7\gamma_6^-$ IVMOs attributed generally to the O2s – $U6p_{1/2}$ electrons (Figure 3). For UF_4 one can formally separate the antibonding $5\gamma_7$, $7\gamma_6(4)$ and $6\gamma_6(5)$ and corresponding bonding $1\gamma_7$, $3\gamma_6(6)$ and $2\gamma_6(7)$ IVMOs, as well as the quasiatomic $4\gamma_7$, $3\gamma_7$, $2\gamma_7$, $5\gamma_6$ and $4\gamma_6(6)$ IVMOs attributed generally to the F2s electrons (Figure 4).

Figure 3. MO schematic diagram for the UO_8^{12-} (O_h) cluster built on the basis of the theoretical and experimental data. Chemical shifts are not indicated. Arrows show some experimentally measurable binding energy differences. Experimental binding energies (eV) are given to the left and the energy scale is not to scale.

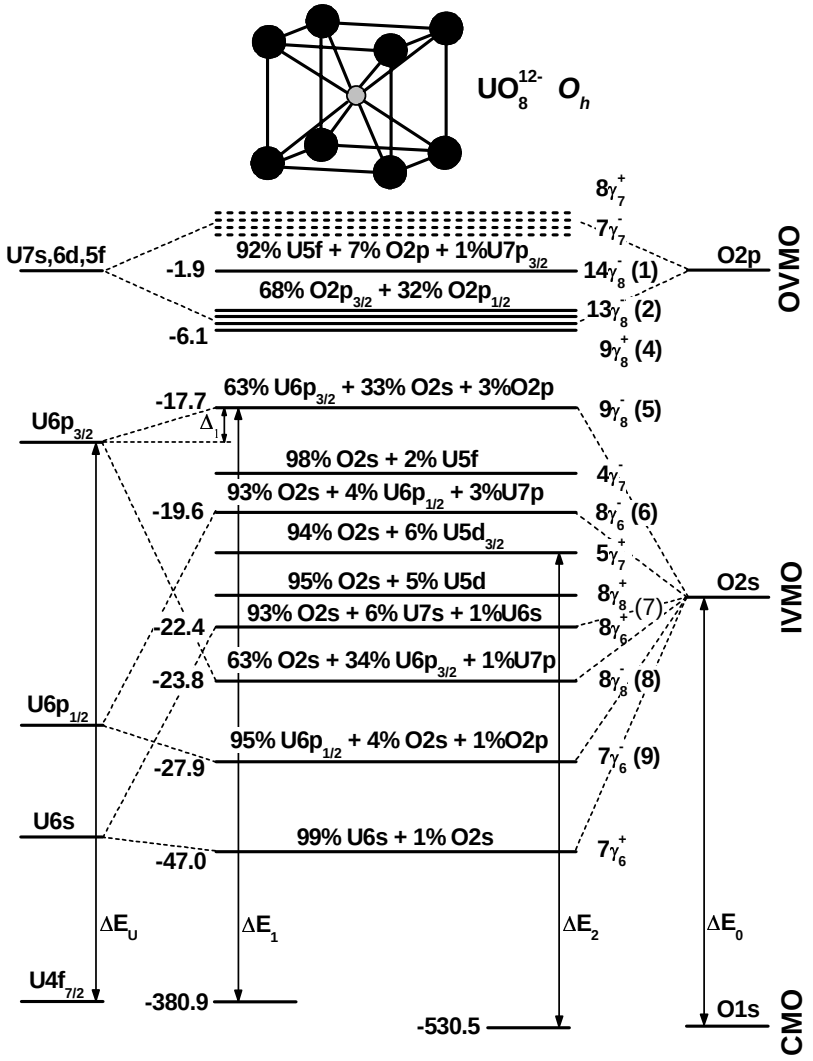

The sharp peak at 3.8 eV is attributed to the U5f electrons weakly participating in the chemical bond, and the outer valence band – to the outer valence U5f,6d,7s,7p and F2p AOs and to a lesser degree – to the U6p AO. For γ-UO_3 [11] experimental evidence for the fact that the U5f electrons can participate in the chemical bonding in γ-UO_3 without loosing their f-nature was established. However, for UF_4 such a strict categorical conclusion could not be made. Indeed, the experimental intensity ratios OVMO/IVMO with (and without) taking into account the U5f intensity at 3.8 eV are 0.60 (0.24), which slightly differs from the corresponding theoretical values 0.76 (0.42) [5]. This indicates that the U5f electron participating in the chemical bond is either strongly delocalized or looses its f-nature. To the greatest degree, the direct participation of the U5f electrons in the chemical bond was observed in γ-UO_3 [8], and to a lesser degree in UO_2 [10]. Unlike γ-UO_3 and UO_2, for which a certain agreement between the theory and experiment on the direct participation of the U5f electrons in the chemical bond was observed, in the case of UF_4 this participation can be much lower because of the higher fluorine electronegativity and higher uranium-fluorine interatomic distance, which can result in

the delocalization of the U5f electrons and decrease of the U5f photoionization cross-section. In the IVMO XPS range for UF_4 the best agreement in the binding energy was reached only for the $5\gamma_7$, $7\gamma_6$ (4) and $2\gamma_6(7)$ orbitals characterizing the spectral width.

Figure 4: MO schematic diagram for UF_8^{4-} (C_{4v}) cluster built on the basis of the theoretical and experimental data. Chemical shifts are not indicated. Arrows show some experimentally measurable binding energy differences. Experimental binding energies (eV) are given to the left and the energy scale is not to scale.

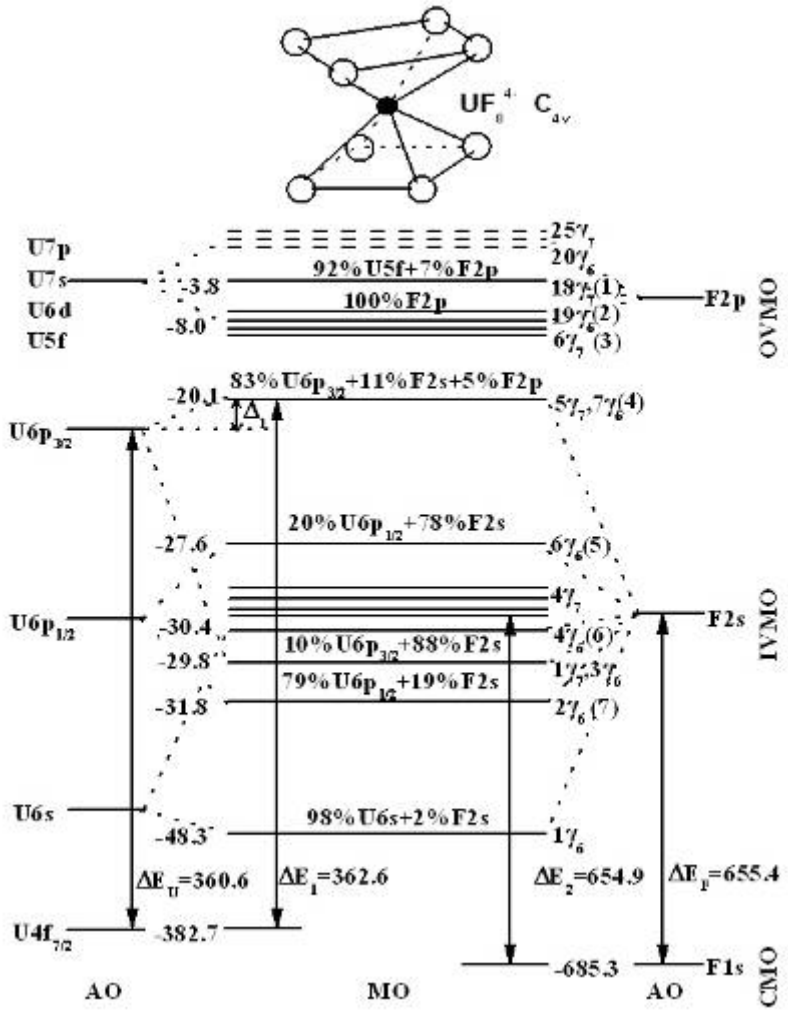

Conversion electron spectroscopy (CES)

One of the experimental confirmations for IVMO formation in the studied compounds is the high resolution conversion electron spectral structure [5, 10, 11]. The qualitative identification of the CES spectra was done on the basis of the XPS parameters using the OVMO and IVMO conception. As a result, it became obvious that the CES parameters can also be a quantitative measure of the theoretical calculation correctness.

Since the U6p conversion cross-section is much higher than that for the other electronic shells, the CES spectrum from the studied compounds reflect the U6p partial electronic density, and the $U6p_{1/2}$ cross-section is about 2.1 times higher than the $U6p_{3/2}$. With this in mind, one can note a satisfactory qualitative agreement between the XPS and CES data (Figures 1-2). Comparison of the XPS and CES data yields the three important conclusions. First, the U6p shell participates effectively in the IVMO formation. Secondly, the U6p shell participates significantly in the OVMO formation. Lastly, the U5f electrons (for example, for UO_2) from the $14\gamma_8^-(1)$ OVMO at 1.9 eV and electrons from the quasiatomic $4\gamma_7^-(6)$, $5\gamma_7^+(6)$, $8\gamma_8^+(7)$, $8\gamma_6^+(7)$ IVMOs at 19.6 and 22.4 eV, as expected, are practically not observed in the CES spectrum in contrast to the XPS spectrum. The $9\gamma_8^-(5)$, $8\gamma_8^-(8)$, $7\gamma_6^-(9)$ IVMO energies in CES spectrum slightly differ from the corresponding theoretical values and to a greater extent agree with the experimental XPS parameters. Similar data were obtained for γ-UO_3 [11] and UF_4 (Figure 2, [5]).

X-ray $O_{4,5}$(U) emission spectroscopy (XES)

X-ray $O_{4,5}$(U) emission spectra reflecting the $U5d_{5/2,3/2}$←$U6p_{3/2,1/2}$,np,5f [$(O_{4,5}(U)$←$P_{2,3}$,$O_6(U)$] electronic transitions in UO_2 [6], γ-UO_3 [6], UO_2F_2 [12] were observed in the photon energy range $60<h\nu<120$ eV and in the high energy region interfered with the absorption spectrum, which distorted its structure (see, for example, Figure 5). Earlier [13] the low energy structure was associated with the ternary electronic transitions involving the core uranium shells $U5d_{5/2,3/2}$←$U6p_{3/2,1/2}$ (Figure 5). Ignoring participation of the $U6p_{3/2,1/2}$ electrons in the IVMO formation one can not identify the X-ray $O_{4,5}$(U) emission fine spectral structure.

Figure 5. X-ray $O_{4,5}$(U) emission spectra reflecting the U5d←U6p,5f,np transitions in UO_2 measured at 1 and 3 kV.

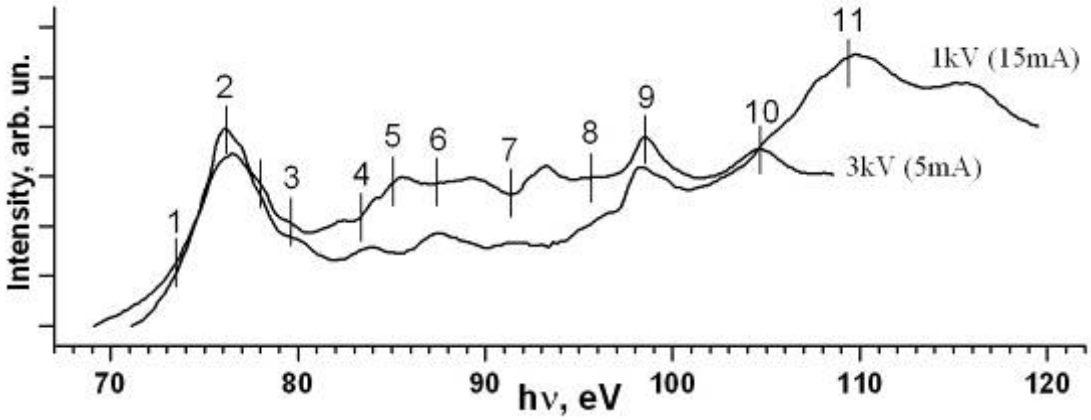

A work [6] for the fine structure interpretation took into account the fact that the U6p shell is not core and participates effectively in the IVMO formation. The low energy band in the $O_{4,5}$(U) XES from UO_2 is wide and poorly resolved despite relatively high instrumental resolution in the energy range 70–80 eV (Figure 5). It can be partially explained by extra electronic transitions (Table 1). Another reason for this can be formation of the higher uranium oxidation state oxides on the sample surface (the vacuum was 5×10^{-6} Torr), which can result in a significant contribution to the emission at 1 kV.

As the voltage on the X-ray tube increases to 3 kV, the contribution to the emission from the sample bulk (i.e. UO_2) grows and the spectrum changes [6]. Thus, the peaks in the low energy range at

73.5 eV, 76.2 eV, 79.6 eV, a small shoulder at 85.1 eV and two peaks at 95.8 eV and 104.7 eV become sharper, while the peak at 91.4 eV diminishes. Decomposition of the surface in this case can not be excluded. Taking all this into account one can attribute the peaks at 91.4 and 98.4 eV to the electronic transitions from the outer valence band to the $U5d_{5/2,3/2}$ shells, and the ones at 95.8 and 104.7 eV – to the transitions $U5f \rightarrow U5d_{5/2,3/2}$. It has to be noted that the XPS and XES data are in a good qualitative agreement (Figure 5, Table 1).

In the low energy transition range involving the bonding MOs ($U5d_{5/2} \leftarrow 8\gamma_8^-$) at 73.5 eV for UO_2 calculated on the basis of the XPS data no sharp peaks were observed (Figure 5), while the peaks reflecting the transitions from the corresponding antibonding MOs ($U5d_{5/2} \leftarrow 8\gamma_8^-$ and $5d_{3/2} \leftarrow 8\gamma_8^-$) are pronounced, although less intense. The calculation results show that if the antibonding $9\gamma_8^-$ orbital consists of 63% of U6p states, the corresponding bonding $8\gamma_8^-$ one of 34% (Figure 3). Therefore, the low intensity transitions $U5d_{5/2} \leftarrow 8\gamma_8^-$ in UO_2 can hardly be separated from the wide band. However, this consideration can be done only in the approximation that the MOs keep partial AO nature. A more strict comparison requires precise theoretical calculations for the emission spectra.

Table 1. X-ray $O_{4,5}(U)$ emission ($U5d_{5/2,3/2} \leftarrow U6p,5f,np$) transitions (eV) in metallic uranium U and UO_2 on the basis of the XPS and XES data.

U				UO_2			
N	Transition	XPS	XES	N	Transition	XPS	XES
				1	$U5d_{5/2} \leftarrow 8\gamma_8^-$	73.5	73.5
1*	$U5d_{3/2} \leftarrow U6p_{1/2}$	76.0		2	$U5d_{3/2} \leftarrow 7\gamma_6^-$	77.6	76.2
					–		78.0
2*	$U5d_{5/2} \leftarrow U6p_{3/2}$	77.4		3	$U5d_{5/2} \leftarrow 9\gamma_8^-$	79.6	79.6
				4	$U5d_{3/2} \leftarrow 8\gamma_8^-$	81.7	83.3
				5	$U5d_{3/2} \leftarrow 8\gamma_6^-$	85.9	85.1
3*	$U5d_{3/2} \leftarrow U6p_{3/2}$	86.0		6	$U5d_{3/2} \leftarrow 9\gamma_8^-$	87.8	87.4
				7	$U5d_{5/2} \leftarrow$ OVMO	91.2	91.4
4*	$U5d_{5/2} \leftarrow U5f_{7/2,5/2}$	95.4[a)]		8	$U5d_{5/2} \leftarrow 5f_{5/2}$	95.4	95.8
				9	$U5d_{3/2} \leftarrow$ OVMO	99.4	98.4
5*	$U5d_{3/2} \leftarrow U5f_{5/2}$	104.0[a)]		10	$U5d_{3/2} \leftarrow 5f_{5/2}$	103.6	104.7
				11			109.2

[a)] values obtained on the basis of the experimental evaluation taking into account the $U5d_{5/2,3/2}$–U5f binding energy difference for $UO_{2,06}$.

The obtained data show that the $O_{4,5}(U)$ XES structure of uranium compounds can be identified only taking into account the effective IVMO formation from, in particular, the relatively deep U6p and O(F)2s AOs. These results are another experimental confirmation of the effective IVMO formation in UO_2.

X-ray near $O_{4,5}(U)$ edge absorption spectroscopy (XAS)

The X-ray near $O_{4,5}(U)$ edge (near the U5d) absorption spectrum in the excitation energy range 90-120 eV exhibits unusual structure for the X-ray absorption spectra from solid materials. This structure consists of the two resonant bands of different widths and intensities. The total electron and

total fluorescence quantum yield spectra from uranium oxides were shown [14] to be similar by shape, energy position, and width and to differ only by the intensity ratio. Since the absorption edge of the less intense peak is 97.5 eV, which is close to the $U5d_{5/2}$ binding energy for UO_2 (97.3 eV), this peak was attributed to the $U5d_{5/2} \rightarrow U5f$ transition (Figure 6). In this case the $U5d_{3/2} \rightarrow U5f$ absorption peak is supposed to be at about 8 eV higher since the $U5d_{3/2}$ binding energy is 105.5 eV [8] and less intense due to the lower $U5d_{3/2}$ population and the selection rule (the total quantum number j=3/2 is less than j=5/2). This explains the shoulder at 107 eV in the quantum yield spectrum from UO_2. The work [15] considers in the ionic approximation for U^{4+} the transition $U5f^2(^3H_4) \rightarrow U5d^9 5f^3(^3G_3, {}^3H_4, {}^3I_5)$ and finds out that the low energy peak reflects generally the $U5d_{5/2} \rightarrow U5f^3$ transitions, and a shoulder at 107 eV is due to the $U5d_{3/2} \rightarrow U5f^3$ transitions. The main intensity of the higher energy peak was attributed to the $U5d \rightarrow U7p,8p$ and 6f transitions. The comparison shows that the low energy peak, apparently, must be attributed to the U5f vacant states. It has to be noted that right after these states the vacant U7p states are located, and the transitions $U5d \rightarrow U7p$ can take place (Figure 6). These data at least do not contradict the suggestion on the direct participation of the U5f electrons in the chemical bond. Indeed, attributing the XAS structure of UO_2 at 100 eV to the antibonding MOs, one can see that the corresponding bonding OVMO states have to be filled with the U5f electrons.

Figure 6. Total electron yield spectrum for UO_2. The $U5d_{5/2,3/2}$ binding energies in UO_2 are given above the spectrum. The densities of the filled (black) and vacant (hollow) U5f electronic states for the ground state of UO_2 are given under the spectrum as vertical bars.

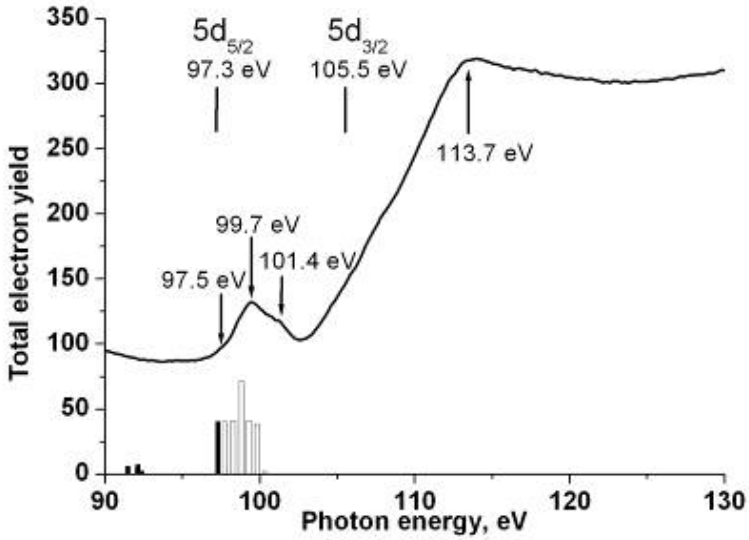

Resonant X-ray photoelectron spectroscopy (RXPS)

The paper [8] considers the electron photoemission under the excitation hν around the $O_{4,5}$(U) edge from UO_2 formed on the surface of uranium foil (Figure 7). The resonance was expected to show up at the excitation energies 100-113 eV (see Figure 6). Indeed, the more intense peaks appear in the spectrum excited at hν=110 eV (Figure 7). If earlier [16] only the OVMO (0-13 eV BE) intensity change was observed, the authors of [8] for the first time observed the resonance in UO_2 and ThO_2 for the OVMO and IVMO electrons in the binding energy range 0-40 eV (Figure 7). In this case to a first approximation this structure for the actinide (An) compounds can be described by the following excitation and decay processes:

$$An5d^{10}(IVMO)^k(OVMO)^m5f^n + h\nu \rightarrow An5d^9(IVMO)^k(OVMO)^m5f^{n+1}, \quad (1)$$

$$An5d^9(IVMO)^k(OVMO)^m5f^{n+1} + (e^2/r) \rightarrow An5d^{10}(IVMO)^k(OVMO)^m5f^{n-1} + e, \quad (2)$$

$$An5d^9(IVMO)^k(OVMO)^m5f^{n+1} + (e^2/r) \rightarrow An5d^{10}(IVMO)^k(OVMO)^{m-1}5f^n + e, \quad (3)$$

$$An5d^9(IVMO)^k(OVMO)^m5f^{n+1} + (e^2/r) \rightarrow An5d^{10}(IVMO)^{k-1}(OVMO)^m5f^n + e. \quad (4)$$

Figure 7. Resonant photoelectron emission spectra from UO_2 formed on the surface of uranium foil at different SR energies hν (eV). The spectral intensities were normalized by the beam current. Binding energies for UO_2 are given under the spectra. The C1s binding energy from surface hydrocarbons was accepted to be 285.0 eV.

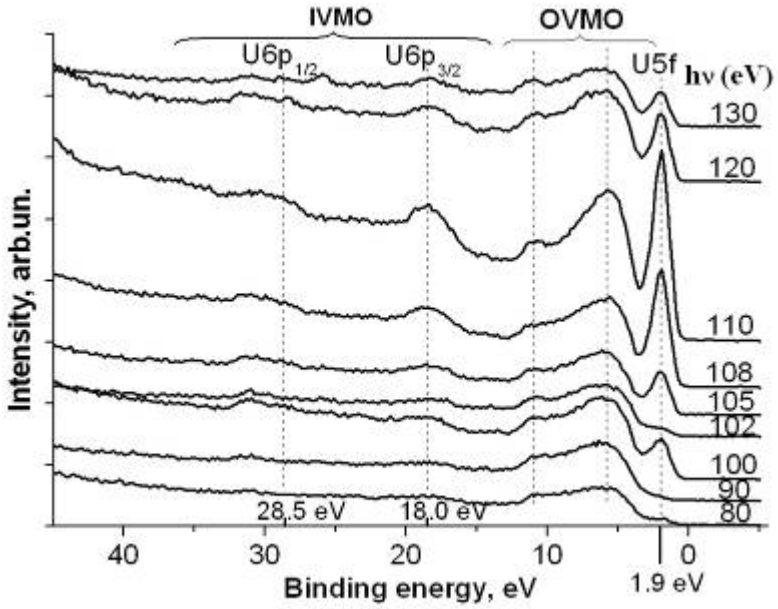

It has to be noted that together with this process a regular photoemission takes place. Since the considered resonant spectra are mostly due to the Auger electrons rather than to the photoemission, they reflect mostly the An*np* and An*5f* partial state densities. The observed washout of the structure in the ~15-40 eV energy range was explained by the IVMO formation. Since during the resonance the biggest intensity changes are expected for the U5f,6p related peaks, the obtained data allows the three important conclusions. First, the peak at 1.9 eV is attributed to the localized U5f electrons. Secondly, the U5f electrons participating directly in the chemical bond are delocalized that results in the OVMO intensity grow. Lastly, the U6p electrons participate effectively in the IVMO and probably OVMO formation, which results in the intense resonant structure in the IVMO energy range. This structure reflects the partial U6p electronic density in this spectral region.

Resonant X-ray $O_{4,5}$(U) emission spectroscopy (RXES)

The RXES from UO_2 collected at the excitation energies 104.4, 107.2, 113.8 and 120 eV [7] are presented in Figure 8. The RXES structure depends strongly on the near resonance excitation energy. One can see a satisfactory agreement between the resonant and non-resonant spectra (Figures 5, 8). Thus, the peaks separated by about 8 eV are attributed to the transitions $U5d_{5/2,3/2}$←OVMO. They are

observed in both resonant and non-resonant spectra. The transition$U5d_{3/2}$←OVMO prevails over the $U5d_{5/2}$←OVMO.

Figure 8 shows that peak B is more intense for UO_2. It indicates that the transitions $U5d_{3/2}$←OVMO prevail over the $U5d_{5/2}$←OVMO. Peak A slightly grows in the non-resonant spectra. It has to be noted that the filled U6p electronic states present in the OVMO ($0.6e^-$ of the U6p electrons in UO_2 [10]), and the transitions from the U6p-containing orbitals have to show up in the spectra. Indeed, peak B in the spectra is obviously structured.

Figure 8. Resonant X-ray $O_{4,5}$(U)- emission spectra from UO_2 at different SR excitation energies hν (eV). The corresponding non-resonant spectrum from UO_2 is given below for comparison (see Figure 5)

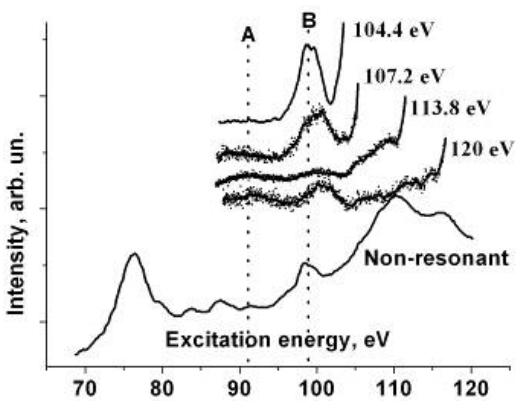

Figure 9. Resonant X-ray $O_{4,5}$(U)- emission spectra from UO_2 and UO_3 at SR excitation energy hν = 101 eV. The spectrum from UO_2 exhibits the ff-excitation related structure

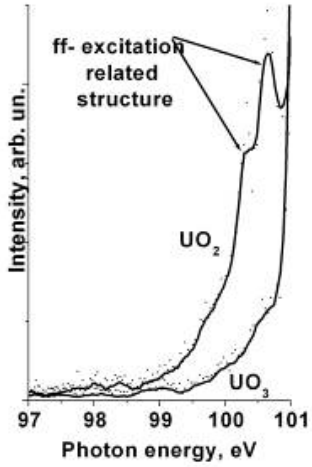

The RXES from UO_2 and UO_3 collected at 101 eV excitation energy show a significant difference (Figure 9). Unlike the UO_3 one, the UO_2 RXES shows the two peaks attributed to the ff-excitation [7]. The ff-excitation is expected to show up with a higher probability in the spectra of compounds with the more ionic type of bond, like UO_2. A more reliable interpretation of the ff-excitation process requires more correct calculations of the RXES structure taking into account the many-body perturbation and charge transfer effects. The observed RXES transitions agree with the suggestion that

the filled U5f and probably U6p states present in the outer valence band. This agrees with the data of other considered methods.

Auger OKLL spectroscopy of oxygen

Auger OKLL spectrum from, for example, Al_2O_3, where the IVMOs do not form effectively, consists of the three well observed structural lines reflecting the $OKL_{2-3}L_{2-3}$ (O1s←O2p), OKL_1L_{2-3} (O1s←O2s,2p), OKL_1L_1 (O1s←O2s) transitions (Figure 10a). The work [17] established a quantitative correlation of the relative Auger intensity defining the partial density of the filled oxygen electronic states on the O1s XPS binding energy characterizing the total density of the valence electronic states on the oxygen ion (Figure 10b). The relative Auger intensities are given as area ratios of OKLL/O1s. The Auger OKLL spectrum of UO_2 differs significantly from the corresponding spectrum of Al_2O_3, SiO_2 and Bi_2O_3 (Figure 10a,b and Table 2). The $OKL_{2-3}L_{2-3}$ FWHM for UO_2 is significantly lower (Γ<5 eV) than the corresponding FWHMs for other oxides. This can be explained by the fact that the partial O2p density OVMO band for UO_2 is significantly narrower than that for other studied oxides. The OKL_1L_{2-3} and OKL_1L_1 Auger regions for UO_2 exhibit more complicated structures than those for the other studied oxides. It can be explained by the IVMO formation from the U6p-O2s interaction. The intensity decrease of the $OKL_{2-3}L_{2-3}$ and OKL_1L_{2-3} Auger lines for UO_2 compared to the other studied oxides apparently can also be attributed to the IVMO formation.

The results of the simultaneous registration of the Auger OKLL and XPS O1s,2s,2p spectra of UO_2 and other oxides in the binding energy range 0–540 eV allowed a qualitative evaluation of the relative valence electronic oxygen state density in UO_2 and an experimental confirmation of the IVMO formation in this oxide.

Figure 10. a – Auger OKLL spectra from Al_2O_3 and UO_2 measured with the $AlK_{\alpha 1,2}$ (1486.6 eV) excitation. b – Dependence of the relative $OKL_{2-3}L_{2-3}$ and $OKL_{2-3}L_{2-3}$ Auger intensities on the O1s binding energy for Bi_2O_3, Al_2O_3, SiO_2 and UO_2.

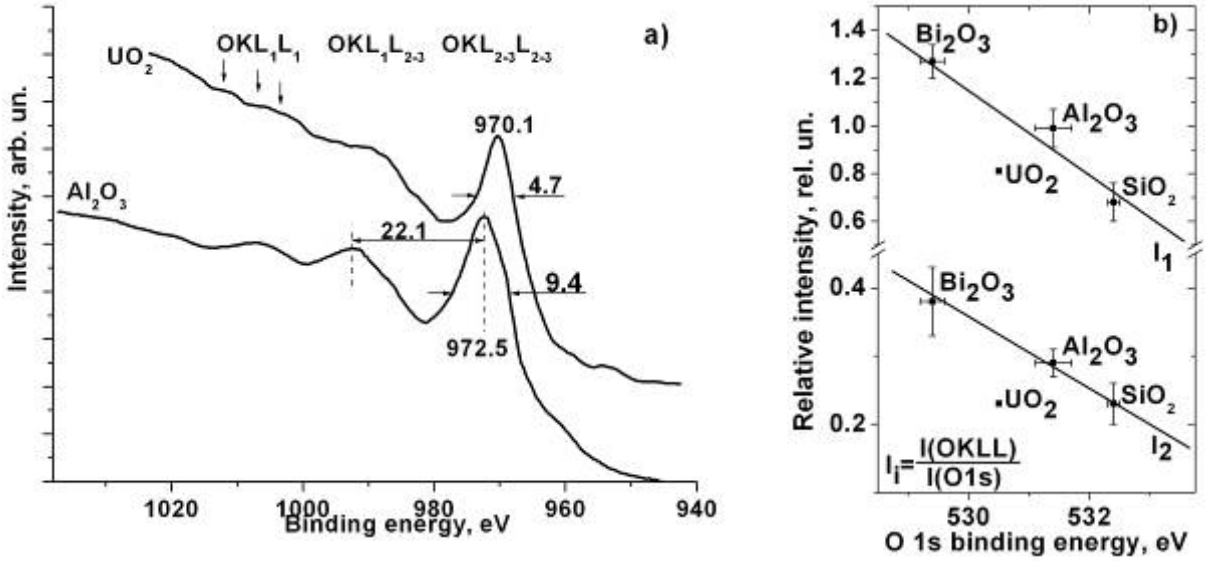

Table 2. O1s binding energies E_b (eV) and $OKL_{2-3}L_{2-3}$ and $OKL_{2-3}L_{2-3}$ Auger relative intensities I[a)] (relative units) for oxides Bi_2O_3, Al_2O_3, SiO_2 and UO_2.

N	Oxides	E_b	I_1	I_2
1	Bi_2O_3	529.4 ± 0.2	1.27 ± 0.07	0.38 ± 0.05
2	Al_2O_3	531.4 ± 0.3	0.99 ± 0.08	0.29 ± 0.02
3	SiO_2	532.4 ± 0.1	0.68 ± 0.08	0.23 ± 0.03
4	UO_2	530.5	0.81	0.23

[a)] Relative intensities were calculated as intensity ratios Auger peak/O1s peak measured in the same experiments.

Conclusions

Using the examples of UO_2, γ-UO_3, UO_2F_2 and UF_4 we analyzed the new data on the nature of the chemical bond obtained by the X-ray photoelectron, conversion electron, non-resonant and resonant X-ray $O_{4,5}$(U) emission, near $O_{4,5}$(U) edge absorption, resonant photoelectron and Auger OKLL spectroscopies taking into account the data of the relativistic electronic structure calculations for the UO_8^{12-} (O_h), $[(UO_2)O_4]^{6-}$ (D_{4h}), $[(UO_2)F_6]^{4-}$ (D_{6h}) and UF_8^{4-} (C_{4v}) clusters reflecting uranium close environment in the studied uranium compounds.

Despite the traditional opinion that before the chemical bond formation the An5f electrons get promoted, for example, to the An6d atomic orbitals, the theoretical calculations show and experimental data confirm that the An5f atomic shells (~1 U5f electron) can participate directly in the formation of molecular orbitals in actinide compounds. About 2 U5f electrons weakly participating in the chemical bond are localized at -1.9 eV, ~1 U5f participating in the chemical bond is delocalized in the OVMO binding energy range from -4 to -9 eV, and the vacant U5f electronic states are generally delocalized in the low positive energy range (0-5 eV). The U6p electrons (0.6 U6p electrons) were experimentally shown to participate significantly in the OVMO formation beside the IVMO formation, which agrees with the theoretical data.

It was established that, for example, for UO_2, the bonding $8\gamma_8^-(8)$ and corresponding antibonding $9\gamma_8^-(5)$ IVMO are formed generally from the $U6p_{3/2}$ and O2s AOs and their calculated compositions (63% of $U6p_{3/2}$ and 33% of O2s and 34% of $U6p_{3/2}$ and 63% of O2s AOs) differ slightly from the experimental data (75% of $U6p_{3/2}$ and 21% of O2s and 22% of $U6p_{3/2}$ and 75% of O2s AOs). Electrons from these orbitals in the aggregate were suggested to strengthen the chemical bond in uranium dioxide.

Acknowledgments

The work was supported by the RFBR grant 04-03-32892, and the grant of the initiative projects on basic researches of the RRC "Kurchatov Institute" 2006-2007.

References

1. P.F. Walch, D.E. Ellis, J. Chem. Phys. **65**(6) (1976) 2387.
2. M. Boring, J.H. Wood, J.W. Moskowitz, J. Chem. Phys. **63**(2) (1975) 638.
3. V.A. Gubanov, A. Rosen, D.E. Ellis, Sol. St. Com. **22**(4) (1977) 219.
4. Yu.A. Teterin, A.Yu. Teterin, Russ. Chem. Rev. **73**(6) (2004) 541.
5. A.Yu. Teterin, Yu.A. Teterin, K.I. Maslakov, A.D. Panov, M.V. Ryzhkov, L. Vukcevic, Phys. Rev. B. **74** (2006) 045101.

6. Yu.A. Teterin, V.A. Terekhov, A.Yu. Teterin, K.E. Ivanov, I.O. Utkin, A.M. Lebedev, L. Vukchevich, J. Electron Spectrosc. Relat Phenom. **96** (1998) 229.

7. K.E. Ivanov, Yu.A. Teterin, D.K. Shuh, A.Yu Teterin, S.M. Butorin, J.-H. Guo, M. Magnuson, J. Nordgren, Proceedings. 4th International Yugoslav Nuclear Society Conference (YUNSC-2002). Belgrade, Yugoslavia, Sep 30- Oct. 4, 2002. VINCA Institute of Nuclear Sciences, Yugoslav Nuclear Society. Belgrade. (2003) 431.

8. Yu.A. Teterin, I.O. Utkin, A.Yu. Teterin, T. Reich, F.U. Hillebrecht, S.L. Molodtsov, A.Yu. Varykhalov, W. Gudat, Annual Report, BESSY GmbH, 12489, Berlin, Germany (2004).

9. I.M. Band, Y.I. Kharitonov, M. B. Trzhaskovskaya, At. Data Nucl. Data Tables **23** (1979) 443.

10. Yu.A.Teterin, A.Yu. Teterin, Nuclear Technology & Radiation Protection **19**(2) (2004) 3.

11. A.Yu. Teterin, M.V. Ryzhkov, A.Yu. Teterin, A.D. Panov, A.S. Nikitin, K.E. Ivanov, I.O. Utkin, J. Nucl. Sci. Technol. Suppl. **3** (2002) 74.

12. I.O. Utkin, Yu.A. Teterin, V.A. Terekhov, M.V. Ryzhkov, A.Yu. Teterin, L. Vukchevich. Radiochemistry **47**(4) (2005) 334.

13. I.I. Lyahovskaya, V.M. Ipatov, T.M. Zimkina, J. Struct. Chem., **18**(4) (1977) 668.

14. T.M. Zimkina, I.I. Lyahovskaya, A.S. Shulakov, Opt. Spektrosk. (Opt. Spectrosc. (USSR)), **62**(2) (1987) 285 (in Russian).

15. S. Imoto, C. Miyake, H. Adachi, Y. Hinatsu, K. Taniguchi, K. Fujima, Abstacts of reports on Actinides – 1981, September 10-15, 1981, LBL and LLNL Berkeley, California. P.99.

16. L. Cox, W.P. Ellis, R. Cowan, J.W. Allen, S.-J. Oh, I. Lindau, B.B. Pate, A.J. Arko, Phys. Rev. B. **35** (1987) 5761.

17. Yu.A. Teterin, K.E. Ivanov, A.Yu. Teterin, A.M. Lebedev, I.O. Utkin, L. Vukchevich, J. Electron Spectrosc. Relat Phenom. **101-103** (1999) 401.

APPLICATIONS OF EXAFS IN NUCLEAR FUEL RESEARCH AND DEVELOPMENT

Marcus Walter, Joseph Somers and Asuncion Fernández–Carretero
European Commission, Joint Research Centre, Institute for Transuranium Elements,
P.O. Box 2340, D–76125 Karlsruhe, Germany

Abstract

EXAFS was used to investigate the local atomic environment of materials designed for the transmutation of minor actinides. Am L_3–edge EXAFS indicate, that ^{241}Am infiltrated in porous spinel pellets forms a perovskite-like $AmAlO_3$ phase during sintering. After 10 years of storage, self-irradation through the ^{241}Am decay amorphizes the $AmAlO_3$ phase and only the first oxygen coordination shell around Am is detected. In a second study, the local structure of the inert matrix fuel analog $(Zr_{1-x}U_x)N$ was probed both at the Zr K and U L_3-edge. The bond distance between U and its six surrounding N atoms follows the Vegard law. In contrast, the Zr-N bond distance at low x (high Zr) increases with x. At $x > 0.6$ $(Zr_{1-x}U_x)N$ the Zr-N distance ceases to increase and remains relatively constant at 2.32-2.35 Å, indicating a limited ability of Zr to accept the $(Zr_{1-x}U_x)N$ lattice expansion induced by uranium.

Introduction

Current research activities in the Nuclear Fuels unit of the Institute for Transuranium Elements (ITU) are focussed on materials for the transmutation of minor actinides (MA: Np, Am, Cm) to reduce their long-term radiotoxicity and on nuclear fuels related to the Gen IV initiative. For transmutation fuels the highest transmutation efficiency is obtained when the minor actinides are supported in an inert matrix. Due to their advantageous physical properties (high melting point, resistance to damage, low neutron capture), spinel ($MgAl_2O_4$), yttria stabilized zirconia $(Zr,Y)O_{2-x}$ and ZrN were selected. Americium is incorporated into the materials by specially developed processes at the ITU's minor actinide laboratory (MA LAB) The Am forms a separate phase (2-3 micron in particle size) in the spinel matrix and cubic $(Zr,Y,Am)O_{2-x}$ in stabilised zirconia. The application of EXAFS spectroscopy in nuclear fuel research is presented here for a ^{241}Am transmutation fuel based on a spinel inert matrix (EFTTRA-T4) and the $(Zr_{1-x}U_x)N$ system as an analogue for (Zr,Am)N. The goal of studies is to compare the local Am structure in the 10 years aged (X-ray amorphous) and freshly annealed (crystalline) spinel-based Am transmutation fuel, and to identify the local Zr and U environment in the $(Zr_{1-x}U_x)N$ solid solution.

Experimental

^{241}Am transmutation fuel

For the XAS measurement, 60 mg of the Am-spinel material was used for the aged (10 years) and annealed sample. The annealed sample was prepared by applying the same sintering conditions (2 hours at 1600°C in an Ar/H_2 atmosphere) as for the fuel production in 1996 [1]. The spinel powder (6.9 mg Am, 880 MBq) was filled in a stainless steel cuvette with Plexiglas windows and sealed with polyethylene foil. Both samples were measured in transmission mode at room temperatue at the INE-Beamline at the Ångströmquelle Karlsruhe, ANKA [2]. The EXAFS oscillations were extracted according to standard procedures using the EXAFSPAK program suite. The threshold energy of the Am L_3-edge, E_0, was set to 18520 eV. Since the crystallographic structures of the transuranium aluminates is not well known, a spherical 8 Å cluster of the rhombohedral $NdAlO_3$ structure [3] was used by replacing Nd with Am for the calculation of the theoretical phase shifts, $\delta(k)$, and backscattering amplitudes, F(k) (FEFF8).

Zirconium-uranium nitride solid solution

$(Zr_{1-x}U_x)N$ samples were prepared according to the sol-gel and the infiltration route [4] combined with subsequent carbothermical reduction of carboneous $(Zr_{1-x}U_x)O_{2+x}$ spheres. Porous ZrO_2+C sol gel spheres were infiltrated by a uranium (VI) solution to obtain uranium concentrations of 4, 10, 20, 25, and 40 mol%. Samples with the composition 60, 75, 90, 96 and 100 mol% U were directly prepared via sol-gel route. Then, the $(Zr_{1-x}U_x)O_{2+x}$ + C spheres were transferred in the nitride form by carbothermic reduction in a nitrogen gas stream at 1600°C [5]. The sintered $(Zr_{1-x}U_x)N$ samples were milled, mixed with boron carbide and prepared for XAS measurement as pressed disks. Zr K-edge and U L_3-edge EXAFS spectra were recorded at the INE-Beamline at ANKA [2]. The measurements were performed at room temperature in transmission mode. For samples with 90 and 96 mol % U, the Zr K-edge EXAFS was measured in fluorescence mode. The threshold energy, E_0, was set to 17185 eV for the U L_3-edge, and to 18010 eV for the Zr K-edge. The theoretical phase shifts, $\delta(k)$, and backscattering amplitudes, F(k) were calculated for a spherical 7.5 Å cluster of $(Zr_{1-x}U_x)N$ using FEFF8.

Results and Discussion

^{241}Am-spinel transmutation fuel

The Am L_3-edge EXAFS of the annealed sample shows a complex behaviour and several peaks can be observed in the corresponding Fourier transform (FT) between 1.7 and 6.3 Å (R+Δ), (see Figure 1). Mainly the second peak at 2.8 Å (R+Δ) and third peak at 3.8 Å (R+Δ) , which are caused by the Am-Al and Am-Am interactions, are indicative of a perovskite-like $AmAlO_3$ structure. The first peak at 1.7 Å represents the first coordination shell with 12 oxygen atoms and is low in intensity compared with the second peak resulting from the second coordination shell of 8 Al atoms. This loss in FT peak amplitude was also observed for rhombohedral $LaAlO_3$ and is due to the splitting of first oxygen coordination shell [6]. In contrast, the aged material exhibits a less complex, strongly damped EXAFS. In the FT a broad peak is located at 1.9 Å (R+Δ), and a second small peak is detected at 2.8 Å (R+Δ). The peak at 1.9 Å (R+Δ) is somewhat higher in intensity compared with the annealed material. No further peaks can be observed at higher radial distances. This indicates that cumulative self-radiation α-damage of 4.3 10^{18} g^{-1} fuel removes all the structural order from the second shell onward.

The assumption of the $NdAlO_3$ structure for $AmAlO_3$ fits the experimental data of the annealed EFTTRA-T4 fuel. The data is well-modelled using three oxygen subshells at 2.37 Å (O_{1a}; N=3), 2.60 Å (O_{1b}; N=6), and 2.86 Å (O_{1c}; N=3). The strongest FT peak is caused by the 8 Al atoms at a mean distance of 3.25 ± 0.01 Å. Furthermore, three Am shells can be distinguished in the higher R-space at 3.75 Å, 5.30 Å and at 6.50 Å, respectively. The Am L_3-edge EXAFS of the aged EFTTRA-T4 fuel shows no FT peaks beyond 2.8 Å (R+Δ) and was fitted applying a model based on $NdAlO_3$ structure including the split oxygen shell O_{1a} (2.36 Å), O_{1b} (2.58 Å), O_{1c} (2.88 Å) and an Al shell with a bond length of 3.28 Å. The coordination number (N) of the Al shell was allowed to vary, indicating N ~ 1.

The Am L_3-edge EXAFS of the annealed EFTTRA-T4 fuel can be described by the rhombohedral $AmAlO_3$ structure. This implies that all of the americium in the EFTTRA-T4 fuel is concentrated in the $AmAlO_3$ phase, which was formed during the sintering by solid state reaction of AmO_2 and $MgAl_2O_4$, following the reduction of AmO_2 in the Ar/H_2 gas stream. The self-irradiation damage of $AmAlO_3$, which is mainly caused by the short-ranging recoil nuclei, removes the structure from the second shell onwards. The first oxygen shell remains split, similar to those in the annealed material, but is altered by several atomic displacements due to the self-irradiation.

Figure 1: Am L_3-edge EXAFS and FT's of aged and annealed EFTTRA-T4 fuel

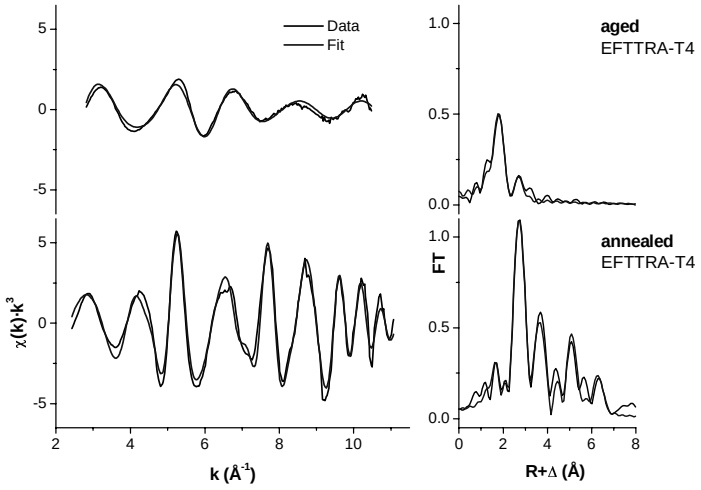

Zirconium-uranium nitride solid solution

Four peaks can be distinguished in the Fourier transforms of the Zr K-edge and U L_3-edge EXAFS data. The first peak corresponds to the six nearest neighbour nitrogen atoms surrounding the Zr/U atoms. Three further peaks lie at about 3.0, 4.2 Å and 5.2 Å (R+Δ). These peaks represent the metal atom coordination shells Me_1, Me_2 and Me_3. The refined interatomic distances of the coordination shells N_1 and Me_3 are plotted in Figure 1 together with values calculated from the lattice parameter (XRD). The Zr and U EXAFS data for the Me_3 shell fall on the Vegard line. Since the distant Me_3 shell represents more the bulk crystal structure than the local environment, it indicates the materials homogeneity at this scale. The N_1 coordination shell, however, is the nearest neighbour and reflects the local atomic scale. Here all U-N_1 bond distances follow the Vegard line. Also the Zr-N bond length follow this trend up to x=0.6 $(Zr_{1-x}U_x)N$, but it remaines constant at 2.32-2.35 Å above x=0.6. This implies that the local environment of U accommodates the lattice parameter contraction with decreasing x (increasing Zr). The ability of Zr to accept the expansion of its local environment with increasing x (increasing U) is limited up to x=0.6. For samples with x>0.6, the environment around Zr is contracted, and the material becomes heterogeneous at the local atomic scale. This behavior becomes more extreme for (Zr,Am)N, as the solid solution as a solid solution seems not exist over the full stoichiometric range [7].

Figure 2: Interatomic distances in the $(Zr_{1-x}U_x)N$ solid solution. An error bar for the Zr and U EXAFS data of 0.02 Å is plotted at the position of the end members ZrN and UN.

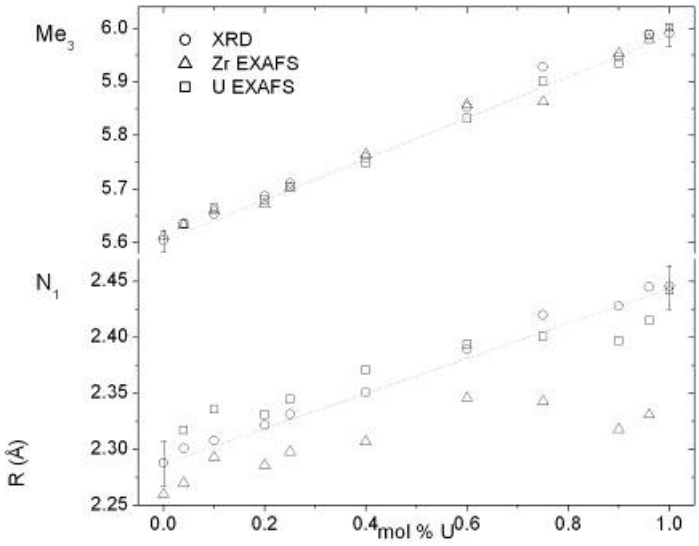

Conclusion

EXAFS permits the determination of the local order around the elements in transmutation fuels. The Am L_3-edge EXAFS of the Am-spinel sample identifies the Am phase as a rhombohedral $AmAlO_3$ perovskite. After 10 years of storage, this phase became amorphous due to the ^{241}Am decay and the local order is limited to the first oxygen shells. Structural order is destroyed from the next nearest Al coordination shell onwards.

For (Zr,MA)N fuels, (Zr,U)N is the experimentally most simple system to characterise. The lattice parameter of the (Zr,U)N solid solution varies linearly with the composition, i.e. it shows Vegard behaviour. This linear dependence is also found in the Zr K and U L_3-edge EXAFS for the more distant metal coordination shells surrounding Zr and U atoms, respectively. The nearest

neighbour U-N bond length also exhibits a linear dependence. In contrast, however, the Zr-N bond length deviates from linearity for U concentrations above x=0.6 $(Zr_{1-x}U_x)N$, and remains nearly constant at 2.32-2.35 Å, indicating a contraction of the immediate Zr environment in the U-rich (Zr,U)N samples.

References

[1] K. Richter, A. Fernandez, J. Somers; (1997) J. Nucl. Mater. 249, 121-127.

[2] M.A. Denecke, J. Rothe, K. Dardenne, H. Blank, J. Hormes; (2005) Phys. Scripta T115, 1001.

[3] C.J. Howard, B.J. Kennedy, B.C. Chakoumakos; (2000) J. Phys.: Condens Matter 12, 349-

[4] A. Fernández, D. Haas, R.J. Konings, J. Somers; (2002) J. Am. Ceram. Soc. 85, 694-696.

[5] G. Ledergerber, Z. Kopajtic, F. Ingold, R.W. Stratton; (1992) J. Nucl. Mater. 188, 28-35.

[6] F. Deganello, A. Longo, A. Martorana; (2003) J. Solid State Chem. 175, 289-298.

[7] K. Minato, M. Akabori, M. Takano, Y. Arai, K. Nakajima, A. Itoh, T. Ogawa; (2003) J. Nucl. Mater. 320, 18-24.

SESSION III

ACTINIDES IN ENVIRONMENTAL AND LIFE SCIENCES

Chair: Reinhard Klenze

MICROBIALLY DRIVEN TRANSFORMATIONS OF TECHNETIUM

K. Morris[1], F.R. Livens[2], J. M. Charnock[3], I.T. Burke[1], J.M. McBeth[4], C. Boothman[4], J.R. Lloyd[4]

1. Institute of Geological Sciences, School of Earth & Environment, University of Leeds, Leeds, LS2 9JT. U.K.
2. Centre for Radiochemistry Research, and School of Earth, Atmospheric and Environmental Sciences, The University of Manchester, Manchester M13 9PL, U.K.
3. CLRC Daresbury Laboratory, Warrington, Cheshire WA4 4AD, U.K.
4. Williamson Centre for Molecular Environmental Science, School of Earth, Atmospheric and Environmental Sciences, The University of Manchester, Manchester M13 9PL, U.K.

Abstract

Technetium-99 (Tc) is a redox active, beta-emitting radionuclide and a mobile contaminant in groundwaters at nuclear facilities in the UK and USA. Additionally, it has been released to the natural environment in authorised and accidental discharges, and is expected to be a radiologically significant component of spent nuclear fuel due to its long half-life (2.13×10^5 y) and potentially high environmental mobility. In terms of its environmental behaviour, the speciation of Tc is the major control on its mobility. Under oxic conditions the highly mobile TcO_4^- is expected to dominate whilst, under reducing conditions, poorly soluble reduced species (predominantly Tc(IV)) are expected. Here we apply XAS techniques to determine the speciation of Tc in a range of sediments that have been subjected to biologically mediated redox transformations. In sediments, microbially-mediated reactions control the development of sediment anoxia and, thus control Tc speciation and mobility. Experiments show that microbially mediated reduction of sediments led to reduction of soluble TcO_4^- to poorly soluble Tc(IV) during Fe(III)-reduction and the Tc was present as hydrous TcO_2 in a range of systems. We also studied the behaviour of Tc on reoxidation of the sediments with air, which is relevant to disturbance of Tc-contaminated sediments, and via microbially mediated "anoxic oxidation" with nitrate. Anoxic oxidation is relevant to proposed bioremediation plans for contaminated sites where reducing conditions are stimulated in the sub-surface by addition of organic matter. In this context, when environmental stewardship of these sites ceases, sub-oxic, nitrate-rich water may flush the anoxic area and mediate reoxidation of the sediments. On air reoxidation 50-80% of the sediment bound Tc was remobilised to solution as TcO_4^- whilst on nitrate reoxidation typically < 10% of the sediment bound Tc was remobilised. The speciation of the Tc remaining on the sediments was site- and biogeochemistry-specific with both a mix of hydrous TcO_2 and Tc(VII) being the most common form of Tc after reoxidation, but with one air reoxidised sediment containing only hydrous TcO_2.

Introduction

Technetium is a mobile contaminant in groundwaters at a number of nuclear facilities in the UK and USA (www.nda.gov.uk) [1], has been released to the natural environment [2, 3], and will be a long term component of radioactive wastes. Its environmental behaviour is dependant on its speciation, under oxic conditions it is present as highly mobile TcO_4^- which is predicted to be one of the most mobile anthropogenic radionuclide species. By contrast under reducing conditions, Tc(IV) predominates and can form poorly soluble oxide and sulfide phases depending on the geochemical environment [4, 5]. In sediments, development of anoxic conditions is controlled by microbially mediated reactions, and Tc speciation and thus mobility will be affected by these microbial processes. The classic model is that anoxia develops as microbes oxidise electron donors during energy yielding respiratory processes and shunt the resultant electrons onto one of a range of terminal electron acceptors. The selection of a particular terminal electron acceptor depends on the availability of relevant electron donors and on the free energy of reaction; classically, a sequence of reactions in the order oxygen-, nitrate- (NR), Mn(IV)- (MnR), Fe(III)- (FeR) and sulfate-reduction (SR) and methanogenesis occurs [6]. For technetium, reduction can be either direct (whereby the reaction is mediated enzymatically by the microorganism and the TcO_4^- itself acts as a terminal electron acceptor; [7, 8]) or indirect (whereby reduction is facilitated by abiotic reaction with enzymatically reduced species such as Fe(II); [9]). In the natural environment, indirect reduction of Tc associated with Fe(III)-reduction in sediments is thought to dominate [10, 11, 12, 13] although there is some evidence that enzymatic routes may be possible at low sediment Fe concentrations [14]. Nonetheless, the body of evidence suggests that, in most systems, on microbial reduction TcO_4^- will be reduced via abiotic reaction with Fe(II) to form insoluble Tc(IV). For sediment reoxidation, the situation is less clear with few detailed studies on Tc reoxidation behaviour. Nonetheless, the reoxidation behaviour of Tc(IV)-labelled sediment is key in understanding the long term fate of sediment-associated Tc in the natural environment where sediment disturbance and remobilization to oxygenated conditions can occur. Additionally, if Tc is reductively retained in sediments of engineered environments, groundwater fluctuations, intentional disturbance, or reoxidation of the anoxic environment with sub-oxic, nitrate-rich groundwaters may all affect the redox cycling behaviour of Tc. The latter scenario is pertinent to nuclear sites which have mobile TcO_4^- contamination in groundwaters and where "biostimulation" of the subsurface to develop anoxic conditions by addition of electron donors such as acetate and ethanol has been proposed as an *in situ* remediation technique [1, 15]. It is likely that, after stewardship of the site ceases, the groundwater chemistry will evolve back towards pre-existing conditions and these may well lead to high levels of nitrate associated with nuclear processing [1]. Here we present the results of a series of sediment microcosm experiments using XAS techniques to determine the speciation of technetium in sediments where reduction is mediated by indigenous microbes. Additionally, we exposed a range of Tc-labelled reduced sediments from these sites to air and nitrate reoxidation and again used XAS techniques to determine the speciation of Tc in both solutions (where possible) and solids from the reoxidation process.

Methods

Safety

^{99}Tc is a radioactive beta emitter (half life 2.13×10^5 y; E_{max} = 294 keV) and should be handled by suitably qualified and experienced personnel in a properly equipped radiochemistry laboratory. The possession and use of radioactive materials is subject to statutory controls.

Reduced Sediment Samples

The two sample sites were an estuarine site, the Humber Estuary, UK, and a freshwater site impacted by radioactive contamination, the Field Research Center (FRC) site, Oak Ridge, TN, USA.

Sediments were sampled using aseptic technique from the surface sediment in the Humber [12, 16], and from the FRC site using a sterile corer which yielded sediment cores 0.5 m long [13]. Sediment microcosms were then prepared with the sedimentary material. Typically, sediments (2 g wet weight, ca 50% moisture content) were mixed with river water (10 ml) in the case of Humber materials, and with a synthetic groundwater in the case of FRC materials [13]. Preliminary experiments indicated that Tc inhibited microbial reduction of Fe(III) and potentially Tc(VII) at the spike concentrations required for XAS experiments (500 μmoles l^{-1}; data not shown) so our approach was to incubate and pre-reduce sediments prior to spiking them with NH_4TcO_4 at between 60 and 300 kBq per experiment (100-500 μmoles l^{-1}). Samples were then left for two weeks, the solution phase counted to see if the Tc had been removed and, where appropriate, sediments were then prepared for XAS data acquisition using triple contained sample holders. Three samples were prepared in this way: Humber FeR; Humber SR; and FRC FeR. Additionally, both Humber and FRC sediments were incubated with 500 μmoles l^{-1} NH_4TcO_4 to try and obtain microbially reduced samples that had been exposed to progressive anoxia mediated by indigenous microorganisms. Only the Tc in Humber sediment reduced under these conditions, and one further reduced sample, Humber BioR, was prepared for XAS analysis.

Reoxidised Samples

Parallel Tc labelled pre-reduced samples (with between 100-500 ppm Tc on sediments) were prepared and then subjected to reoxidation with both air (by daily injection of 40 ml air by syringe for 1-3 weeks) and nitrate (by injection of anaerobic KNO_3 to give a final concentration of 100 mmoles l^{-1} for Humber experiments and 25 mM for FRC sediments and incubation for 1 month). A series of Air or NO_3^- oxidized sediment samples were prepared: Humber FeR Air; Humber FeR NO_3^-; Humber SR Air; Humber SR NO_3^-; FRC FeR Air; FRC FeR NO_3^-. After reoxidation samples were mounted in cells as described below. The Humber sulfate reducing sediment when oxidized with air yielded a solution with between 50-100 ppm Tc present and a final sample Reoxidised Solution, was also analysed.

Sample mounting and XAS analysis.

Sediment slurries were spun down (8000 rpm, 10 minutes) and an approximately 300 μl pellet of the solid sediment or mineral paste (< 50% moisture) was mounted for XAS analysis in triple contained sample cells. Air sensitive sediments were handled and mounted under anaerobic conditions. Tc K-edge X-ray absorption spectra were collected in fluorescence mode on station 16.5 of the Daresbury SRS (see [12, 13, 16] for details of beamline setup, conditions and analysis). Since XAS is an averaging technique, in a sample containing a mixture of species, the spectrum will be a concentration-weighted average of the different spectra of the individual component species. Furthermore, XAS cannot readily distinguish between backscattering atoms of similar atomic number and EXAFS analysis only gives interatomic distances that are accurate to ca ± 0.02 Å in the first shell and ca ± 0.05 Å in second and third shells, and coordination numbers which are only accurate to ca ± 20% [17, 18, 19].

Results & Discussion.

Technetium Fate in Reducing Sediments.

For the pre-reduced sediments prepared for XAS, > 97% Tc removal occurred over the two week incubation period. For the Humber progressively anoxic sediment sample, Tc removal took six months rather than the approximately twenty days seen in parallel experiments run at 1-5 μmoles l^{-1} NH_4TcO_4 (Figure 1; [12]). This suggested that the higher concentration of Tc in the XAS samples (ca 500 μmoles l^{-1}) inhibited the indigenous microbial population. For the reduced sediment samples,

Figure 1. Incubation of 1-5 µmoles l^{-1} $TcO4^-$ with Humber Estuary sediment slurries undergoing progressive anoxia. Experiments with active microbial populations (●) and after autoclaving (+) are shown.

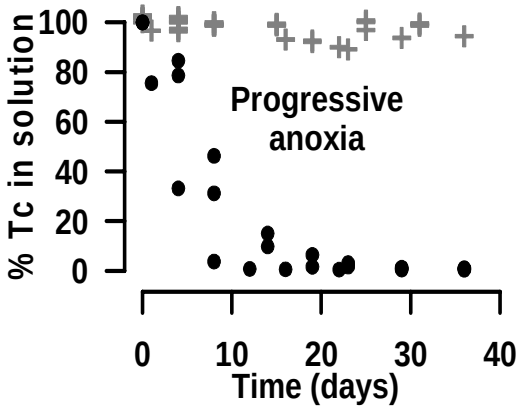

Figure 2. Background-subtracted, normalized, and k-weighted Tc K-edge EXAFS spectra (left) and corresponding Fourier transform (right) obtained for: (A) Humber FeR; (B) Humber SR; (C) FRC FeR; (D) Humber BioR. Black lines represent experimental data, grey lines represent model results.

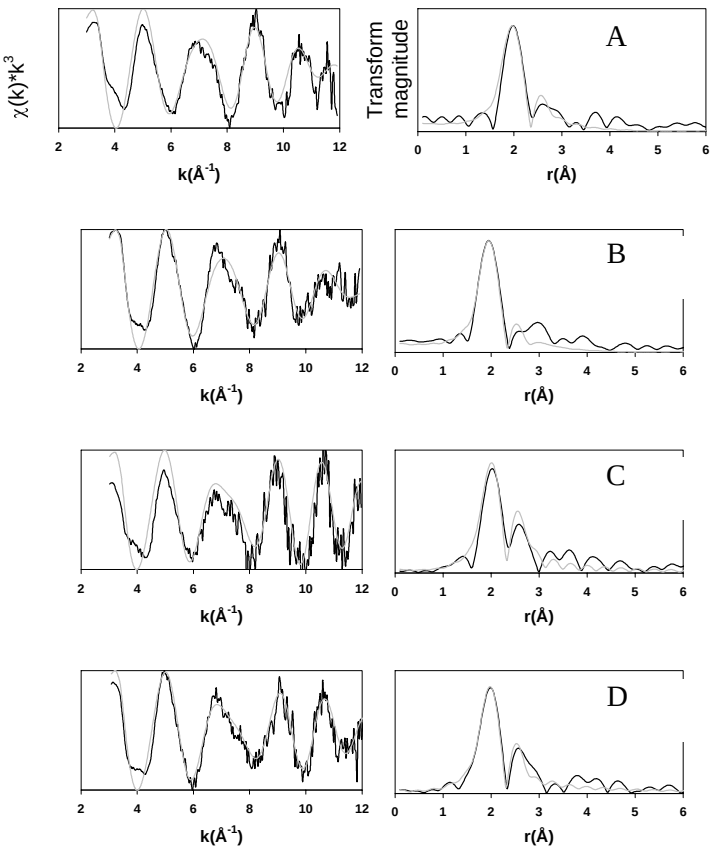

background subtracted, normalized and k^3 weighted EXAFS spectra and their Fourier transforms for the fits described are given in Figure 2 for experimental (black line) and model (grey line) results and model fits are given in Table 1.

For all samples, modelling with a first shell coordination environment of 6O atoms at ca 2.00 Å gave the best fit (Table 1). Indeed, the spectra and modelling fits for the different reduced materials are remarkably consistent and a first shell of 6 O atoms at 2.00 Å is consistent with a hydrous TcO_2-like phase similar to that seen by Maes *et al*. [19]. The lack of any pronounced peaks beyond 3.0 Å in the FTs further suggests the Tc reduction product is hydrous TcO_2 as the crystalline TcO_2 structure has distinctive shells of 4 Tc atoms at 3.64 Å and 4 further Tc atoms at 3.67 Å [19]. In hydrous TcO_2 originating from hydrolysis and precipitation, there is little 3-dimensional order consistent with the lack of major peaks at ca 3.6 Å in the FT. XANES data for the reduced samples are given in Figure 3 and are again consistent across all the samples, and are in agreement with published spectra for hydrous TcO_2-like phases in environmental matrices [5, 19].

Technetium Fate in Reoxidising Sediments.

For the air-reoxidised XAS samples, between 30 and 85% of the Tc initially retained on the sediment as hydrous TcO_2 was remobilized to solution over the 1-3 week period of reoxidation. For nitrate reoxidised samples, less than 10% of the Tc initially retained on the sediment as hydrous TcO_2 was remobilized to solution over the approximately 4 week period of reoxidation, even though almost complete Fe(II) reoxidation had been observed in parallel experiments with estuarine sediments at lower Tc concentrations [16]. Thus, Tc retained on sediments due to microbially mediated reduction is sluggish to remobilise with air reoxidation and is extremely recalcitrant to remobilization via NO_3^--mediated reoxidation.

Figure 3. Normalised Tc-K edge XANES spectra for: (Red. A) Humber FeR; (Red. B) Humber SR; (Red. C) FRC FeR; (Red. D) Humber BioR.

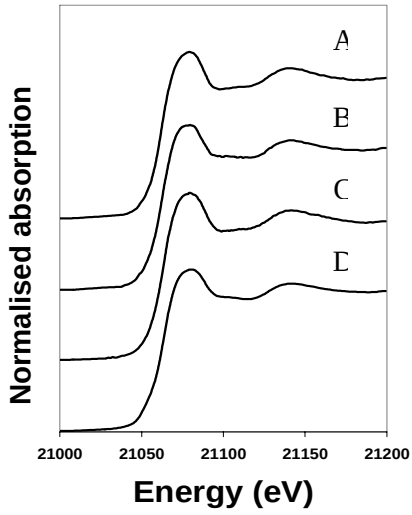

Figure 4 shows the EXAFS spectra (background subtracted, normalised and k^3 weighted) and Fourier transform fits (black line for experimental and grey line for model) for the reoxidised sediment samples and the reoxidised solution. Model fits are given in Table 1.

Figure 4. Background-subtracted, normalized, and k^3-weighted Tc K-edge EXAFS spectra (left) and corresponding Fourier transform (right) obtained for: (A) Humber FeR Air; (B) Humber FeR NO_3^-; (C) Humber SR Air; (D) Humber SR NO_3^-; (E) FRC FeR Air; (F) FRC FeR NO_3^-; (G) Reoxidised solution. Black lines represent experimental data, grey lines represent model results.

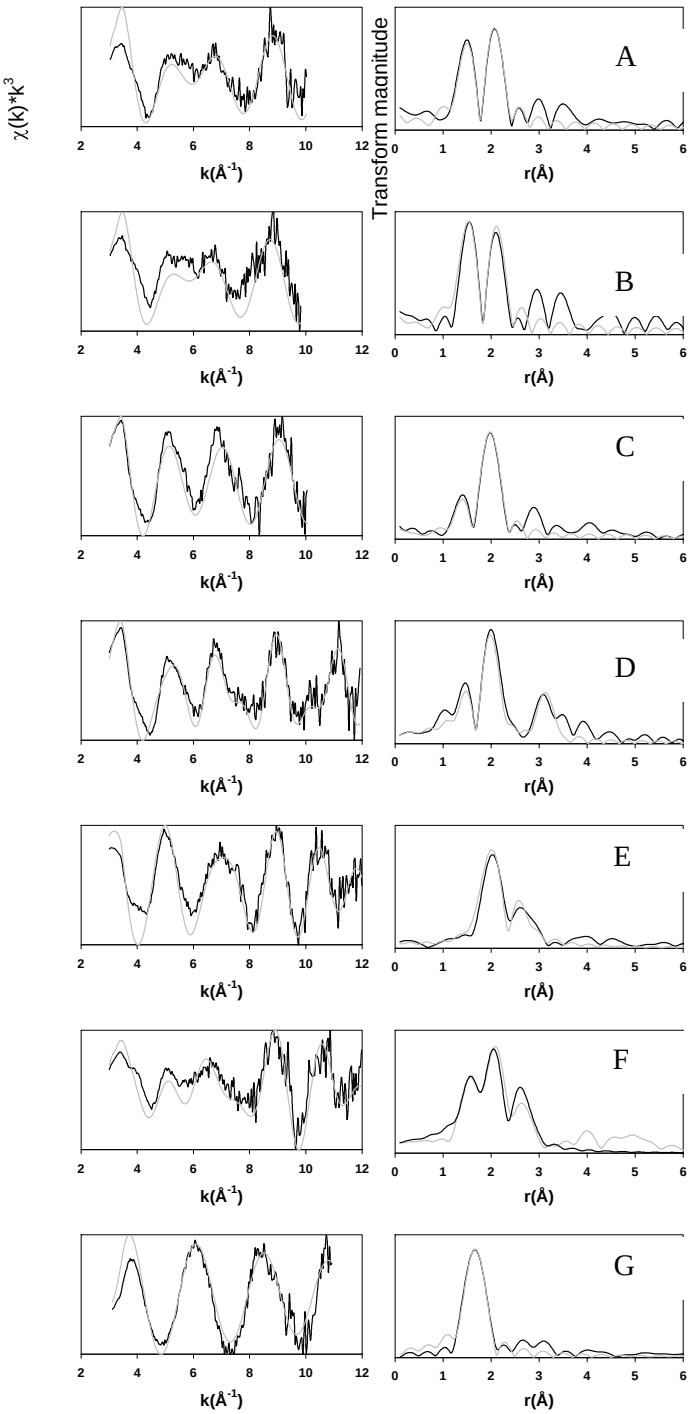

Table 1. Summary of EXAFS modelling results for sediments and reoxidised solution. N is the occupancy (± 25%), r is the interatomic distance (± 0.02 Å for the first shell, ± 0.05 Å for outer shells), $2\sigma^2$ is the Debye-Waller factor (± 25%), and *R* is the least squares residual.

Sample	Shell	N, type	Distance (Å)	$2\sigma^2$	R
Red. A; Humber FeR	1	6 O	2.01	0.014	*51.9*
Red. B; Humber SR	1	6 O	2.00	0.013	*38.0*
Red. C; FRC FeR	1	6 O	2.02	0.011	*66.0*
Red. D; Humber progressively anoxic	1	6 O	2.01	0.014	*45.6*
Ox. A; Humber FeR Air	1 2	1.8 O 3.3 O	1.71 1.99	0.007 0.012	*50.3*
Ox. B; Humber FeR NO_3^-	1 2	2.1 O 2.8 O	1.73 2.01	0.010 0.009	*52.7*
Ox. C; Humber SR Air	1 2	1 O 4.5 O	1.67 1.98	0.004 0.011	*35.5*
Ox. D; Humber SR NO_3^-	1 2	1.3 O 4.1 O	1.69 1.97	0.007 0.014	*45.9*
Ox. E; FRC FeR Air	1	6 O	2.01	0.010	*50.6*
Ox. F; FRC FeR NO_3^-	1 2	2 O 3 O	1.72 2.02	0.014 0.008	*65.4*
Ox. G; Reoxidised Solution	*1*	*4 O*	*1.72*	*0.004*	*31.0*

For the reoxidised solution, the EXAFS spectrum was modelled with 4 O atoms at 1.72 Å (values diagnostic for TcO_4^-) and this confirmed that remobilization to solution was associated with reoxidation of hydrous TcO_2 to TcO_4^-. For the majority of reoxidised sediment samples, the spectra differed from the reduced samples described earlier in that there was a significant (but variable intensity) peak at ca 1.7 Å as well as the peak observed at 2.0 Å. This suggested that both hydrous TcO_2 and TcO_4^- were present in the sediment components. To model the relevant samples, the number of scatterers, N1, in the shorter oxygen shell (1.7 Å; diagnostic for TcO_4^-) was refined, with the number of scatterers in the longer shell (2.0 Å; diagnostic for hydrous TcO_2) constrained to a value equal to (6 - (1.5 x N1)) [16]. Interestingly, for the FRC FeR sediment reoxidised with air, EXAFS modelling suggested a hydrous TcO_2 like coordination environment and accordingly, spectra were modelled using the same method as for the reduced samples. For the Humber sediments, the biogeochemistry of the sediment prior to reoxidation apparently affected the fate of the Tc in the samples. Both the Humber FeR Air and NO_3^- reoxidised sediments were modelled with relatively high occupancies of oxygen at 1.7 Å of 1.8 and 2.1 atoms respectively; Table 1. These values correspond to 50% ± 20% TcO_4^- being present in the sediment components. By contrast, Humber S-R Air and NO_3^- reoxidised sediments were modelled with a lower occupancy of oxygen atoms at 1.7 Å (1.0 and 1.3 atoms respectively; Table 1) indicating a lower proportion of TcO_4^- in the reoxidised, sulfidic sediments of 30 ± 12%, but with considerable uncertainty on these occupancies.

The FRC FeR Air sample was modelled with 6 O atoms at 2.0 Å suggesting that, on reoxidation, sediment-bound Tc remained as hydrous TcO_2 in this sediment. By contrast, the FRC FeR NO_3^-

reoxidised sample showed characteristics similar to the Humber sediments and was modeled with 2 O atoms at 1.7 Å suggesting 50% ± 20% TcO_4^- in the sediment. Overall, the EXAFS analysis of reoxidised sediments shows that a mix of both Tc(IV) and Tc(VII) is present in the majority of reoxidised samples. It is difficult to draw any further conclusion about the nature of the reoxidised Tc in the samples due to lack of information in the literature.

Figure 5. Normalised Tc-K edge XANES spectra for: (A) Humber SR (B) Humber FeR Air; (C) Humber FeR NO_3^-; (D) Humber SR Air; (E) Humber SR NO_3^-; (F) FRC FeR Air; (G) FRC FeR NO_3^-; (H) Reoxidised solution.

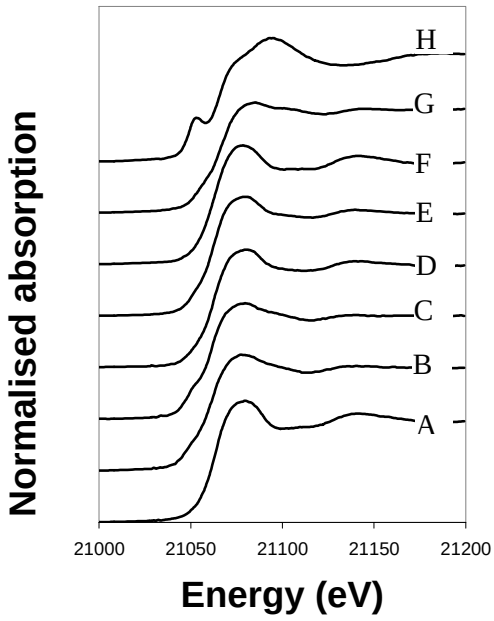

XANES spectra (21000 - 21200 eV) for reoxidised samples were also compiled and compared with a typical reduced sample (Humber SR) and the reoxidised solution (Figure 5). For samples that EXAFS analysis had indicated contained significant quantities of both TcO_4^- and hydrous TcO_2, the XANES spectra were modelled using least squares fitting of the XANES spectra of hydrous TcO_2 and TcO_4^- end members [16, 20] (Table 2). The reoxidised solution was clearly different to any other sample and had a clear "pre-edge" feature characteristic of the forbidden 1 s → 4 d transition seen in TcO_4^- XANES [19]. For the reoxidised sediments, their XANES spectra were between the hydrous TcO_2 and TcO_4^- end members. For example, the FRC FeR Air sample was almost identical to the reduced end member whilst the Humber FeR NO_3^- sample showed evidence of a pre-edge signal typical of the TcO_4^- end member. The results of least squares analysis of the XANES spectra for reoxidised sediment samples are presented in Table 2. Overall, the XANES modelling agrees with EXAFS modelling results, with Humber FeR Air and NO_3^- sediments showing higher TcO_4^- than Humber SR Air and NO_3^- sediments and with the FRC FeR NO_3^- sample showing the highest percentage TcO_4^- in contrast to the FRC FeR Air sample which showed that Tc was present as hydrous TcO_2 alone. In summary, both EXAFS and XANES modelling suggested that, contrary to expectations, in the majority of reoxidised sediments, both TcO_4^- and hydrous TcO_2 were present in the solid phase. Interestingly, all of the nitrate-reoxidised sediment samples contained significant quantities (ca 15 - 50%) of Tc(VII) in their solid phases even though remobilisation of Tc to solution in these systems was very low in the EXAFS experiments described here and was also very low in parallel, lower Tc concentration experiments [13, 16].

Table 2. XANES analysis of reoxidised sediment spectra as linear combinations of "end member" spectra TcO_4^- and hydrous TcO_2 in sediment.

Sample	Percentage Spectrum 1	Percentage Spectrum 8	*Fit index
1. Reduced sediment.	100	0	-
2. Humber FeR Air	70	30	0.33
3. Humber FeR NO_3^-	67	33	0.36
4. Humber SR Air	85	15	0.03
5. Humber SR NO_3^-	82	18	0.11
6. FRC FeR Air	100	0	-
7. FRC FeR NO_3^-	48	52	0.33
8. TcO_4^-	0	100	-

* The fit index of the calculated XANES spectra with experimental XANES spectra is defined as $\Sigma [(I_{obs} - I_{calc})^2]/n$ where n is the number of points in each spectrum.

Conclusions

Here, XAS studies have highlighted that the fate of technetium in reduced sediments is remarkably similar across a range of different aquifer and estuarine sediments and that poorly soluble hydrous TcO_2 forms during Fe(III) reducing conditions in these sediments. Additionally, work on air and nitrate reoxidation of reduced sediments suggests a complex fate for technetium with air reoxidation remobilising significant fractions (> 50%) of sediment bound Tc whilst nitrate reoxidation typically shows less (< 8%) reoxidation. In terms of the fate of technetium in reoxidised sediments, XAS shows that in the majority of sediments there is evidence for a mix of both hydrous TcO_2 and TcO_4^- bound to sediment components after reoxidation. Additionally, XAS confirms that the Tc species that is remobilised to solution on reoxidation is TcO_4^-. The mechanism by which TcO_4^-, in particular, is retained in the solid phase in both estuarine and aquifer sediments warrants further study.

Acknowledgements

We thank Bob Bilsborrow (Daresbury SRS) for his help in acquisition of XAS data. This research was supported by grants NER/A/S/2001/00652 and NER/A/S/2001/00960 from the UK Natural Environment Research Council, grant DE-FG02-04ER63743 from the US DOE Environmental Remediation Sciences program, and CCLRC beamtime awards at Daresbury SRS.

References

1. J.R. Lloyd and J.C. Renshaw, *Bioremediation of radioactive waste: radionuclide-microbe interactions in laboratory and field scale studies.* Curr. Opin. Biotechnol. 2005. **16:** p. 254-260.
2. K. Morris, J.C. Butterworth, and F.R. Livens, *Evidence for the remobilisation of Sellafield waste radionuclides in an intertidal salt marsh, West Cumbria, U.K.* Est. Coast. Shelf Sci. 2000. **51**: p. 613-625.
3. W.J.F. Standring, D.H. Oughton, and B. Salbu, *Potential remobilization of ^{137}Cs, ^{60}Co, ^{99}Tc, and ^{90}Sr from contaminated Mayak sediments in river and estuary environments.* Environ. Sci. Technol., 2002. **36**: p. 2330-2337.

4. E.A. Bondietti and C.W. Francis, *Geologic migration potentials of Tc-99 and Np-237.* Science, 1979. **203**: p. 1337-1340.

5. M.J. Wharton, B. Atkins, J.M. Charnock, F.R. Livens, R.A.D. Pattrick, D. Collison; *An X-ray absorption spectroscopy study of the coprecipitation of Tc and Re with mackinawite (FeS).* Appl. Geochem.,2000. **15**: p. 347-354.

6. K.O. Konhauser, R.J.G. Mortimer, V.A. Dunn, K. Morris; *The role of microorganisms during sediment diagenesis: Implications for radionuclide mobility*, in *Interactions of Microorganisms with Radionuclides*, M.J. Keith-Roach and F.R. Livens, Editors. 2002, Elsevier: London. p. 61-100.

7. J.R. Lloyd, J.A. Cole, and L.E. Macaskie, *Reduction and removal of heptavalent technetium from solution by Escherichia coli.* J. Bacteriol., 1997. **179**: p. 2014-2021.

8. G. De Luca, P. Philip, Z. Dermoun, M. Rousset, A. Vermeglio; *Reduction of Tc(VII) by Desulfovibrio fructosovorans is mediated by the nickel iron hydrogenase.* Appl. Environ. Microbiol., 2001. **67**: p. 4583-4587.

9. J.R. Lloyd, V.A. Solé, C.V.G. Van Praagh, D.R. Lovley; *Direct and Fe(II)-mediated reduction of technetium by Fe(III)-reducing bacteria.* Appl. Environ. Microbiol., 2000. **66**: p. 3743-3749.

10. J.K. Fredrickson, J.M. Zachara, D.W. Kennedy, R.K. Kukkadapu, J.P. McKinley, S.M. Heald, C. Liu, & A.E. Plymale; *Reduction of TcO_4^- by sediment associated biogenic Fe(II).* Geochim. Cosmochim. Acta., 2004. **68**: p. 3171-3187.

11. A. Abdelouas, B. Grambow, M. Fattahi, Y. Andres, E. Leclerc-Cessac; *Microbial reduction of ^{99}Tc in organic matter rich soils.* Sci. Tot. Environ. 2005. **336**: p. 255-268.

12. I.T. Burke, C. Boothman, J.R. Lloyd, F.R. Livens, R.J.G. Mortimer, K. Morris; *Effects of progressive anoxia on the solubility of technetium in sediments.* Environ. Sci. and Technol. 2005. **39**: p. 4109-4116.

13. J.M. McBeth, G. Lear, K. Morris, I.T. Burke, F.R. Livens, J.R. Lloyd; *Technetium reduction and reoxidation in aquifer sediments.* Geomicrobiol. J. (in review), 2006.

14. R.E. Wildung, S.W. Li, C.J. Murray, K.M. Krupka, Y. Xie, N.J. Hess, E.E. Roden; *Technetium reduction in sediments of a shallow aquifer exhibiting dissimilatory iron reduction potential.* FEMS Microbial Ecol., 2004. **49**: p. 151-162.

15. J.D. Istok, J.M. Senko, L.R. Krumholz, D. Watson, M.A. Bogle, A. Peacock, Y.J. Chang, D.C. White; *In-situ bioreduction of technetium and uranium in a nitrate-contaminated aquifer.* Environ. Sci. Technol., 2004. **38**: p. 468-475.

16. I.T. Burke, C. Boothman, J.R. Lloyd, F.R. Livens, J.M. Charnock, J.M. McBeth, R.J.G. Mortimer, K. Morris; *Reoxidation behavior of technetium, iron and sulfur in estuarine sediments.* Environ. Sci. Technol., 2006. **40**: p. 3529-3535.

17. D.C. Koningsberger, R. Prins; 1988. *X-ray Absorption: Principles, Applications,Techniques of EXAFS, SEXAFS, and XANES*. Wiley, New York.

18. F.R. Livens, M.J. Jones, A.J. Hynes, J.M. Charnock, J.F.W. Mosselmans, C. Hennig, H. Steele, D. Collison, D.J. Vaughan, R.A.D. Pattrick, W.A. Reed, L.N. Moyes; *X-ray absorption spectroscopy studies of reactions of technetium, uranium and neptunium with mackinawite.* J. Environ. Radioact., 2004. **74**: p. 211-219.

19. A. Maes, K. Geraedts, C. Bruggeman, J. Vancluysen, A. Rossberg, C. Hennig; *Evidence for the interaction of technetium colloids with humic substances by X-ray absorption spectroscopy.* Environ. Sci. Technol., 2004. **38**: p. 2044-2051.

20. J.D. Cotter-Howells, J.M. Charnock, C. Winters, P. Kille, J.C. Fry, A.J. Morgan; *Metal compartmentation and speciation in a soil sentinel: the earthworm Dendrodilus rubidus.* Environ. Sci. Technol., 2005. **39**: p. 7731-7740.

THREE DIMENSIONAL IMAGING OF ACTINIDE CONTAINING SAMPLES

Koen Janssens
Department of Chemistry, University of Antwerp, Belgium

Abstract

Micro-focused synchrotron radiation techniques to investigate actinide elements in geological samples are becoming an increasingly used tool in nuclear waste disposal research. Confocal X-ray fluorescence analysis is a recently developed method of spatially resolved (trace) analysis that is suitable for the characterization of (actinite-containing) heterogeneous materials of environmental origin in three-dimensions. In comparison to X-ray fluorescence tomography, the method has the advantage that it does not require sample to be rotated through the exciting micro beam, permitting to visualize trace element distributions below the surface of samples thicker than the penetration depth of the primary X-ray beam. An additional advantage is that is can be easily extended towards confocal XANES (X-ray absorption near edge spectroscopy) and confocal EXAFS (Extended X-ray absorption fine-structure spectroscopy).

Confocal μ-XRF is realised by the combined use of two focusing X-ray optical elements (X-ray lenses) at synchrotron beam line setups. The first lens is placed in the primary beam to focus the radiation down to a diameter in the range 1-15 μm while the second lens is positioned in front of the energy-dispersive detector in order to confine the volume within the sample from where fluorescent radiation can reach the detector.

By means of a combination of two polycapillary X-ray lenses, at HASYLAB Beamline L, non-destructive three-dimensional trace analysis with a best depth resolution of ca. 20 μm was realised. In pink-beam mode, absolute detection limits down to the 10 fg level were achieved while in monochromatic mode, confocal μ-XANES and μ-XANES measurements at the 10-100 μg/g concentration level has been demonstrated. At the ESRF, combinations of CRL and polycapillary lenses have been used for the investigation of buried inclusions in deep-earth diamonds.

In this paper, the characteristics, strong and weak points of the above-mentioned confocal method(s) of analysis will be discussed by using the analysis of U- and As-containing bore core samples from Ruprechthov, Czech Republic, a natural analogue to nuclear waste repository scenarios in deep geological formations, as example [1]. At this site, U-immobilization in the sediment is caused by the presence of AsFeS coatings on framboid Fe nodules at which reduction of mobile groundwater-dissolved U(VI) to less-soluble U(IV) take place.

[1] M.A. Denecke, K. Janssens, K. Proost, J. Rothe, U. Noseck, “Confocal micro-XRF and micro-XAFS studies of uranium speciation in a tertiary sediment from a waste disposal natural analogue site”, Env. Sci. Technol., **39** 2049 (2005).

ACTINIDE SPECIATION BOUND TO HYDROUS FERRIC OXIDE COLLOIDS IN THE NEAR-FIELD CONDITIONS OF THE WASTE POND AT "MAYAK" FACILITY (RUSSIA)

Stepan Kalmykov[1], Vladimir Kriventsov[2], Yuri Teterin[3], Aigul Khasanova[1] and Alexander Novikov[4]

[1] Lomonosov Moscow State University, Moscow, Russia,
[2] Siberian Synchrotron Radiation Centre, Novosibirsk, Russia
[3] Scientific Centre "Kurchatov Institute", Moscow, Russia
[4] Vernadsky Institute of Geochemistry and Analytical Chemistry, Moscow, Russia

Abstract

"Mayak" facility is a nuclear waste and spent nuclear fuel reprocessing plant located in Ural Mountains, Russia. The opened pond, Karachay Lake, was used for several decades for the discharge of low- and intermediate level waste solutions containing fission products and traces of actinides. Due to high salt concentration and high density of waste solutions, they are penetrating into the groundwater system that is represented by oxic Eh conditions.

The speciation of actinides in groundwater samples collected close to Karachay Lake was studied by successive micro- and ultrafiltrations with subsequent SEM, TEM, nano-SIMS, membrane extraction and other techniques. It was established that U and Np were found in soluble fraction (pass through 10 kD ultrafilter) in the form of their bi- and tri-carbonate complexes that was supported by chemical thermodynamic calculations. In contrast, Pu and Am were bound to nano-colloids 10 kD - 50 nm in size. The SEM and TEM data indicate the presence of variety of different colloidal particles which relative concentration decrease in the row: hydrous ferric oxides (HFO) >> clays ≈ calcite > rutile ≈ hematite ≈ barite ≈ MnO_2 > monazite > other phases. The SIMS with submicron resolution (Cameca nanoSIMS-50) was used to study local concentration of actinides. According to the obtained data among different colloids detected in the sample actinides were preferentially bound to HFO and MnO_2 while other phases did not sorb actinides.

In order to determine actinide speciation bound to HFO colloids XPS and An L_3 edge XAFS measurements were done at Siberian Synchrotron Radiation Centre. The storage ring VEPP-3 with electron beam energy of 2 GeV and an average stored current of 80 mA was used as the source of radiation. Since the concentration of actinides in actual samples was too low for XAFS, the samples for measurements were prepared by contacting about 10^{-5} M solutions of Np(V) and Pu(V) with HFO colloids at conditions (pH, Eh and salt concentration) relevant to groundwater collected close to Karachay Lake. According to XPS and XANES fingerprinting it was established that Np remains in pentavalent form upon interaction with HFO while Pu(V) is reduced to Pu(IV) upon sorption. According to EXAFS the first coordination sphere of Pu is occupied by two oxygen atoms of HFO with bond distance of about 2 Å. There are four oxygen atoms in the second coordination sphere and one Fe atom in the third coordination sphere at the distances of 2.1 and 3.3 respectively.

X-RAY MICROSCOPY OF URANIUM PRECIPITATES NEAR SINGLE BACTERIAL CELLS

Maxim I. Boyanov[1], Barry Lai[2], Matthew J. Marshall[3], Alice C. Dohnalkova[3], James K. Fredrickson[3], Kenneth M. Kemner[1]

[1] Bioscienes Division, Argonne National Laboratory, Argonne, IL, USA
[2] Advanced Photon Source, Argonne National Laboratory Argonne, IL, USA
[3] Pacific Northwest National Laboratory, Richland, Washington 99354, USA

Abstract

The interactions of bacteria with dissolved metals in their environment take place over the length scale of their size, usually one to several micrometers. The interplay between adsorption, reduction/ oxidation, cross-membrane transfer, precipitation, and mineral dissolution can create several different species of an element in the vicinity of a single cell, making the system less amenable to characterization by bulk methods. Using the current capabilities of the SRI-CAT X-ray microscopy beamline (sector 2-ID-D at the Advanced Photon Source in USA) this inhomogeniety can be addressed on the 150 nm lengthscale and insight on the functioning of cells and their biogeochemical interactions can be obtained.

We have combined the high spatial resolution of TEM imaging with the high elemental sensitivity of the X-ray microprobe to study products of the respiration of *Shewanella oneidensis* MR-1 on U(VI). Incubation of *Shewanella oneidensis* MR-1 in the presence of U(VI) results in the precipitation of uniform uraninite nanoparticles along thin (<100 nm in thickness) fiber-like structures. X-ray elemental analysis revealed co-localization of the uraninite particles with Fe and P, implying the bacterial origin of these structures. Subsequent heme staining and antibody co-localizations corroborated the finding and demonstrated for the first time extracellular localization of two decaheme cytochromes in direct association with UO_2 nanoparticles. These results provide insight on the mechanism of extracellular uranyl reduction and implicate a c-type cytochrome, MtrC, as the reductase.

Reference: “The Role of *Shewanella oneidensis* MR-1 Outer Membrane c-Type Cytochromes in Extracellular U(IV)O2 Nanoparticle Formation”, M. Marshall, A. Beliaev, A. Dohnalkova, D. Kennedy, L. Shi, Z. Wang, M. Boyanov, B. Lai, K. Kemner, J. McLean, S. Reed, D. Culley, V. Bailey, C. Simonson, D. Saffarini, M. Romine, Y. Gorby, J. Zachara, J. Fredrickson. In press, PLoS Biology.

UPTAKE MECHANISMS OF U(VI) BY ILLITE AS DETERMINED BY X-RAY ABSORPTION SPECTROSCOPY

R. Dähn, B. Baeyens and M. H. Bradbury
Paul Scherrer Institut, 5303 Villigen, Switzerland

Abstract

The uptake of metals and radiocontaminants in most natural systems, e.g. bentonites and argillaceous rocks, is inherently complex and multi-faced. Thus, the common approach consists in investigating environmentally-relevant pure clay minerals. Furthermore, in most investigated systems clay minerals are the predominant sorbing phase. Consequently, a fundamental understanding of the surface reactivity and metal uptake mechanisms of clay particles is of key importance to maintain environmental quality and to assess the long-term stability of radioactive waste repositories. Several uptake mechanisms have been proposed on clay particles: Sorption on edge sites, cation exchange in interlayer sites and formation of lamellar nucleation phases, such as neoformed layer silicates and mixed layered double hydroxides.

In this study, X-ray absorption spectroscopy was used to gain molecular-level information on the uptake of U(VI) onto illite. Illite is one of the major clay minerals in argillaceous rocks, which are being considered in many countries as potential host rocks for a high-level waste repository. U(VI) is an important actinide (spent fuel) and hence its uptake behaviour is of major importance in nuclear waste management.

At pH 5, high ionic strength (0.1 M $NaClO_4$) and low U(VI) concentrations (4 □mol/g) the uptake of U(VI) onto illite resulted in the formation of U(VI) inner-sphere mononuclear surface complexes located at the edges of illite platelets. Analysis of the binding sites on the edges of illite suggests that U(VI) sorbs preferentially to [Fe(O,OH)6] octahedral sites over [Al(O,OH)6] sites. This result is in good agreement with the findings of a previous study of Catalano *et al*. [1], investigating the U(VI) uptake by Fe-rich montmorillonites (SWy-2 and SAz-1). Heavy metals binding to edge sites is therefore a possible uptake mechanism for illites. Therefore, the observed attachment of metal ions specifically bond to clay mineral surfaces can severely reduce their bioavailability and mobility in soil and water environments.

[1] J. G. Catalano and G. E. Brown Jr., Geochimica et Cosmochimica Acta,, 69 (2005) 2995

SESSION IV

THEORETICAL AND MODELLING TOOLS

Chair: Tobias Reich

QUANTUM CHEMICAL CALCULATIONS OF ACTINIDE CONTAINING ELEMENTS WITH REGARDS TO SYNCHROTRON-BASED INVESTIGATIONS

Valérie Vallet[1*], Jean-Pierre Flament[1], Ingmar Grenthe[2]

[1] Laboratoire PhLAM (CNRS UMR 8523), CERLA (CNRS FR 2416), Université de Sciences et Technologies de Lille1, F-59655 Villeneuve d'Ascq Cedex, France

[2] Department of Chemistry, Inorganic Chemistry, Royal Institute of Technology (KTH), Teknikringen 36, S-10044 Stockholm, Sweden

Corresponding author: V. Vallet; Tel : + 33-32033-5985 ; Fax : + 33-32043-7020 ;
E-mail : valerie.vallet@univ-lille1.fr

Abstract

Quantum chemical calculations provide information on the local structure of aqueous metal complexes and on the occurrence of bond isomers and their thermodynamic stability. This type of information provides models that are essential for the proper analysis of the "two-dimensional" EXAFS data. In addition, these methods enable the calculation of Debye-Waller factors for single and multiple scattering pathways, from a full *ab initio* normal mode analysis. The latter values can then be used as fixed parameters in the EXAFS fitting procedure, thus reducing the number of parameters to be varied and improving the chemical conclusions drawn from the experimental data. We use examples from the chemistry of uranyl(VI) to illustrate how *ab initio* data can be used to reveal the three-dimensional structure of complexes in solution and discuss the agreement between calculated and EXAFS fitted Debye-Waller factors.

Introduction

Structure information on complexes in solution can be obtained from spectroscopy (NMR, IR and Raman) that provides information on the mode of coordination of a certain ligand and the symmetry of complexes with ligands of known geometry. Another spectroscopic probe is X-Ray absorption fine spectroscopy (XAFS), which refers to the oscillatory structure of the absorption coefficient just above an X-ray absorption edge. It depends on the detailed atomic structure, the electronic and vibrational properties of the compound. Therefore the EXAFS spectrum provides a structural signature, sometimes unique, but one that needs interpretation by physical and chemical models in order to provide information on the local atomic structure. Although the applications of XAFS to material or biological sciences have been extensive since the 1980s, its use for actinide systems is more recent. This is because of problems with the handling of radioactive materials and the need of high-energy synchrotron beams, in particular for the study of dilute solutions of actinide species. These difficulties have now to a large extent been overcome and XAFS has been extensively used to explore the structure and electronic properties of actinide compounds both in the solid state and solution as described in reviews by Allen *et al.* [1], Conradson [2], Den Auwer *et al.* [3] and Denecke [4]. The main goal of this article is to demonstrate that the combination of quantum chemical methods and XAFS data is a powerful tool for the elucidation of structural and electronic properties of actinide complexes in solution.

In XAFS spectroscopy, electronic and structural information on a given complex can be derived from the analysis the modulation amplitude χ of the X-Ray absorption coefficient, defined by:

$$\chi(k) = \frac{\mu - \mu_0}{\mu} \quad , \qquad (1)$$

where μ and μ_0 are the measured absorption coefficients of sample and solvent at different energy. k is the wave-vector:

$$k = \sqrt{\frac{2m_e}{\hbar^2}(E - E_0)} \qquad (2)$$

defined by photoelectron energy E and the threshold energy E_0 that corresponds to the binding energy of the photoelectron. It is divided in the extended X-ray absorption fine structure (EXAFS), referring to structure well above the absorption edge, and X-ray absorption near edge structure (XANES), for structure in the immediate vicinity of the edge. The physical basis of both EXAFS and XANES is the scattering of the X-Ray photoelectron by the surrounding atoms. The interference pattern between the outgoing photoelectron wave and that backscattered by the surrounding atoms results in the sinusoidal oscillations of the modulation amplitude, χ:

$$\chi(k) = \frac{S_0^2}{k} l^{-1} \sum_j N_j \left| f_j(k,\pi) \right| \frac{e^{-2R_j/\lambda(k)}}{R_j^2} e^{-2k^2\sigma_j^2} \sin(2kR_j + \Phi_j(k,R)) \quad , \qquad (3)$$

where N_j is the coordination number of the surrounding atoms j distant by R_j from the absorbing atom; f_j the backscattering amplitude function, Φ_j is the total phase-shift of the photoelectron induced by the scattering atoms; S_0 is the amplitude-reduction factor, which accounts for electronic relaxation effects occurring upon the photoelectron excitation; $\lambda(k)$ is the mean free path of the photoelectron; The Debye-Waller factor σ_j^2 corresponds to the root-mean square deviation of the absorber-scatterer distance. In polyatomic systems it also accounts for structural disorder.

Quantitative structural analysis of EXAFS spectra typically involves the use of an equation like Eq. (3) to model the recorded oscillations by fitting the various parameters. In ideal circumstances (see below for some of the limitations), EXAFS data can be analyzed to determine the absorber-scatterer distance with an accuracy of about 0.02 Å. Coordination numbers can be determined with an accuracy

of 10 to 20%. However there are some limitations in the technique, which involve both the experimental resolution and ambiguities in the fitting models that result from the large number of parameters in Eq. (3), some of which being strongly correlated. Therefore any attempt to reduce the number of fitted parameters is important and should facilitate the attempts to find a unique interpretation of the EXAFS spectrum. There are chemical and physical factors that complicate the determination of structure of complexes in solution:

1. The summation in Eq. (3) reflects the fact that all absorber-scatterer pairs contribute to the observed oscillations. Fortunately, the oscillations can in many cases be grouped into 'shells', a group of similar scatterers at approximately the same distance from the absorber. The definition of shells may be complicated in solutions where the EXAFS spectrum originates from several different species with different concentrations. These species may have different stoichiometric composition, *e.g.* $UO_2(SO_4)_2^{2-}$(aq), $UO_2(SO_4)$(aq) and UO_2^{2+}(aq) [5]; or they may be isomers in the cases where the complex contains multidentate ligands such as sulfate [5] that can coordinate with one or two of the oxygen atoms. Quantum chemical calculations can provide accurate geometries of the relevant isomers and assist in the definition of the 'shells' in the fitting procedure, as illustrated for uranyl tris-oxalate complexes in a forthcoming section.

2. The scattering parameters, ($f_j(k)$, S_0^2, Φ_j and $\lambda(k)$) are usually determined either from theoretical calculations or from model compounds of known structures related to the complex of interest. There are plenty of reliable single crystal X-ray structure for U and Th, but few for the other actinides. In cases where appropriate structure-chemical models are not available, quantum mechanical methods may be an alternative. In addition the scattering by atoms that differ by one or two atomic numbers (C, O and N, for instance) cannot be resolved, also justifying the need of good structure models.

3. The accurate treatment of multiple-scattering effects is of key importance for the accuracy of the fitting of EXAFS spectra. In many cases, the EXAFS fitting takes into account only the simplest, but dominant form of scattering, i.e., reflections by neighboring atoms directly back to the absorbing atom ("back-scattering" or "single scattering"). However, atoms can also reflect the electron wave onto other atoms that then in turn reflect to new atoms (multiple-scattering); unusually large EXAFS amplitudes are observed for an atom which has intermediate atoms lying between it and the absorber, at angles near 180 degrees. This is the so-called "lensing", "focusing" or shadowing effect. Multiple scattering paths have longer effective path lengths than single-scattering (at least twice the single-scattering lengths), and will thus overlap with other EXAFS features at larger distance. It is therefore crucial to include them in order to obtain reliable structure information beyond nearest-neighbor bond distances. In this context, the use of quantum chemical methods can contribute in two ways: from accurate structural models it is possible to compute all relevant effective lengths for the multiple scattering paths; in addition, from the *ab initio* vibrational partition function, one can compute Debye-Waller factors for all the paths.

In order to obtain accurate EXAFS fits with physically meaningful parameters it is necessary to strike a balance between the number of fitting parameters and the number of independent data points. In this context we can remind of the statement known as Occam's razor, "Entities are not to be multiplied without necessity" rephrased by Bertand Russel "It is in vain to do with more what can be done by fewer" [6] from the scholastic scholar William of Occam. In cases where several fitting sets giving comparable absolute "goodness-of-fit" results, one should always prefer the one having the fewer number of free parameters, but still consistent with other structure chemical information. This is achieved by placing constraints on certain parameters or by using values obtained from other sources. In this article we discuss constraints on the structure model, particularly important for solution EXAFS where isomers may occur and also the use of constrained Debye-Waller factors obtained from a full normal mode analysis. By using examples of the solution coordination chemistry of the uranyl(VI) ions, we explore the usefulness of this type of information and of quantum mechanical calculations.

The accuracy of the quantum chemical methods is of course an important point. We will only briefly mention the important points here.

Quantum chemical methods.

Quantum mechanical (QM) methods are based on "first principles" and the solution of the (time-independent) Schrödinger equation. In principle, it provides information on all chemical and physical properties of a particular compound and of its possible reactions by exploring the energy minima in configuration space. Each local minimum defines the geometry, the total energy and all electronic, vibrational and rotational energy levels of the systems. These allow the calculation of thermodynamic quantities, structural parameters and the identification of bond isomers. In the context of actinide chemistry, the choice of the quantum chemical method involves:

1. the choice of a relativistic Hamiltonian,
2. the choice of the number of electrons explicitly treated,
3. the treatment of electron-electron correlation effects,
4. the treatment of solute-solvent interaction.

These various points have been discussed in details in recent review articles [7, 8]. An important conclusion for the present discussion is that the structure parameters deduced using these different methods do not differ much from one another, for strongly bonded atoms they in general agree within 0.05 Å, the deviation may be twice as large for the weaker bonded water ligand. Energetics may be more sensitive as will be indicated below.

Quantum mechanical methods as a tool for structure and coordination assignments

Coordination of the uranyl(VI) aqua ion

We discuss here some examples of the use of QM as a tool to provide structure models to interpret EXAFS data of uranyl(VI) complexes in solution. The coordination number cannot precisely be determined even for simple complexes like UO_2^{2+}(aq). The bond distances and the coordination number have been determined experimentally using EXAFS and LAXS and some results are given in Table 1. The coordination number deduced from these data has an uncertainty between 10 and 20%, making an unambiguous determination difficult. In addition, these data give no information on the orientation of the water ligands. QM can here provide additional information by comparing the relative energy of aqua ions containing the same number of water molecules, but with different distribution between the first and second coordination spheres, e.g. the tetra aqua ion $[UO_2(H_2O)_4]^{2+}$,$(H_2O)_2$, the penta aqua ion $[UO_2(H_2O)_5]^{2+}$,(H_2O) and the hexa $[UO_2(H_2O)_6]^{2+}$, where water outside the square brackets denotes the second coordination sphere. The geometries reported in Table 1 show that the bond distances for the tetra- and penta-aqua models are both consistent with EXAFS values [9, 10], while the hexa model has longer bond distances. The relative energy determined by QM gives a very clear indication that the UO_2^{2+}(aq) ion has five coordinated water ligands (See Figure 1). Here it is important to point out that the computed bond distances do not depend on the quantum mechanical model used (Table 1), this is not the case for the computed energy (Table 2), which is more sensitive to the electron-correlation method. CCSD(T) is a method that provides an accurate description of correlation at a reasonable cost in computer time and can serve as reference against which other methods can be compared. We and others have found that the perturbative MP2 approach yield energies in excellent agreement with the CCSD(T) ones, while the DFT/B3LYP approach results in too small energy difference between four and five coordinated uranyl(VI) aqua ions, as compared to the more exact methods, Table 2 and Refs. [11, 12]. None of the currently available density functionals is able to correct this error. Therefore, when discussing relative

energies, method dependent errors in the computed values should be always checked before drawing any definite conclusions.

Table 1. EXAFS data and QM geometries of the different isomers of UO_2^{2+}(aq) optimized with the MP2 and DFT/B3LYP method in gas phase.

Complex	Method*	d(U-O_{yl})	d(U-O_{wat})	d(U-O_{wat2})	Ref.
UO_2^{2+}(aq)	EXAFS	1.78	2.41	-	[9]
$[UO_2(H_2O)_5]^{2+}$,(H_2O)	MP2	1.78	2.47(1)	4.18	[8]
	B3LYP	1.75	2.49(1)	4.26	[11]
$[UO_2(H_2O)_4]^{2+}$,$(H_2O)_2$	MP2	1.77	2.41	3.87	[8]
	B3LYP	1.75	2.42	3.93	[11]
$[UO_2(H_2O)_6]^{2+}$	MP2	1.785	2.47*2, 2.49*2, 2.64*2	-	[8]
	B3LYP	1.76	2.50*2, 2.52*2, 2.64*2	-	[11]

* Computational level for the geometry optimization

Table 2. Relative energies of the different isomers of UO_2^{2+}(aq) computed at the CCSD(T), MP2 levels and DFT/B3LYP levels using the CPCM solvent model (Ref. [11]). Geometries have been optimized at the DFT/B3LYP level in gas-phase (see Table 1).

Complex	CCSD(T)	MP2	DFT/B3LYP
$[UO_2(H_2O)_5]^{2+}$,(H_2O)	0.0	0.0	0.0
$[UO_2(H_2O)_4]^{2+}$,$(H_2O)_2$	50.6	52.9	44.8
$[UO_2(H_2O)_6]^{2+}$	14.3	11.9	30.0

Figure 1. Perspective view of $[UO_2(H_2O)_5]^{2+}$,(H_2O) calculated with coordinates from Ref. [13] .

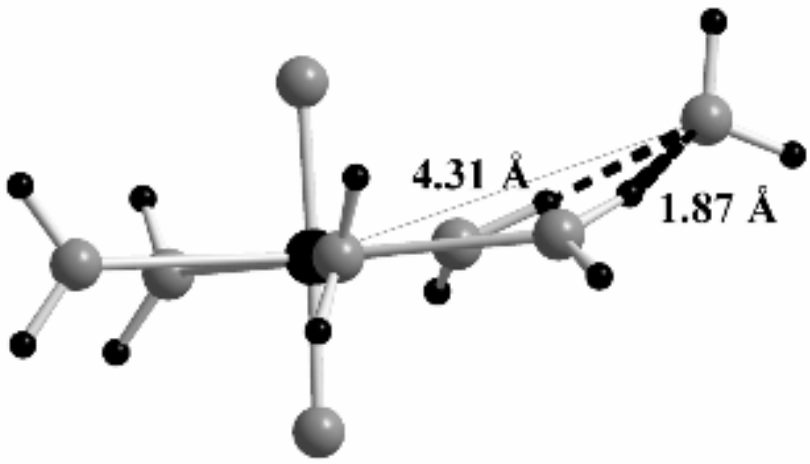

Distinguishing bond isomers: the illustrative example of $[UO_2(oxalate)_3]^{4-}$(aq) ion

The mode of coordination of a ligand is important for the understanding of the chemistry of a system; as indicated earlier equilibrium constants and solution structure data rarely provide this type of information. QM can here be of great assistance as shown by the following example: UO_2^{2+} forms the complexes UO_2(oxalate); $UO_2(oxalate)_2^{2-}$ and $UO_2(oxalate)_3^{4-}$ in aqueous solution. The magnitude of the equilibrium constants indicate and EXAFS data prove that the first two complexes form chelates by coordination of one oxygen from each carboxylate group to uranium; the mode of bonding is less clear for the third ligand [14]. The first EXAFS fit was done using a three-shell model with the coordination number N fixed to 2 for the U-O_{yl} shell. A coordination number of N = 4.8±0.6 for the equatorial oxygen atoms (second shell) and N=3.8±0.8 for the U-C distances (third shell) was obtained. The uncertainty in the coordination number does not allow an unambiguous distinction between four, five and six coordinated isomers. QM can here be used to calculate the relative energy of different bond isomers for the third ligand; isomers where the third oxalate is chelate bonded ($UO_2(oxalate)_2(oxalate\text{-}chel)^{4-}$), bonded through a single carboxylate oxygen ($UO_2(oxalate)_2(oxalate\text{-}uni)^{4-}$) or bonded to two oxygen atoms from the same carboxylate group ($UO_2(oxalate)_2(oxalate\text{-}carb)^{4-}$), *cf.* Figure 2. The comparison is given in Table 3 (Ref. [14]). The tris-chelated structure can be excluded because its bond distances do not match the experimental EXAFS data, the energy is also much higher than that of the other isomers. The U–O average distance in $UO_2(oxalate)_2(oxalate\text{-}carb)^{4-}$ is 2.51 Å, larger than the average, 2.42 Å, in $UO_2(oxalate)_2(oxalate\text{-}uni)^{4-}$ and also 16.8 kJ/mol higher in energy. The complex $UO_2(oxalate)_2(oxalate\text{-}uni)^{4-}$ has the lowest energy. Using the *ab initio* structure of the most stable isomer to define a four-shell model, with two distinct U-O_{eq} distances, and use it to refine the EXAFS spectra by fixing the coordination number in the equatorial shells. The fitted U-O and U-C bond distances are in excellent agreement with the calculated ones. Using EXAFS data alone it had not been possible to deduce the correct structure.

Table 3. EXAFS data and quantum chemical results $UO_2(oxalate)_3^{4-}$ taken from Ref. [14]. QM bond distances were optimized at the Hartree-Fock level and the relative energies computed at the MP2 level in the CPCM solvent. Three different isomers of $UO_2(oxalate)_3^{4-}$ are reported (see text)

Method	Model	Shell	N	R(Å)	ΔE (kJ/mol)
EXAFS	Three-shells model	U-O_{yl}	2[f]	1.79	
		U-O_{eq}	4.8±0.6	2.37	
		U-C	3.8±0.8	3.25	
	Four-shells model	U-O_{yl}	2[f]	1.79	
		U-O_{eq}	4[f]	2.427 (fixed value from QM)	
		U-O_{eq}	1[f]	2.386 (fixed value from QM)	
		U-C	4[f]	3.26	
QM	$UO_2(oxalate)_2(oxalate\text{-}chel)^{4-}$			U-O_{chel} = 2.52 U-C_{chel} = 3.42	+36.3
	$UO_2(oxalate)_2(oxalate\text{-}uni)^{4-}$			U-O_{chel} = 2.43; U-O_{uni}= 2.39 U-C_{chel} = 3.30; U-C_{chel} = 3.30; U-C_{uni} = 3.46	0
	$UO_2(oxalate)_2(oxalate\text{-}carb)^{4-}$			U-O_{ox} = 2.46; U-O_{carb} = 2.61 U-C_{chel} = 3.36; U-C_{carb} = 3.00	+16.8

Figure 2. Perspective views of the three isomers of $UO_2(oxalate)_3^{4-}$ calculated from the co-ordinates given in Ref. [14]. Two of the oxalate ligands form chelates, while the third is co-ordinated (a) as a chelate, (b) through a single carboxylate oxygen, or (c) through two oxygen atoms from the same carboxylate group.

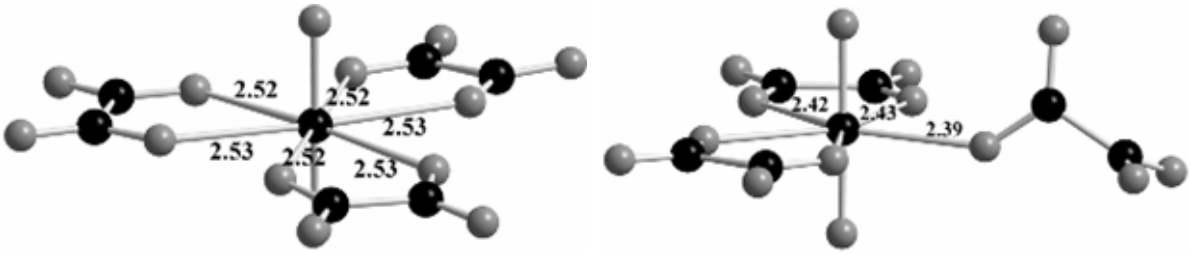

a. **b.**

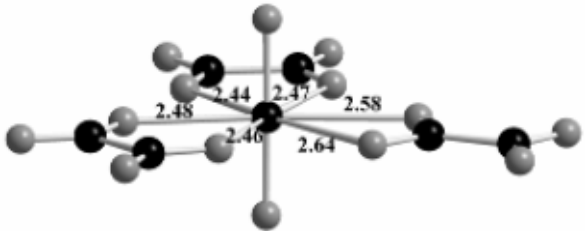

c.

Uranyl sulfate complexes in solution.

Sulfate like oxalate, can bind uranyl(VI) ion either in a monodentate or a bidentate fashion. Both types of coordination have been observed in single crystal X-ray structures. EXAFS [15] and LAXS (Large Angle X-ray Scattering) [16] data of uranyl-monosulfate solutions indicate a change of the mode of coordination of sulfate with the composition of the test solutions. The key signature in the EXAFS or LAXS spectra is the position of the characteristic peak for the U-S distance: a distance of 3.07-3.11 Å is expected for bidentate sulfate ions, while a distance of 3.67 Å is characteristic of monodentate coordination. Both EXAFS and LAXS analysis indicate one single distance between uranium and the equatorial oxygen atoms that is the average distance between coordinated water molecules and sulfate. In a recent study [5], we have used QM methods to compare the bond distances in $UO_2(SO_4)$ and $UO_2(SO_4)_2^{2-}$ for both isomers (See Figure 3). The optimized U-S distances in the mono and bidentate co-ordination, 3.63 Å and 3.08 Å, agree very well with experimental data both for the complexes $UO_2(SO_4)$ and $UO_2(SO_4)_2^{2-}$. The calculated *average* U-O distances are also in excellent agreement. However, QM calculations show that the $U\text{-}O_{sulfate}$ distance is significantly different between mono and bidentate isomers, 2.23 vs. 2.37 Å. All U-O distances are very similar in bidentate coordination, while there is a difference of about 0.18 Å between the $U\text{-}O_{sulfate}$ and $U\text{-}O_{water}$ bond distances in the monodentate isomer. This disparity did *not* appear in the LAXS analysis by Neuefeind *et al*. [16], or in the EXAFS analysis from Moll *et al*. [15]. This difference is of obvious chemical importance and it would therefore be of interest to use the QM optimized structure to refine the fit of the LAXS spectrum. The free energy of reaction between the bond isomers is small, less than 16 kJ/mol, indicating that the mode of coordination may change with the composition of test solutions used, as observed experimentally.

Figure 3. Perspective views of the (a) monodentate $[UO_2(SO_4)(H_2O)_4]$ and (b) bidentate $[UO_2(SO_4)(H_2O)_3]$,(H_2O) isomers of uranyl(VI) monosulfate complex and of the (b) $UO_2(SO_4\text{-mono})_2^{2-}$, (d) $UO_2(SO_4\text{-chelate})_2^{2-}$ isomers of the uranyl(VI) bisulfate. Geometries have been optimized with DFT/B3PW91 functional using the CPCM solvent model.

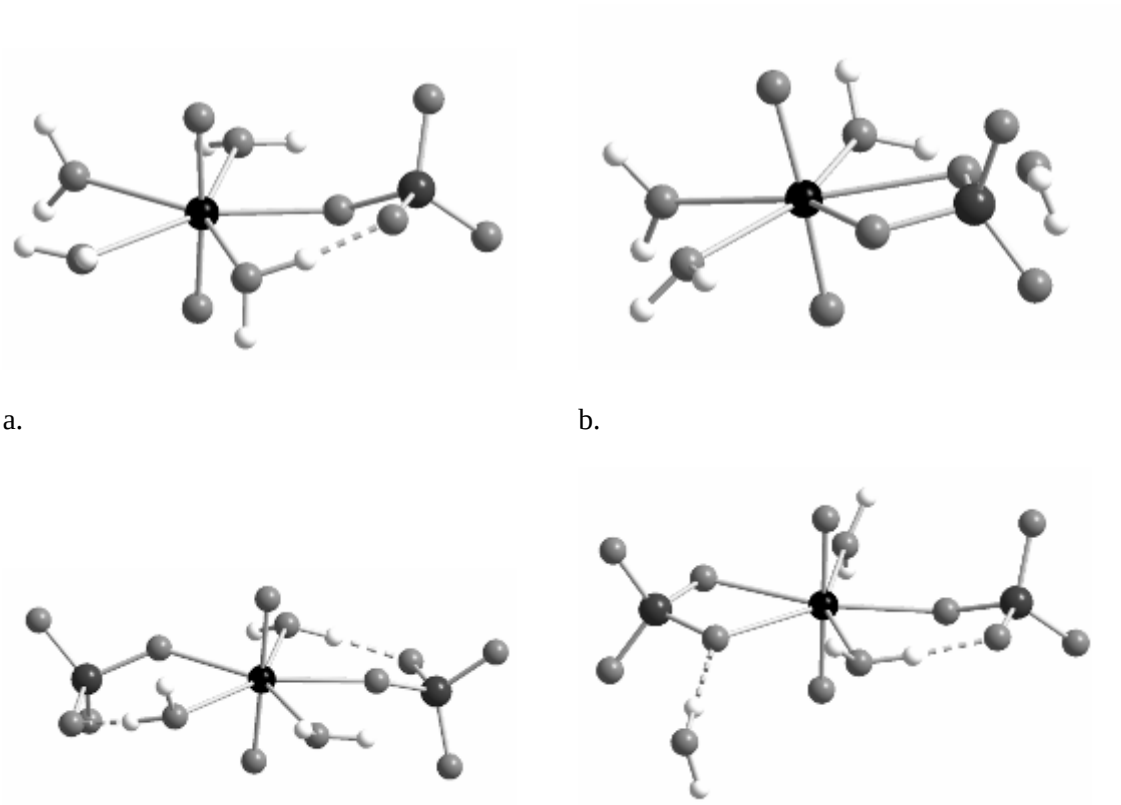

a. b.

c. d.

The use of QM methods to deduce Debye-Waller factors

Debye-Waller factors (DWFs) in the EXAFS equation (1) accounts for structural and thermal disorder in the species studied and they are determined by fitting of the experimental data to Eqn. (3). Single- and multiple-scattering DWFs must be included to obtain a satisfactory agreement between theory and experiment. Since the total number of parameters that can be varied is limited by the experimental conditions, the data cannot, in general, support fitting of all relevant multiple-scattering DWFs (DWFs). However, it is well known that these factors can be deduced from vibration spectra provided that one can identify the normal modes. The problem is straightforward when a particular normal mode corresponds to a well defined “group frequency”, such as the symmetric and asymmetric stretch modes in the linear Actinyl(V) and (VI) bond. The problem is more difficult in the more common case when the normal mode contains “contributions” from several group frequencies. The average thermal displacement of an atom is then calculated using all the normal modes that involve displacement of the atom with respect to the central ion. This requires a full normal mode analysis, which includes the knowledge of both the vibrational frequencies and the nature of each normal mode in terms of atomic or group motions. Many of the published normal coordinate analyses have been made using empirical force constants, but quantum chemical data are inherently more accurate. The resolution of vibration spectra is often difficult and the experimental data are therefore often obtained

from solids at low temperature; this method can for obvious reasons not be used for solutions. A common method is then to compare frequencies from the solid state where an assignment has been made, with the (often poorly resolved) spectra from solutions. In actinyl(VI) systems, there are limited infrared and Raman measurements and assignments are limited to a few characteristic modes, such as symmetric and asymmetric stretch of U-O_{yl} and internal frequencies of the coordinated ligands (for example S-O stretches in sulfate). It is therefore rarely possible to extract relevant information to derive the DWFs for the equatorial ligands.

Table 4. Geometries of the monodentate (mono) and bidentate (chel) uranyl mono- and bisulfate complexes optimized in the solvent using the B3PW91 functional.

Chemical Model	Method	U-O_{yl}	U-O_{wat}	U-O_{chel}	U-O_{mono}	U-O_{aver}	U-S_{chel}	U-S_{mono}
	LAXS [16]					[A]0.017*		3.67
$[UO_2(SO_4$-chel$)(OH_2)_3]$	EXAFS [15]	1.77_3				2.41_2	3.11f	
$[UO_2(OH_2)_5]^{2+}$,(H_2O)	QM [5]	1.746	2.43_1	-	-	2.43_1	-	-
$UO_2(SO_4$-mono$)(OH_2)_4$	QM [5]	1.759	2.48_3	-	2.22	2.43_8	-	3.61
$[UO_2(SO_4$-chel$)(OH_2)_3]$,(H_2O)	QM [5]	1.765	2.46_3	2.37_2	-	2.42_4	3.08	-
$[UO_2(SO_4$-chel$)_2(H_2O)]^{2-}$	EXAFS [15]	[B]1.77_2 [C]1.78_1				2.40_4 2.43_7	[B]3.14_0 [C]3.11_3	
$[UO_2(SO_4$-mono$)_2(OH_2)_3]^{2-}$	QM [5]	1.769	2.49_3	-	2.29	2.4_1	-	3.67
$[UO_2(SO_4$-chel$)(SO_4$-mono$)(OH_2)_2]^{2-}$,(H_2O)	QM [5]	1.769	2.46	2.42_1	2.27	2.41_6	3.11	3.67
$[UO_2(SO_4$-chel$)_2(H_2O)]^{2-}$,$(OH_2)_2$	QM [5]	1.768	2.43	2.40_1	-	2.41_1	3.09	-

f means that the parameter in question has been fixed at the given value in the EXAFS fitting.

[A] Difference of the average U-O distance between uranyl penta aqua ion and uranyl sulfate derived from the difference pair distribution [16].

[B] and [C] refers to test solutions B and C in Table 1 in ref. [15]

Dimakis and Bunker [17-19] have demonstrated that it is possible to calculated DWFs for any single and multiple scattering pathways by performing full normal mode analysis using force constants computed with *ab initio* methods [17]. They used these *ab initio* DWFs as input parameters to the FEFF program [20] to generate a new $\chi(k)$ profile. By testing this approach on small molecules, they found an excellent agreement between the computed DWFs and those derived from the fitting of the experimental spectra. This method has been successfully applied to resolve the EXAFS spectra of Zinc tetradimiazole [18]. They also demonstrated that in cases where the molecular system is too large to be handled with accurate *ab initio* methods, it is possible to use a reduced chemical model to calculate DWFs [19]. One should point out that a full normal mode analysis is a routine task when analytical second derivatives are available but may be very computer-time demanding when there is no analytical expression of the second derivatives have to be derived from numerical differentiation of the first derivatives along each 3N coordinates of the N-atoms molecules. All the reported results make use of analytical second derivatives for DFT methods with continuum solvent models implemented in Gaussian quantum chemistry package [22].

The accuracy of *ab initio* DWFs depends on the accuracy of the relevant normal mode frequencies. In uranyl(VI) complexes, the characteristic U-O_{yl} stretching motions are fully decoupled from other motions and are therefore the only ones that contribute to the DWFs of the O_{yl} oxygens. In Table 5, we report the experimental and computed QM vibrational frequencies for the symmetric, ν_{sym}, and asymmetric ν_{asym}, U-O_{yl} stretches of selected uranyl(VI) complexes. The agreement is very good for the asymmetric vibration, while the calculated values for the symmetric stretch tend to be overestimated by at most 50 cm^{-1}, compared to the experimental ones. We have used both QM and experimental stretching U-Oyl frequencies to compute the DWF of the O_{yl}. The values reported in Table 5 indicate that a change of 50 cm^{-1} has negligible effect, 0.00005 $Å^{2,}$ on the DWFs. This demonstrates that accurate DWFs for the O_{yl} in actinyl species can be derived from QM calculations.

Table 5. Experimental and QM calculated (DFT/B3PW91 with CPCM solvent) symmetric (ν_{sym}) and asymmetric (ν_{asym}) vibrational frequencies in cm^{-1} for U-O_{yl} in various uranyl(VI) complexes. DWFs computed with the QM or experimental frequencies.

	ν_{sym} (U-O_{yl})		ν_{asym} (U-O_{yl})		σ^2(U-O_{yl}) ($Å^2$)		Exp. Ref. *
Complex	QM	Exp.	QM	Exp.	QM Freq.	Exp. Freq.	
$[UO_2(H_2O)_5]^{2+}$	923	870	970	962	0.00122	0.00127	[22] (soln.)
$[UO_2(OH)_4]^{2-}$	770	786	796	-	0.0016	-	[23] (soln.)
$[UO_2Cl(H_2O)_4]^{+}$	900	871	950	956	0.00126	0.00128	[24] (soln.)
$[UO_2F(H_2O)_4]^{+}$	890	827	930	908	0.00128	0.00132	[24] (soln.)
$UO_2Cl_4^{2-}$	853	830 ± 4	906	909 ± 4	0.00133	0.00135	[25-26] (cryst.)
$UO_2F_5^{3-}$	792	803 ± 2	816	857 ± 2	0.00151	0.00145	[27] (cryst.)
$UO_2(SO_4$-uni$)(H_2O)_4$	905	860	937	900	0.00128	0.00134	[24] (soln.)

***** Experimental data in solution (soln.) or in crystal host lattices (cryst.).

There are few data on vibrational frequencies for the uranium equatorial ligand motions. In Tables 6 and 7 we report vibrational frequencies for $UO_2Cl_4^{2-}$ and $UO_2F_5^{3-}$ computed with quantum chemical methods at the DFT/B3PW91 level in the CPCM. The most complete experimental data have been derived from the luminescence spectra in crystal host lattices (Tanner *et al*. [25-27]), but there are also some data from solution from Gál *et al*. [24]. The agreement between the *ab initio* values and the experimental solid-state data is very good. The largest deviations, less than 40 cm^{-1}, are observed for equatorial symmetric and asymmetric stretching mode and in the in-plane bending modes. These discrepancies may be related to packing effects occurring in the crystal lattice but absent in solution. In LiCl:U solution, Gál *et al*. [24] suggested that the 222 cm^{-1} frequency is related to the U-Cl stretching in $UO_2Cl(aq)^{+}$. In the QM normal mode analysis, the normal mode with frequency 248 cm^{-1} corresponds to such motion but this is not a pure stretch mode as other modes with slightly lower frequencies also give some contribution. Using the 248 cm^{-1} normal mode only, the DWF for the U-Cl distance is 0.0033 $Å^2$, while we obtain 0.0043 $Å^2$ if we include contributions of all normal modes. This demonstrates that there is not always a one-to-one correspondence between a specific motion and a normal mode. This makes an empirical assignment of experimental vibrational spectra difficult and in practice the use of the group frequency concept not very useful for the determination of DWFs. A full normal mode analysis is necessary.

Infrared and Raman vibrational frequencies have been measured for uranyl-sulfate solutions with a total concentration of U(VI) of 0.5 $mol.dm^{-3}$ and varying sulfate concentration. There are strong infrared bands at 1144 cm^{-1} and 1047 cm^{-1} that are assigned to sulfate group vibrations, indicating that

the majority of the sulfate groups are coordinated in a monodentate fashion in the test solutions used. We have compared the computed vibrational frequencies to those assigned experimentally, cf. Table 8 and the agreement is excellent. These results demonstrate that *ab initio* methods can provide accurate vibrational frequencies for uranyl complexes.

Table 6. Vibrational frequencies for $UO_2Cl_4^{2-}$ and $[UO_2Cl(H_2O)_4]^+$ computed at the DFT/B3PW91 level in the CPCM solvent. Comparison to experimental data derived from the luminescence spectra of $UO_2Cl_4^{2-}$ in crystal host lattices (ν_s, ν_{as}: symmetric and asymmetric stretches; δ: bend) (Tanner *et al*. [25-27]) and solution IR and Raman data from Gál *et al*. [23].

	QM	Salt [23]	Host lattice [25-27]			QM	Solution [23]
Mode	$UO_2Cl_4^{2-}$	$[Bu_4N][UO_2Cl_4]$	Cs_2NaYCl_6	Cs_2SnCl_6	$Cs_2NaGdCl_6$	$[UO_2Cl(H_2O)_4]^+$	8:1 LiCl:U
ν_s (OUO)	853	833	836	821	832	900	871
ν_{as} (OUO)	906	919	917	905	914	950	956
δ (OUO)	256	262	244	249	252	252	254
ν_s (UCl)	248	258	266	279	-	248	222
ν_{as} (UCl)	232	238	265	276	264		
δ (OUCl)	115	-	115	114	92		
δ' (OUCl)	203	207	200	201	200		

Table 7. Vibrational frequencies for $UO_2F_5^{3-}$ computed at the DFT/B3PW91 level in the CPCM solvent. Comparison to experimental data derived from the luminescence spectra of $UO_2F_5^{3-}$ in crystal host lattices (ν_s, ν_{as}: symmetric and asymmetric stretches; δ: bend; oop δ: out-of-plane bending; ip δ: in plane bending) from Tanner [27].

	QM	Host lattice [27]	
Description	$[UO_2F_5^{3-}]$ (aq)	$K_3UO_2F_5$	$Rb_3UO_2F_5$
ν_s (O-U-O)	791	805	799
ν_{as} (O-U-O)	816	859	855
δ (O-U-O)	278	290	283
ν_s (U-F)	392	439	432
ν_{as} (U-F)	347	376	364
ν_{as} (U-F)	313	330	325
oop δ (O-U-F)	181	197	193
ip δ (F-U-F)	255	221	209
ip δ (F-U-F)	255	215	212
rock (O-U-F)	279	272	268
oop δ (O-U-F)	182	180	172

Table 8. Vibrational frequencies for $[UO_2(SO_4\text{-mono})(H_2O)_4]$ $[UO_2(SO_4\text{-chel})(H_2O)_3](H_2O)$ computed at the DFT/B3PW91 level in the CPCM solvent. The QM values are compared to experimental infrared and Raman bands of uranyl sulfate solution (0.5 mol.dm^{-3}) (Gál *et al*. [23]). In the study by Gál *et al*. there are several observed frequencies that have not been assigned and the authors have not used a normal coordinate analysis in their analysis. The relative amounts of the two complexes $UO_2(SO_4)$ and $UO_2(SO_4)_2^{2-}$ varies in the test solutions used by Gál *et al*. [23], but the frequency changes are not large as indicated in the Table.

	$UO_2(SO_4\text{-mono})(H_2O)_3$	$UO_2(SO_4\text{-chel})(H_2O)_3$	(1:1) to (1:3) solutions
Mode	QM	QM	Infrared and Raman [23]
$\nu_3(SO_4)$ monodentate	1181		1133 – 1147
$\nu_3(SO_4)$ monodentate	1113		1042 – 1047
$\nu_3(SO_4)$ bidentate		1212	1189
$\nu_3(SO_4)$ bidentate	–	1119	1105
UO_2 assymetric	936	937	942 – 950
UO_2 symmetric	901	877, 880, 901	853 – 863
$\nu_1(SO_4)$ monodentate	601	–	610
UO_2 bending	243	241	259 – 264
U-O(SO_4) stretch	208	202	209

In Table 9, we report *ab initio* bond distances and DWFs for UO_2^{2+}(aq), $UO_2Cl_4^{2-}$(aq), $UO_2F_5^{3-}$(aq) and Uranyl(VI) sulfate, and compare to the data obtained by Wahlgren *et al*. [9], Servaes *et al*. [29] and Vallet *et al*. [10], Moll *et al*. [15], respectively, from the EXAFS fit. For UO_2^{2+}(aq), we have investigated the effect of hydrogen bonds between the first sphere water and the second sphere water molecules. We have thus used two chemical models, the first one is the penta aqua ion with the first hydration shell only, $UO_2(H_2O)_5^{2+}$, and the second model involving the penta aqua ion with one second-sphere water molecule, hydrogen bonded to two water molecules from the first sphere. The distances between uranium of the first sphere water molecules hydrogen bonded to the outer sphere one are slightly longer, by 0.03 Å than the three other ones. However, this has no effect on the computed DWFs. In the uranyl-tetrafluoride complex, the computed uranium-water distance is 0.19 Å too long as the EXAFS fitted value. Accordingly, the computed Debye-Waller factor is too small. Infante and Visscher [29] have investigated the geometry of this complex with a more detailed solvation model in which part of the outer sphere solvation is described explicitly at the quantum mechanical (QM) level, or using hybrid QM/molecular mechanics methods (QM/MM). With the largest model (29 outer sphere water molecules), they obtained a uranium-water distance of 2.66 Å as long as that obtained with a continuum model. This indicates that this deviation is not related to solute-solvent interactions but to the metal-equatorial ligand interaction and that it is necessary to use high-level correlation methods to describe them properly. Work in this direction is in progress. It is also of interest to speculate on the origin of the deviation between experimental and calculated DWFs in the sulfate complexes. As noted in Table 9, the experimental value of the Debye-Waller factor for the U-S distance is significantly larger, a factor of about three, than the calculated one. This might be an indication of structure disorder or that low frequency libration modes of the coordinated sulfate group are not well described by the QM model. The “disorder” corresponds to a displacement of about 0.09 Å.

The complete set of data reported in Table 9 show that the agreement between DWFs computed from *ab initio* normal mode analysis agree well with those derived from the EXAFS spectra. This agreement can be used as an additional indicator of the goodness of the EXAFS fitting. In addition, it indicates that *ab initio* methods are able to predict accurate DWFs that can be used as fixed parameters to reduce the number of parameters to fit. The DWFs for multiple scattering pathways, with the exception of the three and four legged O-U-O pathways, can be rarely determined in the fitting of the experimental EXAFS data.

Table 9. Bond distances and Debye-Waller factors for $UO_2(H_2O)_5^{2+}$(aq), $UO_2Cl_4^{2-}$(aq) and $[UO_2F_5]^{3-}$(aq) obtained either from *ab initio* QM methods (DFT/B3PW91 with CPCM solvent model) or fitting of the recorded EXAFS spectra.

		QM			EXAFS			
Complex	Shell	R [Å]	N	σ_{SS}^2 [Å^2]	R [Å]	N	σ^2 [Å^2]	Ref.
$UO_2(H_2O)_5^{2+}$	U-O_{yl}	1.75	2	0.0012	1.77	2	0.0012	[9]
	U-O_{water}	2.43_1	5	0.0059	2.41	5.2 ± 0.4	0.0061	
$UO_2(H_2O)_5^{2+}$,(H_2O)	U-O_{yl}	1.75	2	0.0012				
	U-O_{water} (H-bond)	2.45	2	0.0059				
	U-O_{water}	2.42_1	2	0.0058				
$UO_2Cl_4^{2-}$	U-O_{yl}	1.77	2	0.0013	1.77	2	0.0015	[29]
	U-Cl	2.68	4	0.0046	2.68	3.7	0.0044	
$UO_2F_5^{3-}$	U-O_{yl}	1.82	2	0.0015	1.80	2	0.0016	[10]
	U-F	2.27	5	0.0043	2.26	4.4 ± 0.6	0.0057	
$UO_2F_4(H_2O)^{2-}$	U-O_{yl}	1.81	2	0.0015	1.80	2f	0.0016	[10]
	U-F	2.23	4	0.0038	2.26	4.1 ± 0.7	0.0048	
	U-O_{wat}	2.67	1	0.0014	2.48	1f	0.0046	
$UO_2(SO_4$-chel$)(H_2O)_3$	U-O_{yl}	1.77	2	0.00128	1.77_3	1.9 ± 0.2	0.0013	[15]
	U-O_{aver}	2.42_4	2	0.0068	2.41_2	5.0 ± 0.4	0.0084	
	U-S	3.08	1	0.0032	3.11f	1f	0.0105	
$[UO_2(SO_4$-chel$)_2(H_2O)]^{2-}$,$(OH_2)_2$	U-O_{yl}	1.77	2	0.0013	$^B1.77_2$	1.9 ± 0.2	0.0013	[15]
					$^C1.78$	2.0 ± 0.2	0.0013	
	U-O_{aver}	2.41_1	5	0.0060	$^B2.40_4$	5.0 ± 0.4	0.0082	
					$^C2.43_7$	5.0 ± 0.4	0.0107	
	U-S	3.09		0.0030	$^B3.14_0$	1f	0.0086	
					$^C3.11_3$	2.2 ± 0.5	0.0075	

f means that the parameter in question has been fixed at the given value in the EXAFS fitting.
^{B} and ^{C} refers to test solutions B and C in Table 1 in ref. [15]

Conclusions

We have demonstrated that QM calculations might provide information that improves the analysis of EXAFS spectra both by providing three-dimensional structure models and Debye-Waller factors. The structure models provide information on the number of shells around the "target" atom (U), bond distances and occurrence of bond isomers. Debye-Waller factors can be derived from a full *ab initio* normal mode analysis and can be used as fixed parameters in the data analysis that might lead to an improvement of the reliability of fitting and the convergence of the fitting procedure, in particular for complex molecular systems. If two or more fitting sets give comparable absolute "goodness-of-fit" results, one should always prefer the set having the fewer number of free parameters. Furthermore from the full normal mode analysis one can derive information on all multiple-scattering paths and their Debye-Waller factors that can be used in FEFF [20] like programs that compute the corresponding $\chi(k)$ functions. Work in this direction is in progress.

Acknowledgments

This study was supported by the ACTINET network of excellence and through a grant from the Trygger Foundation. Computational resources have been provided by the Institut de Développement et de Ressources en Informatique Scientifique du Centre National de la Recherche Scientifique, IDRIS (Project 61859), and the Centre informatique National de l'Enseignement Supérieur CINES (Project phl2531). CERLA is supported by the Ministère chargé de la Recherche, Région Nord-Pas-de-Calais and FEDER.

References

[1] P.G. Allen, J.J. Bucher, M.A. Denecke, N.M. Edelstein, N. Kaltsoyannis, H. Nitsche, T. Reich, D.K. Shuh, *Synchrotron Radiation Techniques in Industrial, Chemical and Material Sciences* (Ed.: D'Amico), Plenum Press, **1996**, p. 169-185.

[2] S.D. Conradson, Appl. Spectrosc. **1998**, *52*, 252279.

[3] C. Den Auwer, E. Simoni, S. Conradson, C. Madic, *Eur. J. Inorg. Chem.* **2003**, 3832-3859.

[4] M.A. Denecke, *Coord. Chem. Rev.* **2006**, *250*, 730-754.

[5] V. Vallet, I. Grenthe, *C. R. Chimie*, submitted

[6] B. Russel "A History of Western Philosophy", 12th printing, p. 472, Simon and Schuster Inc., New York 1959.

[7] V. Vallet, Z. Szabó, I. Grenthe, *Dalton Trans.* **2004**, 3799–3807.

[8] V. Vallet, P. Macak, U. Wahlgren, I. Grenthe, *Theor. Chem. Acc.* **2006**, *115*, 145-160.

[9] U. Wahlgren, H. Moll, I. Grenthe, B. Schimmelpfennig, L. Maron, V. Vallet, O. Gropen, *J. Phys. Chem. A* **1999**, *103*, 8257–8264.

[10] V. Vallet, U. Wahlgren, B. Schimmelpfennig, H. Moll, Z. Szabó, I. Grenthe, *Inorg. Chem.* **2001**, *40*, 3516-3525.

[11] P. Wåhlin, C. Danilo, F. Réal, U. Wahlgren, V. Vallet, I. Grenthe, unpublished.

[12] K.E. Gutowski, D.A. Dixon, *Inorg. Chem.* **2006**, *110*, 8840-8856.

[13] V. Vallet, U. Wahlgren, B. Schimmelpfennig, Z. Szabó, I. Grenthe, *J. Am. Chem. Soc.* **2001**, *123*, 11999-12008.

[14] V. Vallet, H. Moll, U. Wahlgren, Z. Szabó, I. Grenthe, *Inorg. Chem.* **2003**, *42*, 1982-1993.

[15] H. Moll, T. Reich, C. Hennig, A. Rossberg, Z. Szabó, I. Grenthe, *Radiochim. Acta* **2000**, *88*, 559.

[16] J. Neuefeind, S. Skanthakumar, L. Soderholm, *Inorg. Chem.* **2004**, *43*, 2422.

[17] N. Dimakis, G. Bunker, *Phys. Rev. B.* **1998**, *58*, 2467-2475.

[18] N. Dimakis, G. Bunker, *J. Synchrotron Rad*. **1999**, *6*, 266-267.

[19] N. Dimakis, G. Bunker, *J. Synchrotron Rad*. **2001**, *8*, 297-299.

[20] A. L. Ankudinov, B. Ravel, J. J. Rehr, and S. D. Conradson, *Phys. Rev. B* **1998**, *58*, 7565.

[21] Gaussian 03, Revision C.02, M.J. Frisch, G.W. Trucks, H.B. Schlegel, G.E. Scuseria, M.A. Robb, J.R. Cheeseman, J.A. Montgomery, Jr., T. Vreven, K.N. Kudin, J.C. Burant, J.M. Millam, S.S. Iyengar, J. Tomasi, V. Barone, B. Mennucci, M. Cossi, G. Scalmani, N. Rega, G.A. Petersson, H. Nakatsuji, M. Hada, M. Ehara, K. Toyota, R. Fukuda, J. Hasegawa, M. Ishida, T. Nakajima, Y. Honda, O. Kitao, H. Nakai, M. Klene, X. Li, J.E. Knox, H.P. Hratchian, J.B. Cross, V. Bakken, C. Adamo, J. Jaramillo, R. Gomperts, R.E. Stratmann, O. Yazyev, A.J. Austin, R. Cammi, C. Pomelli, J.W. Ochterski, P.Y. Ayala, K. Morokuma, G.A. Voth, P. Salvador, J.J. Dannenberg, V.G. Zakrzewski, S. Dapprich, A.D. Daniels, M.C. Strain, O. Farkas, D.K. Malick, A.D. Rabuck, K. Raghavachari, J.B. Foresman, J.V. Ortiz, Q. Cui, A.G. Baboul, S. Clifford, J. Cioslowski, B.B. Stefanov, G. Liu, A. Liashenko, P. Piskorz, I. Komaromi, R.L. Martin, D.J. Fox, T. Keith, M.A. Al-Laham, C.Y. Peng, A. Nanayakkara, M. Challacombe, P.M. W. Gill, B. Johnson, W. Chen, M.W. Wong, C. Gonzalez, and J.A. Pople, Gaussian, Inc., Wallingford CT, 2004.

[22] F. Quilés and A. Burneau, *Vib. Spectrosc.* **2000**, *23*, 231-241.

[23] D.L. Clark, S.D. Conradson, R.J. Donohoe, D.W. Keogh, D.E. Morris, P.D. Palmer, R.D. Rogers and C.D. Tait, *Inorg. Chem.*, **1999**, *38*, 1456–146635.

[24] M. Gál, P.L. Goggin and J. Mink, *Spectrochim. Acta*, **1992**, *48*, 121-132.

[25] P.A. Tanner, C.S.K. Mak, Z-W. Pei, and Y-L. Liu and L. Jun, *J. Phys.: Condens. Matter* **2001**, *13*, 189-194

[26] C.D. Flint and P.A. Tanner, *J. Lumin*. **1979**, *18/19*, 69.

[27] P.A. Tanner, *Spectrochim. Acta*, **1990**, *46*, 1259-1292.

[28] K. Servaes, C. Hennig, R. Van Deun, C. Görller-Walrand, *Inorg. Chem.* **2005**, *44*, 7705-7707.

[29] I. Infante, L. Visscher, *J. Comput. Chem.* **2004**, *25*, 386-392.

THEORETICAL ANALYSIS OF THE U $L_{2,3}$ XANES: OXIDATION STATE OF URANIUM AND LOCAL STRUCTURE IN SOME TERNARY OXIDES

Alexander Soldatov
Faculty of Physics, Rostov State University, Rostov-on-Don, Russia

Dirk Lamoen
TSM, Departement Fysica, Universiteit Antwerpen, Antwerpen, Belgium

Milan Konstantinović, Sven Van den Berghe , Marc Verwerft
SCK-CEN, Reactor Materials Research, Mol, Belgium

Abstract

Theoretical analysis of the U $L_{2,3}$ XANES in some ternary oxides have been done using self-consistent real space full multiple scattering approach. This made it possible to determine the local atomic and electronic structures of two related systematic sets of ternary uranium oxides, $NaUO_3$ - KUO_3 - $RbUO_3$ and $BaUO_3$ - $Ba_2U_2O_7$ - $BaUO_4$. It was found that the uranium ions are in pure U^{5+} oxidation state in $NaUO_3$, KUO_3, $RbUO_3$ and $Ba_2U_2O_7$ compounds. The low energy shoulder in the U L_3 edge XANES is supposed to be an intrinsic feature of the uranium unoccupied 3*d* electronic states of the U^{5+} ions. Specific double shoulder features in the higher energy range of the U L_3 edge XANES can be a finger-print of the cubic perovskite structure.

SESSION V

UPCOMING TECHNIQUES

Chair: Koen Janssens

ULTRA-FAST, TIME-RESOLVED EXAFS: PRESENT CAPABILITIES AND FUTURE PROSPECTS

Daniel Grolimund[1,2], G. Ingold[2], S.L. Johnson[2], P. Beaud[2], R. Abela[2]
[1]Nuclear Energy and Safety Department, Waste Management Laboratory; [2]Swiss Light Source;
Paul Scherrer Institute, CH-5232 Villigen PSI, Switzerland
Ch. Bressler, W. Gawelda, M. Chergui
École Polytechnique Fédérale de Lausanne, Laboratoire de Spectroscopie Ultrarapide, ISIC,
FSB-BSP, CH-1015 Lausanne, Switzerland

Abstract

Observing the motion of atoms during a chemical reaction in real-time is crucial for enhancing our understanding of fundamental physical, chemical and biological phenomena.

Structural changes in molecular systems (e.g., the forming and breaking of bonds) are driven by ultrafast electronic rearrangements. With the development of femtosecond laser systems the investigation of ultrafast phenomena has become possible and is meanwhile well-established. However, optical spectroscopy is limited in providing *structural* information, due to its interaction with electron orbitals distributed over several atoms. A technique capable of simultaneously probing both geometrical changes and the related electronic structures would provide a new observable for understanding the elementary steps of chemical reactivity. X-Ray absorption fine structure spectroscopy (XAFS) delivers both geometric (via EXAFS) and electronic (via XANES) structural information. Interfacing this tool with a femtosecond laser, which excites the sample at time zero, would permit us to investigate time-dependent structures on the picosecond to femtosecond time scales.

This presentation will show the current status of time-resolved XAFS (and x-ray diffraction) as new tools to investigate the dynamics and kinetics of different molecular and solid state systems with 100 ps time resolution (corresponding to the x-ray pulse width at a synchrotron). Further, a new scheme has recently been implemented at the Swiss Light Source, which will deliver 100 fs pulses of hard x-radiation. We will demonstrate the power and potential of structural dynamics research via time-resolved XAFS on selected examples involving charge transfer, spin flip and formation of aqueous radicals.

Selected References:

W. Gawelda, V.T. Pham, M. Benfatto, Y. Zaushitsyn, M. Kaiser, D. Grolimund, S.L. Johnson, Rafael Abela, A. Hauser, M. Chergui, and C. Bressler, Structural Determination of a Short-lived Iron(II) Complex by Picosecond X-ray Absorption Spectroscopy, *submitted.*

Ch. Bressler, M. Saes, R. Abela, D. Grolimund, S.L. Johnson, P.A. Heimann, and M. Chergui, Observing Transient Chemical Changes by Ultrafast X-ray Absorption Spectroscopy, *Physical Review Letters*, 90, 047403, (2003).

STUDIES OF ACTINIDES REDUCTION ON IRON SURFACE BY MEANS OF RESONANT INELASTIC X-RAY SCATTERING

K.O. Kvashnina[1], S.M. Butorin[1], D.K. Shuh[2], K. Ollila[3], I. Soroka[1], J.-H. Guo[4], L. Werme[1,5] and J. Nordgren[1]

[1] Department of Physics, Uppsala University, Box 530, 751 21 Uppsala, Sweden
[2] Chemical Sciences Division, Lawrence Berkeley National Laboratory, Berkeley, CA 94720, USA
[3] VTT, 90571 Oulu, Finland
[4] Advanced Light Source, Lawrence Berkeley National Laboratory, Berkeley, CA 94720, USA
[5] SKB, Stockholm, Sweden

Abstract

The interaction of actinides with corroded iron surfaces was studied using resonant inelastic x-ray scattering (RIXS) spectroscopy at actinide 5d edges. RIXS profiles, corresponding to the f-f excitations are found to be very sensitive to the chemical states of actinides in different systems. Our results clearly indicate that U(VI) (as soluble uranyl ion) was reduced to U(IV) in the form of relatively insoluble uranium species, indicating that the iron presence significantly affects the mobility of actinides, creating reducing conditions. Also Np(V) and Pu (VI) in the ground water solution were getting reduced by the iron surface to Np(IV) and Pu (IV) respectively. Studying the reduction of actinides compounds will have an important process controlling the environmental behaviour. Using RIXS we have shown that actinides, formed by radiolysis of water in the disposal canister, are likely to be reduced on the inset corrosion products and prevent release from the canister.

The deep geological repository concept involves the encapsulation of used nuclear fuel in long-term engineered canisters which are then placed and sealed in a naturally occurring geological formation at a depth of 500 to 1 000 meters below ground surface. A special issue in constructing the underground repository is questions about safety of the canister in the long-term conditions. A way to predict possible risks during long storage period is to study the reactions and interface phenomena of the spent nuclear waste after it has been placed in geological environment. The canister consists of the outer copper shell, as a corrosion resistant barrier and the inner iron shell, in order to add strength to the canister. The essential part in a safety assessment involves a complete understanding of interactions of materials and environment inside the canister.

Scientific understanding of processes that control chemical changes of radioactive species from spent fuel can be achieved by studying interactions of actinide ions (U, Np, Pu) with corroded iron surfaces. We made a study of model systems with different actinides in contact with water and iron. The liquid reaction cell was used in some experiments for the in-situ monitoring of the reaction between iron and uranium. The systems were studied with the help of resonant inelastic x-ray scattering (RIXS) spectroscopy, which enables us to determine the oxidation states of actinides in different species. The important advantage of the RIXS spectroscopy in this case in comparison with other spectroscopic techniques, in particular x-ray absorption is the ability to distinguish contributions from species in very small concentrations. Their signal can be clearly separated from that of dominating species as a result of difference in oxidation state and the corresponding 5f multiplet. By going to the actinide 5d edges, the energy resolution of the RIXS experiment can be significantly improved for the same slit settings of the spectrometer.

Our results indicate that actinide ions with high valences in ground water solutions became reduced by the iron surfaces. This fact became significantly important, since the reduction of actinides inside the canister can prevent their release due to the much lower solubility of reduced Np (IV), U(IV) or Pu (IV) than those species with valency V (Np, Pu) and VI (U, Pu).

The Fe samples with U were made by exposing iron strip (99.9994%) to the anoxic allard groundwater solution of uranyl nitride for 17 days. The neptunium containing samples were also prepared by Fe foil exposure to the neptunyl solutions in groundwater. The starting concentration was 2×10^{-6} M for uranium and 4×10^{-7} M for neptunium. The species in solution were calculated to be $UO_2(CO_3)_3^{4-}$ (70%) and $UO_2(CO_3)_2^{2-}$ (25%) for U and $NpO_2CO_3^-$ (75%) and NpO_2^+ (25%) for Np. The U samples were prepared in an inert gas glove box while the Np samples were prepared in pressure vessels with a 50 bar H_2 overpressure.

The liquid reaction cell was utilized for in-situ studies of uranium reduction on Fe from the groundwater solution. The schematics of the cell are shown on Figure 1. The liquid cell consists of the 20mm x 20mm frame, which is holding the 10mm x 10mm Si_3N_4 window and O-ring in order to prevent the leaking processes. The height of the liquid cell is 4 mm, which is enough to put one drop of liquid. On the backside of the 100nm thick Si_3N_4 window, the 100Å Fe film was deposited in order to study the chemical reactions between this film and uranium ions in solution. The initial concentration of the UO_2^{2+} (VI) in solution was 2 ppm.

Figure 1. Schematic drawing of liquid cell

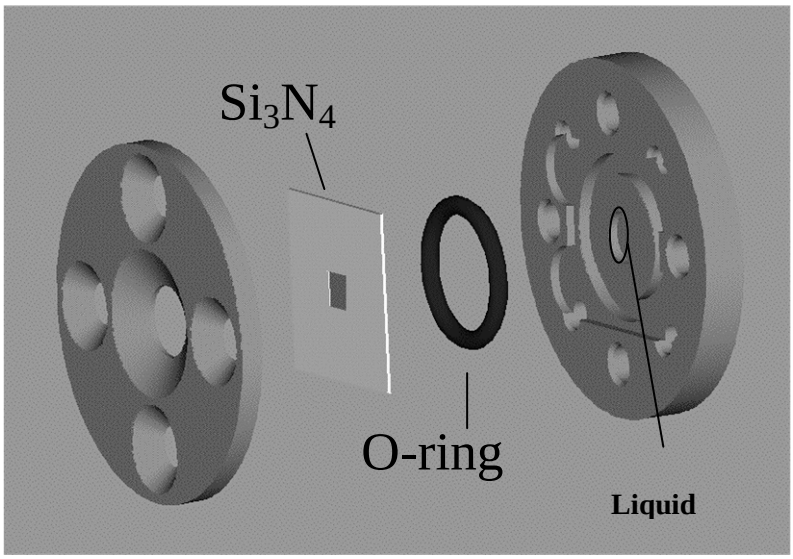

The experiments were made at beamline 7.0 of the Advance Light Source, Lawrence Berkeley Laboratory, USA. This undulator beamline includes a spherical grating monochromator, which gives resolution of 50 meV at ~110 eV. RIXS spectra were recorded, using grazing incident grating spectrometer [1-2] with 160 meV resolution for U and Np and 110 meV for Pu samples. The instrument is based on three gratings, mounted at fixed angles of incidence and a large two-dimensional multichannel detector. The incident angle of the photon beam was 20º from the surface for solid samples and 35º for the liquid cell.

Figure 2 shows U 5d RIXS spectra of the iron films exposed to the U(VI) solution in ground water for 17 days. Scattering data were recorded at excitation energy of 100.5 eV, which corresponds to the pre-threshold structure in the U 5d XA spectrum. For simplicity, we plotted RIXS spectra in the energy-loss scale. U 5d scattering spectra for the reference UO_2 sample are also displayed in Figure 2. All the spectra have the elastic peak at 0 eV and inelastic scattering structures at -1.0 –2.0 eV on the energy-loss scale. These structures correspond to the f-f excitations and could be very well reproduced by theoretical calculations, using atomic multiplet theory [3]. Note that the RIXS cross-section for f-f transitions is enhanced at all the energies throughout the pre-threshold structure in the 5d XA spectrum. Such f-f transitions are absent in the UO_3 spectrum [4] (see Figure 3), which could be used as a good “fingerprint” in the study of oxidation states of uranium. Therefore, a reduction of the uranium valency from VI to IV on the iron surface should manifest itself in an appearance of the f-f excitations in the resonant spectra. Our data clearly indicate the presence of the f-f excitations in the RIXS spectra for uranium on the iron film, thus allowing us to conclude that U(VI) is reduced by iron to U(IV). We are also able to derive the amount of reduced uranium by comparison the area under the profile of f-f excitations for UO_2 and studied iron films. The spectra were normalised to the characteristic core-to-core U 6p→ 5d fluorescence lines, which allowed us to deduce the total amount of reduced U (IV) after 17 days of exposure (73%).

Figure 2. U 5d RIXS spectra representing f-f excitations in single crystal UO_2 and U on Fe after 17 days exposure to the U(VI) solution in groundwater. Recorded data are shown by solid lines with markers and broken lines represent a fit to the elastic peak.

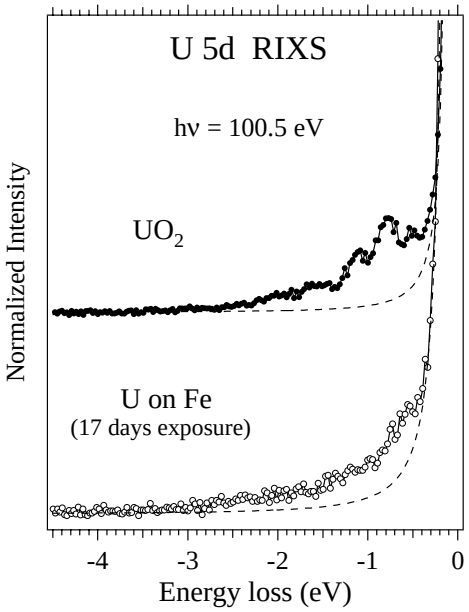

Similar results were obtained for Np and Pu samples. Figure 4 shows the Np 5d and Pu 5d RIXS spectra of Np and Pu species formed on the iron strips together with spectra of NpO_2 and PuO_2 . The RIXS spectra of Np and Pu on Fe reveal f-f excitation patterns similar to those of NpO_2 and PuO_2 respectively, thus indicating the existence of Pu(IV), Np(IV) on the iron strips and that reduction of Np(V), Pu (VI) had been taken place.

Figure 3. U5d RIXS scattering spectra of poly-crystalline UO_2, UO_3. The energy of the incident photons was set to 100 eV.

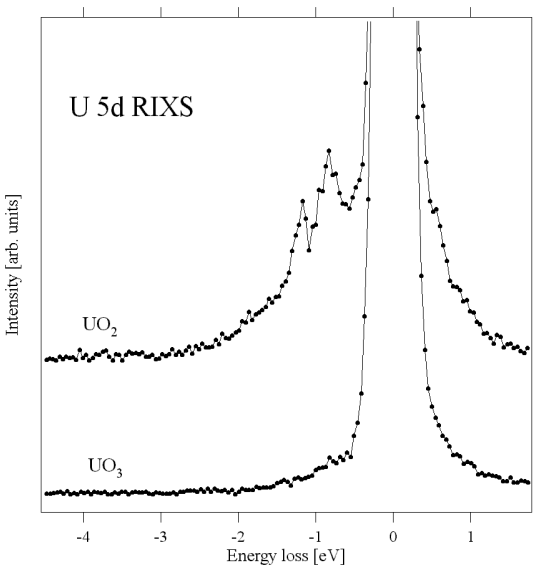

Figure 4. Comparison of RIXS spectra of NpO_2, PuO_2 (reference) and Np, Pu formed on the Fe strip (respectively), recorded at the excitation energies, close to that of the pre-threshold structure in the Np 5d and Pu 5d XA spectra.

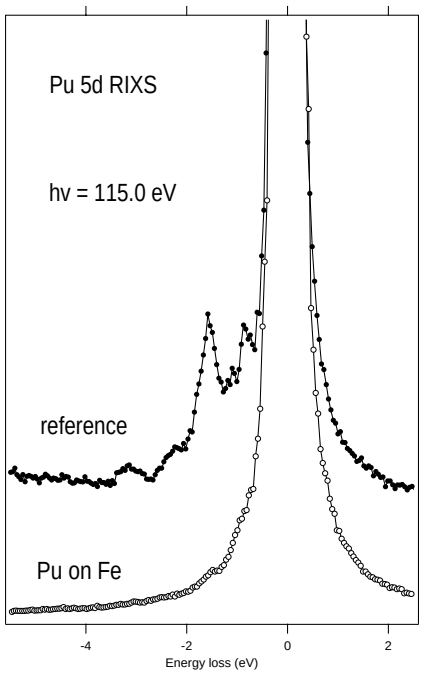

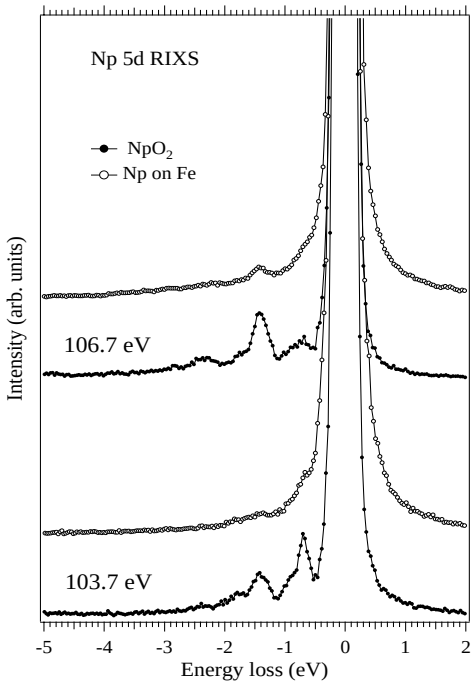

We also monitored a reaction between U(VI) ions and iron using the liquid cell (Figure 1) for the in-situ studies. We used a silicon nitride window for these measurements and therefore the silicon contribution can be observed below 99 eV (Figure 5). After three days of exposure of Fe film to the solution, the f-f transitions can be observed in RIXS spectrum, thus indicating that U(IV) was formed on the thin iron film in the cell.

Fig 5. U 5d RIXS spectra of uranium in the liquid reaction cell

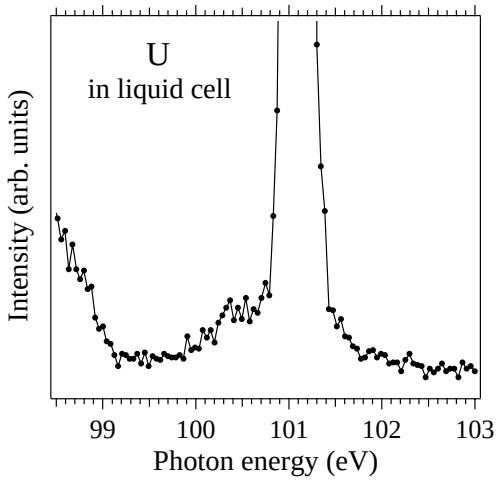

The results of our studies unambiguously indicate that RIXS profiles, corresponding to the f-f excitations are very sensitive to the oxidation states of actinides in different systems, which allowed us to suggest that soluble actinides species (U, Pu, Np) in the disposal canister can be reduced by iron to lower solubility form and prevent release from the canister.

Acknowledgements

This work was financially supported by the European Commission under Contract EU FIKW-CT-2000-00019, by the Swedish Research Council and Goran Gustafsson Foundation for Research in Natural Sciences and Medicine. The ALS work was supported by the Director, Office of Science, Office of Basic Energy Sciences, and Biosciences of the U.S. Department of Energy at Lawrence Berkeley National Laboratory under contract No. DE-AC03-76SF00098.

References

[1] T.Warwick, P. Heimann, D. Mossesian, W. McKinney and H. Padmore, Rev.Sci. Instrum. 66, 2037 (1995).

[2] J. Nordgren, G. Bray, S. Cramm, R. Nyholm, J.-E. Rubensson and N. Wassadahl, Rev. Sci. Instrum. 60, 1690 (1989).

[3] S. M. Butorin, J. of Eletron. Spec. and Rel. Phen. 110-111 (2000) 213-233.

[4] S.M. Butorin, D.K. Shuh, K. Kvashnina, I. Soroka, K. Ollila, K.E. Roberts, J.-H. Guo, L.Werme and J. Nordgren, Mat. Res. Soc symp. Proc. Vol 807, 113 (2004).

SOFT X-RAY SCANNING TRANSMISSION X-RAY MICROSCOPY (STXM) OF ACTINIDE MATERIALS

David K. Shuh,[1] Tolek Tyliszczak,[2] Peter S. Nico,[3] Hans J. Nilsson,[1,5] Richard E. Wilson,[1] and Lars Werme[4,5]

[1]Chemical Sciences Division, [2]Advanced Light Source Division, and [3]Earth Sciences Division, Lawrence Berkeley National Laboratory, Berkeley, California, USA
[4]SKB, Box 5864, S-102 40, Stockholm, Sweden

[5]Dept of Physics, Uppsala Univ., Box 530, S-751 21, Uppsala, Sweden

Abstract

Scanning transmission x-ray microscopy (STXM) spectromicroscopy at the Advanced Light Source Molecular Environmental Science (ALS-MES) Beamline 11.0.2 has been utilized to investigate actinide materials, particulates, and actinide-related materials. The ALS-MES STXM utilizes near-edge x-ray absorption fine structure (NEXAFS) at the actinide 4d core level edges (700 eV to 900 eV) to obtain direct spectroscopic information from actinide materials and is capable of imaging particles in several modes, both with a spatial resolution better than 30 nm. An important characteristic of the ALS-MES STXM is the capability to directly probe light element K-edges by NEXAFS, such as the oxygen and nitrogen K-edges, that are frequently key constitutents of actinide materials. The safety precautions for STXM investigations of actinides require sealed encapsulation of the actinide materials between two thin silicon nitride windows. This practical level of experimental safety makes STXM an efficient method for collecting NEXAFS spectra from radioactive materials.

The results from early studies of model, light actinide oxides will be presented, demonstrating the experimental capabilities and limitations of soft x-ray STXM spectromicroscopy for investigations of actinide materials. The spectroscopic results from recent transuranic STXM investigations, along with their light element constituents, will be presented. The imaging capabilities of STXM provide a means to observe the morphology actinide-containing particulates, even when fully-hydrated, at a level that approaches the nanoscale. The results from actinide, radionuclide, and lanthanide (used as a surrogate or for a direct comparison to actinide behaviour) experiments including those focused on elucidating fundamental bonding characteristics and of environmental interests, will also be highlighted. However, there are drawbacks and the need to work at the actinide 4d edges imposes cross-sectional senstivity requirements making low concentration STXM work difficult without actinide agglomeration.

The work at the ALS and ALS BL 11.0.2 was supported in part by the Director, Office of Science, Office of Basic Energy Sciences, Division of Materials Sciences and Division of Chemical Sciences, Geosciences, and Biosciences of the U.S. Department of Energy at Lawrence Berkeley National Laboratory under Contract No. DE-AC02-05CH11231.

SESSION VI

FACILITY REPORTS AND CLOSING DISCUSSION

Chair: Stéphane Lequien

SCIENTIFIC CAPABILITIES OF THE ADVANCED LIGHT SOURCE FOR RADIOACTIVE MATERIALS

David K. Shuh
MS70A1150, One Cyclotron Road, Chemical Sciences Division
Lawrence Berkeley National Laboratory (LBNL)
Berkeley, CA 94720 USA

Abstract

The Advanced Light Source (ALS) of Lawrence Berkeley National Laboratory (LBNL) is a third-generation synchrotron radiation light source and is a U.S. Department of Energy (DOE) national user facility. Currently, the ALS has approximately forty-five operational beamlines spanning a spectrum of scientific disciplines, and provides scientific opportunities for more than 2 000 users a year. Access to the resources of the ALS is through a competitive proposal mechanism within the general user program. Several ALS beamlines are currently being employed for a range of radioactive materials investigations. These experiments are reviewed individually relying on a graded hazard approach implemented by the ALS in conjunction with the LBNL Environmental, Health, and Safety (EH&S) Radiation Protection Program. The ALS provides radiological work authorization and radiological control technician support and assistance for accepted user experimental programs. LBNL has several radioactive laboratory facilities located near the ALS that provide support for ALS users performing experiments with radioactive materials. The capabilities of the ALS beamlines for investigating radioactive materials are given and examples of several past studies are summarised.

Introduction

The Advanced Light Source (ALS) of Lawrence Berkeley National Laboratory (LBNL) is a third-generation synchrotron radiation (SR) light source. It is a U.S. Department of Energy (DOE) national user facility generating intense light for scientific and technological research. As one of the world's brightest sources of ultraviolet and soft x-ray beams and the world's first third-generation synchrotron light source in its energy range, the ALS makes previously impossible studies possible. The ALS has approximately 45 operational beamlines (BLs) spanning a spectrum of scientific disciplines and provides scientific opportunities for more than 2000 users a year. The current configuration and complement of the ALS BLs is shown in Figure 1.

Although at this time there are no fully dedicated BL facilities for studying radioactive materials at the ALS, which have been primarily actinides, several ALS BLs are being used on a regular basis for a range of radioactive materials investigations. These BLs are in general high performance, undulator beamlines in which one of the BL general user endstations is utilised to conduct the "hot" experiment. In 2006, this core complement consists of soft x-ray BLs 7.0.1, 8.0.1, 10.0.1, 11.0.2, and the x-ray BL 11.3.1. Another class of ALS BLs is utilized to study non-radioactive materials that are directly related to actinide science. This group of beamlines is composed of soft x-ray bend magnet BLs 5.3.2, 6.3.1, and 9.3.2 along with the x-ray bend magnet BLs 10.3.1 and 10.3.2. The other standard class of BL at the ALS is the superconducting bend magnets (superbends) and such a BL (BL 12.2.2) may become useful for actinide science in the future. A full description and summary of experimental capabilities of ALS BLs can be found on the ALS website at *http://www-als.lbl.gov/als/als_users_bl/bl_Table.html*.

Figure 1. Complement of ALS beamlines as of calendar year 2006 with the legend describing the BL source and BL status.

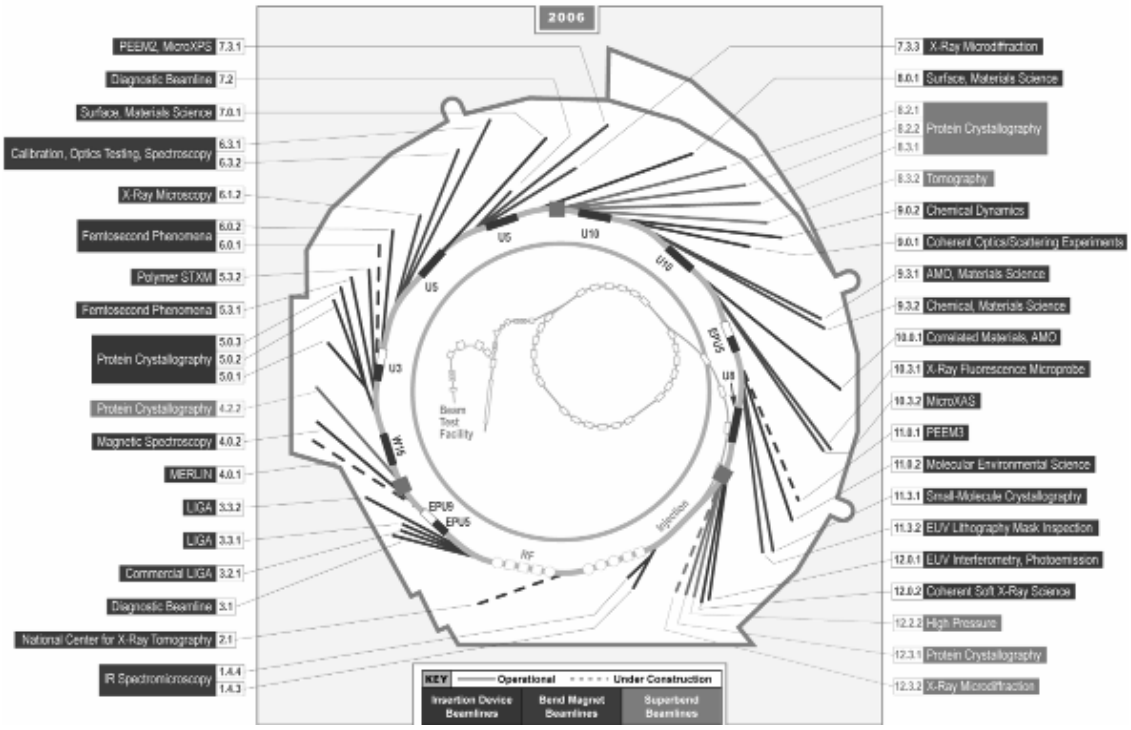

The ALS is recently undergoing a great deal of change at the time of manuscript preparation. Most sadly and unexpected has been the recent passing of Dr. N.V. Smith who was the scientific director of the ALS for most of its operational lifetime. The ALS scientific community will greatly miss N.V. Smith. Prof. R. Falcone of the University of California Berkeley Physics Dept./LBNL has been named director of the ALS, taking the helm from Prof. J. Kirz who served as the interim director for more than a year following Director Prof. D. Chemla. The ALS is also emerging from an intensive ten-month period in which the management structure has been optimized, ALS environment, safety and health (ESH) procedures and ALS safety environment thoroughly re-worked, and a new ALS ESH manager hired. The ALS will install new apparatus and transition to a new mode of operation that will provide users with even more photons per unit time, namely top-off mode. Lastly, LBNL and the ALS have successfully obtained the support to construct a new user support building. This new building requires the full demolition of the existing Building 10 and the subsequent construction of a new, much larger Building 10 in the same general location.

General Safety Considerations

LBNL and its ALS National User Facility are both supported by U.S. Dept. of Energy through its contract with the University of California. Thus all experiments, including those with radioactive materials, must conform to LBNL Environmental, Health and Safety (EH&S) Division standards as well as DOE regulations. One important consideration that ALS users should be cognizant of is the DOE definition of radioactive materials which is quite strict and recognizes the lowest levels of activity as fully radioactive materials in terms of safety (even for extremely small amounts of non-depleted uranium). Experiments with radioactive materials are reviewed individually relying on a graded hazard approach applied by the ALS in conjunction with a radiological work authorization (RWA) that is issued by the LBNL EH&S. A completed and signed ALS experimental safety summary (ESS) form, including the radioactive materials addendum in addition to a mandatory RWA, is required. RWAs are isotope, amount, experimental technique, and personnel specific (see *http://www.lbl.gov/ehs/pub3000/CH21.html#_Toc407168399* for a complete description of the LBNL RWA program). Finally, the ESSs for radioactive materials must be signed off by a representative of ALS management. For the beamlines being utilized in a similar manner with actinide materials on a frequent basis, the respective experimental safety protocols and procedures have been defined in a consistent manner to make experiments as straightforward as possible within the permitted safety envelope.

The ALS and LBNL provide user radiological control technician (RCT) support and RWA assistance for users with approved experiments, respectively. All experiments with radioactive materials are commissioned with the RCT present and all handling of radioactive samples must be done with the RCT present at this time. At the conclusion of radioactive experiments, the RCT certifies the experimental end station to be free of radioactivity and returns the station to normal use. An important component of proper and safe radiological work involves the proper transportation of radioactive materials to and from LBNL. LBNL EH&S provides radioactive transportation assistance to users. The contact information of the LBNL EH&S radioactive materials: shipping and receiving subject matter expert can be found at http://www.lbl.gov/ehs/html/subject_matter.shtml. LBNL has several radioactive laboratory facilities that have been made available for users and can provide support for experiments requiring laboratory facilities capabilities to perform experiments.

There are three basic categories of experiments with radioactive materials at the ALS that serve to define the general safety measures that must be present to perform experiments. These safety guidelines were developed in early 2003 following recommendations from the ALS Scientific Advisory Committee (SAC) along with a DOE-based risk assessment analysis by the ALS. The first class of experiments requires complete and redundant multiple containment of the actinide materials, such as traditionally actinide x-ray absorption spectroscopy conducted with x-rays that does not

require a vacuum environment with which a reasonable amount of material and isotopes can be used. The second category is one in which a sample may be singly contained, used in a vacuum environment, and generally employs an extremely small amount of material with no restrictions on isotopes. The final category is for experiments to be performed with open material in an ultra-high vacuum (UHV) environment, frequently in existing user endstations, and these experiments are much more restrictive in terms of total activity and are even more carefully reviewed in terms of procedures.

Access to the ALS

The first step in planning an experiment with radioactive materials at the ALS is to contact the responsible scientist at the BL of interest to evaluate the experimental feasibility of the envisioned experiment. A prudent intermediate step would be to contact the ALS environment, safety, and health (ES&H) manager concerning the proposed experiment while at the same time completing an ESS form (with the radioactive materials addendum) describing the experiment so that it can be understood and formally evaluated from a safety perspective. Assuming the feasibility of the experiments from a safety standpoint and concurrence by the ALS, an RWA for the experiment will be have to be obtained with the assistance of LBNL EH&S personnel.

There are several methods of obtaining beamtime for experiments at the ALS which is a general user facility with most beamlines operated by the ALS facility. The main route is through the submission of a scientific proposal to the general user program (GUP) which is a highly competitive process for the BLs in high demand. The GUP proposals are reviewed, assigned a rating with a smaller value being the highest rated, assigned beamtime in the order of rating, and are valid for two years. The full updated descriptions of the access modes, review process, and scheduling can be found at http://www-als.lbl.gov/als/quickguide/becomealsuser.html. Another mode of access is through the approved program (AP) mechanism which is intended for intensive users with a need for substantial amounts of beamtime over an extended period of time. The AP application entails a more comprehensive scientific proposal and review process. Of course, one effective method to obtain access is to collaborate with a scientist receiving beamtime through the GUP or AP mechanisms. The final manner to obtain a small amount of seed beamtime is via the scientific director's discretionary allocation.

Capabilities of ALS Beamlines for Investigations of Radioactive Materials

The SR techniques that are or have been utilized at ALS BLs with a diverse set of materials containing actinides include photoelectron spectroscopy (PES), angle-resolved PES (ARPES), near-edge x-ray absorption fine structure (NEXAFS), soft x-ray emission spectroscopy (XES), resonant inelastic x-ray scattering (RIXS), and scanning transmission x-ray microscopy (STXM). Several BLs at the ALS are also used to perform experiments on materials intimately related to actinide science even though the sample materials themselves may not be radioactive. Recent and past results highlights from the ALS with these aforementioned techniques will be briefly described to illustrate the capabilities of the ALS for the investigation of radioactive materials.

One of the earliest objectives at the ALS has been to perform soft x-ray PES measurements on actinide materials to ascertain the behavior of the 5f electrons for a range of materials. The location of the ALS at LBNL is ideal for such investigations, as it was the only soft x-ray SR facility located at the site of an active actinide science research program at the time of construction. The scientific opportunities and technical issues pertaining to soft x-ray PES have been recognised.[1] The first transuranic soft x-ray PES experiment, likely the first time a transuranic sample was examined without barriers under UHV with soft x-ray SR, was performed at BL 7.0.1 of the ALS in 1994 from a Cm-248 oxide target of about a single μg.[2] Following these initial demonstrations, more complex PES measurements with 30 mg samples of Pu-239 were performed at BL 7.0.1 and resulted in several publications.[3-5] After these experiments, largely as a result of the safety guidelines established in

2003, there has been no active transuranic PES program at the ALS after these new guidelines were put in place. However, several groups continue to successfully and safely perform regular PES/ARPES measurements on large bulk crystals of U heavy fermion materials to this day.[6-7]

The first transuranic NEXAFS measurements were performed in conjunction with the first PES experiments in 1994 at BL 7.0.1. These experiments also included studies of the materials first used for PES which included a plutonium-242 oxide prepared on a Pt counting plate. The capability to use a tunable source not only lead to the NEXAFS of the actinides in the soft x-ray but also permitted resonant PES and pointed to the future possibilities of utilizing ALS BLs for XES and RIXS with radioactive materials. The performance characteristics of ALS bend magnet beamlines has lead to their use for investigating non-radioactive materials of importance in actinide science by both PES and NEXAFS. In particular, a series of scientific issues related to the structure of and radiation damage mechanisms in pyrochlore-structured lanthanide titanates and their corresponding increasingly doped Zr substituted have been characterized by NEXAFS at several core level K edge thresholds (BLs 6.3.1and 9.3.2) [8-10]. A recent development at the ALS has been the use of STXM to obtain NEXAFS spectra from actinide materials and this will be discussed further towards the end of the section.

Figure 2. RIXS spectra (lower panel, dotted upper solid traces) from UF_4 collected near the U 5d threshold along with the results of broadened atomic multiplet calculations (lower solid lines) for the U(IV) ion. The excitation energies used are indicated on the total electron yield spectrum at the U 5d absorption edge (upper panel, uppermost trace experiment; lowermost trace calculation).

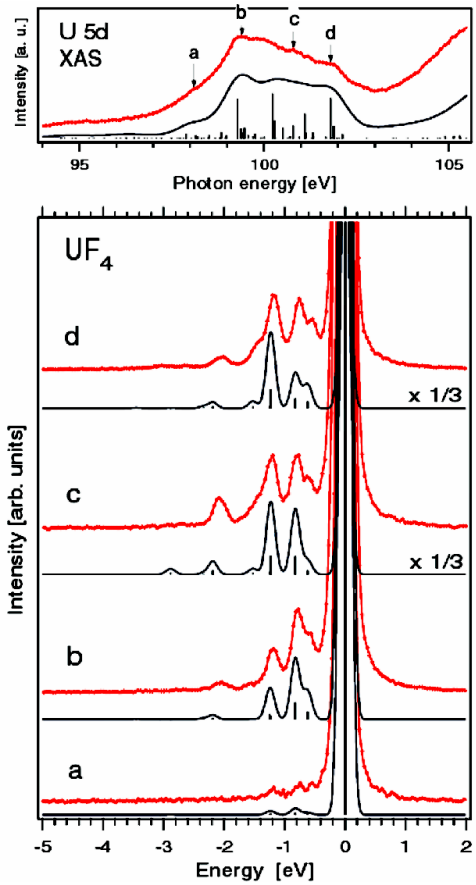

The brightness and flux properties of the ALS which have enabled and permitted more rapid experiments have lead to a renaissance in the photon-in, photon-out techniques of XES and RIXS.[11] Based on the success of XES and RIXS for probing the electronic structural properties of lanthanide materials, a natural extension has been to actinide materials. These studies by their nature require very small amounts of actinide to be used directly under UHV conditions at the present time and special safety precautions have been developed. One particular attribute of XES/RIXS amenable to actinides is its simple ability to be either bulk or surface-sensitive, thereby avoiding sample preparation issues while yet having the option to probe only interfacial regions if so desired. Early experiments focused on U oxides and recent studies have examined actinide materials containing the radionuclides Np-237, Pu-242, and most recently, Cm-248.[12-15] XES and RIXS studies are applicable to a range of topics in actinide science, from fundamental studies of 5f electron behavior to speciation for environmental purposes. An example of the RIXS spectra is shown in Figure 2.[15]

As improved spectrometers are built for XES/RIXS, this should translate to increased capabilities and opportunities for actinide experiments in the future.The ALS has two STXMs with the one at the ALS-Molecular Environmental Sciences (MES) BL 11.0.2 utilized for NEXAFS at the actinide 4d core level edges (700 eV to 900 eV) resident downstream of an elliptical polarization undulator (EPU). The ALS-MES STXM can image particles in several modes with a spatial resolution better than 30 nm and has an operational photon energy range from 110 eV to 2160 eV.[16, also see website http://beamline1102.als.lbl.gov/] An important characteristic is the capability to directly probe light element K-edges by NEXAFS, such as the oxygen and nitrogen K-edges, that are frequently key constituents of actinide materials. The safety precautions for STXM investigations of actinides require sealed encapsulation of the actinide materials between two thin silicon nitride windows (except for the case of materials embedded in transmission electron microscopy grids or U materials firmly adhered to the grid). Samples must be thin to permit x-ray transmission but can be solids, liquids, or even “wet” materials. An example of an elemental map from a large particle containing Pu is shown in Figure 3. The ALS-MES STXM has performed spectromicroscopy studies of radioactive materials in systems including oxides of the light actinides, actinide colloids, molecular complexes of actinides through Cm, U in microbiological systems, and several others.[17-18] The second ALS STXM is located at BL 5.3.2 downstream of a bend magnet and has a limited upper photon energy insufficient to probe the actinide 4d. As a result of over-subscription at the ALS-MES STXM, the STXMs are utilised in a complementary fashion and BL 5.3.2 will be used with radioactive materials for the first time to obtain the light element K-edge spectra.

Figure 3. Plutonium elemental map image from large borosilicate glass particles generated using the enhanced contrast provided at the Pu $4d_{5/2}$ edge. The regions with high concentrations of Pu appear light in comparison to the particles.

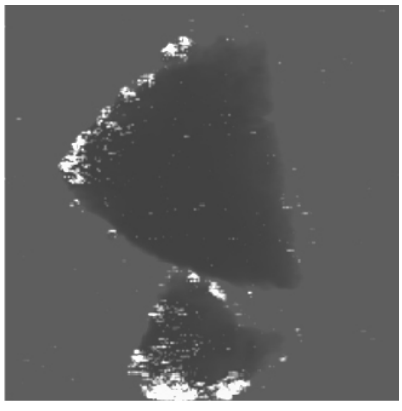

The newest application of one of the ALS BLs, small molecule crystallography at BL 11.3.1, is for regular single crystal structure determination of transuranic complexes using a tunable source of ~17 keV x-rays rather than a laboratory source. This BL provides capability to determine the structures of small and weakly diffracting crystals, which the former is of great importance to several types of actinide complexes which have a tendency to form crystals with dimensions of 30Å or less. The BL has the ability to screen and collect data from samples very rapidly. The diffractometer system is a Bruker AXS Pt200 CCD detector and has the ability to cryogenically cool sample crystals to 100K. Standard radioactive materials safety precautions are utilized at the BL. Figure 4 shows the interior of the BL 11.3.1 hutch along with view of the goniometer head region. In the first length period of regular operation in which actinide complexes were examined, several crystal structures were determined. These included the first Pu small molecule crystal structure collected with SR, [19], additional Pu complexes [20], and Np complexes.[21]

Figure 4. The experimental interior of the ALS and the University of California Berkeley College of Chemistry Small Molecule Crystallography BL 11.3.1 facility during an experimental run when conFigured for use with small actinide crystals (left panel). The right panel shows a closeup of a sealed 0.3 mm quartz capillary containing a small actinide crystal protruding from standard goniometer head with a red indicator denoting the end of the capillary for safety purposes. The plastic assembly below the crystal is a safety tray, designed to catch the capillary before it falls into 11.3.1 laser Table in the unlikely event of a collision.

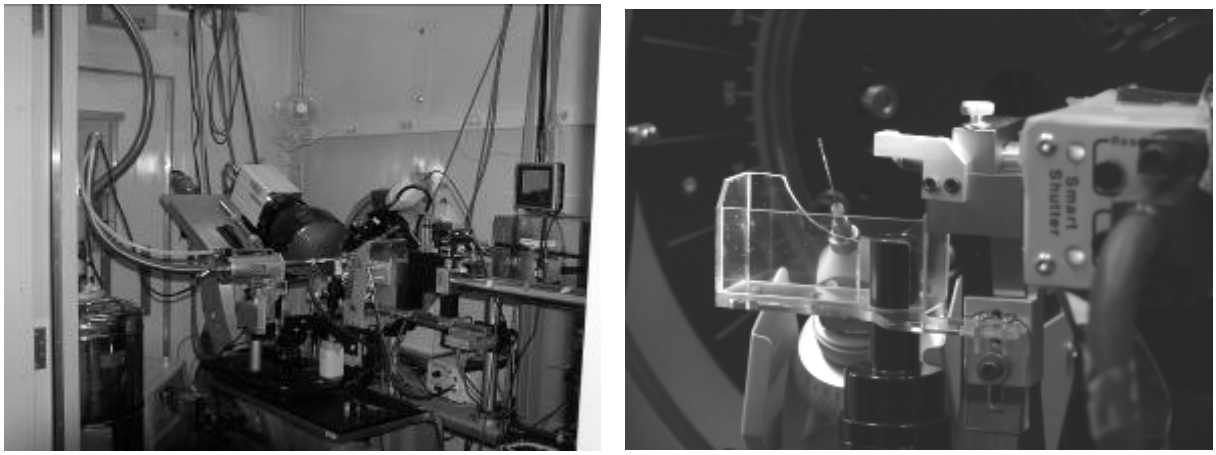

There are several intermediate x-ray and hard x-ray BLs at the ALS that either are or could be used for investigations related to radioactive materials. Several of these BLs incorporate capabilities for elemental-mapping, x-ray absorption spectroscopy (XAS), micro-XAS, micro-diffraction studies, and/or a combination of these techniques. The microprobe (BL10.3.1) and the microXAS (BL 10.3.2) have spatial resolutions of nearly a micron and can be used in combination with BL 7.3.3.3 to obtain microdiffraction information. The microXAS line is also incorporating a microdiffraction system. These two BLs do not have sufficient flux for regular studies at or beyond the U L_{III} edge (17.16 keV) but both have the capability to work at or obtain information from below the energy of the actinide M edges. BL 9.3.1 is used for XAS and emission spectroscopy (~2.2 keV to 6 keV) but is not used with radioactive materials although it has studied materials related to actinides science and could be used at the actinide M edges. Superbend BL 12.2.2 has the potential to be utilized with actinides for XAS because of its hard spectrum flux, focal properties, and as well as its inherent dedicated ability to work with materials systems under high pressure.

Conclusions

Soft x-ray SR has been used successfully for a range of investigations with actinide materials up to Cm. The degree of experimental difficulty scales with the specific type of experiment and technique being employed, and these considerations define the safety measures that must be implemented per ALS/LBNL guidelines. Early work focused on the use of PES but for technical and safety reasons, this work has slowed temporarily. The fluorescence techniques of XES and RIXS have shown great utility and have been developed for a wide range of actinide investigations while limiting risk. The technique of soft x-ray STXM has been utilised to obtain NEXAFS spectra from actinides at the 4d edges which are sensitive to oxidation state, and most importantly, provide a reasonable mechanism for obtaining K-edge spectra of light elements. STXM also has the potential for investigating small particles, engineered actinide materials, and actinides in biological systems. The small x-ray beams of the ALS are extremely useful for crystallography of actinide complexes and in the near future it is possible that superbend BL 12.2.2 could be used for actinide XAS/diffraction measurements. The other useful aspect of several ALS beamlines for actinide science is that their high performance characteristics lend themselves to the investigation of the speciation of non-actinide elements in both radioactive and non-radioactive materials. Finally, there are several new BLs being built and/or fully upgraded at this time. Some of these BLs may offer new opportunities for use with actinides although none has been been optimized or designed for actinide science.

Acknowledgments

This work and the ALS are supported by the Director, Office of Science, Office of Basic Energy Sciences, Facilities Division and parts of this work are funded by the Division of Chemical Sciences, Geosciences, and Biosciences of the U.S. Department of Energy at LBNL under Contract No. DE-AC02-05CH11231. The author specially acknowledges the assistance and contributions of N. V. Smith to the ALS and the SR community.

References

1. Synchrotron Radiation in Transactinium Research," U.S. DOE Workshop Report, LBNL, Berkeley, CA, 1992.
2. D.K. Shuh, J.J. Bucher, N.M. Edelstein, A. Warwick, J. Denlinger, B. Tonner, E. Rotenberg, S. Kevan, and J. Tobin, Edited by A. Robinson, "Researchers Use ALS for TRU Analysis" ER News, Office of Energy Research, U.S. Department of Energy, Vol. **4** (4) August, 1994, p.4, 6.
3. J. Terry, R.K. Schulze, J. Lashley, J.D. Farr, T. Zocco, K. Heinzelman, E. Rotenberg, D.K. Shuh, G. Van der Laan, and J.G. Tobin, "5f Resonant Photoemission From Plutonium," Surf. Sci. **499**, L141-147 (2002). LBNL-47323
4. J.G. Tobin, B.W. Chung, G.D. Waddill, R.K. Schulze, J. Terry, J.D. Farr, T. Zocco, D.K. Shuh, K. Heinzelman, E. Rotenberg, and G. Van der Laan,"Resonant Photoemission in f Electron Systems: Pu and Gd," Phys. Rev. B **68**, 155109 (2003). LBNL-531224CD
5. K.T. Moore, M.A. Wall, A.J. Schwartz, B.W. Chung, D.K. Shuh, R.K. Schulze, and J.G. Tobin, "The Failure of Russell-Saunders Coupling in the 5f States of Plutonium," Phys. Rev. Lett. **90**, 196064 (2003). LBNL-53119ND
6. J.D. Denlinger, G.H. Gweon, J.W. Allen, and J.L. Sarrao, "Temperature Dependent 5f-states in URu_2Si_2," Physica B-Cond. Mattter **312**, 655-657 (2002).

7. J.W. Allen, J.D. Denlinger, Y.X. Zhang, G.H. Gweon, S.H. Yang, S.J. Oh, W.P. Ellis, D.A. Gajewski, R. Cahu, and M.B. Maple, "U 5f Spectral Weight Variation in $UPd_{3-x}Pt_x$," Physica B **281**, 725-726 (2000).

8. P. Nachimuthu, S. Thevuthasan, M.H. Engelhard, W.J. Weber, D.K. Shuh, N.M. Hamdan, B.S. Mun, E.M. Adams, D.E. McCready, V. Shutthanandan, D.W. Lindle, G. Balakrishnan, D.M. Paul, E.M. Gullikson, R.C. C. Perera, J. Lian, L.M. Wang, and R.C. Ewing, "Probing Cation Antisite Disorder in $Gd_2Ti_2O_7$ Pyrochlore by Site-specific Near-edge X-ray Absorption Fine Structure and X-ray Photoelectron Spectroscopy," Phys. Rev. B **70**, 100101 (2004).

9. P. Nachimuthu, S. Thevuthasan, E.M. Adams, B.S. Mun, W.J. Weber, B.D. Begg, D.K. Shuh, D.W. Lindle, E.M. Gullikson, and R.C.C. Perera, "Effect of Zr Substitution for Ti in $Gd_2Ti_2O_7$ Pyrochlore: Ti 2p and O 1s NEXAFS Study," J. Phys. Chem. B **109**, 1337-1339 (2005).

10. P. Nachimuthu, S. Thevuthasan, V. Shutthanandan, E.M. Adams, W.J. Weber, B.D. Begg, D.K. Shuh, D.W. Lindle, E.M. Gullikson, and R.C.C. Perera, "The Impact of Au^{2+} Ion Beam Irradiation on the Structural and Electronic Properties of $Gd_2(Ti_{1-y}Zr_y)_2O_7$ Pyrochlores: Ti 2p and O 1s NEXAFS Study," J. Appl. Phys. **97**, 033518 1-5 (2005).

11. Soft X-ray Science in the Next Millennium: The Future of Photon-In/Photon-Out Experiments, "An Assessment of the Scientific and Technological Opportunities and the Instrumentation and Synchrotron Radiation Facility Needs at the Beginning of the New Millennium," Fall Creek Falls State Park, Pikeville, TN. 16-18 March 2000

12. M. Magnuson, S.M. Butorin, L. Werme, J. Nordgren, K.E. Ivanov, J.-H. Guo, and D.K. Shuh, "Uranium Oxides Investigated by X-ray Absorption and Emission Spectroscopies," Appl. Surf. Sci. **252**, 5615-5618 (2006).

13. S.M. Butorin, D.K. Shuh, K. Kvashnina, I. Soroka, K. Ollila, J.-H. Guo, K.E. Roberts, L. Werme, and J. Nordgren, "Resonant Inelastic Soft X-ray Scattering Studies of U(VI) Reduction on Iron Surfaces," Mater. Res. Soc. Symp. Proc. **807**, 166-171 (2004).

14. D.K. Shuh, S.M. Butorin, J.-H. Guo, and J. Nordgren, "Soft X-ray Synchrotron Radiation Investigations of Actinide Materials Systems Utilizing X-ray Emission Spectroscopy and Resonant Inelastic X-ray Scattering," Mater. Res. Soc. Symp. Proc. **802**, 131-136 (2004).

15. S.M. Butorin, "Resonant Inelastic X-ray Scattering from Strongly Electron-Correlated Systems as a Probe of Optical Scale Excitations: Quasi-localized View," J. Electron Spectrosc. **110-111**, 213-233 (2000).

16. H. Bluhm, K. Andersson, T. Araki, K. Benzerara, H. Bluhm, G.E. Brown, Jr., J.J. Dynes, S. Ghosal, H.-Ch. Hansen, J.C. Hemminger, A.P. Hitchcock, G. Ketteler, E. Kneedler, J.R. Lawrence, G.G. Leppard, J. Majzlam, B.S. Mun, S.C.B. Myneni, A. Nilsson, H. Ogasawara, D.F. Ogletree, K. Pecher, D.K. Shuh, M. Salmeron, B. Tonner, T. Tyliszczak, and T.H. Yoon, "Soft X-ray Microscopy and Spectroscopy at the Molecular Environmental Science Beamline of the Advanced Light Source," J. Electron Spectros. Rel. Phenom. **150**, 86-104 (2006).

17. H.J. Nilsson, T. Tyliszczak, R.E. Wilson, L. Werme, and D.K. Shuh, "Soft X-ray Scanning Transmission X-ray Microscopy (STXM) of Actinide Particles," J. Anal. Bioanal. Chem. **383**, 41-47 (2005).

18. S. Glasauer, S. Langley, T. Beveridge, S. Fakra, T. Tyliszczak, J. Bargar, D.K. Shuh, M. Boyanov, and K. Kemner, to be submitted (2006).

19. A.E.V. Gorden, D.K. Shuh, B.E. Tiedemann, R.E. Wilson, J. Xu, and K.N. Raymond, "Sequestered Plutonium: $[Pu^{IV}\{5LIO(Me\text{-}3,2\text{-}HOPO)\}_2]$-The First Structurally Characterized Plutonium Hydroxipyridonate Complex," Chem. Eur. J. **11**, 2842-2848 (2005).

20. J. Xu, A.E.V. Gorden, G. Szigethy, D.K. Shuh, and K.N. Raymond, “3-Hydroxy-2-methyl-pyran-4-one (Maltol): a Common Natural Product as a Complexing Agent for Pu(IV),” to be submitted to J. Amer. Chem. Soc. (Sept. 2006).

21. G.D. Tian, J.X. Xu, and L.F. Rao, “Optical Absorption and Structure of a Highly Symmetrical Neptunium(V) Diamide Complex,” Angew. Chem. Intern. Ed. **44**, 6200-6203 (2005).

THE INE-BEAMLINE FOR ACTINIDE RESEARCH AT ANKA – A STATUS REPORT

Boris Brendebach, Pascal Boulet, Kathy Dardenne, Melissa A. Denecke, Jürgen Römer, Jörg Rothe, Wolfgang Mexner[1], Karlheinz Cerff[1]
Forschungszentrum Karlsruhe, Institut für Nukleare Entsorgung, P.O. Box 3640, D-76021 Karlsruhe, Germany
[1]Forschungszentrum Karlsruhe, Institut für Synchrotronstrahlung, P.O. Box 3640, D-76021 Karlsruhe, Germany

Abstract

The INE-Beamline for actinide research at the synchrotron source ANKA is now fully operational. This beamline was designed, built, and commissioned by the Institut für Nukleare Entsorgung (INE) at the Forschungszentrum Karlsruhe (FZK), Germany. It is dedicated to actinide speciation investigations related to nuclear waste disposal as well as applied and basic actinide research. Experiments on radioactive samples with activities up to 10^6 times the exemption limit inside a safe and flexible double containment concept are possible. The close proximity of the beamline to INE's radiochemistry laboratories is unique in Europe. Currently, experiments can be performed in an X-ray energy range from around 2.15 keV (P K-edge) to 24.35 keV (Pd K-edge). Recent developments at the beamline include implementing a QuickEXAFS mode for time-resolved investigations. The beam spot at the sample position has been optimized and is measured to be about 500 µm in diameter. Currently the INE-Beamline is being upgraded to include a micro-focus option. Access to the INE-Beamline is possible through cooperation with INE, through the ANKA proposal system, and via the European Network of Excellence for Actinide Sciences (ACTINET).

Introduction

The Institut für Nukleare Entsorgung (INE) at the Forschungszentrum Karlsruhe (FZK) has constructed and commissioned a beamline dedicated to actinide research at the synchrotron source Ångströmquelle Karlsruhe (ANKA). Official operation of the INE-Beamline started on October 1st, 2005. There is presently a growing demand for synchrotron facilities, where the infrastructure, safety equipment, and expertise are available for performing research on radioactive samples. One great advantage of the INE-Beamline is that the ANKA accelerator and INE's active laboratories are both located within the same FZK site. This symbiosis has numerous advantages including profiting from the existing infrastructure, backed by decades of know-how. Samples can be prepared, characterized, and analyzed using the spectroscopic, analytical, microscopic, and structural methods available at INE radiochemistry laboratories before being transported to ANKA and investigated using synchrotron based methods at the INE-Beamline. The time-span between sample preparation and experiment is relatively short, which allows investigations of dynamic systems within a time-frame of hours. The samples are also retrievable, so that sample characterization in INE laboratories following the experiments at the INE-Beamline is possible. In addition, hazards associated with transporting radioactive samples to and from INE and nearby ANKA are minimized and the administrative requirements associated with such transports simplified.

Beamline Design

Because actinide speciation associated with nuclear disposal concerns is manifold, the major aim in the INE-Beamline design was to ensure variability, i.e., provide a multi-purpose station, where a number of methods are possible, including standard, surface sensitive, and spatially resolved methods.

For details of the optics section of the INE-Beamline design see ref. [1]. Some major updates are described hereafter. Recent improvements of the beamline optics include enabling time-resolved XAFS measurements and maximizing the photon flux at the sample position. The Lemonnier-type double crystal monochromator (DCM) installed at the beamline is driven by one single Bragg axis. This configuration allows straightforward fast scanning, in a so called QuickEXAFS-mode with a fixed exit beam. First test measurements at the Nb K-edge of a niobium foil recorded in less then one minute show promising results (see Figure 1).

Figure 1: QuickEXAFS spectrum (a) and resulting χ(k)-function (b) of a niobium foil measured at the Nb K-edge in less than one minute.

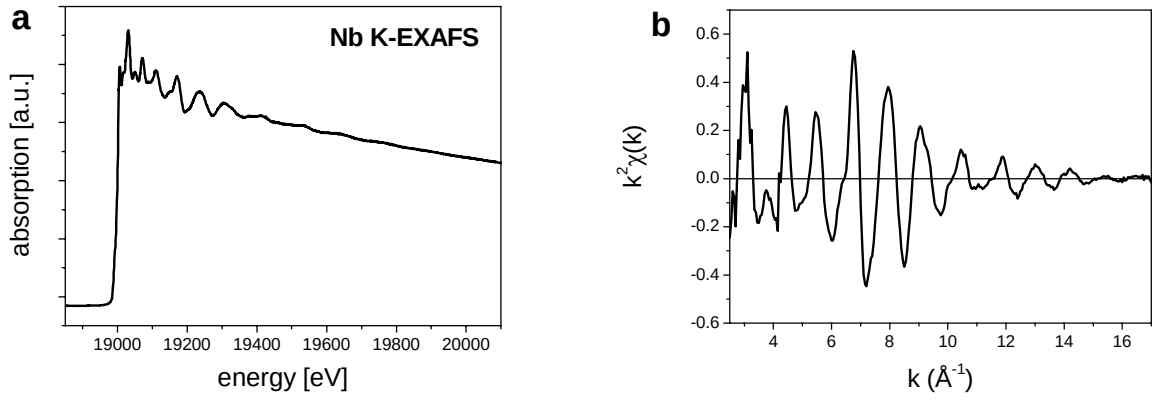

Figure 2 illustrates the beam dimensions at the sample position. A SESO X-ray Beam Position Monitor is used to estimate the beam dimensions to be 507 μm in the vertical direction and the beam width to be 522 μm.

Figure 2: Beam profile measured at the sample position without (a) and with (b) focusing. The width (c) and height (d) of the focused beam are estimated by single Gaussian profiles.

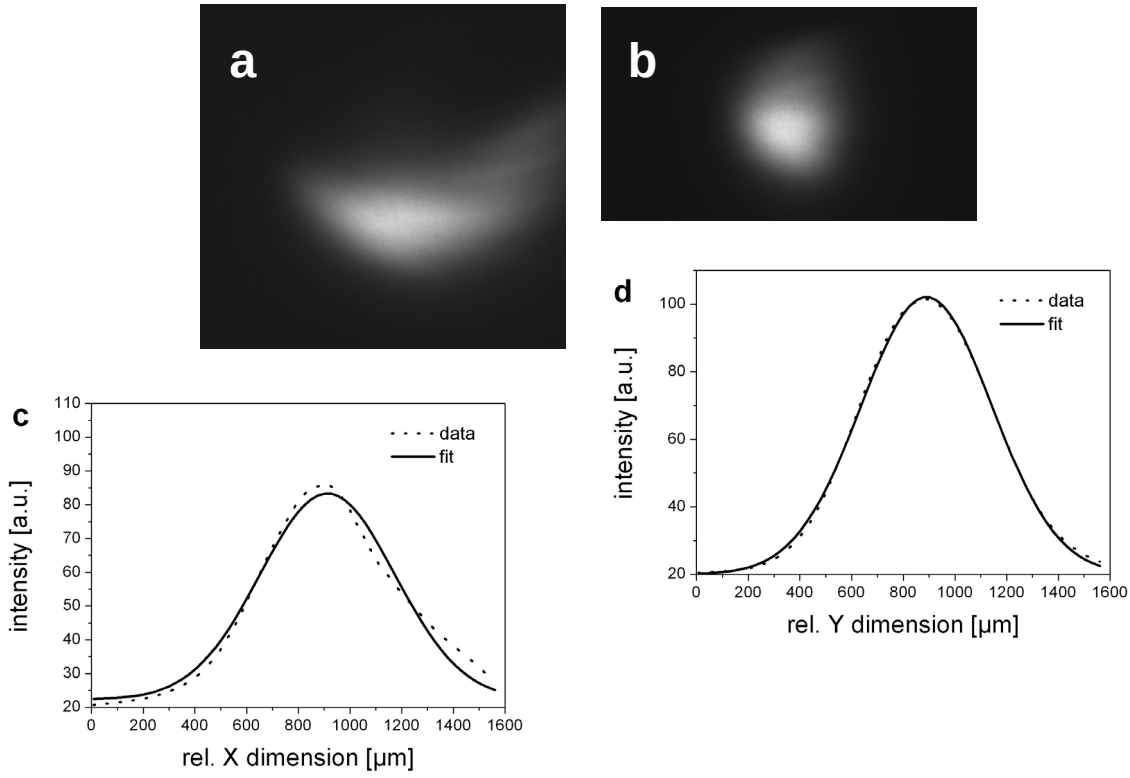

Experimental Station and Exemplary Measurements

The INE-Beamline is optimized for spectroscopic X-ray methods, X-ray absorption fine structure (XAFS), X-ray fluorescence (XRF), and combined XAFS and X-ray diffraction (XRD). We have designed, constructed and tested an inexpensive position sensitive XRD setup for performing combined XAFS/XRD investigations using flexible image plates made of radiation-sensitive, europium-doped barium fluoride films with a high dynamic range. The films are read out using a scanner with a laser beam and can be re-used after exposure to day UV-light. The experimental setup is depicted in Figure 3. As proof of feasibility, an yttrium K-XANES and a XRD pattern are recorded for Y_2O_3 powder. The test samples are either mixed with quartz as an internal standard and pressed to a pellet with addition of polyethylene or filled into a Lindemann capillary. Latter was used to perform the first combined XAFS/XRD measurement on the same sample spot. The Debye-Scherrer diffractograms are measured with excitation energies near the Y K-edge (17.038 keV). As shown in Figure 3d the full profile refinement thus obtained on pure Y_2O_3 encapsulated in a capillary gives reliable results.

Figure 3: Combined XAFS/XRD setup used for measurements (a). Debye-Scherrer diffractograms of Y_2O_3 test samples (b) and corresponding Y K-XANES spectrum (c) recorded at the same sample spot. The full profile refinement of the pure Y_2O_3 X-ray powder pattern from 2θ 12° to 72° is shown in (d) (experimental data as dots, refinement as solid line, Bragg reflections as vertical lines and the residual as the bottom line).

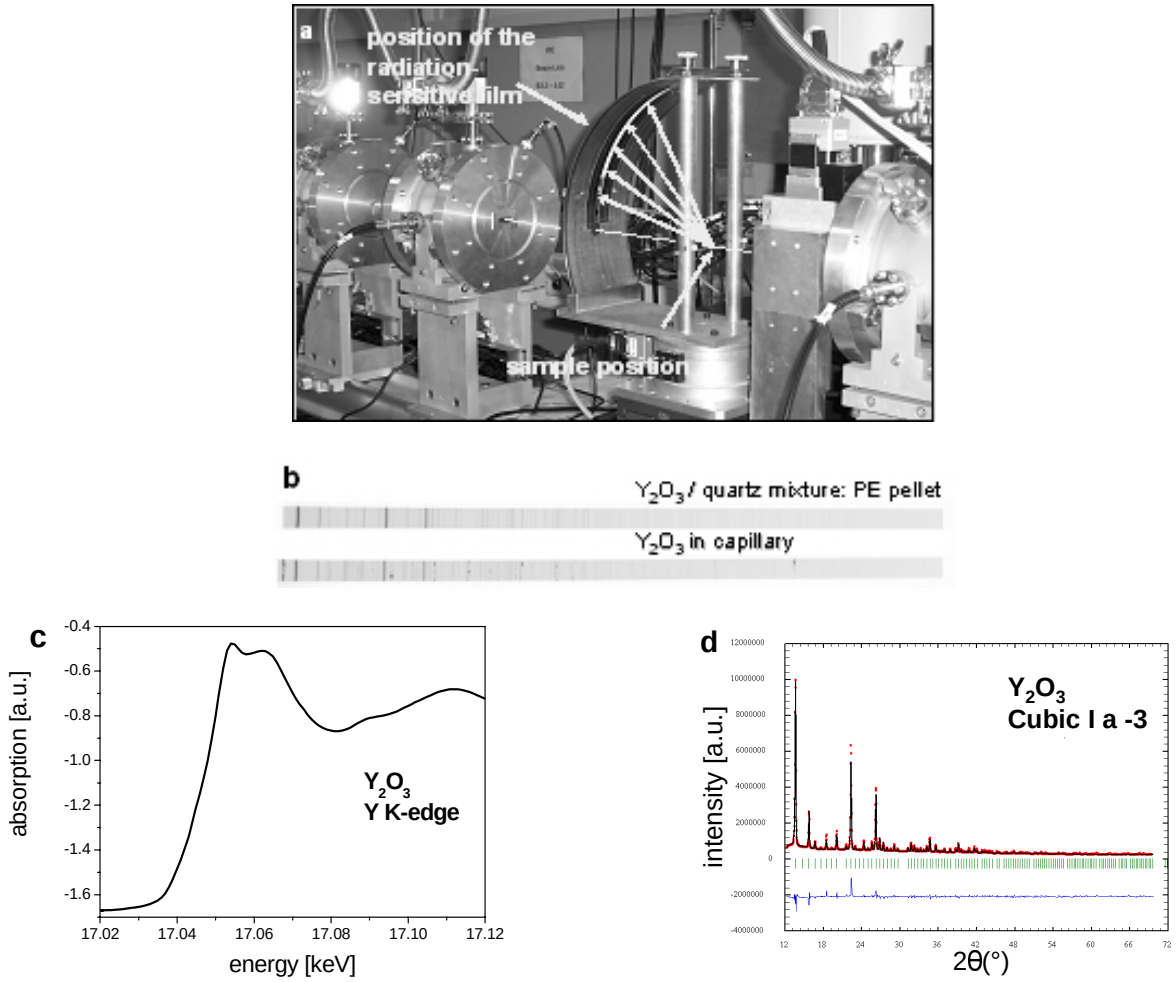

In cooperation with the Physikalische Institut, Bonn University, Germany, a setup for measurements down to the phosphorous K-edge has been constructed, installed, and first measurements successfully performed at the INE-Beamline (see Figure 4). The experimental setup is connected to the end of the beamline separated by a 14 µm Kapton® window. It is pumped to low pressure to reduce the loss of incoming photons by absorption in air. An additional mirror chamber is installed in front of the first ionization chamber. It contains a fused silica crystal, which can be positioned into the beam near the angle of total external reflection to suppress contributions from higher harmonic reflections from the DCM.

Planned Upgrades

A micro-focus option is currently being developed at the INE-Beamline in order to offer spatially resolved measurements. First tests using a planar compound refractive lens (CRL) as a one dimensional focusing optic are planned for the end of 2006. A hexapod positioner (Physik

Instrumente) for aligning the CRL is already purchased, integrated in the beamline control, and successfully tested. The CRL can be used as a virtual slit to maximize photon flux in surface sensitive techniques based on grazing incidence (GI) geometry, without having to reduce the number of photons by collimating the beam vertical dimension down using a slit. Because many reactions of actinides in the hydro- and geo-sphere are at interfaces and junctions, emphasis at the INE-Beamline is being placed on GI techniques such as GI-XAFS, X-ray reflectivity and total external reflection X-ray fluorescence analysis (TXRF). The next step in our micro-focus upgrade will be to focus the beam in both the vertical and horizontal direction using cross CRLs or polycapillaries. This will allow chemical state imaging (µ-XAFS), elemental mapping (µ-XRF), and after securing a suitable detector identification of phases (µ-XRD).

Figure 4: A setup for measurements down to the P K-edge is available (a) and directly connected to the beamline exit (b). First test spectra at the S K and P K-edge are presented in (c) and (d), respectively.

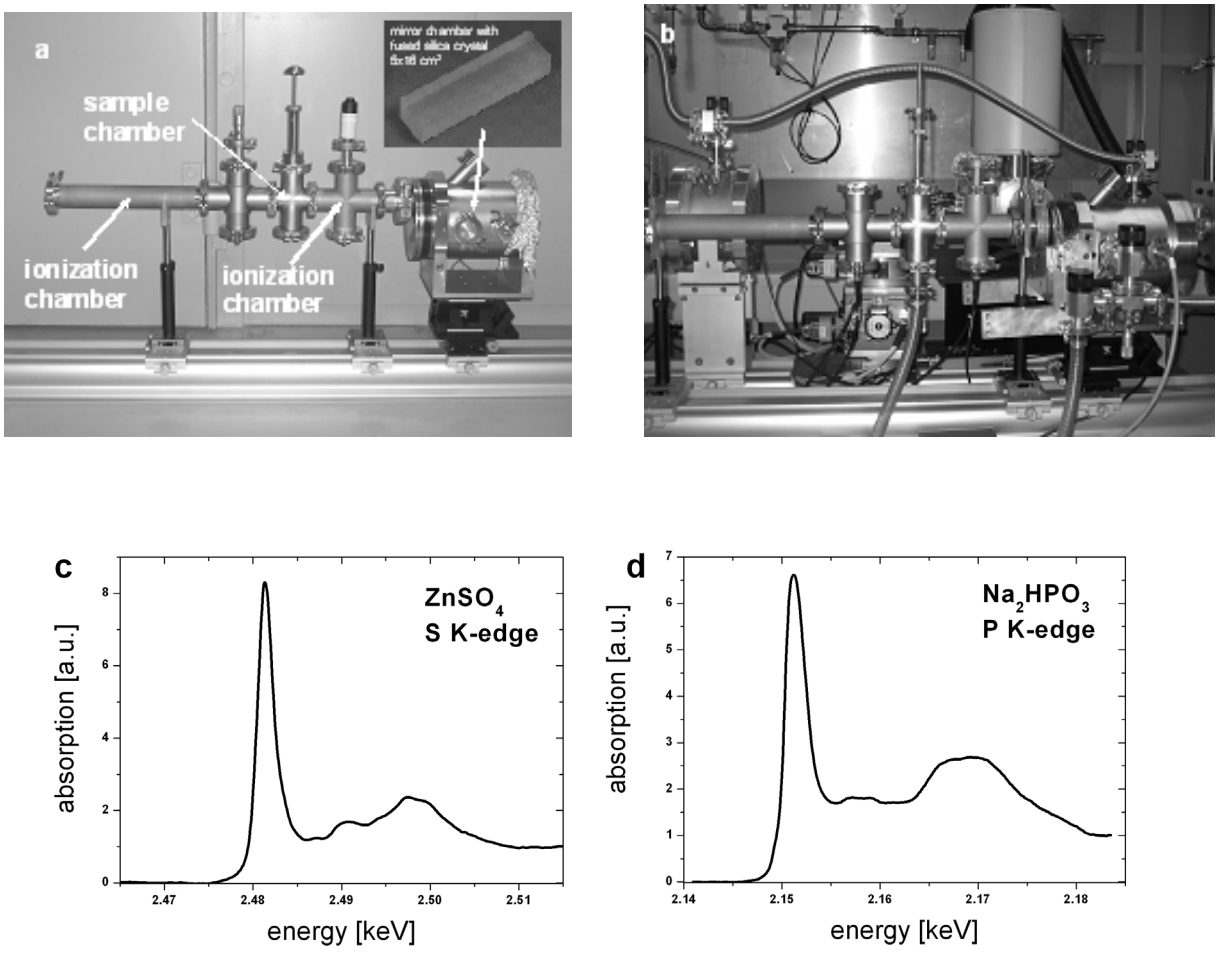

Future planned upgrades are as follows:

- In cooperation with the Joint Research Center Institute for Transuranium Elements (ITU) a cryostat to perform measurements down to 77 K and a silicon drift (vortex) detector as a second solid state detector system will be purchased in 2007.

- The LEGe 5-pixel detector (Canberra) available at the INE-Beamline for fluorescence measurements will be upgraded with a fully digital XIA electronics system.
- The 100 μm thick beryllium window, which separates the storage ring vacuum from the DCM, will be replaced by a 50 μm window. This will allow measurements down to the Si K-edge at 1.839 keV in combination with the use of a pair of InSb(111) monochromator crystals.
- A temperature controlled sample cell for combined XAS/XRD measurements is under construction and an electrochemical cell is in the design stage.
- A special windowed sample cell allowing a combination of X-ray methods with other techniques, e.g., laser based methods, will also be available in the future at the INE-Beamline.

Beamtime Request

The INE-Beamline and INE active laboratories are one of the pooled facilities of the European Network of Excellence for Actinide Science (ACTINET) and access to the beamline is possible via this avenue. A portion of annual beamtime at the INE-Beamline (30%) is available via the standard ANKA facility proposal procedure (for detailed information see [2]. ACTINET users are prompted to also submit a proposal to the ANKA facility for their beamtime. Experiments are also possible through cooperation with INE. INE-Beamline scientists are to be contacted prior to proposal submittal to ensure feasibility of any experiment involving radioactivity (contact persons can be found in [3]. INE provides a radiation protection officer during active measurements, who is responsible for all radioactive substances.

Acknowledgments

Part of the beamline development is a contractual cooperation between FZK-INE and the Physikalisches Institut, Universität Bonn. We acknowledge the ANKA Ångströmquelle Karlsruhe for the provision of beamtime. The micro-focus upgrade of the INE-Beamline is supported by ACTINET (JP 04-09).

References

[1] M.A. Denecke, J. Rothe, K. Dardenne, H. Blank, J. Hormes, *Phys. Scr.* **T115**, 1001 (2005).

[2] *http://ankaweb.fzk.de/*

[3] *http://ankaweb.fzk.de/instrumentation_at_anka/beamlines.php?id=9&field=7*

ROSSENDORF BEAMLINE AT ESRF: AN XAS EXPERIMENTAL STATION FOR ACTINIDE RESEARCH

A.C. Scheinost,* Ch. Hennig, H. Funke, A. Rossberg, W. Oehme, S. Dienel, J. Claussner, D. Proehl, G. Bernhard
Institute of Radiochemistry, FZR, D-01314 Dresden, Germany, and The Rossendorf Beamline at ESRF, F-38043 Grenoble, France
*scheinost@esrf.fr

Abstract

The Rossendorf Beamline with its X-ray absorption spectroscopy (XAS) station dedicated to actinide research was the first of its kind at a European synchrotron. Since its opening in 1999, it serves for about 30 experiments each year. An overview on the current status of operation modes, the technical details and on access conditions is presented.

Introduction

The Rossendorf Beamline is located at the European Synchrotron Radiation Facility (ESRF) as an independent collaborative research group (CRG), owned and operated by the Forschungszentrum Rossendorf (FZR). Two experimental stations run alternatively, one for diffraction and reflectivity experiments in Materials Sciences, the other for X-ray absorption spectroscopy (XAS) experiments related to Radiochemistry. Only the latter is dealt with here. Detailed descriptions of the beamline and the XAS endstation are published [1, 2]. Here we will update that earlier information and summarise the features most important for prospective users.

The radiochemical endstation of the Rossendorf Beamline has been constructed to serve the main research goals of the Institute of Radiochemistry at the FZR. Since these are related to the environmental behavior of actinides and other radionuclides, XAS experiments are predominantly conducted to solve the molecular structure and speciation of low concentrations of radionuclides in a large variety of media, including aqueous and nonaqueous solutions, rock minerals, clay minerals, microorganisms, plants, etc., but also combined systems like soils and sediments. This demand is supported by the XAS technique itself with its element selectivity, as well as by the high brilliance of the ESRF for low detection limits, and by special equipment at the beamline, for instance a sensitive fluorescence detector and a cryostat. The research interest as well as safety concerns of the ESRF restrict the list of radionuclides to α-emitters, hence the safety features include no shielding for γ-radiation, and the total activity is restricted to 185 MBq (see safety features below).

Figure 1. Beamline Optics:Schematic drawing of the beamline optics (top) and of the MOSTAB feedback system (bottom left). A typical I_0 signal resulting from this beam stabilization procedure is shown on the right (30-cm Oxford ionization chamber, filled with N_2/Ar=3 at ambient pressure, amplification 500 nA/V, ring current 190 mA)

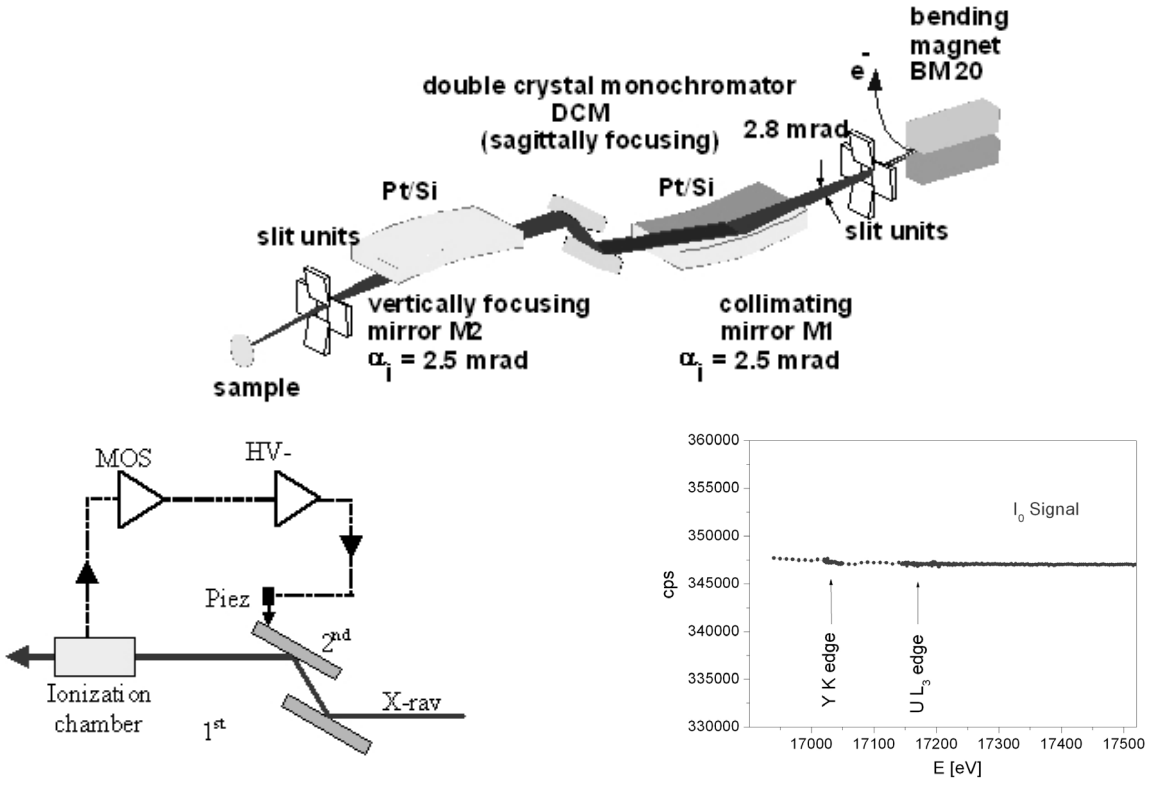

Optics

The beamline is located on bending magnet BM20 of the ESRF. The electron storage ring operates at 6 GeV in several modes (uniform fill, 2/3 fill, 16-bunch, single bunch) providing ring currents between 20 and 200 mA. Within the beamline's optics hutch, the white light is collimated by a water-cooled mirror (Zeiss), converted to a monochromatic beam by a water-cooled double-crystal monochromator (Si(111), Oxford) running either in channel-cut or fixed-exit mode, and then vertically focused by a second mirror (Zeiss, Figure 1). Depending on energy range, either the Si-coated (5-13 keV) or the Pt-coated surfaces (13-35 keV) of the two mirrors are used to reject higher harmonics. The integrated flux at 200 mA and 20 keV is $6 \cdot 10^{11}$ photons/s. The standard beam size for XAS is 1 x 10 mm^2. Smaller beam sizes may be achieved by a slit aperture. With the energy range covered by the monochromator and the other optical components including Be windows, the K-edges of elements V to Sb and the L-edges of elements Ba to Cm can be investigated (5-35 keV). A special feature to provide a very stable beam on the sample is the MOSTAB feedback system (HASYLAB, Figure 1).

XAS technical features

For transmission XAS measurements, three gas-filled ion chambers (Oxford) are available. Three software-controlled mass flow controllers are used to prepare mixtures of He, N_2, Ar and/or Kr suited for the respective energy ranges.

The measurement of environmental samples with typically low concentrations of the target element in a complex matrix often results in overlapping fluorescence lines, which require special fluorescence detection techniques. A high-throughput/high energy resolution 13-element solid state Ge detector (Canberra, 100 mm^2 LEGes), equipped with a XIA digital x-ray spectrometer (DXP-2X4T-M, 4-channel, 40 MHz, timing model) is available for this purpose. Figure 2 demonstrates the low detection limit resulting from the high and stable photon flux and the high count rate handled by the detector. The energy resolution at a shaping time of 0.25 μs is shown in Figure 3. Even at these conditions, which are very unfavorable in terms of energy resolution, but typical for XAS spectroscopy of environmental samples, the energy resolution is sufficient to isolate the U-Lα from the Rb-Kα line by selecting a narrow SCA.

Figure 2. Example for the low detection limit in fluorescence mode
U-L_{III} edge EXAFS spectra of U(VI) sorbed to gibbsite, with a total concentration of 20 μg/g U, measured at 15 K in the cryostat (2 samples prepared at identical lab conditions)

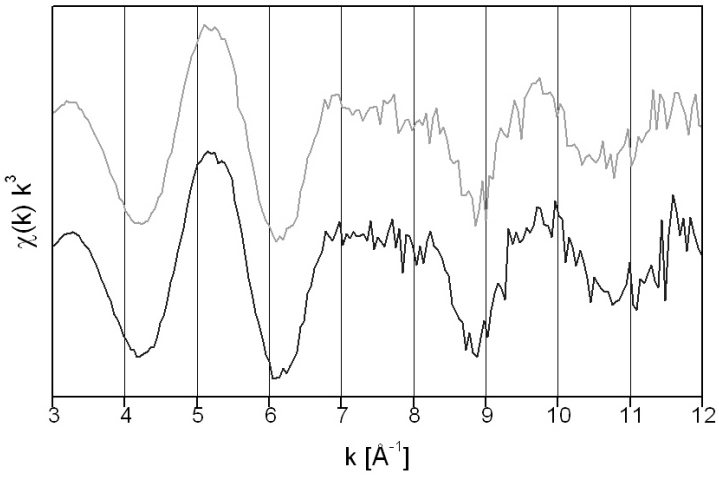

Figure 3. X-ray fluorescence spectra of two uranium mill-tailing samples Shaping time 0.25 μs, integration time 1 hour (top) and 5 s (bottom). The hatched area marks the U-Lα line, producing only a shoulder on the right side of the more pronounced Rb-Kα line.

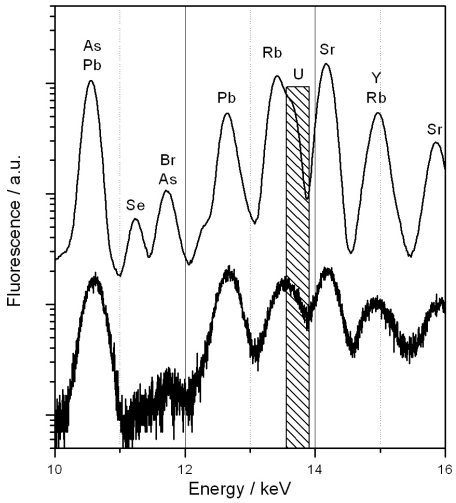

For sample cooling down to 12-30 K, a closed-cycle He cryostat (CryoVac) with negligible vibration and large exit window for fluorescence detection is available. This cryostat is routinely used for several reasons. First, in crystalline phases the detection of atomic shells beyond the first coordination sphere is greatly enhanced due to the reduction of the thermal (vibrational) component of the Debye-Waller term (Figure 4). Second, cooling to cryogenic temperatures greatly reduces the risk that biological or other organic samples are "fried-up" by the intense X-ray beam. Third, redox processes are inhibited, which is especially important when measuring actinides with several labile oxidation states. Finally, measuring samples at a range of temperatures allows investigating temperature-dependant structural effects.

Figure 4. Temperature effect on the U-L_{III} EXAFS spectrum of soddyite

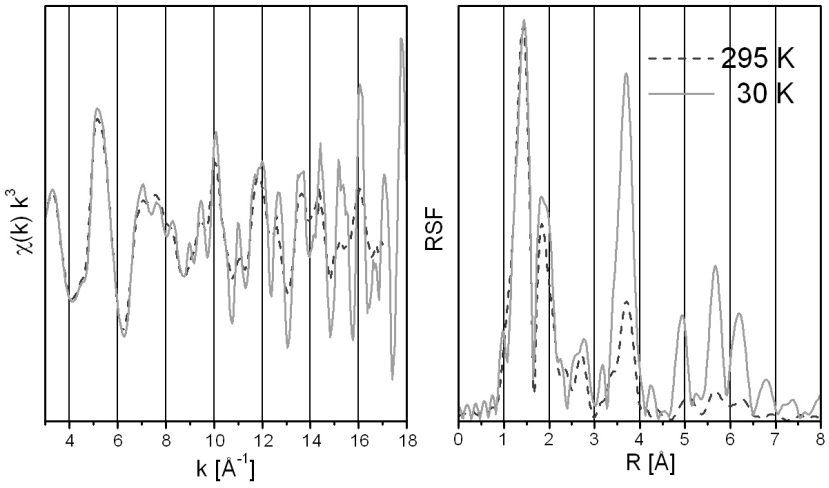

Figure 5. EXAFS polarization dependence of uranyl sorbed to montmorillonite angle α between the surface and the polarization vector

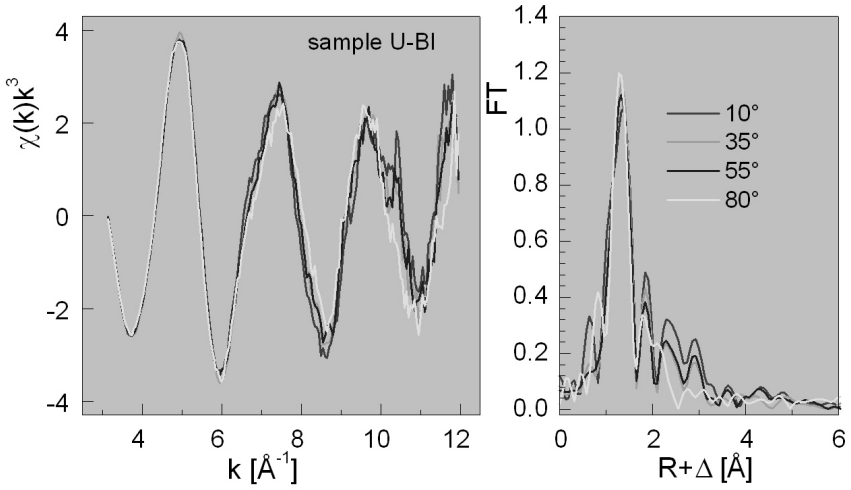

Redox control of aqueous and ionic liquids is possible by employing a spectro-electrochemical cell, which was specifically designed to suit the safety demands of the ESRF and prevents release of hydrogen gas by using second-order anode reactions [3]. Furthermore, a uniaxial goniometer is available to investigate the polarization dependency of structures (Figure 5) and to cancel the unwanted preferred orientation of particles within a sample by the magic angle technique.

Radiochemical safety features

The XAS experimental station is fully equipped and licensed to run a list of presently 18 radionuclides. Note that the maximum activity of all samples present at one time at the beamline may not exceed 185 MBq (Table 1).

The technical safety features are adjusted to handle predominantly α-emitting radionuclides. The central safety equipment is a glove box with negative pressure gradient towards the experimental hutch (which in turn has a negative gradient towards the ESRF hall). The ventilation system encompasses air filters and α-, β-, and γ-radiation monitor systems, with all components backed up by a parallel system in case of component failure (redundancy principle) [4]. The monochromatic X-ray beam enters and leaves the glovebox through Kapton bay-windows which are inserted in the stainless steel walls of the glovebox. Detection of fluorescence radiation is possible through a third, large (80 mm diameter) Kapton window. Because of this arrangement, the samples remain inside the glove box during an experiment, while X-ray transmission and fluorescence detectors, filters, calibration foils and additional slit systems remain outside.

Samples are commonly placed inside double-confinement sample holders. Sample intervention is restricted to modification of temperature (15-300 K with the cryostat), of redox potential (with the closed-system electrochemical cell), and of pH (injection of acids or caustics through a septic membrane).

A variety of holders for liquids, wet pastes, dry powders and pressed pellets, approved by the ESRF safety group for room or cryo-temperatures is available. A detailed description of these sample holders together with technical drawings may be downloaded from the beamline home page (*http://www.esrf.fr/exp_facilities/BM20*).

Table 1. List of approved radionuclides.

Nuclide	Max amount [g]	Exemption [Bq]	Half-life [y]	Specific activity [Bq/g]
Tc-99 (β -)	29.1	$5 \cdot 10^{6}$	$2.1 \cdot 10^{5}$	$6.4 \cdot 10^{8}$
Po-208 (α)	$8 \cdot 10^{-6}$	0	2.898	$2.2 \cdot 10^{13}$
Po-209 (α)	$3 \cdot 10^{-4}$	0	102	$6.2 \cdot 10^{11}$
Ra-226 (α)	$5 \cdot 10^{-3}$	$5 \cdot 10^{3}$	1600	$3.7 \cdot 10^{10}$
Th-nat (α)	1000	$5 \cdot 10^{4}$	$1.4 \cdot 10^{10}$	$8.2 \cdot 10^{3}$
Pa-231 (α)	0.106	$5 \cdot 10^{3}$	$3.28 \cdot 10^{4}$	$1.7 \cdot 10^{9}$
U-nat (α)	1000	$5 \cdot 10^{6}$	$4.47 \cdot 10^{9}$	$2.6 \cdot 10^{4}$
Np-237 (α)	6.97	$5 \cdot 10^{5}$	$2.1 \cdot 10^{6}$	$2.6 \cdot 10^{7}$
Pu-238 (α)	$2.9 \cdot 10^{-4}$	$5 \cdot 10^{3}$	87.7	$6.3 \cdot 10^{11}$
Pu-239 (α)	0.08	$5 \cdot 10^{3}$	$2.411 \cdot 10^{4}$	$2.3 \cdot 10^{9}$
Pu-240 (α)	0.022	$5 \cdot 10^{3}$	6563	$8.4 \cdot 10^{9}$
Pu-241 (α)	$4.9 \cdot 10^{-5}$	$5 \cdot 10^{3}$	14.35	$3.8 \cdot 10^{12}$
Pu-242 (α)	1.24	$5 \cdot 10^{3}$	$3.735 \cdot 10^{5}$	$1.5 \cdot 10^{8}$
Am-241 (α)	$1.4 \cdot 10^{-3}$	$5 \cdot 10^{3}$	432.2	$1.3 \cdot 10^{11}$
Am-243 (α)	$25 \cdot 10^{-3}$	$5 \cdot 10^{3}$	7365	$7.4 \cdot 10^{9}$
Cm-244 (α)	$6.2 \cdot 10^{-5}$	$5 \cdot 10^{3}$	18.1	$3.0 \cdot 10^{12}$
Cm-246 (α)	0.017	$5 \cdot 10^{3}$	4750	$1.1 \cdot 10^{10}$
Cm-248 (α)	1.156	$5 \cdot 10^{3}$	$3.39 \cdot 10^{5}$	$1.6 \cdot 10^{8}$

Figure 6. EXAFS data analysis with Monte Carlo methods: the molecular structure of aqueous uranyl acetate [7] The figure shows the last steps of the structure refinement. The position of the uranyl ion in relation to acetate is depicted by shaded dots, their color changing from blue to yellow as the likelihood increases. The final solution is indicated by a black point.

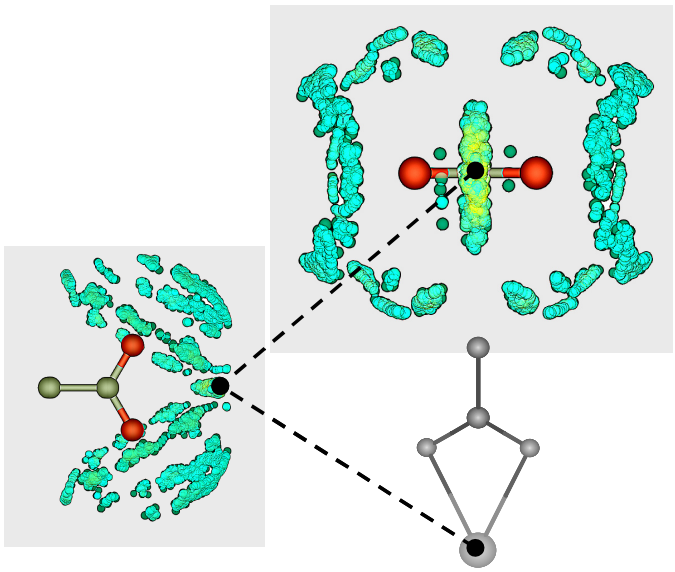

The samples are mounted in fully-automated sample stages. For room-temperature measurements, up to 8 samples can be mounted and measured without any user intervention. A uniaxial goniometer allows to rotate the 8-fold sample holder towards the polarization vector of the X-ray beam (DT- 80 Micos with 0.01° angle resolution). For measurements at temperatures down to 15 K, up to three samples are placed into a closed-cycle He cryostat, which is mounted inside the glovebox.

Data analysis

Besides standard data reduction and analysis tools (FEFF8, IFEFFIT, EXAFSPAK, WinXAS, Six-Pack), we provide advanced statistical tools like iterative transformation factor analysis [5, 6] and Monte-Carlo simulations (Figure 6) [7]. These methods greatly improve the detection, quantification and structural analysis of species from samples, which contain several species simultaneously. Furthermore, a wavelet analysis tool improves the analysis of the scattering amplitude distribution and hence the discrimination of atoms (Figure 7) [8, 9]. Finally, X-ray diffraction data may be collected in the neighboring Materials Science hutch to make use of the drastically improved line width of synchrotron radiation (Figure 8) and the synergy effects when analyzing both XAS and XRD. Software is available to refine both the XRD and the EXAFS information simultaneously [10].

Spectra collected at the beamline are stored in a data base for easy retrieval. A combined database and spectral analysis tool has been developed, which allows to search for spectra based on similarity. This tool will simplify the identification of the species in ill-defined samples by comparison with spectra of well-characterized samples.

Figure 7. EXAFS data analysis with Wavelet methods: Discrimination of Al and Ni in layered Ni-Al double hydroxide [9]. Note the different values of the Morlet parameters κ and σ to enhance resolution in either k (wave vector) or r (distance) space.

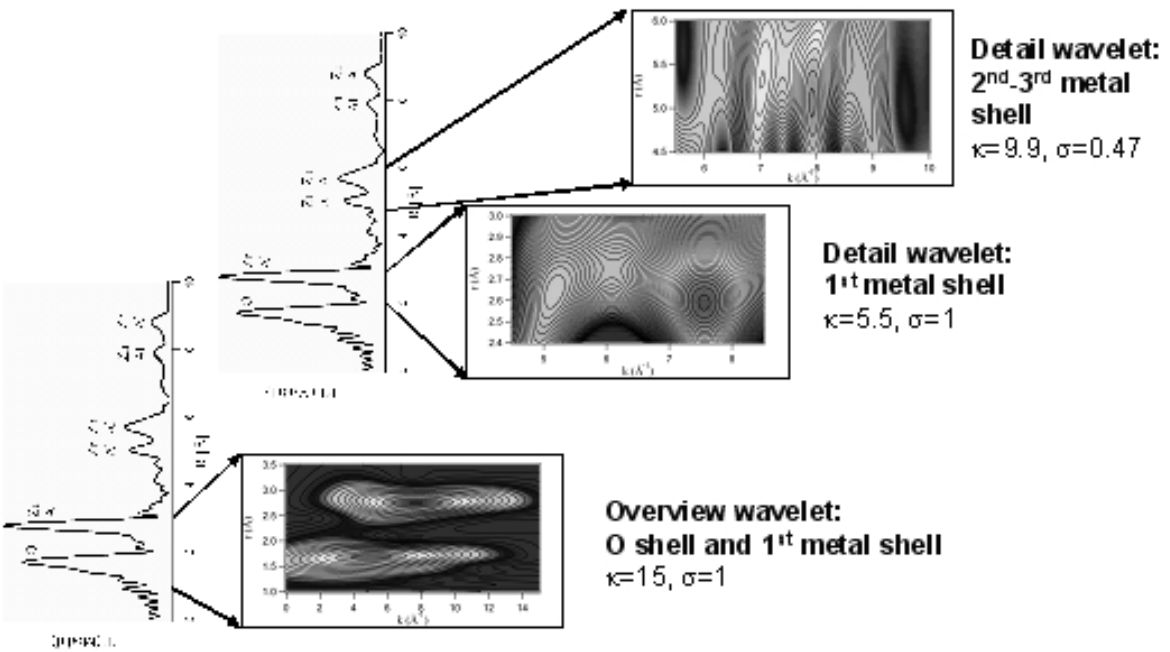

Modes of access

Due to the CRG-status of the Rossendorf Beamline at the ESRF, users may apply for beamtime in two different ways. Two-thirds of the beamtime at the radiochemistry station, corresponding to approximately 200 8-hour shifts or 67 days per year, are in-house beamtime of the FZR. Outside users have access to this beamtime by collaboration with scientists of the FZR. Applications for beamtime are accepted any time by submitting an application form to the acting head of the radiochemistry station (see http://www.esrf.fr/exp_facilities/BM20). Beamtime will be scheduled after acceptance of the proposal, usually within 4 months.

Figure 8. Comparison of X-ray diffraction with synchrotron and lab sources [10] $UO_2[H_2AsO_4]_2 \cdot H_2O$, powder pattern collected with synchrotron radiation (top), and with a conventional lab source (bottom)

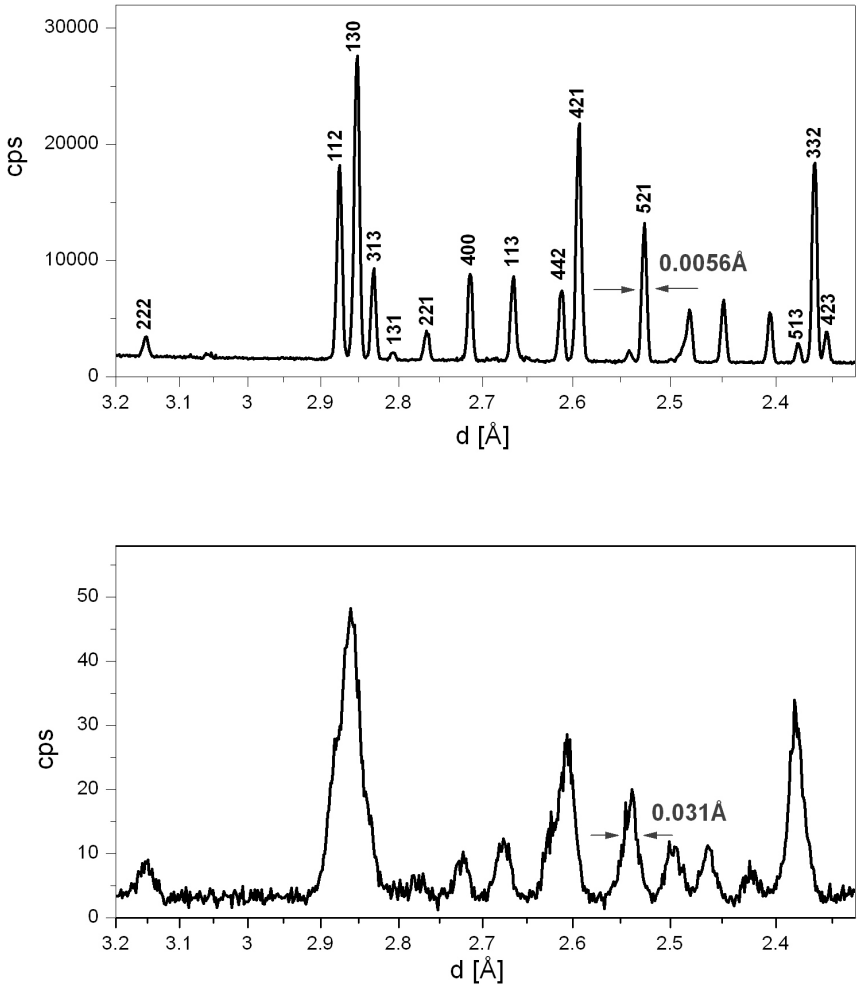

One-third of the beamtime (100 shifts or 33 days) is managed by the ESRF. Accordingly, proposals have to be submitted to the ESRF. Deadlines are March 1st and September 1st. The proposals are evaluated by the scientific advisory committee of the ESRF. In case of approval, beamtime is scheduled by the beamline personnel, usually between 6 and 12 months after the proposal deadlines.

For ESRF experiments, travel and accommodation expenses are reimbursed by the ESRF. For a detailed user guide please visit the ESRF home page (www.esrf.fr).

The Rossendorf Beamline is part of the ACTINET network, and provides beamtime for ACTINET Joint Research Projects. Information on how to apply for these projects can be found at http://www.actinet-network.org.

All radioactive samples for both types of access mode have to be delivered, stored, and handled according to the safety regulations agreed upon with ESRF. It is recommended to contact the beamline personnel at least 2 months in advance of the scheduled experiment to discuss sample preparation, transport, and measurement procedures. If an experiment is labeled “red” by the ESRF Safety Group (generally experiments involving Np, Pu, Am, Cm samples), two persons must be present at the beamline, 24 hours a day. These experimentalists have to be provided by the user group.

References

[1] W. Matz, N. Schell, G. Bernhard, F. Prokert, T. Reich, J. Claussner, W. Oehme, R. Schlenk, S. Dienel, H. Funke, F. Eichhorn, M. Betzl, D. Prohl, U. Strauch, G. Huttig, H. Krug, W. Neumann, V. Brendler, P. Reichel, M.A. Denecke and H. Nitsche, Journal of Synchrotron Radiation 6 (1999) 1076-1085.

[2] T. Reich, G. Bernhard, G. Geipel, H. Funke, C. Hennig, A. Rossberg, W. Matz, N. Schell and H. Nitsche, Radiochimica Acta 88 (2000) 633-637.

[3] C. Hennig, J. Tutschku, A. Rossberg, G. Bernhard and A.C. Scheinost, Inorganic Chemistry 44 (2005) 6655-6661.

[4] H. Funke, G. Bernhard, J. Claussner, K. Jansen, W. Matz, H. Nitsche, W. Oehme, T. Reich and D. Rollig, Kerntechnik 66 (2001) 195-201.

[5] A. Rossberg, T. Reich and G. Bernhard, Analytical and Bioanalytical Chemistry 376 (2003) 631-638.

[6] A.C. Scheinost, A. Rossberg, M. Marcus, S. Pfister and R. Kretzschmar, Physica Scripta T115 (2005) 1038-1040.

[7] A. Rossberg and A.C. Scheinost, Analytical and Bioanalytical Chemistry 383 (2005) 56-66.

[8] H. Funke, M. Chukalina and A. Rossberg, Physica Scripta T115 (2005) 232-234.

[9] H. Funke, A.C. Scheinost and M. Chukalina, Physical Review B 71 (2005) 094110.

[10] C. Hennig, T. Reich, W. Kraus, G. Reck, F. Prokert and N. Schell, Physica Scripta T115 (2005) 352-355.

DESIGN AND STATUS OF THE RADIOACTIVE MATTER BEAMLINE AT THE SOLEIL SYNCHROTRON

Bruno Sitaud[1], **Stéphane Lequien**[2], **Hervé Hermange**[1] **and Pier Lorenzo Solari**[1]
[1] Synchrotron SOLEIL, Saint Aubin BP48, F-91192 Gif sur Yvette, France
[2] Laboratoire Pierre Süe, UMR 9956 CEA-CNRS, CEA Saclay, F-91191Gif-sur-Yvette, France

Abstract

During the past two years, numerous actions have been completed for the construction of the new French synchrotron source, SOLEIL, and the associated beamlines. The MARS beamline which is dedicated to Multi Analyses on Radioactive Samples, should be one of the first beamlines to be operational during the second phase of beamline construction around the storage ring. This beamline will support a multidisciplinary research programs connected to radionuclides in general with the specificity of allowing measurements on highly radioactive samples, up to 18.5 GBq. Hence, the MARS beamline design has been optimized with respect to the national safety regulations and the scientific and technological requirements, in order to obtain the status of an installation for the protection for the environment. This beamline, located on a bending magnet port, has been developed for XAS spectroscopy analyses including millisecond time resolution and diffraction experiments with an energy ranging from approximately 3.5 to 35 keV. Three complementary experimental end-stations that will be used alternatively have been defined, as well as some special equipment, including confinements or shielding around the samples. The installation of the different components should be ended during the first semester 2007 and user access for experiments with radioactive samples is targeted for 2008.

Introduction

The storage ring of the SOLEIL synchrotron [1], the new third generation synchrotron facility located at Saint-Aubin, near Paris (France), began commissioning in May 2006 [2] with an initial set of eleven beamlines (phase 1 of construction). At the time of writing, stable beam conditions have been obtained at the nominal energy of 2.75 GeV with a current up to 300 mA, the maximum value currently permitted by the present available power supply RF. The synchrotron beam was already injected with success in the first bending magnet beamline for hard X-ray diffraction and absorption spectroscopy (DIFFABS) and on the first HU80 undulator beamline for soft-X ray photoemission spectroscopy (TEMPO).

At SOLEIL, studies of radioactive matter are planned to be performed on a dedicated beamline taking into account the French safety regulations for these special materials. Since beginning of 2004, the project of construction of the MARS beamline (standing for Multi Analyses on Radioactive Samples), has been officially launched at SOLEIL with a scientific and a partial financial support coming from the French Atomic Energy Commission (CEA). This dedicated beamline should be one of the first to be operational among the new thirteen beamlines of the second phase of construction.

The MARS beamline will be the fourth beamline in Europe for studying radionuclides, after the ROBL beamline at ESRF, the INE beamline at ANKA and the µXAS beamline at SLS. The aim is clearly to get an extension of the possibilities of analyses on radioactive samples toward higher activity. Hence, the design of the MARS beamline has been optimized for performing analyses with different experimental techniques, on a large variety of radioactive samples (α, β, γ and n emitters) with an activity of up to 18.5 GBq per sample (value referring to the group 1 of radionuclides). In addition the dose rate limitation has been fixed to 7.5 µSv/h inside the experimental area (restricted zone). It is the first time that both values will be offered to the scientific community for studying any radionuclide emitters on a synchrotron.

Infrastructure and security

The MARS beamline is built on the bending magnet port D03-1 of the SOLEIL storage ring. The 1.71 T bending magnet field provides a continuous spectrum of photons with a critical energy of 8.6 keV. A 3-D view showing the overall layout of the beamline is given in Figure 1.

Figure 1: General layout of the MARS beamline from the optics hutch (right side) to the control room (left side). The central part is the ICPE restricted area for radioactive sample preparation and experiments (diffraction and absorption spectroscopy). The total length of the beamline is equal to 40 m.

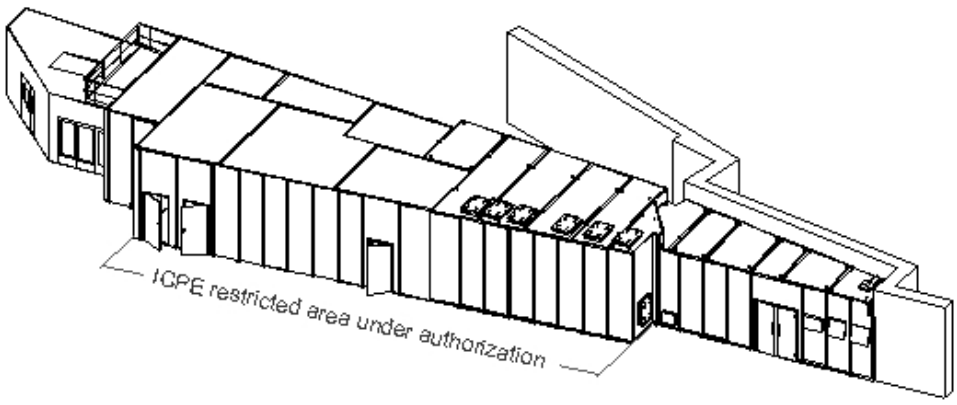

The different hutches and the rooms have been designed by SOLEIL and their construction is currently realized by the NTC Company. Basically the beamline is separated into three main functional areas. The first one corresponds to the Pb shielded optics hutch. Its overall height is equal to 3.4 m (Figure 2) in order to use an internal crane for maintenance operations on the mirror and monochromator vacuum vessels. The second area includes the experimental hutch and the sample preparation hutch, three airlocks, a technical room and two changing rooms. This part will be classified as a "Listed Installation for the Protection of the Environment" (ICPE in French), under authorization. Referring to the main prescriptions for the installations dedicated to the manipulation of sealed or non sealed sources, walls, ceilings, grounds and doors have to be constructed using materials which can be easily cleaned (in case of contamination) and fireproof, with a degree of resistance of 2 hours. Also, due to the weight limitation onto the experimental floor, it was decided to build the infrastructure of this beamline starting from a "classical" metallic structure on which several layers of selected materials are fixed, in agreement with the security functions associated to each hutch. In addition, the air tightness of the internal layer will be optimized in order to obtain inside the hutches a negative pressure with respect to the atmospheric pressure. The depressurised atmosphere will be ensured by a dedicated ventilation system which is designed and constructed by the COFATHEC Omega-Concept Company (Lille, France). As a result, a dynamical confinement will be created inside the ICPE area for operation. Absolute filters located at the intake air and the blowing points will trap radioactive material particles in case of a failure of sample confinement barriers. The dynamical confinement represents in fact the third barrier for the samples, the first and the second one being provided by the users by means of special air tight sample containers. Pressure, temperature and radioactivity will be continuously controlled and recorded by a specific monitoring unit.

Figure 2: Picture of the optics hutch at the end of its construction

Inside the sample preparation hutch, two glove boxes under air atmosphere will be available, (a) for checking the samples (contamination, composition) after their transportation and before positioning in one of the experimental stations, and (b) for an eventual exchange of the second sample container in case it is not suitable for use in connection with the appropriate sample holder. Theses operations will be done only by specially trained people. In any case it will be possible to manipulate a sample without the first static confinement inside the glove boxes. In addition, in some cases, it will be

necessary to add a adapted shielding around the samples in order to fulfil public safety regulations. In order to facilitate transportation of samples to SOLEIL, storage could be temporarily done inside a special shielded and secured cabinet, before and/or after experiments. A maximum global activity of 185 GBq for the whole samples stored inside the different beamline hutches will be allowed.

The main part of this restricted area is the experimental hutch. Its height is 4 m with a crane capacity of 5000 N that leaves about 3.2 m effective height inside. Three complementary end stations have been designed and located in this hutch as presented on Figure 3. In addition a third glove box can be connected to the XAS station and be used for radioactive samples (liquid state for instance) when the safety guaranties for their second barriers are considered insufficient for the experimental process. In that case samples will be positioned using motorised stages inside the glove box. This arrangement is actually limited to the absorption station. The experimental hutch communicates with an internal airlock in which a remote control computer will be installed for the initial operations (sample alignment for instance) or in case of very short X-ray acquisitions. At each exit from the restricted area, people will have to pass through the preparation hutch, use the radiological controller inside the personnel airlock and remove their protective clothes inside the changing rooms.

Figure 3: Top view of the experimental hutch of the MARS beamline showing the three end stations and the internal airlock for access and the use of the remote control. The surface of this hutch is around 40 m^2.

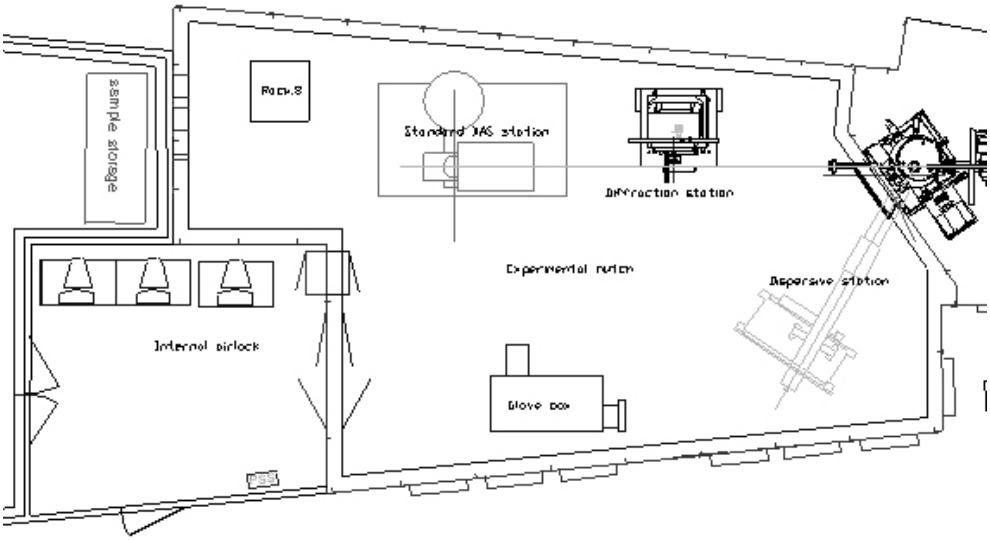

The last area is free of radiological (irradiation and contamination) safety regulations and is composed of the main control room and the ventilation and pump units room.

Optical elements

The original design [3] for this beamline is based on the alternative use of two long mirrors and two monochromators in order to obtain two complementary optical configurations (standard and dispersive). The working configuration will be selected according the experimental needs, i.e. the techniques of analysis, the energy, the spatial resolution and the time resolution required. The optical elements have been designed taking into account the characteristics of the bending magnet source, in order to reach the maximum of the beam flux inside the energy range of 3.5 to 35 KeV, and with the

possibility of focusing the beam to a minimum size of around 100 x 100 μm^2. Furthermore, provision of micro beams with dimensions below 20 x 20 μm^2 will be achievable, by using of a set of mirrors in the Kirkpatrick-Baez (KB) geometry. At present time and except for the KB optics, the four main components, as well as the slit units, the filters and beam imagers, have been manufactured and several reception tests are in progress.

Both mirrors are designed and built by the SESO Company and their vacuum chamber and translation stages by the IRELEC Company. These mirrors suppress the higher order harmonics and provide a vertically collimated or focused beam to the experimental hutches. Both mirrors are water cooled systems, because of the dispersive configuration, and will operate in an ultra high vacuum. These mirrors consist of a Si block with a 600 Å Pt coating on half of the active width, thus providing two complementary reflective stripes for low and high energy setups. Factory controls show that their roughness are less than 3 Å rms and their longitudinal slope errors are around 1.8 μrad rms for both mirrors over all their active surfaces (1200 x 116 mm^2).

The first monochromator set after the X-ray source is a double crystal monochromator (DCM) designed and manufactured by Oxford Danfysik. Two successive reflections will select the desired energy and will orient the outgoing photons in order to be parallel to the incoming beam direction after the second mirror, but with a constant upward offset of 20 mm. The original feature of this DCM is the integration of a new technical solution for which an *in situ* exchange of the two crystal sets, here Si(111) and Si(220), can be done, without venting the vessel. Both second crystals can be also bended sagittally in order to focus the beam in the horizontal plane.

The second monochromator is a single crystal monochromator (SCM) designed by the SOLEIL group. It is integrated in a common vacuum vessel with the beam shutter and is installed after the second mirror as shown on Figure 4. The SCM is switched on by a single vertical translation for the dispersive station. It is based on the use of a crystal elliptically bended in the horizontal plane. The minimal distance between the SCM axis and the sample is around 1 m which gives a focused beam size of 10 x 45 μm^2 at 10 keV considering an incoming beam divergence of 1 mrad. However the energy bandwidth for this third station is limited from 5 to 25 keV because of technical constraints and occurrence of two other end stations. In practice EXAFS spectra should be correctly measured above 7 keV using the energy dispersive optics with a time resolution of around 1 ms.

Figure 4: Cross section of the single crystal monochromator, designed by the SOLEIL group, inside the vacuum vessel with the included the beam shutter just before the wall pass through. The X-ray beams are also represented for the standard optics configuration (upper beam) and the dispersive configuration (lower beam interacting with the water cooled crystal).

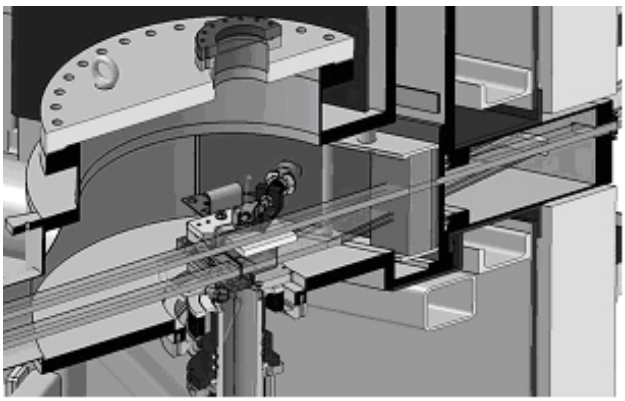

Experimental end stations

At least four main techniques of analysis will be proposed from the three end stations: high resolution powder diffraction (XRD), X-ray fluorescence (XRF), standard X-ray absorption spectroscopy (XAS) and dispersive XAS (DXAS) with the ability of focusing the X-ray beam over the whole energy range for all of them. In addition a micro focused beam will be available by using the KB optics on the XAS station. The lower energy of 3.5 keV, just below the M_{IV-V} absorption edge of U, is mainly given by the absorption of the mandatory Be windows. The upper energy of around 35 keV was chosen to allow XAS experiments up to the K edge absorption of Xe and Cs, both elements been found among the fusion products of nuclear fuels.

The robust 2-circle goniometer of the diffraction station is manufactured by the SMP Company. The main characteristics of this instrument are a very high accuracy on the 2 theta circle (around 3 arcsec or 1.10^{-3} degree) with a loading capacity up to 750 N on both circles for using shielded containers and a relative wobble of 5 arcsec between both axes at the maximum weights. In addition an open Eulerian cradle will be mounted on the omega circle to provide two more circles for particular studies (single crystal, stress and texture measurements).

A general purpose X-ray absorption spectroscopy setup will be available 3 m downstream the diffraction station. This second station will be also equipped for X-ray fluorescence analyses. Samples shall be directly analyzed inside either standard sample holders or the glove box depending on the risks estimated for each experiment (sample state, variations of external parameters, etc…).

Optimized sample environments are already developed with the end users of the beamline. As an example, a working group composed of persons belonging to the CEA and SOLEIL has designed a special cryostat (Figure 5) to perform experiments at low temperatures (down to 10 K). This cryostat is currently manufactured by the Air Liquide Company and should be tested by the end of this year.

Figure 5: External view of the He cryostat designed for radioactive samples.

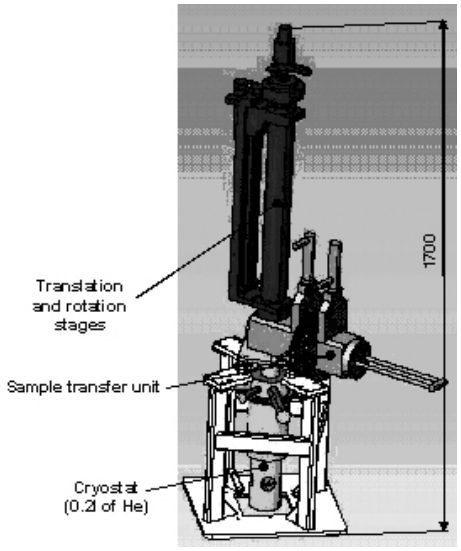

Because of the increase of hazards at low temperature, the third barrier which is generally the hutch is replaced by the cryogenic device itself. A special transfer unit is inserted between the cooled part and the upper translation and rotation stages, for placing/removing the samples without breaking the confinement. Like this, a secure transfer of the sample-holder is possible to a glove box for activity measurements.

This technical development is a good example to encourage users to define sample environments with the beamline staff prior to the beamline routine operation. The aim is indeed to be able to propose progressively to the user community a set of standard and well known equipment which are optimized for radioactive samples and the dedicated experiments to be performed.

This principle is also applicable for the detection devices. In that case, the noise due to the sample radiations is the main difficulty encountered. Additional equipment like bandpass filter devices that remove unwanted energies will be necessary for optimizing the signal-to-noise ratio on the different end stations. Different solutions for the detection systems are already analysed and the final selections will be achieved very soon. The MARS beamline commissioning is scheduled the last trimester of 2007 with the XRD and XAS experimental stations. User access with radioactive samples is planned for the beginning of 2008 depending on the operation permission delivered by the French authorities.

References

[1] Synchrotron SOLEIL, Synchrotron Radiation News, 2003, 16, 49-56.

[2] A. Nadji *et al.*, Proceedings of the SRI conference 2006, Daegu (Korea), to be published.

[3] B. Sitaud and S. Lequien, Proceedings of the Actinide-XAS workshop 2004, Berkeley (USA).

RECENT DEVELOPMENT OF THE JAEA BEAMLINES IN THE RADIONUCLIDE FACILITY OF SPRING-8 AND TOPICS

Tsuyoshi Yaita
Actinide Coordination Chemistry Group, Synchrotron Radiation Research Center
Quantum Beam Science Directorate, Japan Atomic Energy Agency (JAEA)
1-1-1 Koto, Sayo-cho, Sayo-gun, Hyogo 679-5148, Japan

Abstract

Japan Atomic Energy Research Institute (JAERI) and Japan Nuclear Cycle Development Institute (JNC) were unified last October and, a new research institute was launched as Japan Atomic Agency (JAEA). JAEA continues to maintain the four beamlines of SPring-8 (also one beamline at PF, KEK) and keeps the research activity for radioactive materials. Furthermore, the research for actinide materials has been strengthened since the unification. The four JAEA's beamlines are formed as follows, 1) BL11XU (undulator, 6-130keV) for High Energy XAFS, Nuclear Inelastic Scattering, Resonance Inelastic x-ray scattering (RIXS), 2) BL14B (4-100keV) for Dispersive XAFS (DXAFS), high pressure diffractometer equipped with cubic-anvil press, 3)BL22XU (undulator, 3-90keV)) for high pressure diffractometer equipped with multiple- and diamond-anvil press, deffractometer for x-ray crystallography etc., 4) BL23SU (undulator, 0.3~1keV) angle resolved photoemission spectroscopy (ARPES), x-ray magnetic circular dichromism (XMCD). Sealed Np, U and Th samples can be measured at all the beamlines. Also, measurement of unsealed Np, U, Th and the other radioactive samples will become possible next year. These beamlines are opened for international users. In this report, the performance of these beamlines and recent topics will be presented.

POSTER SESSION CONTRIBUTIONS

EXAFS STUDY OF NEPTUNIUM(V) SORPTION ONTO HEMATITE

Samer Amayri, Markus Breckheimer, Jakob Drebert, and Tobias Reich
Institute of Nuclear Chemistry, Johannes Gutenberg-Universität Mainz, 55099 Mainz, Germany

Abstract

The fate and transport of neptunium from nuclear waste repositories in rock systems may be affected by adsorption onto the surface of minerals such as iron mineral hematite (α-Fe_2O_3). We have studied Np(V) adsorption on hematite using batch experiments as a function of pH in the presence and absence of ambient CO_2. These macroscopic studies were combined with extended x-ray absorption fine structure (EXAFS) spectroscopy to determine the speciation of Np(V) at the hematite surface. EXAFS investigations were done under conditions relevant to surface waters and aquifers (8µM Np(V) concentration in equilibrium with atmospheric CO_2 and under Argon atmosphere, respectively, pH 4.0 to 10.5 at ionic strength 0.1 M $NaClO_4$). The uptake studies of Np(V) with hematite show that pH and CO_2 have a significant influence on the sorption. Sorption experiments showed that the sorption edge (pH where 50 % sorption occurs) of Np(V) occurs at pH 7.0-7.5 with a sorption maximum at pH 8.5. The structure parameters of near-neighbour surrounding of Np(V) sorbed onto hematite surface have been determined by Np L_{III}-edge EXAFS. The distances of the co-ordination shells Np-O_{ax}, Np-O_{eq}, and Np-Fe measured by EXAFS suggest that Np(V) was bonded in an inner-sphere fashion. In the presence/absence of atmospheric CO_2, the average Np-O_{eq} distances are the same in all samples and smaller than in $NpO_2(CO_3)_3^{5-}$. There is no evidence of the formation of Np(V) carbonato species at the hematite surface in the samples prepared in air. There is no evidence for Np neighbors in the EXAFS spectra, suggesting that the adsorbed Np(V) complexes are predominantly monomeric.

Introduction

An important factor which determines the mobility of radionuclides in the environment is their interaction with the mineral-water interface [1]. To predict the radionuclide mobility, it is necessary to extend the knowledge about the retardation and mobilization phenomena and the underlying basic processes and interactions, such as physissorption, chemisorption, co-precipitation, inclusion, diffusion, and surface-precipitation or surface-complexation [2].

^{237}Np from high-level radioactive waste is considered as a possible long-term pollutant of the ecosystem, because of its toxicity, long half-life (2.14 million years), and its mobile nature under aerobic conditions due to the high chemical stability of its pentavalent state, NpO_2^+ [3, 4].

In rock systems, iron oxides are expected to play an important role in regulating the migration of radionuclides because of their widespread existence, high surface areas, high sorptive capacities, and common occurrence as grain coatings [5, 6]. Iron oxide grain coatings, often formed by weathering processes, have been shown to be important metal-ion-adsorbing phases even in Fe-poor aquifers [7]. Kohler *et al*. provided a data set for the sorption of Np(V) on hematite and the effect of the carbonate species on neptunyl (NpO_2^+) sorption as a function of partial pressures of CO_2. They analysed their sorption data with FITEQL and Triple Layer Model (TLM) using several postulated surface species. One important species, which greatly improved the model fits, was a ternary neptunyl-carbonato surface complex, $\equiv FeONpO_2(O_2COH)_2^{2-}$ [8]. This species was also important for modelling the batch experiments of Kohler *et al*. using the Diffuse Double layer Model (DDLM) by Richter *et al*. [9].

The aim of this study is to understand the sorption mechanism of neptunium(V) on hematite at a molecular level and to obtain spectroscopic evidence using EXAFS for the postulated inner-sphere complexes $\equiv FeONpO_2$ and $\equiv FeONpO_2(O_2COH)_2^{2-}$. Combes at al. performed Np L_{III}-edge EXAFS measurements on Np(V) sorbed from $1.3 \cdot 10^{-5}$ M solution on goethite (α-FeOOH) at pH 7.2 [10]. They observed that the local geometry of Np(V) is similar to that of NpO_2^+ dissolved in water. However, their "data provide permissive evidence for the formation of inner-sphere complexes of Np at the goethite/water interface". In case of U(VI), inner-sphere sorption and formation of ternary uranyl-carbonato surface complexes on several iron oxides were shown by EXAFS spectroscopy [11,12]. Therefore, we propose to apply EXAFS spectroscopy to the system Np(V)/hematite to validate the postulated species. EXAFS measurements provide element-specific short-range structural and chemical information for Np(V) co-ordination environments, including co-ordination numbers and bond distances to neighbouring atoms.

Materials and Methods

Materials

Hematite powders used in these experiments were synthesized from 0.2 M $Fe(ClO_4)_3$ solution at 98°C for 7 days following the method of Schwertmann *et al*. [13]. The synthesized hematite was purified by repeated intensive washing with Milli-Q water. Separation of the phases was achieved by centrifugation. With this procedure clean hematite was produced. Hematite surfaces have only Fe, O, and very small amount of adventitious carbon, as measured by XPS (x-ray photoelectron spectroscopy) (Figure 1). Photoelectron spectra were collected under UHV conditions ($<10^{-9}$ mbar) on SPECS x-ray photoelectron spectrometer using Al-K_α radiation. The resulting photoelectrons were detected by a hemispherical electron energy analyzer. N_2-BET (single point Brunauer-Emmett-Teller (BET) N_2 adsorption isotherms obtained with a Quantasorb Jr.) surface areas of the dried powders were 41.2 m^2/g. Powder XRD (x-ray diffraction) showed it to be crystalline α-Fe_2O_3 comparing to

structural data of Maslen *et al*. [14]. There is no evidence for goethite or other foreign phases. No impurities were detected.

Neptunium solution chemistry

Actinide concentration in groundwaters outside the waste package can be limited by two mechanisms: the low dissolution rate of the solid waste form or the solubilities of individual nuclides. Solubility establishes an upper limit for the source term for radionuclide transport from a repository [15]. The estimates of the solubilities and the speciation of the actinides are predicted from thermodynamic data, taking into account the presence of inorganic ligands in the groundwaters studied, mainly OH^-, HCO_3^-, CO_3^{2-}, ($C1^-$ in case of disposal in rock-salt formation), and the properties of these waters (redox potential). Detailed information on neptunium chemistry in hydrosphere and geosphere is given by Lieser and Mühlenweg [4]. Neptunium forms oxidation states from III to VII.

Figure 1: X-ray photoelectron spectra of synthetic hematite (α-Fe_2O_3). The spectra were corrected for Al-K_α satellites due to non-monochromatic excitation.

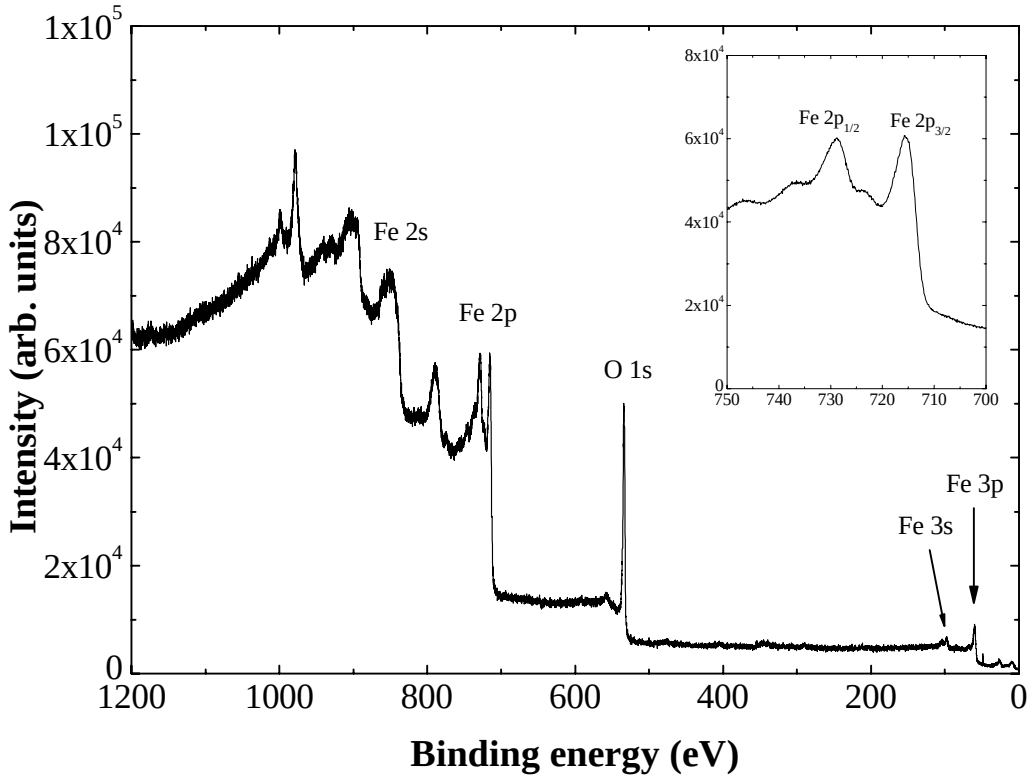

Np(V) is the most stable oxidation state under oxidizing conditions [16]. In the system Np(V)/hematite, the predominant aqueous chemical species are complexes between neptunyl ion and water (the hydrolysis products) and carbonate species. Carbonate complexation of Np(V) dominates over hydrolysis in an alkaline system. Figure 2 (left) shows the neptunium speciation under ambient CO_2 as a function of pH. Within pH 6 to 12, the following species are present: NpO_2^+, $NpO_2CO_3^-$, $NpO_2(CO_3)_2^{3-}$, and $NpO_2(CO_3)_3^{5-}$, indicating the complexity of neptunium geochemistry.

Figure 2. Calculated speciation of NpO_2^+ as a function of pH for a 8 µM solution of Np(V) in 0.1 M $NaClO_4$. Ambient CO_2 ($P_{CO2}=10^{-3.5}$ atm) (left); without CO_2 (right).

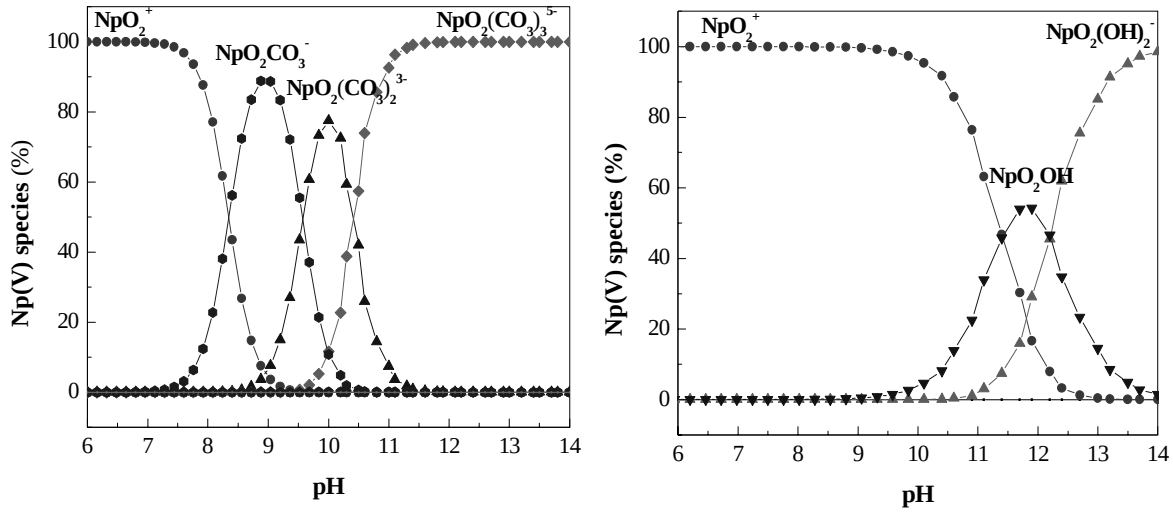

Figure 2 (right) shows the neptunium speciation without CO_2 as a function of pH. Np speciation within pH 10 to 14 is dominated by hydrolysis complexes, NpO_2OH and $NpO_2(OH)_2^-$.
The Np(V) speciation in aqueous solution is calculated with the chemical equilibrium software MEDUSA [17] applying the Np(V) hydrolysis and carbonato constants evaluated by Neck *et al*. [18], and Lemire *et al*. [19].

Batch sorption experiments with Np(V)

Sorption experiments of Np(V) on hematite were conducted at room temperature as a function of pH in the presence and absence of ambient CO_2. Experiments under anaerobic condition were carried out in an atmospheric control chamber with high purity Ar gas and all the solutions used under anaerobic condition were prepared with CO_2-free Milli-Q water (18 megaohm).

Batch experiments were carried out by suspending 0.5 mg of hematite in 9.5 mL 0.1 M $NaClO_4$ solution in 15 mL polypropylene centrifuge tubes and rotated for 72 hours in the overhead rotator. After such preconditioning these solutions were then titrated to the appropriated pH between 4.0 to 10.5 using $HClO_4$ or NaOH, and maintaining the ionic strength near 0.1 M. In air equilibrated samples with a pH greater than 6.5, a calculated amount of 1.0 M $NaHCO_3$ was added to the system to speed up the CO_2 equilibrium. This pH adjustment was repeated for several days until the pH value was stable. pH values of solutions were measured by pH meter (WTW inoLab pH Level 1) equipped with temperature detector WTW TFK 150 and electrode SCHOTT Blue line 16 pH. 3M NaCl was used as inner electrode solution instead of the usual 3M KCl to avoid a possible precipitation of $KClO_4$ at the diaphragm of the electrode. Neptunium was added to each sample and the total solution volume was adjusted to 10 mL by adding 0.1 M $NaClO_4$ solution. The total neptunium concentration was $8 \cdot 10^{-6}$ M. This is below the solubility of any solid phase, e.g., $NaNpO_2CO_3(s)$ [18]. The pH was readjusted to the desired value immediately after the addition of neptunium. Then the samples were overhead rotated for 60 hours. During this time, the pH of the solutions was checked for two times more and, if necessary, was adjusted.

After a contact time of 60 hours, the solid and liquid phases were separated by centrifugation at 4025 g for 30 minutes in a centrifuge SIGMA 3K30. The neptunium uptake by hematite was determined by liquid scintillation counting (LSC) and γ-spectrometry of the supernatant.

The used ^{237}Np stock solution was purified from traces of ^{239}Pu and ^{233}Pa by ion exchange chromatography on a column of Dowex 1X8 (150.0 x 4.0 mm, 200-400 mesh, Bio-Rad), and the oxidation state and concentration of Np(V) was verified and determined by absorption spectrophotometry. The resulting Np(V) stock solution had a pH of 1.0 and a Np concentration of 1.3 mM with high oxidation-state purity (as determined by UV-Vis).

Sorption results

The results of sorption experiments on hematite are summarized in Figure 3. In the air-equilibrated system the uptake of Np(V) by hematite increases from pH 6.5 to 8.5 (83 % sorption) and decreases, due to the formation of strong carbonato complexes in aqueous solution, above pH 8.5 to pH 9.5 (54 % sorption). The increase in the sorption after pH 9.5 can be due to the change of CO_2 equilibrium. These two points at pH 10.0 and 10.5 must be checked again. No decrease in uptake is observed in the absence of CO_2. The sorption maximum is ~100 % in the pH range 9.5 to 10.5. The adsorption edge occurs at pH 7.0 and 7.5 in both atmospheres, respectively.

The fraction of sorbed Np was calculated by using the following equation, $\Gamma\%(Np) = \left(1 - \frac{C_f}{C_0}\right) \times 100$, where $\Gamma\%(Np)$ is the amount of Np(V) sorbed onto hematite (%), C_0 and C_f represent the final concentrations of Np in solution in the absence and presence of iron oxides, respectively. After the sorption experiment the presence of Np(V) in the liquid phase was investigated by liquid scintillation counting (LSC) or γ-spectroscopy. For the calculations we used the average intensities of ^{237}Np γ-lines at 29.374 keV (14.12 %) and 86.477 keV (12.4 %).

Figure 3. Sorption of 8.0 µM Np(V) on hematite in the presence and absence of ambient CO_2 as a function of pH.

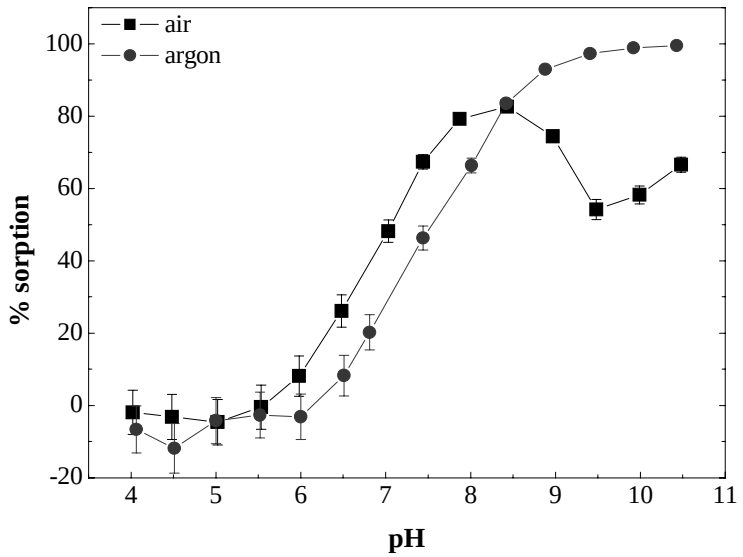

EXAFS data collection, analysis, theoretical calculations and results

For EXAFS investigations at room temperature, centrifuged wet hematite pastes were loaded into standard Perspex sample holders with Kapton windows. For low temperature measurements (at 13K), the solid residues were dried and loaded into a polyethylene sample holder.

Table 1 summarises the preparation conditions of samples A-E and the amount of neptunium sorbed in each sample. Three EXAFS samples labeled A, B, and C were prepared in the presence of ambient CO_2 at pH 7.0, 9.0, and 10.0, respectively. Samples D and E were prepared in a glove box with Ar atmosphere at pH 8.5 and 9.0, respectively. These samples can be compared with samples which were prepared in equilibrium with air. The total Np(V) concentration in each sample was 8 µM. The neptunium loading of the samples was between 422-474 ppm.

Table 1: Summary of the hematite wet-paste samples prepared at $8 \cdot 10^{-6}$ M Np(V), M/V 4.0g hematite/L and 0.1 M $NaClO_4$ for EXAFS measurements.

Sample	Atmosphere	T/K	pH	Np loading/ppm
A	CO_2	298	7.0	460
B	CO_2	13	9.0	469
C	CO_2	298	10.0	422
D	Ar	298	8.5	474
E	Ar	13	9.0	474

Np L_{III}-edge (17610 eV) fluorescence spectra were collected at room/low-temperature at the Rossendorf beamline ROBL at the European Synchrotron Radiation Facility (ESRF) in Grenoble using a Canberra 13-element Germanium detector. A silicon (111) double-crystal monochromator was used to tune the incident x-ray beam to the desired energies [20]. Slits were used to define 2.5x20 mm^2 beam profile. Two Cr foils (3x6 absorption lengths) were used to reject Fe-K fluorescence from the samples.

The x-ray energy was calibrated before analyzing each sample using an yttrium foil. The first inflection point in the Y K-edge was set to 17038 eV. The raw Np L_{III}-edge data were analysed using the EXAFSPAK software [21]. Backscattering phase and amplitude functions required for fitting the spectra were obtained from FEFF 8.20 calculations [22, 23] using the crystal structure of iron(III) uranium oxide [24], where U was replaced by Np to model a possible Np-Fe interaction with the hematite surface.

All Np L_{III}-Edge XANES spectra of the samples show neither a shift in the absorption edge energy (at 17610 eV) nor a significant structure difference at the high energy side of XANES. The neptunium in all samples is sorbed at the surface of hematite as Np(V).

Figure 4. Np L_{III}-edge k^3-weighted EXAFS spectra (left) and their Fourier transforms (right) for Np(V) adsorbed on hematite at 8 µM $[Np(V)]_T$. Dashed lines are fits.

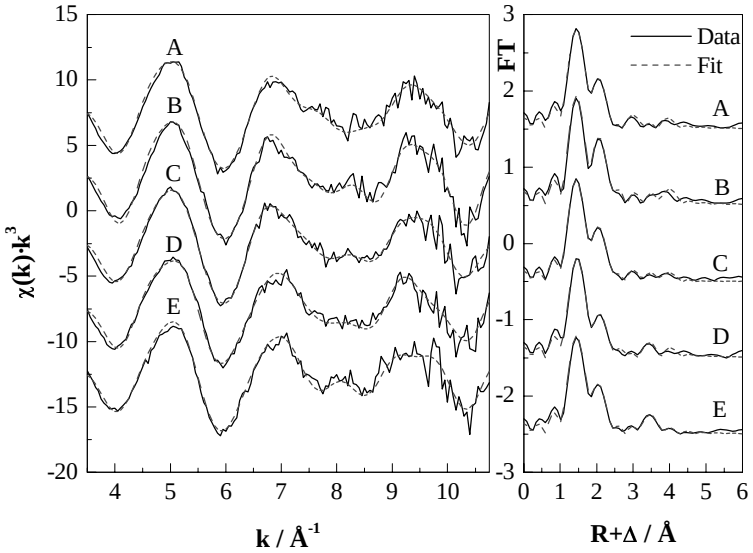

The raw Np L_{III}-edge k^3-weighted EXAFS spectra of all samples together with the best fit to the data and their corresponding Fourier transforms (FTs) are shown in Figure 4. Note that the FTs are uncorrected for scattering phase shifts (R+Δ) causing peaks to appear at shorter distances. The EXAFS spectra of all samples show similar oscillations indicating similar neptunium near-neighbor surroundings. The samples in Ar atmosphere (D and E) show clearly a peak at ~3.7 Å in the FTs. (see Figure 4). The scattering interactions with the iron atom of the FeO_6 octahedra of hematite are expected in this region.

The calculation of the best theoretical fit to the raw EXAFS data shown in Figure 4 included two steps. In the first step, we assumed the NpO_2^+ cluster as a structural model (see Figure 5 (lower left)) and fitted the raw EXAFS data with the single scattering path SS Np–$O_{ax,}$ multiple scattering path MS Np–O_{ax}, SS path Np–O_{eq}, and SS path Np–$O_{(FeO6)}$. The distances of the Np-O_{ax}, Np-O_{eq}, and Np-$O_{(FeO6)}$ for all samples were 1.87±0.01, 2.48±0.02, and 2.86±0.02, respectively, and agree with the formation of the NpO_2^+ cluster for the first two shells. The second step aimed at determining the structural parameters of the Fe and Np shells. To be more sensitive in the fit to these minor components, we isolated the Fe and Np scattering contributions from the raw data according to the difference technique [25].

Briefly, the theoretical fit obtained in the first step was subtracted from the raw data followed by Fourier filtering of the residual in the R range of 3.0-4.5 Å. The residual EXAFS was modelled using the SS path Np-Fe and SS path Np-Np. For the final fit to the raw data, the co-ordination numbers of all shells were held constant at the values determined during the previous two modelling steps. The results are presented in Figure 4, summarised and compared to $NpO_2(H_2O)_4^+$ [26] and $NpO_2(CO_3)_3^{5-}$ [27] data in Table 2.

An equally good fit to the EXAFS could be obtained with including Np-Fe shell and without including the Np-Np shell. The EXAFS measurements of samples D und E detected Fe atom at a distance of 3.73±0.01 Å. Samples A, B und C detected Fe atom at a distance of 3.43±0.02 Å. The Np-O_{eq} bond distances in all samples are comparable to or smaller than those for NpO_2^+ (aq.) (see Tab. 2). All FTs contain a peak at 2.4+Δ Å. This feature has been a structure part of the proposed sorption complex, because of its short distance. This peak at 2.4+Δ Å is related to the Np-$O_{(FeO6)}$ shell. The obtained Np-O_{eq} distances in all samples are shorter than in $NpO_2(CO_3)_3^{5-}$(aq.). There is no significant

difference in the Np-O distances at pH 9.0 between samples B and E. In all samples there is also no evidence for the formation of Np(V) carbonato species at the hematite surface. At pH 9.0 and 10.0 the presence of HCO_3^-/CO_3^{2-} has no effect on the Np(V) species sorbed (Figure 4).

EXAFS fit of all samples does not show any Np-Np interaction, indicative of formation of mononuclear Np(V) species at the hematite surface.

According to the fit results, the structure model of possible Np(V) surface species on hematite is shown in Figure 5 (upper left). One possible bidentate inner-sphere structural model implying an edge sharing between the Np(V) and Fe-octahedra was developed on the basis of structural parameters determined by EXAFS. Figure 5 shows the co-ordination of Np(V) sorbed on hematite if the ∠(Np, Fe, $O_{(FeO6)}$) is ~ 60°. In this case the calculated Np-Fe and Np-$O_{(FeO6)}$ distances are in relative good agreement with fit results. In this model a short distance of 2.0 Å is obtained between O_{ax} and $O_{(FeO6)}$. A more complicated model may be necessary to interpret the EXAFS results better. As a conclusion, the EXAFS investigations indicate that Np(V) is coordinated directly to the surface FeO_6 octahedra in a bidentate fashion. There is no spectroscopic evidence of the postulated ternary carbonate complexes (e.g. $\equiv FeONpO_2(O_2COH)_2^{2-}$) by Kohler *et al*. [8]. In the system U(VI)/iron oxides, Waite *et al*. [5, 6] postulated the existence of ($\equiv FeO_2UO_2CO_3^{2-}$) ternary complexes to model U(VI) adsorption on ferrihydrite. They found that models not having this species underpredicted U(VI) uptake between pH 7 and 9. Manceau *et al*. [28] and Waite *et al*. [6] used EXAFS to study U(VI) sorption on ferrihydrite, but did not report any findings regarding carbonate ligands. Ho and Miller [29] observed that hematite particles, which were positively charged in near- and sub-neutral pH carbonate-bearing solutions (i.e., at pH 7.5), acquired net negative charges following adsorption of U(VI). They attributed this charge reversal to the presence of negatively charged U(VI)-carbonato-hematite complexes. Dent *et al*. [30] and Bargar *et al*. [12, 31] reported evidence form EXAFS for the existence of adsorbed U(VI)-carbonato complexes on montmorillonite and hematite, respectively. The absence of Np(V)-carbonato complexes at the hematite surface observed in our EXAFS study agree with several EXAFS measurements [6, 11, 28] of U(VI)/iron oxide systems.

Table 2. EXAFS fitting results.

Sample	Description	2x(Np-O_{ax})		4x(Np-O_{eq})		2x(Np-O)		0.5x(Np-Fe)		ΔE_0 (eV)
		R (Å)	σ^2 (Å^2)	R (Å)	σ^2 (Å^2)	R (Å)	σ^2 (Å^2)	R (Å)	σ^2 (Å^2)	
A	pH 7.0, air	1.87	0.003	2.48	0.010	2.86	0.016	3.43	0.006	5.7
B	pH 9.0, air, 13 K	1.88	0.002	2.48	0.006	2.84	0.010	3.44	0.011	7.0
C	pH 10.0, air	1.87	0.003	2.46	0.009	2.86	0.013	3.46	0.014	4.2
D	pH 8.5, argon	1.88	0.003	2.49	0.013	2.87	0.010	3.74	0.003	7.2
E	pH 9.0, argon, 13 K	1.87	0.003	2.46	0.010	2.84	0.015	3.73	0.002	5.1
[26]	$NpO_2(H_2O)_4^+$	1.82	0.002	2.49	0.006	-	-	-	-	-
[27]	$NpO_2(CO_3)_3^{5-}$	1.86	0.001	2.53	0.013	-	-	-	-	-

$\Delta R = \pm 0.02$ Å, $\Delta\sigma^2 = 0.001$ Å^2

Figure 5. Schematic diagram illustrating a possible Np(V) co-ordination environment on the hematite surface (upper left), the arrangement of the FeO_6 octahedra in the hematite structure (right), and the used neptunyl ion (NpO_2^+) as a fit model (lower left)

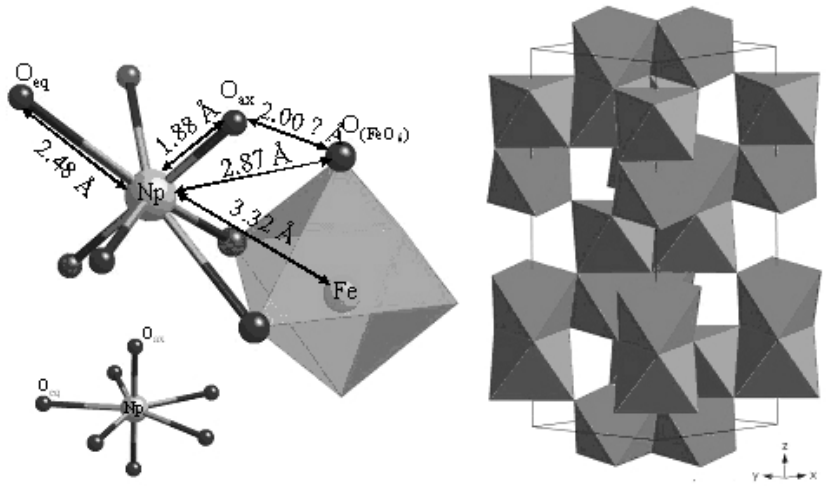

Conclusion

Batch sorption experiments at 8µM Np(V) concentration, M/V ratio (0.5 g synthetic hematite/L), and ionic strength (0.1M $NaClO_4$) were conducted to determine the effects of varying pH and p_{CO_2} on Np(V) sorption on hematite. The results show that Np(V) sorption on hematite is strongly influenced by pH and p_{CO_2}. In the absence of CO_2, Np(V) sorption increases continuously until 100 % sorption in pH range 9.5-10.5. For experiments open to atmospheric CO_2 ($p_{CO_2}=10^{-3.5}$ atm), Np(V) sorption increases up to pH 8.5 and decreases after that at higher pH. A comparison of the pH-dependence of Np(V) sorption with that of Np(V) aqueous speciation indicates a close correlation between Np(V) sorption and the stability field of the Np(V)-carbonato and -hydroxo complexes. In the presence of CO_2, sorption is inhibited at pH >8 due to formation of aqueous Np(V)-carbonato complexes. The EXAFS investigation shows that Np L_{III}-edge EXAFS spectroscopy is a valuable tool to determinate the structure parameters for the neptunium near-neighbour environment at water-solid interfaces. In this study the Np(V) species on hematite surface have been identified as mononuclear, inner-sphere complexes. This is based on the absence of Np-Np interaction and the presence of a Np-Fe interaction near 3.46 Å. This distance is in accord with an edge-sharing, bidentate surface complex. There is no evidence for the formation of Np(V) carbonato species at the hematite surface. The obtained results show the complex sorption behaviour observed in the Np(V)-hematite system. These data suggest that surface complexation based on parameters derived from a limited set of data could be useful in extrapolating radionuclide sorption over a range of geochemical conditions. Such study could be used to support transport modelling and could provide a better understanding for the release of radioactive elements in the environment and is important in performance assessment transport calculations.

Acknowledgment

The authors would like to thank N. Zink (University Mainz, JOGU) and C. Eckardt (Research center Dresden-Rossendorf, FZD) for their XRD and BET measurements. We thank also H. Funke,

C. Hennig, A. Rossberg, and A. Scheinost (FZD/ROBL) for their assistance during the EXAFS measurements. A preliminary EXAFS measurement was performed at ANKA (Research center Karlsruhe, FZK) and assisted by K. Dardenne, M.A. Denecke, and B. Brendebach. We acknowledge the European Synchrotron Radiation Facility (ESRF) and Angstromquelle Karlsruhe Facility (ANKA) for provision of radiation facilities. This work was supported by Bundesministerium für Wirtschaft und Technologie (BMWi) under contract No. 02E9653.

References

[1] R.J. Silvia, H. Nitsche: Actinide environmental chemistry; Radiochim. Acta **70/71**, 377-396 (1995).

[2] K.V. Ticknor: Uranium sorption on geological materials; Radiochim. Acta **64**, 229-236 (1994).

[3] R.C. Thompson: Neptunium – The neglected actinide: A review of the biological and environmental literature; Radiat. Res. **90**, 1-32 (1982).

[4] K.H. Lieser, U. Mühlenweg: Neptunium in the hydrosphere and in the geosphere; Radiochim. Acta **43**, 27-35 (1988).

[5] T.D. Waite, T.E. Payne, J.A. Davis, and K. Sekine: Uranium Sorption: Alligator Rivers Analogue Project; Final Report, **13.** Australian Nuclear Science and Technology Organization (1992).

[6] T.D. Waite, J.A. Davis, T.E. Payne, G.A. Waychunas, and N. Xu: Uranium(VI) adsorption to ferrihydrite: Application of a surface complexation model; Geochim. Cosmochim. Acta **58**, 5465-5478 (1994).

[7] J.A. Coston, C.C. Fuller, and J.A. Davis: Pb^{2+} and Zn^{2+} adsorption by a natural aluminium- and iron-bearing surface coating on an aquifer sand; Geochim. Cosmochim. Acta **59**, 3535–3547 (1995).

[8] M. Kohler, B.D. Honeyman, and J.O. Leckie: Neptunium(V) sorption on hematite (α-Fe_2O_3) in aqueous suspension: The effect of CO_2; Radiochim. Acta **85**, 33-48 (1999).

[9] A. Richter, V. Brendler, and C. Nebelung: Effects of data scatter and inconsistency in sorption modeling; Geochim. Cosmochim. Acta Supplement, Vol. **69**, Issue 10, Supplement 1, Goldschmidt Conference Abstracts 2005, A421.

[10] J.-M. Combes, C.J. Chisholm-Brause, G.E. Brown Jr., G.A. Parks, S.D. Conradson, P.G. Eller, I.R. Triay, D.E. Hobart, and A. Meijer: EXAFS spectroscopic study of neptunium(V) sorption at the α-FeOOH/water interface; Environ. Sci. Technol. **26**, 376-382 (1992).

[11] T. Reich, H. Moll, T. Arnold, M.A. Denecke, C. Hennig, G. Geipel, G. Bernhard, H. Nitsche, P.G. Allen, J.J. Bucher, N.M. Edelstein, and D.K. Shuh: An EXAFS study of uranium(VI) sorption onto silica gel and ferrihydrite; J. Electron Spectrosc. Related Phenom. **96**, 237-243 (1998).

[12] J.R. Bargar, R. Reitmeyer, J.J. Lenhart, and J.A. Davis: Characterization of U(VI)-carbonato ternary complexes on hematite: EXAFS and electrophoretic mobility measurements; Geochim. Cosmochim. Acta **64,** 2737-2749 (2000).

[13] U. Schwertmann and R.M. Cornell, Wiley-VCH, Weinheim, 121-122 (2000).

[14] E.N. Maslen, V.A. Streltsov, N.R. Streltsova, and N. Ishizawa: Synchrotron x-ray study of the electron density in α-Fe_2O_3; Acta Cryst. B**50**, 435-441 (1994).

[15] H. Nitsche: Solubility studies of transuranium elements for nuclear waste disposal: Principles and overview, Presented at the Second International Conference on Chemistry and Migration

behavior of Actinides and Fission Products in the Geosphere; Monterey, California, USA, 6-10 Nov. LBL – 27173 (1989).

[16] B. Allard, H. Kipatsi, and J. O. Liljenzin: Expected species of uranium, neptunium and plutonium in neutral aqueous solutions; J. Inorg. Nucl. Chem. **42**, 1015-1027 (1980).

[17] I. Puigdomenech: Chemical equilibrium software (Make Equilibrium Diagrams Using Sophisticated Algorithms); Inorganic Chemistry Royal Institute of Technology (KTH), SE-100 44 Stockholm, Sweden.

[18] V. Neck, W. Runde, J.I. Kim, and B. Kanellakopulos: Solid-Liquid equilibrium reaction of neptunium(V) in carbonate solution at different ionic strenght; Radiochim. Acta **65**, 29-37 (1994).

[19] R.J. Lemire, J. Fuger, H. Nitsche, P. Potter, M.H. Rand, J. Rydberg, K. Spahiu, J.C. Sullivan, W.J. Ullman, P. Vitorge, and H. Wanner: Chemical Thermodynamics of Neptunium and Plutonium (edited by OECD Nuclear Energy Agency), Elsevier Science, North-Holland, Amsterdam (2001).

[20] W. Matz, N. Schell, G. Bernhard, F. Prokert, T. Reich, J. Claußner, W. Oehme, R. Schlenk, S. Dienel, H. Funke, F. Eichhorn, M. Betzl, D. Pröhl, U. Strauch, G. Hüttig, H. Krug, W. Neumann, V. Brendler, P. Reichel, M.A. Denecke, and H. Nitsche: ROBL - A CRG beamline for radiochemistry and materials research at the ESRF; J. Synchr. Rad. **6**, 1076-1085 (1999).

[21] G.N. George and I.J. Pickering: EXAFSPAK: A suite of computer programs for analysis of x-ray absorption spectra; Stanford Synchrotron Radiation Laboratory, Stanford, CA, USA (1995).

[22] S.I. Zabinsky, J.J. Rehr, A. Ankudinov, R.C. Albers, and M.J. Eller: Multiple scattering calculations of x-ray absorption spectra; Phys. Rev. B **52**, 2995-3009 (1995).

[23] A.L. Ankudinov, C.E. Bouldin, J.J. Rehr, J. Sims, and H. Hung: Parallel calculation of electron multiple scattering using Lanczos algorithms; Phys. Rev. B **65** (10), 104107/1-11 (2002).

[24] M. Bacmann and E.F. Bertaut: Structure du nouveau compose UFeO4; Bull. Soc. fr. Min. Christ. 90, 57-58 (1969)

[25] B.K. Teo: EXAFS: Basic principles and data analysis; Springer-Verlag, Berlin (1986).

[26] T. Reich, G. Bernhard, G. Geipel, H. Funke, C. Hennig, A. Rossberg, W. Matz, N. Schell, and H. Nitsche: The Rossendorf Beamline ROBL - A dedicated experimental station for XAFS measurements of actinides and other radionuclides; Radiochim. Acta **88**, 633-637 (2000).

[27] D.L. Clark, S.D. Conradson, S.A. Ekberg, N.J. Hess, M.P. Neu, P.D. Palmer, W. Runde, and C.D. Tait: EXAFS studies of pentavalent neptunium carbonato complexes. Structural elucidation of the principal constituents of neptunium in groundwater environments; J. Am. Chem. Soc. **118**, 2089-2090 (1996).

[28] A. Manceau, L. Charlet, M.C. Boisset, B. Didier, and L. Spadini: Sorption and speciation of heavy metals on hydrous Fe and Mn oxides. From microscopic to macroscopic; Appl. Clay Sci. **7**, 201–223 (1992).

[29] C.H. Ho and N.H. Miller: Adsorption of uranly species from bicarbonate solution onto hematite particles; J. Colloid Interf. Sci. **110**, 165-171 (1986).

[30] A.J. Dent, J.D.F. Ramsay, and S.W. Swanton: An EXAFS study of uranyl ion in solution and sorbed onto silica and montmorillonite clay colloids; J. Colloid Interf. Sci. **150(1)**, 45-60 (1992).

[31] J.R. Bargar, R. Reitmeyer, and J.A. Davis: Spectroscopic confirmation of uranium(VI)-carbonato adsorption complexes on hematite; Environ. Sci. and Technol. **33(14)**, 2481–2484 (1999).

EXAFS STUDY OF NEPTUNIUM(V) SORPTION ONTO KAOLINITE

Samer Amayri, Tanja Reich and Tobias Reich
Institute of Nuclear Chemistry, Johannes Gutenberg-Universität Mainz, 55099 Mainz, Germany

Abstract

Neptunium is an important element from the safety point of view due to its radiotoxic Np-237 nuclide with a half-life of $2.1 \cdot 10^6$ years. Clay formations are considered as a possible geological barrier to prevent the release of actinides and fission products into the environment from nuclear waste stored in a repository. The risk assessment of future nuclear waste repositories requires knowledge on the migration behavior of neptunium in potential host rock formations such as clay. The aim of this study is to derive basic sorption data (dependency of the sorption isotherm on pH, metal ion concentration and ionic strength) as a complement to the direct spectroscopic speciation (EXAFS).

We performed EXAFS measurements on Np(V) sorption on kaolinite as a function of pH in the presence and absence of ambient CO_2. Seven samples in the pH range 8.0-10.5 with different amounts of Np(V) sorbed were prepared from a 1.1 mM Np(V)-237 stock solution. 160 mg kaolinite KGa-1b (Source Clays Repository) were suspended in 40 mL deionized water. The ionic strength was 0.1 M $NaClO_4$. The total neptunium concentration in each sample was $8 \cdot 10^{-6}$ mol/L. After a contact time of 72 hours, the solid and liquid phases were separated by centrifugation at 4025 g for 30 minutes. The neptunium uptake was determined by measuring the neptunium concentration in solution by liquid scintillation counting. The solid residues were loaded as a wet paste into EXAFS sample holders. The amount of neptunium sorbed in the EXAFS samples was in the range of 70-430 ppm.

The EXAFS results show that the neptunium co-ordination shells and bond distances of all samples prepared in air are consistent with the formation of a Np(V) carbonato species at the kaolinite surface. The obtained Np-O_{ax} and Np-O_{eq} distances agree well with the distances in $NpO_2(CO_3)_3^{5-}$ (aq.) [1]. The average Np-O_{eq} bond distance (2.45 Å) of samples, which were prepared under Ar atmosphere, is somewhat shorter than in the Np(V) aquo ion (2.49 Å [2]). This could indicate the existence of a Np(V) hydrolysis species at pH $\geq$ 9.0 at the kaolinite surface.

The authors acknowledge the ESRF for provision of synchrotron beam time and thank H. Funke, C. Hennig, A. Rossberg, and A. Scheinost from Forschungszentrum Rossendorf for assistance in using beamline BM20. This work was supported by the German Federal Ministry of Economics and Technology (grant No 02E9653).

[1] D.L. Clark, S.D. Conradson, S.A. Ekberg, N.J. Hess, M.P. Neu, P.D. Palmer, W. Runde, and C.D. Tait: J. Am. Chem. Soc. **118**, 2089-2090 (1996).
[2] T. Reich, G. Bernhard, G. Geipel, H. Funke, C. Hennig, A. Rossberg, W. Matz, N. Schell, and H. Nitsche: Radiochim. Acta **88**, 633-637 (2000).

APPLICATION OF X-RAY SINGLE CRYSTAL DIFFRACTOMETRY TO INVESTIGATION OF Np(V) COMPLEXES WITH N-DONOR LIGANDS

Grigory Andreev
Institute of Physical Chemistry of Russian Academy of Sciences, Moscow, Russia

Abstract

We present here some results of application of conventional X-ray single crystal diffractometry to the research on the interaction of Np(V) with N-donor ligands. Compounds that can coordinate to actinides through one or several nitrogen atoms are of a great variety and occur widely in the biosphere. For example, imidazole, pyridine and their derivatives are the building blocks of many biologically important molecules; triazines are known to occur in some aquatic plants. The presence of anthropogenic organic agents like amine-N-carboxylic acids in surface waters has the potential to remobilise metals from sediments and aquifers and to influence their bioavailability. The interaction of radionuclides with such ligands needs to be studied in detail to give fundamental understanding the conditions of the incorporation of long lived α-emitters (Np and Pu primarily) into the food chain. Another aspect of the same problem is the design of new chelating ligands for selective co-ordination of actinide ions as an alternative to the traditional sequestering agents. The problem of the separation of long-lived minor actinides and their transmutation also calls for design of new highly selective ligands for solvent extraction. Polydentate N-donor ligands are now considered to be very promising.

A detailed study of structural chemistry is crucial for understanding the relationship between the architecture of the ligands and their binding affinity for actinides. The X-ray single crystal diffractometry became conventional technique as applied to the investigation of actinides in spite of difficulties regarding safe handling of radionuclides. This technique provides unambiguous information about modes of the ligand co-ordination to the metal ion and geometrical parameters of complexes. Moreover, the employment of a synchrotron radiation shows considerable promise for determination of solid state structures as well as obtaining structural information on complexation in solution. The ligands discussed in this work are widely diversified: certain of them can only serve as monodentate (imidazole, acetonitrile and isothiocyanate), bidentate (bipyridine, phenanthroline), terdentate (terpyridine, TPTZ, nPr-BTP) or tetradentate (Et-BTBP), others being the polyfunctional ligands with different binding sites (N- and O-donor) may coordinate to the metal in various modes. In the latter case, the linking of the adjacent An co-ordination polyhedra with the formation of polymeric structures is possible. Although the formation of usual co-ordination polyhedra for actinide atoms is observed for complexes with N-donor ligands, the ligands architecture is the key factor in the control of the complexes topology. By this means, the difference in co-ordination modes reflects in geometrical parameters of the structures. We will present the data on geometrical parameters for Np complexes with different N-donor ligands and try to establish a link between these parameters and binding modes. This information is not only important for crystal chemistry, but can be also useful for the interpretation of data obtained by EXAFS analysis of actinide complexes in solutions.

Np RETENTION ONTO UO_{2+x} AND ITS ALTERATION PHASES DURING HYDROTHERMAL TREATMENT

Olga Batuk[1], Yuri Teterin[2], Anton Teterin[2], Stepan Kalmykov[1], and Elena Zakharova[3]
[1] Lomonosov Moscow State University, Moscow, Russia,
[2] Scientific Centre "Kurchatov Institute", Moscow, Russia
[3] Frumkin Institute of Physical Chemistry and Electrochemistry RAS, Moscow, Russia,

Abstract

Alteration of spent nuclear fuel (SNF) upon storage in deep geological repositories under oxidizing conditions will likely result in formation of secondary phases on UO_2 surface. This may influence the solubility of SNF and release of radionuclides to the environment. On the other hand precipitated phases may limit the leaching of other radionuclides and prevent SNF from further oxidation. The goal of this work was the study solubility, secondary phase formation and Np(V) retention on the surface of UO_{2+X} sample during hydrothermal treatment in simulated oxic groundwater.

The UO_2 sample was characterized by X-ray powder diffraction (XRD) and X-ray photoelectron spectroscopy (XPS) to determine bulk and surface phase composition that were UO_2 and $UO_{2.25}$ respectively. The hydrothermal experiments were performed at 25°C, 70°C and 150°C during 6 months in the presence of about $1 \cdot 10^{-5}$ M of Np(V). For room temperature experiments the retention of Np(V) by UO_2 sample was also studied as a function pH in batch mode. Solid phase and solution aliquots were taken periodically for various analyses: determination of neptunium and uranium concentrations in solutions, for XRD, XPS, SEM and TEM analyses of solid phases. Neptunium sorption was almost quantitative for all studied temperature conditions after one week of equilibration. Uranium solubility increased in time and reached the equilibrium values typical for U(VI) also in about one week. The progressive oxidation of the sample with formation of U(VI) alteration phases were detected by XPS, XRD and TEM for samples treated at 70°C and 150°C.

For Np sorption experiments that were done at room temperature the reduction of Np(V) to Np(IV) was observed at pH<4.5. This was possible either due to its interaction with the surface that had a shoichiometry close to UO_2 at low pH as determined by XPS or through the reduction by U(IV) present in solution. Upon the increase of pH the UO_2 surface became more oxidized and its stoichiometry became close to $UO_{2.25}$ as determined by XPS. At pH>4.5 neptunium was presenting in pentavalent form and was sorbed by the surface complexation mechanism.

THE EFFECT OF Fe(II)-Fe(II) CO-ORDINATION ON THE REDUCTION OF U(VI) AT A CARBOXYL SURFACE DETERMINED BY TITRATION AND XAFS

Maxim I. Boyanov[1, 3], Edward J. O'Loughlin[1], Eric E. Roden[2], Jeremy B. Fein[3], Kenneth M. Kemner[1]

[1] Biosciences Division, Argonne National Laboratory, Argonne, IL 60439, USA
[2] Department of Geology & Geophysics, University of Wisconsin-Madison, Madison, WI 53706, USA
[3] Department of Civil Engineering & Geological Sciences, University of Notre Dame, Notre Dame, IN 46556, USA

Abstract

The abiotic reduction of U(VI) to U(IV) by Fe(II) is currently studied as a strategy for uranium immobilisation in subsurface environments, where dissimilatory metal reducing bacteria produce significant amounts of Fe(II) during their anaerobic respiration. The U(VI)-Fe(II) redox reaction is kinetically inhibited in homogeneous solution. However, dramatically increased reduction rates are observed when an oxide surface is present. To understand the role of the surface in enhancing redox reactivity, we have performed Fe K-edge and U L-edge X-ray absorption fine-structure (XAFS) experiments on aqueous suspensions containing 1.0 mM Fe(II), 0.1 mM U(VI), and a non-conducting, carboxyl-functionalised colloid. Under conditions for which Fe EXAFS data indicated only monomeric Fe(II) present in the system, U XAFS data indicated only U(VI) species that were inner-sphere complexed to the surface carboxyl groups. No uranium reduction was observed over a 4 month period, despite the presence of sufficient adsorbed and solvated Fe(II) in the system. Under conditions for which Fe EXAFS data indicated Fe-Fe correlation in the colloid+Fe system, the U EXAFS data indicated complete reduction of U(VI) to U(IV) and the formation of uraninite nanoparticles in the colloid+Fe+U system. The Fe-U electron transfer was further confirmed by Fe XAFS, which indicated oxidation of the Fe species. Fe atoms were found coordinated around the reduced U(IV) atoms at 3.56 Å. These results and the structure of the reduced U(IV) product will be discussed in the context of a proposed U(VI)-Fe(II) redox mechanism that may explain the enhanced redox reactivity observed in the presence of an oxide surface.

XAFS INVESTIGATION OF HIGH LEVEL WASTE GLASSES

Boris Brendebach, Melissa A. Denecke, Kathy Dardenne, Jörg Rothe, Siegfried Weisenburger, Günther Roth, Berthold Luckscheiter, Marija Nesovic, Stefan Mangold[1]
Forschungszentrum Karlsruhe (FZK), Institut für Nukleare Entsorgung, P.O. Box 3640, D-76021 Karlsruhe, Germany
[1]Forschungszentrum Karlsruhe, Institut für Synchrotronstrahlung, P.O. Box 3640, D-76021 Karlsruhe, Germany

Abstract

X-ray absorption fine structure (XAFS) investigations of borosilicate glasses used for the immobilization of high level liquid waste from spent fuel reprocessing of nuclear power plants are reported. X-ray absorption near edge structure (XANES) measurements of glasses, which are developed to maximise the incorporation of sulfur, show that the sulfur is present as SO_4^{2-}, i.e., sulfate, regardless whether the glass melt is stirred or not during production. Fingerprinting suggests that the sulfate is predominantly bound to sodium in the waste glass. In addition, the leaching behaviour of uranium containing borosilicate glasses is investigated. The glass samples were kept for two years in a solution containing opalinus clay at temperatures of 50°C and 90°C, respectively. The bulk structure is modelled by two oxygen atoms at 1.77 Å and four oxygen atoms at 3.6 Å around U, i.e., a uranyl type structure. Surface selective gracing incidence X-ray absorption fine structure (GI-XAFS) measurements show an increase of the oxygen co-ordination number at the longer distance. Agglomeration of uranium atoms in the corrosion layer is ruled out as no uranium-uranium interactions are visible in the spectra. An increase in the most pronounced XANES feature corroborates the finding that additional water molecules are bound to U in the corrosion layers.

Introduction

Borosilicate glasses are widely used for the immobilisation of high level liquid waste originating from spent fuel reprocessing of nuclear power plants. They posses remarkable chemical, especially radio-chemical and thermal stability and the possibility for incorporating a variety of chemical elements in different concentrations into the glass structure during melting [e.g., 1-3]. The Institut für Nukleare Entsorgung (INE) at the Forschungszentrum Karslruhe (FZK) has developed a vitrification technology to convert high level liquid wastes to glass by a single stage process [1]. X-ray absorption fine structure (XAFS) investigations can serve as an analytical technique to characterise the glass structure. Two examples are discussed within this report: a study of the sulfur uptake of a high level waste glass and an investigation of uranium precipitation onto the corrosion layer of a high level waste glass during leaching.

Glasses used to vitrify high level liquid waste from spent fuel from reprocessing may contain up to 50 different chemical elements, which are present in different chemical forms. By varying the glass characteristics, i.e., composition or basicity, designing a glass for a specific waste is feasible. High level liquid waste from the 1960s to 1970s often contains a significant amount of sulfur, which tends to undergo phase separation when incorporated into borosilicate glasses. This can lead to undesirable glass characteristics including concentration of Cs and Sr into the separated phase and higher water solubility of this phase. Knowledge of the chemical form of the sulfur in the glass is needed in order to adjust the glass composition to completely dissolve the sulfur into the glass structure. X-ray absorption near edge structure (XANES) is widely used as a tool to reveal the formal oxidation state of sulfur in a variety of materials. Thus information can be used to improve and optimise the glass composition [e.g., 4-10]. The onset of the excitation of 1s inner shell sulfur electrons serves as a fingerprint for the sulfur species present. The energy position of the main XANES feature, the so-called white line (WL), is observed to shift over 10 eV with increasing formal oxidation state from -2 to +6 (Figure 1).

Figure 1: Comparison of the energy position of the near edge spectra of some sulfur compounds. The white line position shifts to higher energies with increasing formal oxidation state beginning from –2 (AsFeS, FeS) to +6 (the inorganic sulfates).

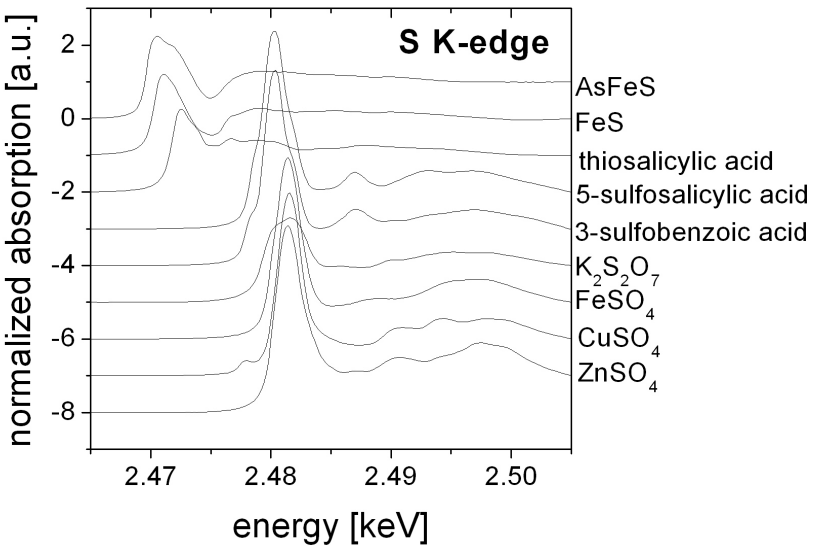

Investigating the leaching behaviour of high level waste glasses is essential to demonstrate their safe, long term storage capabilities. Actinides can precipitate onto corrosion layers, which form on borosilicate glasses when in contact with aqueous alkaline solutions at elevated temperatures. Such solutions simulate possible repository conditions. Surface sensitive grazing incidence (GI) XAFS investigations of the local structure around uranium atoms in the corrosion layer of two different glasses are presented. They are compared with the bulk structure and the structure within a freshly prepared glass. GI-XAFS is thus well suited to characterise surface layers, as the penetration depth of the X-ray photons is limited to a few nm [11]. The structural information from GI-XAFS analysis describes the corrosion layer of the leached glass. This information is compared with the bulk structure obtained from analysis of standard fluorescence mode spectra.

Experimental

We investigate two sulfur containing glasses produced in the glass lab at 1050°C with or without stirring. Pieces of the glasses are ground and the powders fixed onto self-adhesive Kapton®-tape. Crystalline Na_2SO_4, K_2SO_4, and $CaSO_4*2H_2O$ powders are measured as reference compounds. XANES spectra are recorded at the XAS-Beamline of the Ångströmquelle Karlsruhe (ANKA) [12] with the storage ring operating at 2.5 GeV and electron currents ranging from 200-100 mA. A fixed exit double crystal monochromator (DCM) equipped with a pair of Si(111)-crystals, 2d=6.271 Å, and a pair of Si(311)-crystals, 2d=3.275 Å, is available. In case of sulfur K-edge measurements the Si(111)-crystals are used to produce a monochromatic photon beam. Energy calibration is done with respect to the WL of a $ZnSO_4$ powder sample, defined as 2.48144 keV. The spectra are recorded at a step width of 1 eV in an energy interval from 2.455 to 2.465 keV, thereafter a step width of 0.2 eV until 2.52 keV. Ionization chambers are used filled with N_2 at 80 mbar pressure. The reference samples are measured in transmission mode. Glass sample spectra are recorded in fluorescence mode using a 5-element Ge-detector (Canberra). Five spectra are averaged to increase the signal-to-noise ratio. Data treatment is done using standard techniques described elsewhere [13].

Figure 2: Schematic drawing of the grazing incidence setup [19].

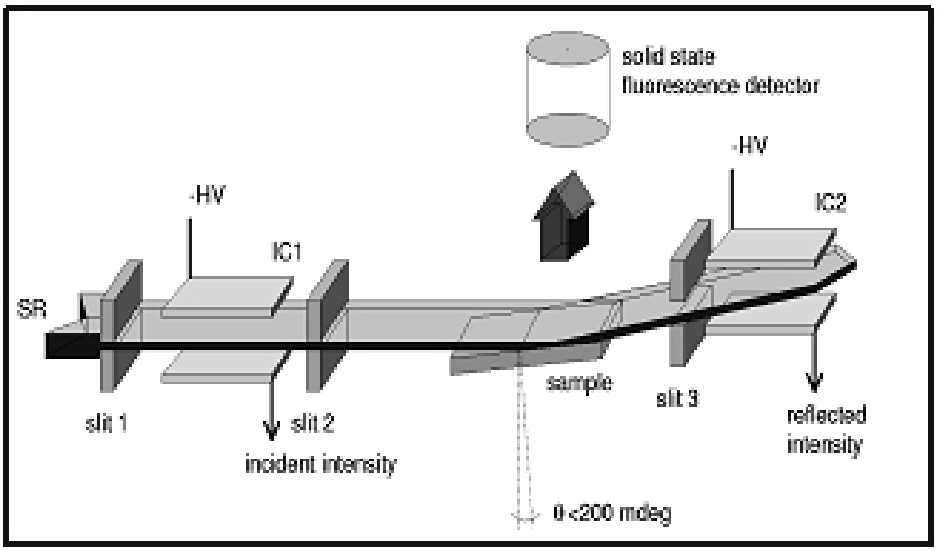

Surface specific GI-XAFS characterisation of freshly prepared U-bearing glass and two glasses after two years of leaching in a solution containing opalinus clay at either 50°C or 90°C is performed at the INE-Beamline for Actinide Research [14] at ANKA. The leached samples are designated GI 50°

and GI 90°, respectively. A Lemonnier-type DCM [15], designed and built at the Physikalisches Institut, Bonn University, equipped with a set of Ge(422) crystals (2d = 2.304 Å) is used. Energy calibration is performed with respect to the position of the first inflection point of an yttrium foil K-edge absorption spectrum, which is set to 17.038 keV [16]. The DCM-crystals are detuned from parallel alignment to 70% to reduce the amount of higher harmonics using a MOSTAB driven piezo-actuator. A schematic overview of the experimental setup is shown in Figure 2. The incident and reflected beam intensities are measured by argon-filled ionization chambers. Auxiliary slits with a vertical width of 100 μm are positioned before and after the first ionization chamber. This setup produces a beam with a small angular divergence. The fluorescence photons are recorded with a five pixel Ge fluorescence detector (Canberra LEGe) mounted above the sample surface. The samples were positioned by use of a goniometer cradle (HUBER Diffraktionstechnik GmbH) with a step size of 0.0001° and a z-stage with a step size of 40 nm.

GI-XAFS data are recorded with an incidence angle of approximately 100 mdeg. Seven spectra are averaged for each sample to improve the signal-to-noise ratio. A freshly prepared glass (bulk fresh) and the sample leached at 90°C (bulk leached) are also measured three times in standard fluorescence mode and the results averaged. The spectra are analyzed using standard techniques applying the UWXAFS suites of programs [17]. Single scattering backscattering amplitude and phase functions are calculated using the FEFF8.2 program [18]. The amplitude reduction factor S_0^2 is held fixed at 1.

Sulfur speciation in high level waste borosilicate glasses

S K-XANES measurements of the lab-scale glass samples and the reference compounds are presented in Figure 3. The spectra of the glass samples show no significant differences, whether stirred during the production or not. The energy position of the WL in all five spectra is located at 2.4815 keV, a value typical for sulfate species. As no contributions are visible at lower energies, this finding clarifies that only sulfate species are present in the glasses, which have been manufactured in the lab under oxidizing conditions.

Figure 3: Comparison of the near edge spectra of the two glasses and Na_2SO_4, K_2SO_4, and $CaSO_4$*$2H_2O$ powder samples

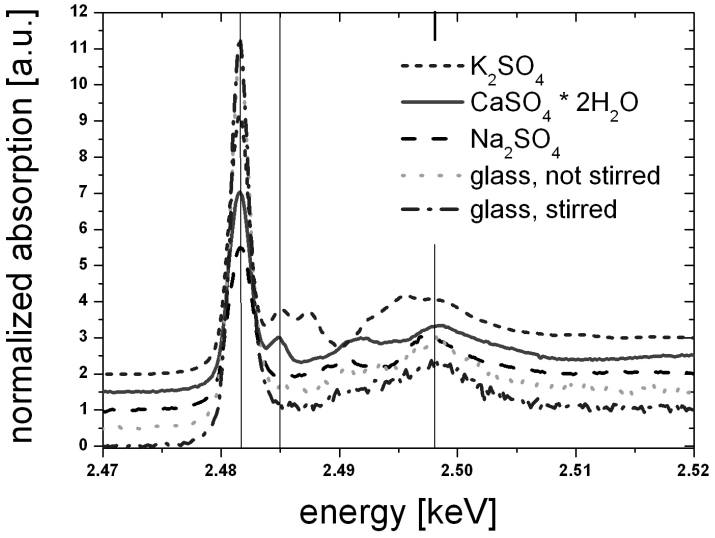

The broad resonance at approximately 2.498 keV in all spectra is due to multiple scattering of the outgoing electron wave at the first oxygen shell around the sulfur ions. Small deviations in the peak position result from slightly different sulfur-oxygen distances and/or distortion of the sulfur-oxygen tetrahedra. In case of Na_2SO_4 all four oxygen atoms are bound to the central sulfur atom at a distance of 1.47181 Å [19]; the sulfate tetrahedra in K_2SO_4 consist of one short bound oxygen atom at 1.459 Å and three further distant oxygen atoms at about 1.472 Å [20]; in $CaSO_4*2H_2O$ two oxygen atoms are bound at a distance of 1.47131 Å and the remaining two atoms at 1.47427 Å [21].

Remarkable in case of the calcium reference is the single pronounced feature just above the WL at approximately 2.485 keV. It is seen neither in the other reference spectra nor in the glasses. Therefore, we rule out calcium co-ordination around the sulfate species within the glasses. The same argument holds when considering the spectrum of K_2SO_4. There a double feature is present, whereas the glass spectra show a local minimum in this energy region. An EXAFS-analysis might corroborate the hypothesis that the sulfur within the glasses is bound as sodium sulfate.

Leaching behavior of uranium containing high level waste glasses

We employ XAFS as a non-destructive, element specific technique to characterise the electronic and geometric structure of U-bearing borosilicate glasses. As it requires no medium or long range order, XAFS is widely used to elucidate the structure of disordered materials, e.g., solutions or glasses [22-24]. The U L3-spectra of the leached samples are recorded in GI geometry.

The k^3-weighted U L3-GI-XAFS are presented in Figure 4; the corresponding Fourier transforms (FT), k-range 3.1-9.85 $Å^{-1}$, and back transforms of the first co-ordination shell contributions are depicted in Figure 5. Structural parameters, co-ordination numbers (N), distances (R), and Debye-Waller-factors (σ), are obtained by fitting the Fourier transformed χ(k)-functions shown in Figure 5 in the range from 0.8 to 2.1 Å. Least-square fit results are summarised in Table 1 using a model of two O co-ordination shells. The FT spectra exhibit no contributions at R-Δ values beyond the U-O peak, indicating that neither U agglomerates are present in the bulk glass nor do secondary U-phases form on the surface of the glass after leaching.

Figure 4: Measured U L3 k^3-weighted χ(k)-functions.

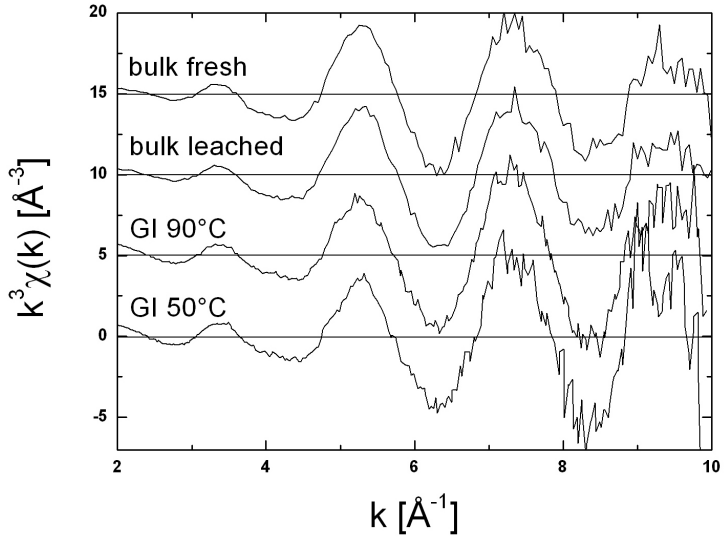

Figure 5: Fourier transforms (left) of the data shown in Figure 4 and back transformed χ(k)-functions of the first shell signal of each investigated sample (right). Experimental functions are shown as lines and fit curved as symbols

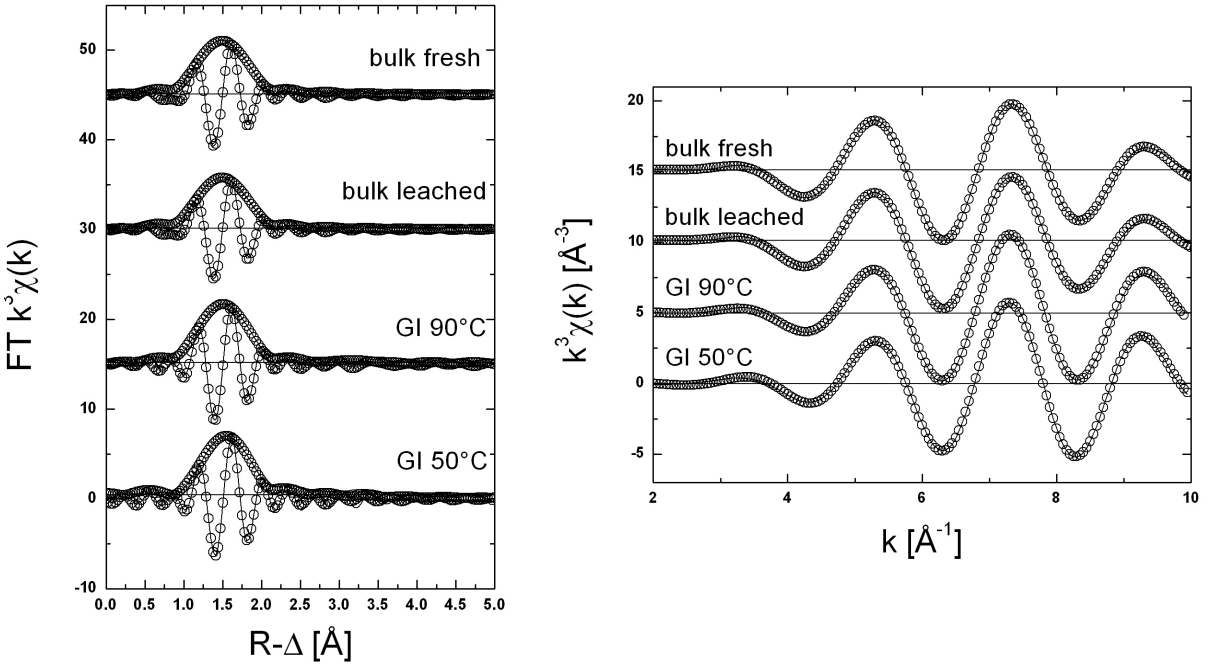

This is in contrast to previous GI-XAFS investigations of the leaching behavior of other borosilicate glasses [25], where the agglomeration of uranium oxides was reported. Fits to the back transformed χ(k) of the first shell contributions are also shown in Figure 5 and lead to identical structural parameters. Results for the bulk samples are comparable to known uranyl containing compound structures [26] with two short axial O distances (O1) and four further distant O atoms bound to U(VI) in the equatorial plane (O2). The U co-ordination structure in the glass bulk is not affected by leaching, as both bulk fresh and the bulk leached results are the same. Analysis of the GI-XAFS shows that U retains two shorter O1 distances within the corrosion layers. The second co-ordination shell changes in the corrosion layer compared to the bulk. The number of O2 atoms increases from approximately four in the bulk to five in the corrosion layer. This increase we interpret as indication that U is coordinated with additional water molecules within this layer. This is corroborated by XANES spectra (Figure 6). The WL of samples GI 50° and GI 90° is more intense than the bulk. Similar trends have been reported for Hf(IV) sorbed onto mineral surfaces [11]. Therein, the increase in WL intensity when changing from an embedded Hf(IV) species in a condensed material to a surface sorption onto an oxidized silicon wafer is explained by a decrease of condensation. Both the decrease of condensation inferred from the XANES and the O2 number increase observed in the EXAFS of U in the glass corrosion layer can be explained by additional coordinated water molecules within this layer [27].

Figure 6: U L3 XANES spectra of the four samples.

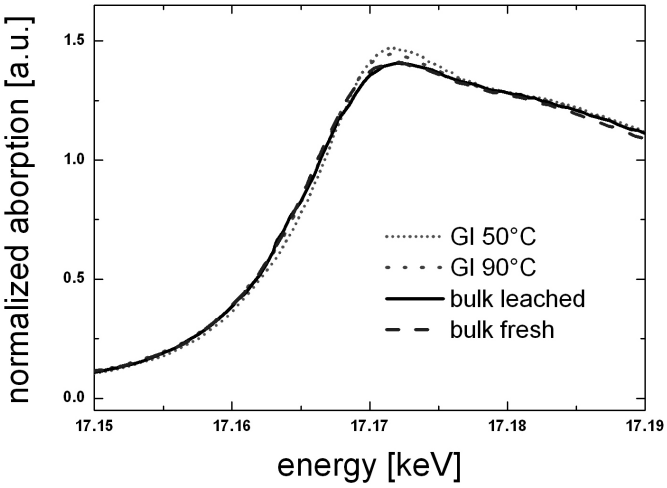

Table 1: Structural parameters from first shell fits using a two oxygen shell (O1 and O2) model. ΔE_0 = relative shift in ionization energy, used as a global parameter for both O distances. R-factor (overall goodness of fit) = χ^2 divided by the degrees of freedom. A value of, e.g., 0.003 means that theory and experimental data agree within ±0.3%.

Parameter	Bulk fresh	Bulk leached	GI 90°C	GI 50°C
N O1	1.8(3)	1.8(3)	2.0(3)	2.1(2)
R O1 (Å)	1.77(2)	1.77(2)	1.79(1)	1.81(1)
σ^2 O1 (Å^2)	0.003(1)	0.003(1)	0.003(1)	0.003(1)
N O2	3.9(6)	3.6(6)	4.7(5)	5.2(3)
R O2 (Å)	2.21(3)	2.21(3)	2.18(2)	2.18(1)
σ^2 O2 (Å^2)	0.003(2)	0.003(2)	0.003(2)	0.003(2)
ΔE_0 (eV)	-4.4(6.4)	-3.1(7.1)	-8.7(5.4)	-8.5(3.1)
R-factor	0.0029	0.0030	0.0034	0.0016

Conclusions

Sulfur speciation investigations of borosilicate glasses developed for the immobilization of high level liquid waste originating from spent fuel reprocessing from nuclear power plants show that sulfur is present as SO_4^{2-}, i.e., sulfate, regardless whether the glass melt is stirred or not during production. The sulfur is predominantly bound to sodium. This result can aid in modifying the glass composition in order to maximize the sulfur incorporation capacity and to inhibit phase separation.

Surface specific GI-XAFS measurements of uranium containing borosilicate glasses leached for two years in a solution containing opalinus clay show a slight structural change of the uranium sites in the corrosion layer, compared to the bulk glass. Two short axial oxygen neighbors remain unchanged but the number of oxygen neighbours bound to the equatorial plane increases. This finding is explained by additional co-ordination of U by water molecules. No agglomeration of uranium atoms is

detected in the samples under glass preparation and leaching conditions used, as no signs of uranium-uranium interactions are visible in the data.

Acknowledgment

We acknowledge the ANKA Ångströmquelle Karlsruhe for the provision of beamtime.

References

[1] W. Grünewald, G. Roth, W. Tobie, S. Weisenburger, *FZK Nachrichten* **36**, 91 (2004).

[2] M. Yoshioka, H. Igarashi, Glass as a waste form, National Academic Press, Washington D.C. (1996).

[3] B. Luckscheiter, M. Nesovic, *Waste Management* **16**, 571 (1996).

[4] N.E. Pingitore Jr., G. Meitzner, K.M. Love, *Geochim. Cosmochim. Acta* **59**, 2477 (1995).

[5] A. Vairavamurthy, *Spectrochim. Acta A* **54**, 2009 (1998).

[6] G. Sarret, J. Connan, M. Kasrai, G.M. Bancroft, A. Charrié-Duhaut, S. Lemoine, P. Adam, P. Albrecht, L. Eybert-Bérard, *Geochim. Cosmochim. Acta* **63**, 3767 (1999).

[7] H. Modrow, Dissertation, University of Bonn, BONN-IR-99-11 (1999).

[8] N. Okude, M. Nagoshi, H. Noro, Y. Baba, H. Yamamoto, T.A. Sasaki, *J. Electron Spectrosc. Relat. Phenom.* **101-103**, 607 (1999).

[9] F.E. Huggins, G.P. Huffman, J.D. Robertson, *J. Hazard. Mater.* **75**, 1 (2000).

[10] D.A. McKeown, I.S. Muller, H. Gan, I.L. Pegg, W.C. Stolte, *J. Non-Cryst. Solids* **333**, 74 (2004).

[11] M.A. Denecke, J. Rothe, K. Dardenne, P. Lindqvist-Reis, *Phys. Chem. Chem. Phys.* **5**, 939 (2003).

[12] J.D. Grunwaldt, S. Nannemann, J. Göttlicher, S. Mangold, M.A. Denecke, A. Baiker, *Phys. Scr.* **T115**, 2005 (2005).

[13] D.C. Koningsberger, R. Prins, X-ray Absorption. Principles, Applications, Techniques of EXAFS, SEXAFS, and XANES, Wiley, New York (1988).

[14] M.A. Denecke, J. Rothe, K. Dardenne, H. Blank, J. Hormes, *Phys. Scr.* **T115**, 1001 (2005).

[15] M. Lemonnier, O. Collet, C. Depautex, J.M. Esteva, D. Raoux, *Nucl. Instr. Meth. A* **152**, 109 (1978).

[16] J.A. Bearden, A.F. Burr, *Rev. Mod. Phys.* **39**, 125 (1967).

[17] E.A. Stern, M. Newville, B. Ravel, Y. Yacoby, D. Haskel, *Physica B* **208/209**, 117 (1995).

[18] A. Ankudinov, B. Ravel, J.J. Rehr, S.D. Conradson, *Phys. Rev. B* **58**, 7565 (1998).

[19] S.E. Rasmussen, J.-E. Jørgensen, B. Lundtoft, *J. Appl. Crystallogr.* **29**, 42 (1996).

[20] J.A. McGinnety, *Acta Cryst. B* **28**, 2845 (1972).

[21] P.E. Schofield, C.C. Wilson, K.S. Knight, I.C. Stretton, *Z. Kristallogr.* **215**, 707 (2000).

[22] H.-R. Cho, C. Walther, J. Rothe, V. Neck, M.A. Denecke, K. Dardenne, T. Fanghänel, *Anal. Bioanal. Chem.* **383**, 28 (2005).

[23] B. Brendebach, F. Reinauer, N. Zotov, M. Funke, R. Glaum, J. Hormes, H. Modrow, *J. Non-Cryst. Solids* **351**, 1072 (2005).

[24] B. Brendebach, R. Glaum, M. Funke, F. Reinauer, J. Hormes, H. Modrow, *Z. Naturforsch.* **60a**, 449 (2005).

[25] G.N. Greaves, N.T. Barrett, G.M. Antonini, F.R. Thornley, B.T.M. Willis, A. Steel, *J. Am. Ceramic Soc.* **111**, 4313 (1989).

[26] C. DenAuwer, E. Simoni, S.D. Conradson, C. Madic, *Eur. J. Inorg. Chem.*, 3843 (2003).

[27] R.W. Douglas, T.M.M. El-Shamy, *J. Am. Ceramic Soc.* **50**, 1 (1967).

EXAFS INVESTIGATION OF THE $NaLn(MoO_4)_2 – Ca_2(MoO_4)_2$ SOLID SOLUTION SERIES LOCAL STRUCTURE

K. Dardenne, D. Bosbach, M.A. Denecke, B. Brendebach
Forschungszentrum Karlsruhe, Institut für Nukleare Entsorgung, P.O. Box 3640, D-76021 Karlsruhe, Germany

Abstract

Under conditions typical for a deep geological nuclear waste repository, high level waste (HLW) borosilicate glasses may dissolve/corrode upon contact with ground water over geological time scales. Secondary alteration phases can form during dissolution/corrosion of the waste matrix once their solubility limit has been reached. Radionuclides, which have been released from the waste matrix, may co-precipitate with these secondary phases and form thermodynamically stable solid solutions. Powellite ($CaMoO_4$) is one of the secondary phases identified in static batch-type corrosion experiments with HLW glass. The powellite structure exhibits a significant compositional flexibility, which accommodates a wide range of substitutions, including coupled substitutions of Ca^{2+} with monovalent and trivalent cations. Trivalent actinide and lanthanide containing powellite-like molybdate compounds have been synthesized (at high temperature T > 1 000°C) and structurally characterized with powder XRD. Under these conditions a complete solid solution series between $Ca_2Mo_2O_8$ and $NaAn(III)/Ln(III)Mo_2O_8$ seems likely, with a random distribution of the monovalent and trivalent cations. In order to obtain information on the local ordering in these phases around the La(III) and Eu(III) as substituting lanthanide cations, we investigate a substitution series (1%, 10%, 50%, and 100% Ca replacement) with EXAFS at the La/Eu L3 edge at varying temperature. The results show that the La-powellite series has a much more disordered structure than the Eu-powellite series. The largest structural variation with the substitution ratio is observed for the Eu series, where the static disorder reaches a maximum for the fully substituted powellite $NaEuMoO_4$.

Introduction

Under conditions typical for a deep geological nuclear waste repository, high level waste (HLW) borosilicate glasses may dissolve/corrode upon contact with ground water over geological time scales. Secondary alteration phases are formed during dissolution/corrosion of the waste matrix once their solubility limit has been reached. Radionuclides, which have been released from the waste matrix may co-precipitate with these secondary phases and form thermodynamically stable solid solutions [1-4]. Powellite ($CaMoO_4$) is one of the secondary phases, which have been identified in static batch-type corrosion experiments with HLW glass (Figure 1). In nature, powellite occurs as an alteration product of molybdenite (MoS_2) under oxidising conditions. Its structure has the scheelite structure type [5] and exhibits a significant compositional flexibility, which accommodates a wide range of substitutions. Coupled substitutions of Ca^{2+} with monovalent and trivalent cations can occur. The mono- and trivalent cations replace Ca^{2+} in the crystal lattice, being coordinated by eight oxygen atoms belonging to eight individual MoO_4^{2-} tetrahedra. Trivalent actinide and lanthanide containing molybdate compounds have been synthesised at high temperature T > 1000°C and structurally characterised [6-8]. A complete solid solution series between $CaMoO_4$ and $(Na_{0.5}, An(III)/Ln(III)_{0.5})MoO_4$ seems likely, with a random distribution of the monovalent and trivalent cations [9]. Formation of such a solid solution system represents a significant retention mechanism for trivalent actinides and a sound understanding could improve geochemical source term modelling for near field conditions. We cannot, however, a priori exclude cation or defect ordering effects. Molecular modelling calculations indicate short range ordering phenomena for the intermediate composition [7]. In order to characterise the local order around substituting lanthanide cations (La or Eu) in these phases, we investigate a substitution series (1%, 10%, 50%, and 100% Ca replacement) with EXAFS at the La/Eu L3 edge. EXAFS spectra are recorded at variable temperature (15K, 70K, 180K, 290K=RT), in order to discriminate between static and thermal disorder.

Experimental method

EXAFS

La/Eu L3-XAFS measurements are performed at the ANKA-XAS Beamline at ANKA. The data are recorded in fluorescence detection mode for 1% Ca substituted samples or transmission mode for the remaining samples. N_2-filled ionization chambers are used at ambient pressure for Eu and at 330mbar in the first chamber and 680mbar in the second ionization chamber for La L3 measurements. Spectra are energy calibrated to the first inflection point in the XANES of either a V or Fe foil (5.465keV and 7.112 keV, respectively) recorded simultaneously. For fluorescence measurement, we use a Canberra LEGe 5-element solid state detector. An Oxford He-Cryostat is used for low temperature measurements (down to 15K). Si<111> crystals are used in the double crystal monochromator, operating in fixed-exit mode and incident intensity held constant by means of a piezo-driven feedback system to the second crystal. The parallel alignment of the crystal faces is detuned to ~65% of the maximum beam intensity to suppress contamination of the incident photons with higher order reflections from the monochromator crystals. The IFEFFIT [10] software is used to extract the $\chi(k)$ from the absorption spectra and FEFFIT [11] is used to perform the fit to the data. Theoretical back-scattering amplitude and phase functions for fitting the experimental data are modeled with the multiple scattering code FEFF8 [12] using the structural data reported for the powellite [5] (Figure 1 and Table 1). For the lowest La/Eu concentration of the Eu/La substituted powellite samples, no self-absorption occurs. The XANES (1 and 10%) and EXAFS (10%) spectra are identical for data recorded in fluorescence and transmission mode.

Figure 1: Perspective view of the powellite unit cell. Mo atoms are in tetrahedrons surrounding the Ca (La/Eu/Na) 8 fold coordinated polyhedron.

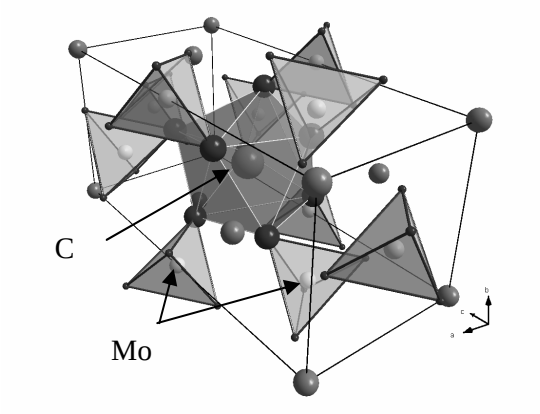

Table 1: Distances between Ca central atom and the next neighbours

Cation	N	R[Å]
O	4	2.432
O	**4 / 8**	**2.447**
Mo	**4**	**3.677**
O	**4**	**3.757**
Ca	4	3.851
Mo	4	3.851
O	4	4.377
O	4	4.385
O	**4 / 12**	**4.401**
O	4	4.954
O	4	4.982

Results and discussion

Powellite has the scheelite structure type (space group: 41/a, no. 88) [5]. A perspective view of the unit cell is depicted in Figure 1 and a typical SEM (scanning electron microscopy) image of the crystals in Figure 2. The distances up to 5Å between Ca and its next neighbouring atoms calculated from XRD data are listed in Table 1. The structural data used are taken from the ISCD database (#60553). The co-ordination shells written in bold are used for fits to the EXAFS data. The co-ordination numbers (N) are fixed to the expected values except for the first O co-ordination shell, where N is varied. S_0^2 is set to 1. Interatomic distances (R), Debye-Waller factor (σ^2) and relative shifts in ionization energy (ΔE_0) are varied. N, R, ΔE_0 are correlated to the same value for both temperatures. σ^2 is independently varied for both temperatures of measurement.

Figure 2: SEM picture of powellite crystals

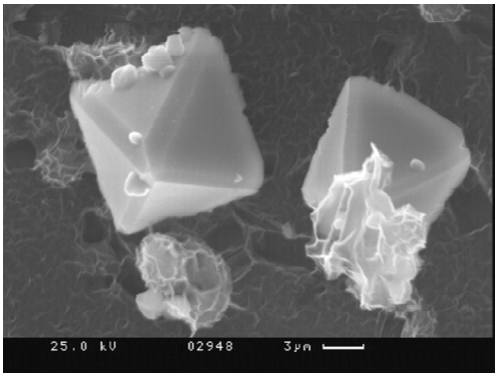

Figure 3 shows the Fourier transform (FT) of the Eu L3 EXAFS for the Eu(III) substituted samples at room temperature (RT~290K) and at 15K. For this Eu-substituted powellite series we observe an Eu concentration dependency of the FT for both temperatures; both the shape and intensity of the FT peaks changes. The FT peak height of the first shell decreases with increasing Eu concentration. This suggests that the static local disorder increases with an increasing amount of Eu substitution. This is confirmed by the EXAFS fit results (see below). The σ^2 of the first shell increases with increasing added Eu(III), whereas the O co-ordination number remains nearly constant at about 8 (Table 2).

Figure 3: FTs of the Eu-substituted powellite at RT and 15K

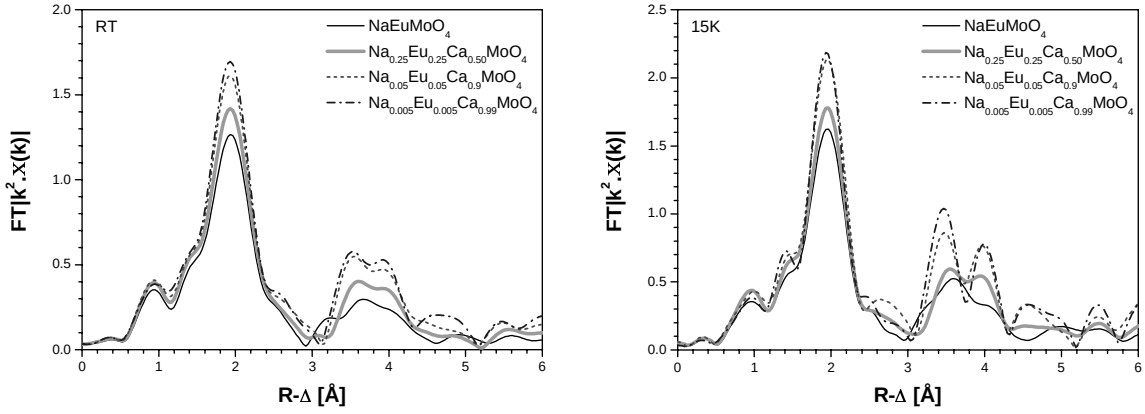

The Eu L3 EXAFS and results of the fits to the data are shown in Figure 4. The structural parameters from the fits are listed in Table 2. Fits are performed in R-space in the range 1.2 - 4.3Å. The k-range used is 2.5 - 11.35 $Å^{-1}$. The interatomic distances obtained are compatible with but somewhat different than the XRD structural model (Table 1). The Eu-O distance is ~0.03Å shorter than the Ca-O distance. This is what one would expect based on the difference in ionic radii (1.12 Å for Ca^{2+}, 1.06 Å for Eu^{3+} in 8-fold co-ordination [13]). The Eu next neighbour shells are shifted 0.01Å to 0.05Å to longer distances. Fitting the Eu data yields good results using a three ($NaEuMoO_4$) or four shell model. Only the $Na_{0.05}Eu_{0.05}Ca_{0.90}MoO_4$ sample requires inclusion of a fifth shell at low

temperature, 15K. We have seen that the static disorder decreases with the Eu concentration. The spectra of $NaEuMoO_4$, having the highest disorder, is perfectly reproduced using only three shells. There is no special local cation ordering for the intermediate composition $Na_{0.25}Eu_{0.25}Ca_{0.50}MoO_4$.

Figure 4: k^2-weighted Eu L3 edge EXAFS (Fourier filtered in the fit window range) and fit results; below, their corresponding FT spectra. Fits are drawn as symbols and data as lines.

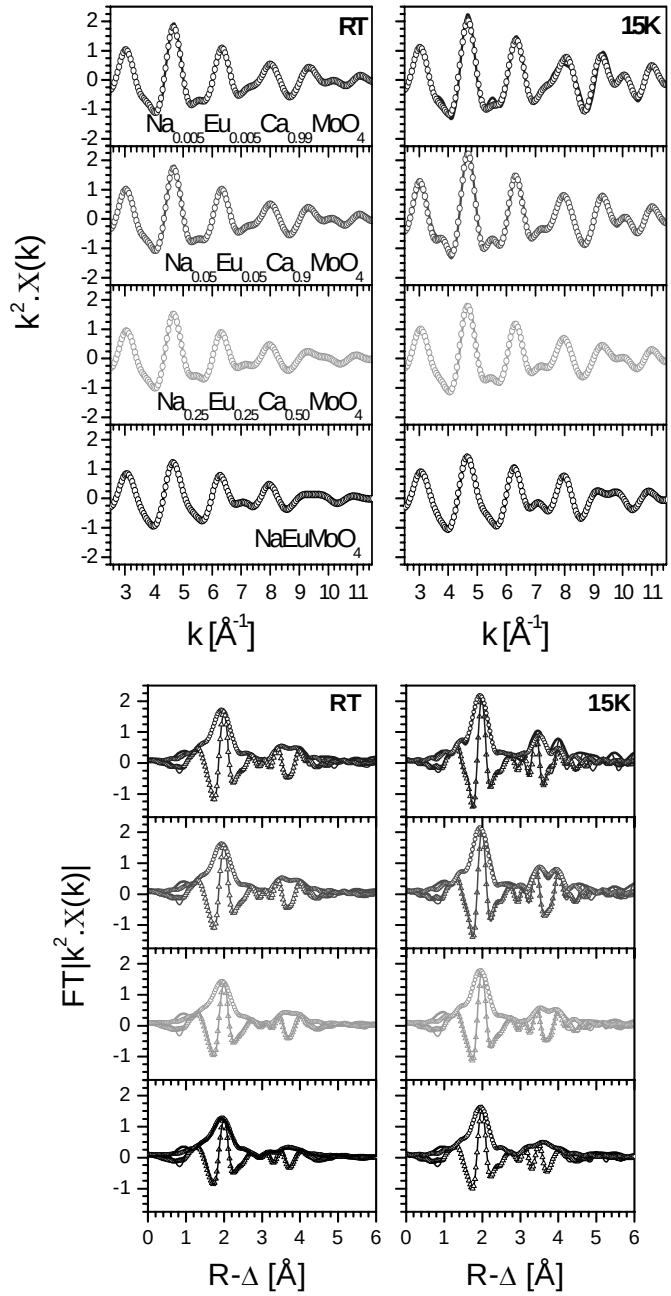

Table 2: Structural parameters of the fit to the Eu L3 edge EXAFS.

Sample	Neighbour	N	R [Å]	ΔE0 [eV]	σ^2 [10^{-3} Å^2]
$NaEuMoO_4$	O	8.0	2.41	2.55	7.2 / *4.0*
	Mo	4.0*	3.73	1.32	7.8 / *2.9*
	Mo	4.0*	3.89	1.32	8.6 / *4.1*
$Na_{0.25}Eu_{0.25}Ca_{0.50}MoO_4$	O	8.0	2.41	2.43	7.0 / *3.9*
	Mo	4.0*	3.75	4.11	5.6 / *1.3*
	O	4.0*	3.82	2.43	7.8 / *0.3*
	Mo	4.0*	3.92	4.11	6.3 / *1.5*
$Na_{0.05}Eu_{0.05}Ca_{0.90}MoO_4$	O	7.4	2.41	2.06	5.8 / *2.3*
	Mo	4.0*	3.72	2.72	2.7 / *0.1**
	O	4.0*	3.77	2.06	2.8 / *0.1**
	Mo	4.0*	3.88	2.72	3.4 / *1.5*
	O	12.0*	4.45	2.06	---- / *12.2*
$Na_{0.005}Eu_{0.005}Ca_{0.99}MoO_4$	O	8.0	2.41	1.76	5.2 / *2.3*
	Mo	4.0*	3.72	2.59	2.3 / *0.1**
	O	4.0*	3.77	1.76	0.2 / *0.1**
	Mo	4.0*	3.88	2.59	2.8 / *2.8*

*fixed or reached the limit set. σ^2 for 15K is given in italics.

Figure 5 shows FTs of the La-substituted powellite samples at RT and at 15K. In contrast to the Eu-substituted powellite series we do not observe a large La concentration dependency of the FT at RT. All FTs have the same profile, the intensity of the 1% substituted powellite is only slightly higher. At 15K, we observe a variation of the FT peak intensity with the La substitution but no change in the shape of the FT. The static local disorder reaches a minimum for the 10% substituted sample and attains maximum values for the end-member of the solid solution series. These qualitative observations are confirmed by the EXAFS fit results. The σ^2 of the first shell increases until the end-member is reached, where it again decreases (Table 3).

Figure 5: FTs of the La L3 EXAFS for the La-substituted powellite at RT and 15K.

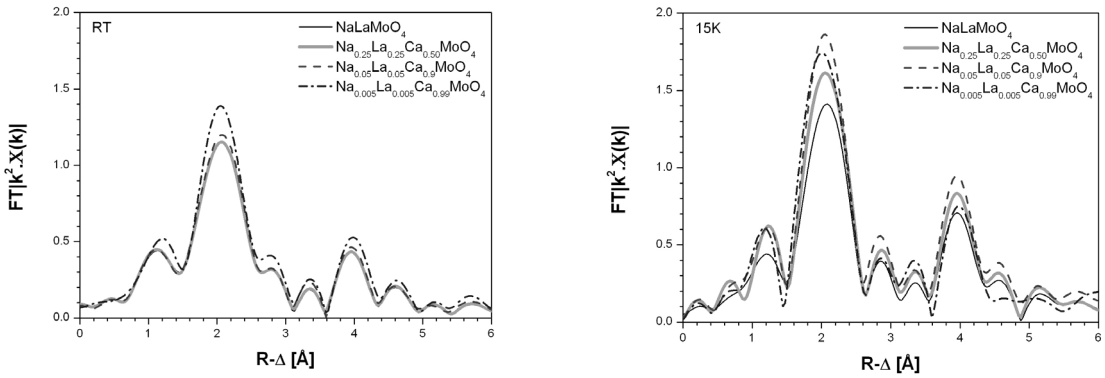

The results of the fit to the EXAFS data are shown in Figure 6 and the structural parameters are listed in Table 3. Fits are performed in R-space in the range 1.2-4.5Å. The k range used is 2.5-9.35 $Å^{-1}$. Fits to the La data only yield good results when a model of five shells is used. As for the Eu-series, the La-series exhibits interatomic distances compatible with but not the same as the XRD structural model. At 15K, a small discrepancy between fit and data around 7 $Å^{-1}$ persists for the 1% and the 10% substituted samples. The optimized interatomic distance for their first Mo shell is larger than that found in the two other La samples. This shell has a considerably large σ^2, which remains large for the higher substitutions at 15K. This reflects a significant static disorder.

Table 3: Structural parameters of the fit to the La L3 edge EXAFS. * fixed during the fit. The distances expected from the XRD data [ICSD-71389] for the $NaLaMoO_4$ are given in the first column, corresponding N are given Table 1. # manually optimized. * fixed or reached the limit set. σ^2 for 15K is given in italic.

Sample		Neighbour	N	R [Å]	ΔE0 [eV]	σ^2 [10^{-3} $Å^2$]
$NaLaMoO_4$	*2.56/2.62 Å*	O	7.6	2.57	3.42	10.5 / *6.2*
	3.78Å	Mo	4.0*	3.82#	-0.53	23.1 / *19.5*
	3.80 Å	O	4.0*	4.04	3.42	9.9 / *0.05**
	4.00 Å	Mo	4.0*	4.00	-0.53	5.8 / *0.3*
	4.46 Å	O	12.0*	4.50	3.42	10.9 / *5.0*
$Na_{0.25}La_{0.25}Ca_{0.50}MoO_4$		O	8.1	2.57	3.44	11.8 / *5.1*
		Mo	4.0*	3.82#	-1.14	30.0* / *20.0**
		O	4.0*	4.02	3.44	10.0 / *3.5.*
		Mo	4.0*	3.99	-1.14	6.3 / *0.1**
		O	12.0*	4.50	3.44	10.7 / *2.1*
$Na_{0.05}La_{0.05}Ca_{0.90}MoO_4$		O	8.0	2.57	3.09	11.5 / *3.8*
		Mo	4.0*	3.91#	-1.03	15.5 / *8.7*
		O	4.0*	4.00	3.09	19.9 / *3.4*
		Mo	4.0*	4.01	-1.03	6.4 / *0.08*
		O	12.0*	4.50	3.09	7.2 / *0.08*
$Na_{0.005}La_{0.005}Ca_{0.99}MoO_4$		O	8.8	2.57	3.11	10.0 / *5.7*
		Mo	4.0*	3.90#	-1.2	5.6 / *5.5*
		O	4.0*	3.96	3.11	12.6 / *12.2*
		Mo	4.0*	4.05	-1.2	2.0 / *0.1*
		O	12.0*	4.50	3.11	4.5 / *0.1**

Figure 6: k^2-weighted La L3 edge EXAFS (Fourier filtered on the fit windows range) and fit results (left), their corresponding FT (right). Fits are drawn as symbols and data as lines.

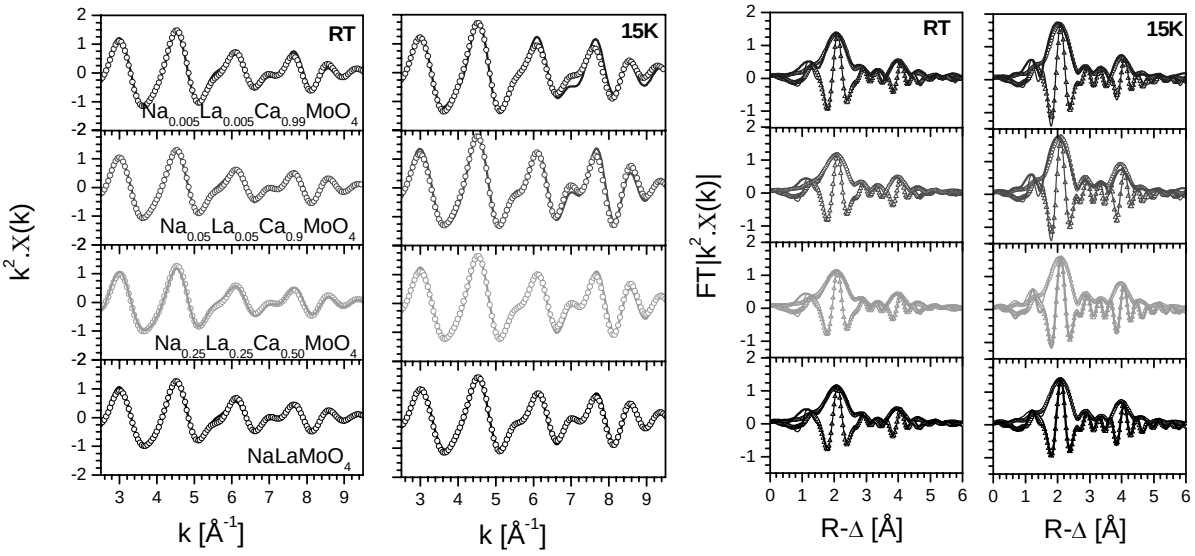

Conclusion

Comparison of the Eu and La L3 edge FTs shows that both cations affect changes to the powellite structure in the solid solution series differently. The Eu series shows the largest variation in the powellite structure as a function of the amount of substitution and of temperature although both cations, Na and Eu, have the same mean size as Ca (1.12Å in 8-fold co-ordination) and no significant variation in unit cell parameter can be detected with XRD in the series. Measurements and simulations of free enthalpy of mixing [14] reveal that no excess volume of mixing is observed for Eu. In contrast, a strong negative excess volume of mixing exists for La, where the maximum negative excess is obtained for the intermediate composition of the solid solution (50% Ca substituted).

Comparing the FT and the EXAFS fit results confirm the differences between substituting the Ca by La/Na or Eu/Na. Increasing the amount of Eu increases the static disorder to reach the highest value in the fully substituted compound, $NaEuMoO_4$. The La-substitution series shows generally a much larger overall disorder (reflected in large σ^2 values, even at low temperature). The size difference between La, Na, and Ca introduces static perturbations of the local order already at low La concentration.

In both series no lanthanide-lanthanide interaction could have been evidenced. This ruled out the possibility of Eu or La cluster formation inside the powellite structure.

Acknowledgments

We thank Stefan Mangold for his kind assistance at the ANKA-XAS beamline. Beamtime allotment at ANKA is gratefully acknowledged.

References

[1] A. Abdelouas, J.L. Crovisier, W. Lutze, B. Grambow, J.C. Dran, R. Muller: *J. Nucl. Mater.* **240**, 100 (1997).

[2[B. Grambow, R. Muller, A. Rother, W. Lutze: *Radiochim. Acta* **52**(3), 501 (1991).

[3] W. Lutze, B. Grambow: *Radiochim. Acta* **58**(9), 3 (1992).

[4] P. Zimmer, E. Bohnert, D. Bosbach, J.I. Kim, E. Althaus: *Radiochim. Acta* **90**, 529 (2002).

[5] V.B. Aleksandrov, L.V. Gorbatyii, V.V. Ilyukhin: *Kristallografiya* **13**, 512 (1968).

[6] U. Kolitsch: *Zeitschrift für Kristallographie* **216**, 449 (2001).

[7] V.P. Korsun: *Russian J. Inorg. Chem.* **45**, 957 (2000).

[8] L. Macalik, J. Hanuza, B. Macalik, W. Strek, J. Legendziewicz: *Eur. J. Solid State Inorg. Chem.* **33**, 397 (1996).

[9] J. Hanuza, A. Haznar, M. Maczka, A. Pietraszko, A. Lemiec, J.H. van der Maas, E.T.G.Lutz: *Raman Spectrosc.* **28**, 953 (1997).

[10] IFEFFIT 1.2.9 Copyright © 2006 Matt Newville, University of Chicago. http://cars9.uchicago.edu/ifeffit

[11] M. Newville, P. Livins, Y. Yacoby, J.J. Rehr, E.A. Stern: *Phys. Rev. B* **47**, 14126 (1993).

[12] L.A. Ankudinov, B. Ravel, J.J. Rehr, S.D. Conradson: *Phys. Rev. B* **58**, 7565 (1998).

[13] R.D. Shannon: *Acta Cryst.* **A32**, 751 (1976).

[14] V.L: Vinograd, D. Bosbach, B. Winkler, T. Fanghänel: *Bericht der Deutschen Mineralogischen Ges. Beih. Z. Eur. J. Mineral.* **18**, (2006).

CONFOCAL µ-XRF AND µ-XAFS STUDIES OF FRACTURED GRANITE FOLLOWING A RADIOTRACER MIGRATION EXPERIMENT

Melissa A. Denecke[1], Koen Janssens[2], Boris Brendebach[1], Gerald Falkenberg[3], Jürgen Römer[1], Rolf Simon[4], Bart Vekemans[2]

[1] Forschungszentrum Karlsruhe (FZK), Institut für Nukleare Entsorgung, P.O. Box 3640, D-76021 Karlsruhe, Germany

[2] Department of Chemistry, University of Antwerp, Universiteitsplein 1, B-2610 Antwerp, Belgium

[3] Hamburger Synchrotronstrahlungslabor (HASYLAB) at DESY, Notkestr. 85, D-22603 Hamburg, Germany

[4]FZK, Institut für Synchrotronstrahlung, P.O. Box 3640, D-76021 Karlsruhe, Germany

Abstract

We perform spatially resolved X-ray absorption fine structure and fluorescence investigations with a micrometer-scale resolution (µ-XAFS, µ-XRF) for neptunium speciation in a fractured granite bore core stemming from the Swedish Äspö Hard Rock Laboratory following a radiotracer experiment. These investigations are relevant for safety assessment of nuclear waste disposal in assessing mechanisms leading to immobilization of actinide elements in the environment. In order to probe micro-volumes below the sample surface, a confocal irradiation-detection geometry is employed. Upon scanning sample areas at defined depths below the sample surface, cross sections visualizing the distribution of elements are recorded. By varying the energy of the beam at a constant sample position, Np L3 edge XANES spectra of a selected sample volume are recorded. Results reveal that Np, originally introduced as Np(V) in the tracer cocktail, is reduced to Np(IV). The tracer Np is observed to be located near or on fissures in the granite and associated with Zn. Further work is needed to support the conclusion that the distribution of Np results from local geometries, surface areas, and flow paths in the granite.

Introduction

We report results of spatially resolved investigations with a micrometer-scale resolution (µ-focus XRF and XAFS) of Np speciation in a fractured granite bore section from the Swedish Äspö Hard Rock Laboratory (HRL) following a radiotracer experiment. The Äspö HRL is an underground laboratory site in a granite rock formation located near Oskarshamn. Sweden plans to deposit spent nuclear fuel in granite bedrock [1]. The HRL allows *in situ* testing of radioactive waste disposal techniques and investigating radionuclide migration behavior. Groundwater flow in fractures in the granite host rock is thought to be capable of influencing the migration of radionuclides released from a repository. As part of a co-operation between the Swedish Nuclear Fuel and Waste Management Company (Svensk Kärnbränslehantering AB, SKB) and the Institute for Nuclear Waste Disposal (Institut für Nukleare Entsorgung, INE) of the Research Center Karlsruhe (Forschungszentrum Karlsruhe, FZK), radionuclide migration experiments are conducted on granite bore cores from Äspö under *in situ* conditions. After termination of the experiments, we have determined Np speciation in a polished slice, approximately 4 mm thick, of a fractured granite bore core column (52 mm in diameter) from the Äspö HRL used in a laboratory radiotracer experiment. We are interested in determining if the Np immobilized in the granite is found to be associated with any identifiable elements. In addition, the valence state of the Np is to be determined from Np L3 µ-XANES. Finally, we wish to explore the applicability of the technique to a sample containing only a trace concentration level, in this case Np. Elemental distribution maps are obtained from XRF measurements with 10-20 µm lateral resolution (µ-XRF). A Np L3 µ-XANES spectrum of a Np "hot spot" is recorded at a selected region of high Np concentration identified and localized in the µ-XRF maps. The µ-XRF/µ-XANES measurements are recorded in a confocal geometry to provide added depth information, to minimize spectral interference from other elements by limiting the sample volume probed, as well as to enable recording XANES below the sample cut surface, thereby avoiding any surface oxidation artifacts possibly caused by cutting and polishing the granite slice.

Materials and Methods

An approximately 4 mm slice of a HRL granite core following a laboratory migration experiment is investigated [[2]]. In the migration experiment, the core was subjected under pressure to groundwater with added Np containing radiotracer cocktail (10^{-5} mol ^{237}Np /dm^3; added as Np(V)). About 25% of the Np introduced onto the column is recovered in the elute. Following termination of the experiment, the cores were cut perpendicular to their cylinder axis. ICP-MS analysis of the abraded material from cutting the granite and γ-counting (detection of the ^{233}Pa daughter) of the slices shows that the slice selected for this investigation contains most of the tracer activity remaining in the column (approximately 3 nmol Np/g in the slice 30 mm from the core column top). A high resolution photograph of this core slice is shown in Figure 1. Also shown in Figure 1 is an autoradiographic image of the slice; radioactive areas containing ^{237}Np appear dark in the image. Comparison of the photograph and the autoradiogram reveals that the places of highest Np-activity are not at the large fracture in the granite; the highest activity is localized in smaller fissures.

µ-XRF measurements using a band pass of wavelengths are made at the Fluo-Topo Beamline (ANKA) and at beamline L (HASYLAB) with an average weighted energy above the Np L2 ionization energy of 21.615 keV [[3]]. Monochromatic X-rays are used at beamline L for collecting Np L3 edge XANES data. XANES spectra are recorded from 17550 to 17700 eV in 1 eV steps with 30s counting time. The confocal setup used is described in [4,5]. The primary focusing optic used at ANKA is a planar compound refractive lens (CRL) [6]. A polycapillary (PC) half lens is used at HASYLAB. A second PC between sample and detector is used as collimating optic in the confocal setup at both stations. The CRL delivered a focal spot of 2 µm × 5 µm (V×H). Depending on the PC used, the focal spot diameter varied between 16 and 11 µm. The depth resolution is determined by scanning depth profiles of a thin glass standard to be ~ 16 µm.

Figure 1. High resolution photograph of the core slice studied (left) and its autoradiographic image (right)

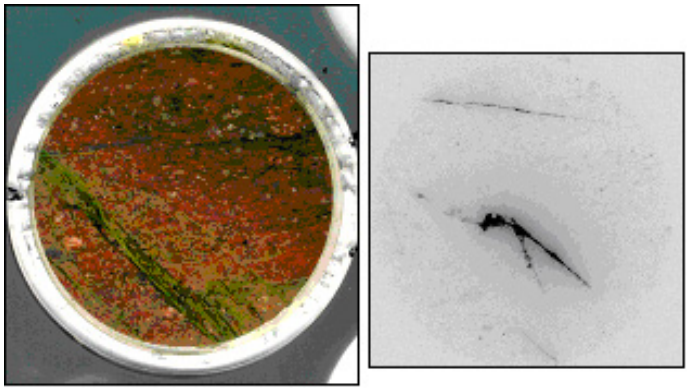

Results and Discussion

The µ-XRF distribution for a number of elements in the fractured granite measured in confocal geometry at two different depths below the sample surface (-60 µm and -40 µm) for a 300 x 300 μm^2 area, with each pixel in the image being 20 x 20 μm^2, is shown in Figure 2.

Figure 2. Elemental distributions at two different depths below the surface (-60 µm and -40 µm) in a 300 x 300 μm^2 area, 20 µm stepsize for K, Ca, Ti, V, Mn, Fe, Cu, Zn, Ga, As, Rb, Sr, Y, Zr, Nb, Pb, U, and Np

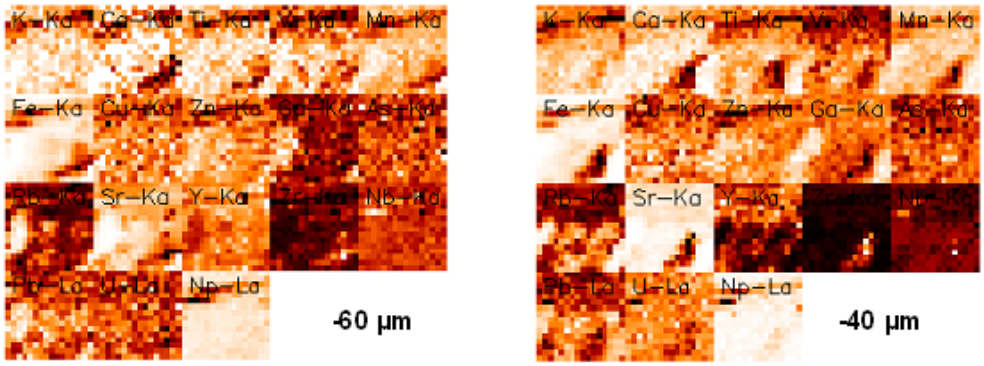

The scaling in the distribution maps is such that dark pixels are regions where that particular element has a high concentration, i.e. pixels exhibiting high florescence intensity, while light pixels exhibit low intensity, corresponding to a relatively low concentration. Pixels having the highest Np concentration in Figure 2 are found at both depths in the upper half of the area studied, clustered along a fissure so that the dark pixels form a line 1 to 4 pixels in width (around 20-80 µm). A different 300 x 300 μm^2 area recorded at about -60 µm below the surface is shown in Figure 3. This image is recorded with the CRL yielding a higher resolution. Each pixel in Figure 3 is 10 x 10 μm^2. The micrograph of the granite surface where this image is recorded has visible pits, likely cross sections of minute, permeable channels. The Np distribution suggests that high Np concentrations are associated with these channels.

Figure 3. Elemental distributions at about -60 µm below the surface in a 300 x 300 µm^2 area, 10µm stepsize

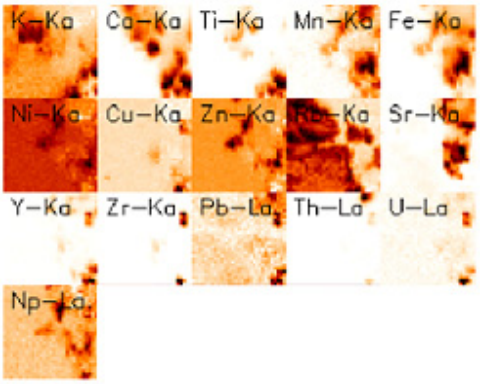

If we compare the Np distribution with the other element distributions, a correlation between Np with Zn becomes apparent. This is corroborated in the correlation plot in Figure 4, where the normalized Np Lα signal versus normalized Zn Kα signal from the images in Figure 3 is plotted.

Figure 4. Correlation plot between Np and Zn

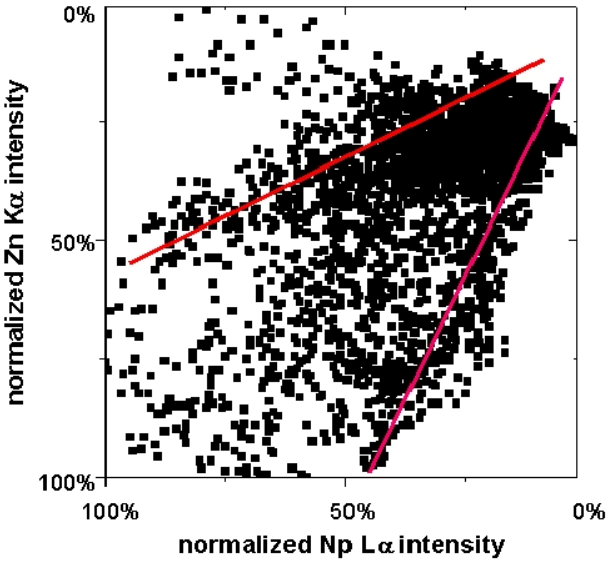

The lines in the Figure are a guide to the eye with slopes ½ and 2. The Np/Zn-correlation lies mainly within the fan defined by these two slopes. The element distributions from a larger area at about -110 µm below the sample surface (700 x 700 µm^2, 20 x 20 µm^2 pixel size) are shown in Figure 5.

Figure 5. Elemental distributions at about -110 µm below the surface in a 700 x 700 µm^2 area, 20 µm step size

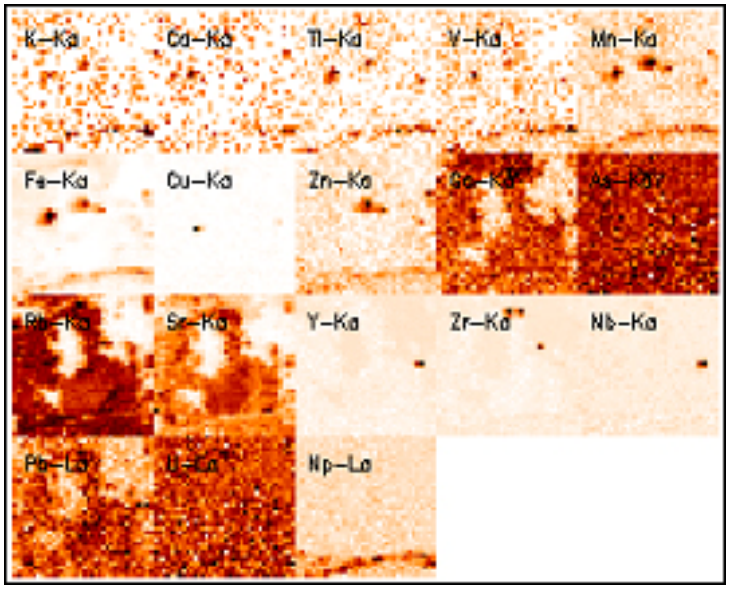

Again we find the Np distribution to follow small fractures or fissures in the granite. One can see that the lower energetic fluorescence lines of the lighter elements are not easily detected at this greater depth due to self-absorption of the overlying material. This illustrates one of the challenges in working the confocal mode. While the confocal geometry has the advantage that it allows to obtain depth information, quantification of confocal fluorescence data is not easily done as corrections for self-absorption are difficult. For this reason to date one generally finds reports of qualitative distributions and not often quantitative data. It is nearly impossible to ascertain what the absorption of overlying material in a heterogeneous system is, as thickness, densities and take-off angles are essentially unknown and an extrapolation method cannot be applied. For confocal studies of layered samples, for example paint layers in non-destructive analysis of archaeometric or cultural heritage specimens, or where the sample is less heterogeneous, for example trace metal concentrations in diamond [7], this might be an easier task.

Another word of caution is needed in analysing XRF data from natural samples such as these, where spectral interference between fluorescence lines can be a challenge. This granite sample has a natural background of U and Th (measured concentrations: [U] 6 µg/g and [Th] 40 µg/g). In addition it contains Sr and Rb. All of these elements have energetically close lying $K\alpha_1$ and $L\alpha_1$ florescence lines ($L\alpha_1$ energies: Th= 12.97 keV, U= 13.61 keV, Np= 13.95 keV; $K\alpha_1$ energies: Rb= 13.40 keV, Sr= 14.17 keV). Figure 6A shows the fluorescence spectrum obtained by integrating the fluorescence spectra of all pixels in the 300 x 300 µm^2 area in Figure 3. The Np $L\alpha_1$ line is expected to lie between the U $L\alpha_1$ and the Sr $K\alpha_1$ peaks. Clearly the Np $L\alpha_1$ line is not resolved. The fluorescence spectrum recorded at the pixel with the highest Np $L\alpha_1$ intensities in Figure 3 is depicted in Figure 6B.

Figure 6. Fluorescence spectrum integrated over all pixels in the same sample area as the distributions shown in Figure 3 (A) compared to that for the single darkest Np pixel (B)

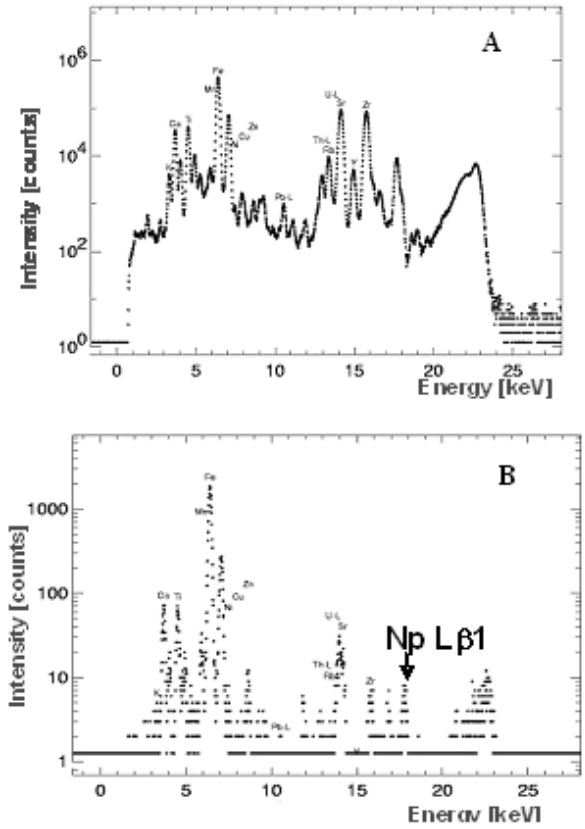

The Np $L\alpha_1$ (an L3 → M5 transition) is not well-resolved and the integrated intensities must be extracted from the spectrum by careful peak fitting after background subtraction [8]. We check these Np intensities by employing an excitation energy above the Np L2 excitation so that the $L\beta_1$ line (an L2 → M4 transition) at 18.85 keV is also registered. This line is marked in Figure 6B and appears well-separated from other lines. The Np distribution near the hot spot in Figure 2 is compared to the Fe, Zn and Sr distributions in Figure 7. The Fe distribution reflects branched fissures in the granite. The Np is associated with the smaller branch in the upper part of the image. The Sr distribution in contrast follows the lower branch of the fissure. This contrast demonstrates the good resolution achieved. The confocal geometry is helpful here where spectral interference is a problem by probing restricted volumes. Parenthetically note that this particular µ-XRF map (Figure 7) also displays our observation that Np is often found associated with Zn.

Figure 7 Confocal µ-XRF distribution maps Np, Fe, Zn, and Sr, measured with E_{excite}= 21.6 keV, of a 300 x 300 µm^2 section (20 × 20 µm^2 step size) at -40 µm below the surface

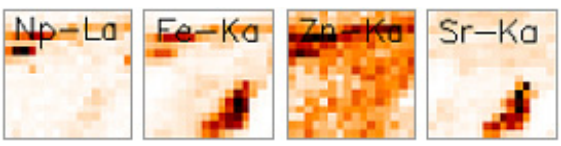

In order to determine the valence state of the Np-tracer in the granite, a Np L3 µ-XANES is recorded at the darkest pixel in the Np distribution shown in Figure 7. The XANES (Figure 8) features indicate that the Np hot spot contains Np(IV). For comparison, the Np L3 XANES of Np(IV) and Np(V) reference solutions are shown in the inset of the Figure. The granite Np hot spot XANES is similar to the Np(IV) reference spectrum. The strong white line, the energy position of the white line (17.621 keV), and the lack of the multiple scattering (MS) feature indicative of the neptunyl (Np(V)) ion [9] all indicate that Np in the granite is in the tetravalent state. A Np(V) XANES would have a white line maximum below 17.620 keV, instead of above, and would exhibit a shoulder on the high energy side of the white line (the MS feature). Note that this XANES is recorded for a specimen with a nominal Np concentration of 3 nmol/g or <1 ppm. The clear advantage of using a microfocus beam for X-ray spectroscopy on dilute, heterogeneous samples is obvious.

FIGURE 8. Np L3 µ-XANES of the granite core slice Np hot spot in Figure 7. The inset shows acidic solution Np(IV) and Np(V) reference spectra (shifted along the y-axis for clarity) for comparison

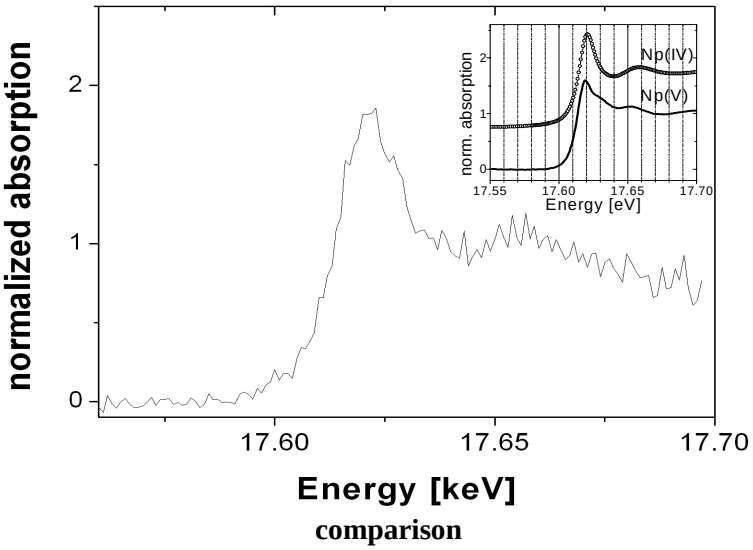

Conclusions

Studying the fractured granite following the radiotracer column experiment reveal that Np, originally as Np(V), is reduced to Np(IV). The Np distribution appears to follow fissures and permeable channels not larger than 100 µm. It is feasible that Np has a lower residence time in the large fractures, while in the smaller fissures migration is slower leading to longer residence times, i.e., reaction times. The Np(IV) is apparently associated with Zn. Surprisingly we observe fissure branches containing Fe (presumably Fe(II)), where we do not detect any Np. Further work is needed to support the conclusion that the distribution of Np results from local geometries, surface areas, and flow paths in the granite [2].

Acknowledgments

This research receives funding by the European Network of Excellence for Actinide Sciences (ACTINET). We thank ANKA and HASYLAB for beamtime and E. Soballa for autoradiographic results and sample preparation.

References

1. C.R. Bayliss, K.F. Langley, Nuclear Decommissioning, Waste Management, and Environmental Site Remediation, Elsevier, Heidelberg, (2003).
2. J. Römer, B. Kienzler, P. Vejmelka, E. Soballa, A. Görtzen, M. Fuß, FZK-Wissenschaftliche Berichte FZKA6770 (Oktober 2002).
3. M.A. Denecke, Coord. Chem. Rev. **250**, 730–754 (2006).
4. M.A. Denecke, K. Janssens, K. Proost, J. Rothe, U. Noseck, Environ. Sci. Technol. **39**(7), 2049-2058 (2005).
5. K. Janssens, K. Proost, G. Falkenberg, Spectrochim. Acta B **59**, 1637-1645 (2004) .
6. V. Nazmov, E. Reznikova, A. Somogyi, J. Mohr, V. Saile, Planar sets of cross X-ray refractive lenses from SU-8 polymer. Proceedings of SPIE 2004, Vol. 5539, 235-242.
7. L. Vincze, B. Vekemans, F.E. Brenker, G. Falkenberg, K. Rickers, A. Somogyi, M. Kersten, F. Adams, Anal. Chem. **76** (22), 6786-6791 (2004)
8. B. Vekemans, K. Janssens, L. Vincze, F. Adams, P. Van Espen, X-ray Spectrometry **23**, 278-285 (1994).
9. M.A. Denecke, K. Dardenne, C.M. Marquardt, Talanta **65**(4), 1008-1014 (2005).

THE STRUCTURE OF SODDYITE-EXAFS SHELL FITTING AND WAVELET ANALYSIS

Harald Funke, Christoph Hennig and Andreas C. Scheinost
Institute of Radiochemistry, FZ-Rossendorf, Dresden, Germany and
Rossendorf Beamline (BM20), ESRF-CRG, Grenoble, France

Abstract

Many uranyl (U(VI)) minerals have a characteristic layer structure in the equatorial plane due to the strong electrovalence of the two axial oxygen atoms. For structures containing heavy atoms like U, the XRD patterns are dominated by the backscattering from the heavy atoms, while the positions of light atoms like O or Si may be occasionally inaccurate. The EXAFS spectrum was measured of a soddyite sample of Renaud Vochten's collection of uranium minerals at 30 K. The local structure determined by shell fitting is fairly consistent with crystallographic data. Wavelet analysis clearly resolved the Si and U atoms at nearly the same distance between 3.6 and 3.9 Å.

Np(V) CO-PRECIPITATION WITH CALCITE

F. Heberling, M.A. Denecke, D. Bosbach
Institute for Nuclear Waste Disposal, Forschungszentrum Karlsruhe,
PO Box 3640, 76021 Karlsruhe, Germany

Abstract

The migration behaviour of the actinyl ions $U(VI)O_2^{2+}$, $Np(V)O_2^{+}$ and $Pu(V,VI)O_2^{(+,2+)}$ in the geosphere is to a large extend controlled by sorption reactions (inner- and outer-sphere adsorption, ion-exchange, co-precipitation/structural incorporation) with minerals. We study the structural incorporation of Np(V) into the host mineral calcite by co-precipitation in mixed flow reactors under steady-state conditions at room temperature. In this way reaction rates and partition coefficients can be determined under varying conditions. We found that homogeneous partition coefficients for Np in calcite (0.5-11) are significantly higher than those reported for U(VI) (0.01-0.2 [1]). The local structural environment of incorporated Np(V) is characterised from the Np L3 EXAFS. Our data suggest that the Np(V)-ions occupy calcium lattice sites. The two axial oxygen atoms of the linear neptunyl-ions substitute two carbonate groups in the first co-ordination sphere. Consequently, only four carbonate ions are observed to co-ordinate the neptunyl-ion. Np-O and Np-C interatomic distances (2,4Å, 3,3Å, respectively) indicate slight structural relaxation of the carbonate groups from their ideal sites. A similar structural model is reported for U(VI) incorporated into calcite [2].

Introduction

The disposal of high-level nuclear waste in deep geological formations poses major scientific and social challenges to be met in the next decades. One of the key issues is the long-term safety of a waste repository over extended periods of time, up to 10^6 years. Demonstrating the repository safety over geological time spans requires a sound understanding of the migration behaviour of radionuclides in the geosphere. The environmental behaviour of the actinyl ions $U(VI)O_2^{2+}$, $Np(V)O_2^+$ and $Pu(V,VI)O_2^{(+,2+)}$ is to a large extent controlled by sorption reactions (inner- and outer-sphere adsorption, ion-exchange, co-precipitation/structural incorporation) with minerals. Structural incorporation is not yet commonly considered in the safety analysis for repository systems, although these phenomena are quite common and extensively studied in natural systems. The main reason for this discrepancy is the lack of thermodynamic and kinetic data needed for the quantitative description of these processes. Here we study the structural incorporation of Np(V) into the host mineral calcite by co-precipitation. The aim of this work is to investigate if neptunyl-ions can be incorporated onto stable lattice sites in the calcite crystal lattice and to quantify the uptake by the homogeneous Henderson-Kracek partition coefficient. The structural environment of neptunyl in calcite is characterised by EXAFS Spectroscopy in order to identify the substitution mechanism. The results will provide basic information for modeling the neptunyl-calcite aqueous-solution solid-solution system.

Experimental

Four neptunium containing calcite samples are synthesized in a mixed-flow-reactor under varying conditions, two at a pH of about 10.3, one at pH 12.8, and one at pH 8.2 to check if the aqueous speciation has an influence on the incorporation. At the chosen solution compositions the pure NpO_2^+-ion dominates the aqueous speciation at pH 8.2, at pH 10.3 the neptunyl monocarbonato complex dominates, and at pH 12.8 the neptunyl dihydroxo complex. SI(calcite) of the input solutions is chosen to be between 1 and 1.3 in order to avoid homogeneous nucleation ($SI = \log_{10}(IAP/K_{sp})$, with the Ion Activity Product, IAP, and the Solubility Product, K_{sp}). All the experiments are conducted with a Np concentration of 1µmol/L and a background electrolyte concentration of 0.01M NaCl. The input solution is undersaturated with respect to all known solid neptunium phases. As seed crystals we use ~150mg Merck suprapur calcium carbonate with a diameter of 11-15µm (sieved). The reactive surface in the reactor is ~0.2m^2 (measured by BET). The stock solutions are prepared with MilliQ water and Merck p.a. chemicals. Three stock solutions, the first containing NaCl and Na_2CO_3 (+ $NaHCO_3$ or NaOH, to adjust the pH), the second NaCl and NpO_2^+ (taken from a 0.073 mol/L pH 3 perchloric acid stock solution) and the third NaCl and $CaCl_2$, are pumped continuously into the reactor (see Figure 1). Calcium and neptunium concentrations are sampled before and after the reactor and analyzed by ICP-MS. The calcite suspension in the reactor is stirred by a magnetic stirring bar ((1) in Figure 1). In the reactor steady-state conditions are attained and the neptunium containing calcite grows homogeneously onto the seed crystals. From the concentrations, the mole balance Δc ($= c_{in} - c_{out}$) and the flowrate the reaction rate R (equation(1)) and the homogeneous partition coefficient D (equation (2)) can be calculated.

$$R = \frac{flowrate \cdot \Delta c}{surface} \qquad (1)$$

$$D = \frac{X_{Np} / X_{Ca}}{[NpO_2^+]/[Ca^{2+}]} \qquad (2)$$

with X_a being the molfraction of *a* in the precipitated solid phase and [*a*] being the concentration of *a* in the steady-state solution.

Figure 1: The mixed-flow-reactor used for the co-precipitation experiment. The suspension in the reactor is stirred by a magnetic stirring bar (1). A filter (2) before the output tube keeps the seed crystals in the reactor.

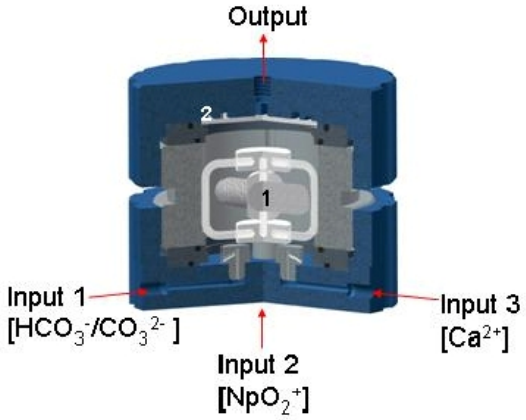

The four samples are examined by EXAFS measurement at the Np L3 edge (17.608keV). The measurements are performed at the INE-Beamline at ANKA in fluorescence-mode. As monochromator crystals we use Ge(422). The energy calibration is done by parallel measurement of a Zr-foil, defining the first inflection point as 17.998keV. We record seven to ten spectra for each sample from about 150eV beneath the absorption edge up to 700eV-1100eV above the edge and analyse the resulting averaged spectra using backscattering amplitude and phase shift functions calculated with Feff 8 [3] and the FEFFIT 2.54 software. Background removal is done with WinXAS 3.1 [4].

Table 1: Results of the mixed-flow-reactor experiments.

Experiment	pH_{input}	SI_{input}(calcite)	R [$\cdot 10^{-8}$ mol/($m^2 \cdot s$)]	D
1	10.3	1.0	1.0	2
2	10.3	1.1	1.1	0.5
3	12.8	1.3	3.2	8
4	8.2	1.3	3.5	11

Results and Discussion

Results from the mixed-flow-reactor experiments are summarized in Table 1. The partition coefficients D range from 0.5 to 11. They are therefore significantly higher than those reported for the structurally equivalent uranyl (0.01-0.2 [1]). The experimental conditions at which the calcite precipitates are close to equilibrium. No homogeneous nucleation takes place. The precipitation rates at which we conduct our experiments of 1.0 -3.5$\cdot 10^{-8}$ mol/(m^2*s) are very low (see summary in [1] for comparison). Therefore the measured partition coefficients should be well applicable for further modeling of the aqueous solution – solid solution system. The different aqueous neptunium speciation at the differing pH values chosen for the synthesis of the four samples has no observable influence on the incorporation. We do find an indication that reaction rate and partition coefficient correlate; samples 3 and 4 with the largest D precipitated at the highest rate.

Np L3 k-weighted EXAFS for all four samples and their corresponding fit curves are displayed in Figure 2. The model spectra fit the data very well. The structural parameters obtained from the EXAFS fits are summarized in Table 2. The relative shift in ionization energy ($\Delta e0$) and the amplitude reduction factor (S_0^2) are held constant at their initial first and second shell fit values (6.1, 5.6, 9.2, and 9.8 and 0.92, 0.87, 0.89, and 0.87 for the samples 1, 2, 3, and 4, respectively) and than repeating the fit. All samples show within the uncertainties the same result, i.e. the same nearest neighbour ordering of atoms surrounding Np. The degeneracy of the scattering paths corresponding to the carbonate ions in the first co-ordination sphere around the central neptunyl-ion (i.e. co-ordination number for O-carb1, C-carb, and O-carb2) is about four. Therefore we conclude that the neptunyl-ions occupy calcium sites in the calcite lattice with the oxygens of the linear neptunyl molecule substituting two carbonate ions in the first co-ordination sphere. Consequently the neptunyl is co-ordinated by four carbonate ions only. The interatomic distances indicate structural relaxation of the remaining four carbonate groups from their ideal sites (r(O-carb1) = 2.39Å to 2.41Å instead of 2.35Å [5], r(C-Carb) = 3.26Å -3.41Å instead of 3.20Å [5], and r(O-carb2) = 3.52Å instead of 3.44Å [5]). This relaxation causing structural strain indicates a positive enthalpy of mixing. Therefore a complete solid solution series of mixing at room temperature cannot be expected. The small Debye-Waller Factors (σ^2) are evidence for the high order in this structure. A picture of the suggested near-ordered structure for neptunyl incorporated into the calcite host at a calcium site is shown in Figure 3. A similar structural model was reported for U(VI) incorporated into natural calcite [2].

Figure 2: EXAFS spectra of the samples 1 to 4 and the corresponding fits in K-space. (Spectra and fits are shifted along the y-axis for clarity.)

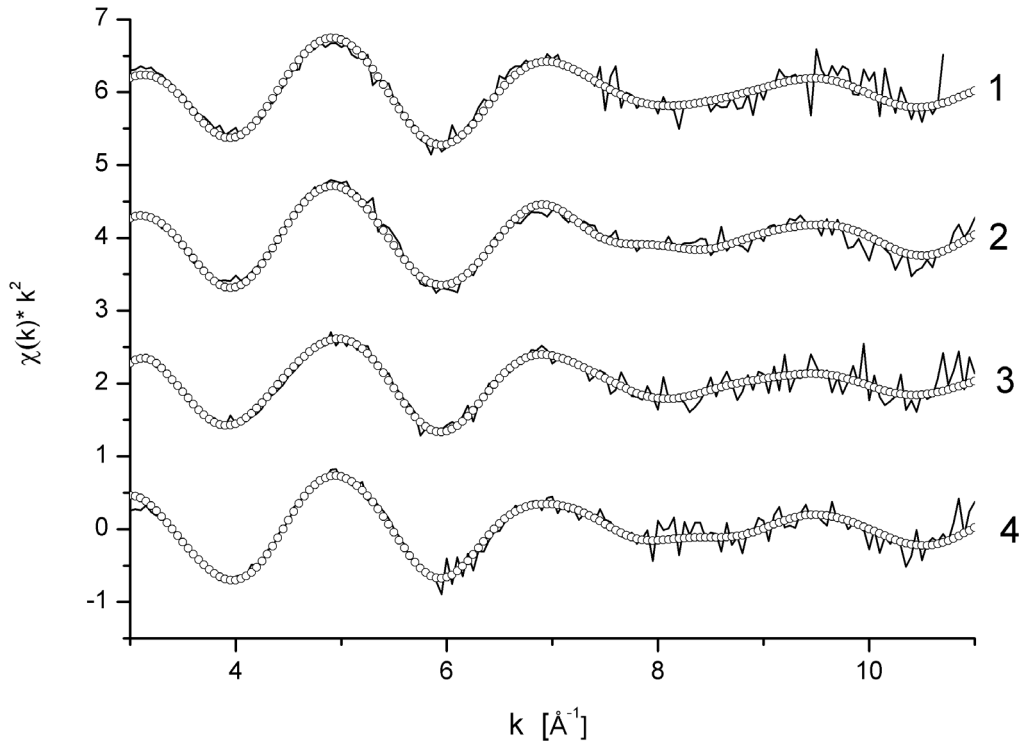

Table 2: Results of the EXAFS fits. Co-ordination numbers N, interatomic distances r and Debye-Waller Factors σ^2 (uncertainties in parenthesis) for the neptunium environment in the calcite samples 1 to 4. ([1)]: held constant during the fit; = means the parameter is correlated to the parameter given)

1	N	r [Å]	σ^2 [Å^2]	2	N	r [Å]	σ^2 [Å^2]
1st shell O-yl	2[1)]	1.843 (0.006)	0.0018 (0.0008)	1st shell O-yl	2[1)]	1.855 (0.008)	0.002[1)]
2nd shell O-carb1	4.08 (1.05)	2.402 (0.011)	0.0093 (0.0039)	2nd shell O-carb1	3.61 (1.41)	2.414 (0.015)	0.0065 (0.0044)
3rd shell C-carb	= $N_{O\text{-}carb1}$	3.257 (0.168)	0.0395 (0.0370)	3rd shell C-carb	= $N_{O\text{-}carb1}$	3.344 (0.114)	= $\sigma^2_{O\text{-}carb1}$
3	**N**	**r [Å]**	**σ^2 [Å^2]**	**4**	**N**	**r [Å]**	**σ^2 [Å^2]**
1st shell O-yl	2[1)]	1.857 (0.008)	0.0029 (0.0019)	1st shell O-yl	2[1)]	1.855 (0.010)	0.0017 (0.0013)
2nd shell O-carb1	4.88 (1.15)	2.399 (0.011)	0.0125 (0.0048)	2nd shell O-carb1	4.3[1)]	2.413 (0.017)	0.0073 (0.0022)
3rd shell O-carb2	4[1)]	3.411 (0.015)	0.0132 (0.0028)	3rd shell C-carb	4[1)]	3.380 (0.127)	0.0140 (0.0246)
				4th shell O-carb2	4[1)]	3.527 (0.084)	0.0102 (0.0138)
				5th shell Ca	6[1)]	4.003 (0.071)	0.0245 (0.0103)

Figure 3: Structural model of neptunyl incorporated into the calcite host.

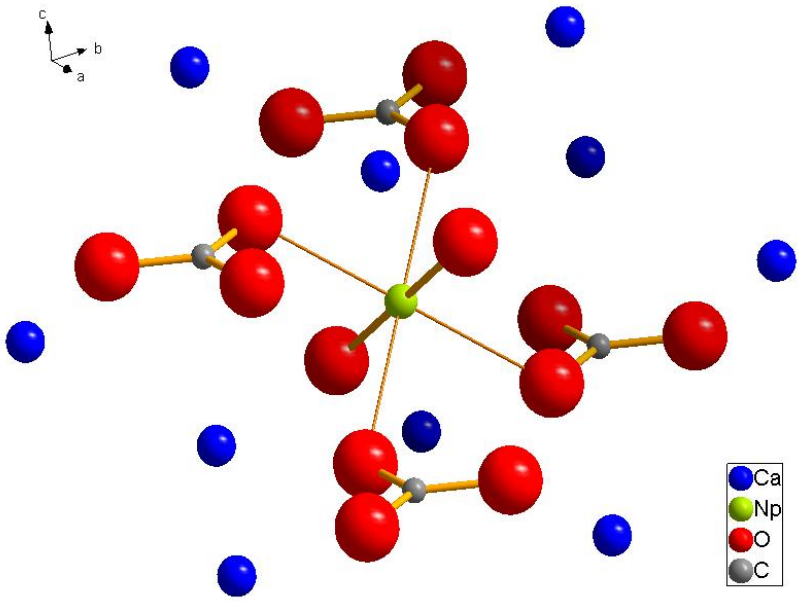

The charge excess of the observed structure gives us one possible reason for the apparent higher affinity of Np(V) for calcite compared to U(VI). Incorporation of the pentavalent neptunium leads to a charge excess of only +3, while for the hexavalent uranium as doubly charged uranyl cation this charge excess is +4.

Conclusions

In this study neptunium(V) doped calcite is synthesised at low precipitation rates at conditions close to equilibrium. No homogeneous nucleation takes place during the co-precipitation experiments and the solid-solution precipitates homogeneously under steady state conditions. The measured partition coefficients D range from 0.5 to 11. These are one to two orders of magnitude higher than those reported for uranyl [1]. We observe that the neptunyl aqueous speciation has no major influence on the incorporation. Neptunyl is found to occupy a calcium lattice site in the calcite host. The two oxygen atoms of the linear neptunyl molecule substitute two carbonate groups in the first co-ordination sphere, consequently only four carbonate ions co-ordinate the neptunyl ion.

References

[1] E. Curti (1997) PSI-Bericht, volume 97.

[2] S.D. Kelly, M.G. Newville, L. Cheng, K.M. Kemner, S.R. Sutton, P. Fenter, N.C. Sturchio and C. Spötl (2003), Environmental Science and Technology 37, 1284-1287.

[3] J.J. Rehr, J. Mustre de Leon, S.I. Zabinsky and R.C. Albers (1991), Journal of the American Chemical Society 113, 5135

[4] T.Ressler (1997), Journal of Physics, IV 7 (C2), 267-270.

[5] R. Warchtow (1989), Zeitschrift für Kristallographie 186, 300-302.

DOUBLE-ELECTRON EXCITATIONS IN *L* EDGE X-RAY ABSORPTION SPECTRA OF ACTINIDES

Christoph Hennig
Forschungszentrum Rossendorf, Institute of Radiochemistry, D-01314 Dresden, Germany

Abstract

Double-electron excitation effects in L_3 edge X-ray absorption spectra of actinides has been investigated. The effect will be demonstrated here by using experimental data of Th^{4+}, U^{4+}, and Np^{4+} hydrates. The double-electron excitation was identified as a $L_3N_{6,7}$ shake-up effect.

Introduction

Multielectron excitations in X-ray absorption spectra are well known. They have been observed above the *K* edge of Ne [1], Xe [2], Ar [3] and Kr [4]. In noble gases, the absorption signal is not affected by photoelectron backscattering effects from neighbored atoms that cause the extended X-ray absorption fine structure (EXAFS). EXAFS oscillations are able to cover double-electron excitations. Nevertheless, they have been also revealed in the spectra of liquids and solids. As example, solid compounds of the 3^{rd} period show *KL* multielectron transitions, e.g α-Si [5] and salts of P, S, and Cl [6]. Ca^{2+} hydrate, as example of the 4^{th} period, shows KM_1 and $KM_{2,3}$ resonances [7]. For 5^{th} period, multielectron transitions has been observed at the KN_1, $KM_{4,5}$, and $KM_{2,3}$ edges of gaseous Br_2 and HBr [8]. In the 6^{th} period, e.g. for the lanthanides, the resonances are associated with $LN_{4,5}$ edges [9, 10].

Up to now it has not been investigated whether the actinides, as members of the 7^{th} period, show also multielectron excitations. The low vapour pressure and radioprotection aspects prevent investigations in the gas phase. In the last decade, several EXAFS data of actinides in aqueous solution has been published with the aim to reveal their near-order structure. A part of these spectra will be reinvestigated here with regard to multielectron features.

Experimental details

The X-ray absorption data were collected on the Rossendorf Beamline [11] at the ESRF, Grenoble. The monochromator is equipped with Si(111) double-crystals. Higher harmonics were rejected by two Pt coated mirrors and a detuned second monochromator crystal. The monochromator energy scale was calibrated according to the *K*-edge of a Y metal foil. As reference for the Y 1s ionization energy served the first inflection point of the absorption edge at 17038.0 eV. The samples used in this study are Th^{4+} (0.05 M Th(IV) in 0.5 M $HClO_4$), U^{4+} (0.01 M U(IV) in 0.1 M $HClO_4$), Np^{4+} (0.05 M Np(IV) in 0.1 M HNO_3). The preparation conditions have been described previously [12, 13]. All solutions were filled in polyethylene cuvettes with an optical path length of 13 mm, and encapsulated in a second hot sealed polyethylene bag. The XAFS measurements were performed at 25°C.

Results and discussion

The L_3-edge k^3 EXAFS spectra are reported in Figure 1. The signal is formed by a single-frequency sinusoidal oscillation. In the *k* range 9.8–11.2 $Å^{-1}$ small anomalous features appear superimposed to the main oscillations. These features are indicated individually by arrows. The energy values of these features are given as E_f in Table 1. Their position appears shifted to higher *k* values with increasing atomic number *Z*. All features show a relative sharp maximum. Sharp, resonance-like absorption features appear if the core electron excitation is accompanied by a shake-up of the second electron to a bound state. In contrast, the cross-section appears gradually increased with increasing photon energy, if both electrons are excited to the continuum. Therefore, the sharp features in Figure 1 might be originated by a shake-up process.

Table 1. Listing of the L_3 edge energy E_{1st}, the difference between the white line energy and the L_3 edge energie $\Delta E_{WL\text{-}1st}$, and the energy of the anomalous feature, E_f, the double excitation onset energies E_S and the related $Z+1$ $4f$ energies taken from Porter and Freedman [14]. All values are given in eV.

Z	An^{n+}	E_{1st}	$\Delta E_{WL\text{-}1st}$	E_f	E_S	N_6 ($4f_{5/2}$)	N_7 ($4f_{7/2}$)
90	Th^{4+}	16301.8	3.6	16678.8	373.4	366	355
92	U^{4+}	17171.8	3.7	17594.7	419.2	414	403
93	Np^{4+}	17613.6	3.9	18061.2	443.7	436	424

In order to assign the experimental features to a specific electron excitation channel, the difference between the energy of the anomalous maximum E_f and the energy of the absorption edge threshold, E_0, was estimated. The energy position of the anomalous maximum E_f is taken directly from the raw data, without fitting and subtracting the $\chi(E)$ background signal. The L_3 absorption edge energy, i.e., the ionization energy, is superimposed by transitions of the $2p_{3/2}$ core electron to unoccupied *nd* states and continuum εd states. The threshold region can be deconvoluted by an arctangent function describing the transition into the continuum, and at least one Lorenz function representing the transition into the *nd* states. This data treatment suffers from the strong correlation between the arctangent and the Lorentz function that needs to include some arbitrary constraints. An analysis of the EXAFS oscillations using phase functions from self-consistent field (SCF) codes allow to determine the origin of the wave vector *k* as ionization energy $E_{k=0}$ [15, 16]. Especially for low *k* range, this procedure depends on the chosen potentials and can lead to some energy differences depending on the elements and its oxidation states. A more simple procedure is the use of the first maximum of the derivative of the raising edge, E_{1st}. The reproducibility of this procedure is in the range of 0.3 eV, but the value is expected to be up to ~ 2 eV too high in relation to the true edge energy. Because this systematic energy shift seems to be a tolerable deviation for the purpose of this study, the energy value of E_{1st} is used for E_0. The estimated values of E_{1st} are given in Table 1 and the corresponding L_3 edge XANES spectra are shown in Figure 2.

Figure 1. L_3-edge k^3 weighted EXAFS data (left) of Th^{4+}, U^{4+}, Np^{6+}, and Np^{4+} and their corresponding Fourier transforms (right).

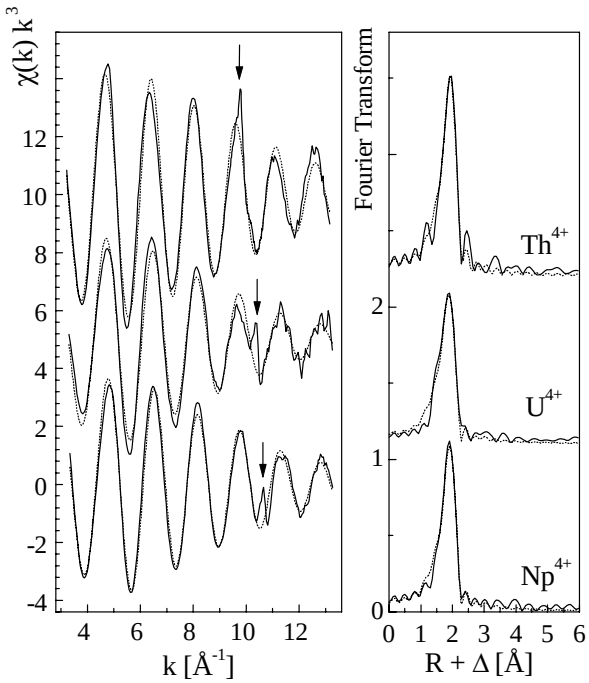

Figure 2. L_3 edge XANES, aligned according E-E_{1st}, where E is the photon energy and E_{1st} is taken from the 1st derivative of the spectrum. E_{WL} is the white line maximum.

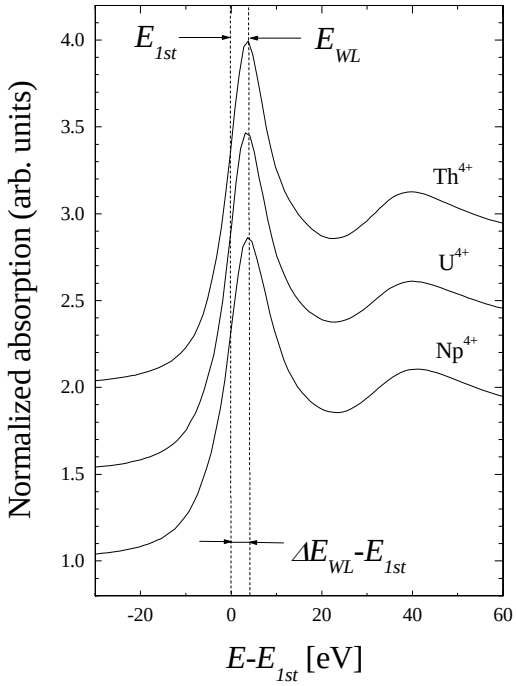

The energy for the electron shell, which is related with the shake-up transition E_S, was estimated by the difference of the maximum of the double-electron excitation E_f and E_{1st}. Due to the edge-like structure of the shake-up effect, as discussed later, E_S needs a correction for the energy difference between the white line maximum E_{WL} and E_{1st}. This energy difference, $\Delta E_{WL\text{-}1st}$, is included in the estimation according

$$E_s = E_f - E_{1st} - \Delta E_{WL\text{-}1st}.$$

$\Delta E_{WL\text{-}1s}$ of the double-electron excitation is assumed to be similar to the L_3 edge. The values of $\Delta E_{WL\text{-}1s}$ at the L_3 edges and the resulting E_s are given in Table 1. In order to assign the shake-up process to the experimental value E_S, a comparison with the electron energies in presence of the $2p_{3/2}$ core-hole is required. The relaxation of an atom due to core-hole creation is usually described in the frame of the $Z+1$ approximation. The energies for this study were taken from Porter and Freedman [17]. Evidence was found between E_S and the $Z+1$ $4f_{5/2}$ and $4f_{7/2}$ energy level, except a energy difference from the valence state of An^{4+}. The related $Z+1$ energies are listed in Table 1. The comparison allows to assign the spectral feature to an excitation of a core $2p_{3/2}$ electron accompanied by the auto-ionization of a $4f$ electron. This process creates a [$2p_{3/2}4f_{5/2}/4f_{7/2}$] double hole configuration, or, in the edge terminology, a $L_3N_{6,7}$ edge. The shake-up of one of the 14 $4f$ electrons to the lowest unoccupied MO results in a feature strong enough to be detecTable. Double excitation effects from other energy levels were not observed in the spectra. Equivalent LN transitions were observed for Pb [18] and Hg vapor samples [19], where the $4f$ shell is already completely occupied. There, the double-electron excitations affect only the background slope. In contrast to these spectra, the LN transitions in actinides are sharp. Figure 3 shows the experimental energy for the shake-up feature in comparison with the $Z+1$ $4f_{5/2}$ and $4f_{7/2}$ energies. For Pa, Z = 91, is no experimental value available. The only reported spectrum does not reach the energy predicted for the shake-up effect [20].

Figure 3. Experimental energy for the shake-up feature (square dots) in comparison with the *Z+1* $4f_{5/2}$ and $4f_{7/2}$ energy (dotted line).

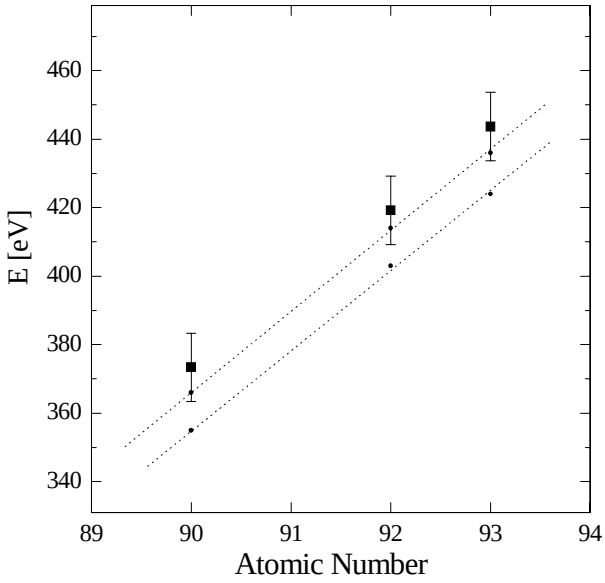

Acknowledgement

The author thanks M.A. Denecke, K. H. Hallmeier, A. Kodre and J. Padežnik Gomilšek for hints and fruitful discussions. The measurement of U^{4+} hydrate was performed with an *in situ* spectroelectrochemical cell in the frame of a project supported by the Deutsche Forschungsgemeinschaft under Grant No. HE 2297/2-1.

References

1. J.M. Esteva, B. Gauthé, P. Dhez, and C.R. Karnatak, J. Phys B **16**, L263 (1983).
2. M. Deutsch and P. Kizler, Phys. Rev. A **45**, 2112 (1992).
3. R.D. Deslattes, R.E. LaVilla, P.L. Cowan, and A. Henins, Phys. Rev. A **27**, 923 (1983).
4. E. Bernieri and E. Burattini, Phys. Rev. A **35**, 3322 (1987).
5. A. Filipponi, E. Bernieri, and S. Mobilio, Phys. Rev. B **38**, 3298 (1988).
6. A. Filipponi, T. A. Tyson, K.O. Hodgson, and S. Mobilio, Phys. Rev. A **48**, 1328 (1993).
7. P. D'Angelo, P.-E. Petit, and N.V. Pavel, J. Phys. Chem. B **108**, 11857 (2004).
8. P. D'Angelo, A. Di Cicco, A. Filipponi, and N. V. Pavel, Phys. Rev. A **47**, 2055 (1993).
9. J. Chaboy, A. Marcelli, and T.A. Tyson, Phys. Rev. B **49**, 11652 (1994).
10. J.A. Solera, J. García, and M.G. Proietti, Phys. Rev. B **51**, 2678 (1995).

11. W. Matz, N. Schell, G. Bernhard, F. Prokert, T. Reich, J. Claußner, W. Oehme, R. Schlenk, S. Dienel, H. Funke, F. Eichhorn, M. Betzl, D. Pröhl, U. Strauch, G. Hüttig, H. Krug, W. Neumann, V. Brendler, P. Reichel, M.A. Denecke, and H. Nitsche, J. Synchrotron Rad. **6**, 1076 (1999).
12. T. Reich, G. Bernhard, G. Geipel, H. Funke, C. Hennig, A. Rossberg, W. Matz, N. Schell, and H. Nitsche, Radiochim. Acta **88**, 633 (2000).
13. C. Hennig, J. Tutschku, A. Rossberg, G. Bernhard, and A.C. Scheinost, Inorg. Chem. **44**, 6655 (2005).
14. C. Le Naour, D. Trubert, M.V. Di Giandomenico, C. Fillaux, C. Den Auwer, P. Moisy, and C. Hennig, Inorg. Chem. **44**, 9542 (2005).
15. A.L. Ankudinov, S.D. Conradson, J. Mustre de Leon, and J.J. Rehr, Phys. Rev. B **57**, 7518 (1998).
16. A.L. Ankudinov, B. Ravel, J.J. Rehr, and S.D. Conradson, Phys. Rev. B **58**, 7565 (1998).
17. C. Le Naour, D. Trubert, M.V. Di Giandomenico, C. Fillaux, C. Den Auwer, P. Moisy, and C. Hennig, Inorg. Chem. **44**, 9542 (2005).
18. G. Li, F. Bridges, and G.S. Brown, Phys. Rev. Lett. **68**, 1609 (1992).
19. A. Filipponi, L. Ottaviano, and T.A. Tyson, Phys. Rev. A **48**, 2098 (1993).
20. C. Le Naour, D. Trubert, M.V. Di Giandomenico, C. Fillaux, C. Den Auwer, P. Moisy, and C. Hennig, Inorg. Chem. **44**, 9542 (2005).

A COMPARATIVE STUDY OF $U^{V}O_2^{+}$- AND $U^{VI}O_2^{2+}$-CARBONATO COMPLEXES IN AQUEOUS SOLUTION

Atsushi Ikeda*, Christoph Hennig, André Rossberg, Andreas C. Scheinost, Gert Bernhard
Institute of Radiochemistry, Forschungszentrum Dresden-Rossendorf,
P.O. Box 510119, 01314 Dresden, Germany

Koichiro Takao, Yasuhisa Ikeda

Research Laboratory for Nuclear Reactors, Tokyo Institute of Technology, Meguro-ku,
Tokyo 152-8550, Japan
(*Contact: +49-351-260-2076, E-mail: A.Ikeda@fzd.de)

Abstract

Electrochemical and spectroscopic (UV-vis and X-ray absorption) studies have been performed for the uranyl (UO_2^{n+}) species in aqueous carbonate solution in order to reveal the redox behavior of uranyl ion and to identify the structural difference between pentavalent and hexavalent UO_2^{n+}. Cyclic voltammetry and bulk electrolysis experiments using a 50 mM U solution suggest that $U^{V}O_2^{+}$, the reduction product of $U^{VI}O_2^{2+}$, is stabilized only in the limited concentration range of 0.8 M < [Na_2CO_3] and 11.7 < pH < 12.0. The $U^{V}O_2^{+}$ species is confirmed to be stable for at least 1 month in a sealed glass cuvette by successive UV-vis absorption measurements. X-ray absorption measurements show that both $U^{V}O_2^{+}$ and $U^{VI}O_2^{2+}$ are co-ordinated by three carbonate ions in their equatorial planes with a bidentate arrangement, forming a tricarbonato complex, $[UO_2(CO_3)_3]^{m-}$ (m = 5 for U(V) and 4 for U(VI)). The electron density of the uranium atom affects the U-O bond lengths that lengthen upon reduction from $U^{VI}O_2^{2+}$ to $U^{V}O_2^{+}$.

Introduction

It is well-known that uranium forms various oxidation states (III, IV, V, and VI) in solution and a large number of studies have been carried out in various chemical systems for each oxidation state. However, there are few data on pentavalent uranium (*i.e.* $U^{V}O_2^{+}$) because this oxidation state is unstable due to its disproportionation reaction, $2U^{V}O_2^{+} \rightarrow U^{IV}O_2\downarrow + U^{VI}O_2^{2+}$ [1].

Recently, several studies have indicated that it is possible to stabilize $U^{V}O_2^{+}$ in organic solvents [2,3] and in ionic liquids [4] by using specific multidentate ligands. In contrast, $U^{V}O_2^{+}$ is significantly unstable in aqueous solution. The uranyl carbonato complex is actually the only known species that is stabilized as $U^{V}O_2^{+}$ in aqueous solution [5-8]. The detailed knowledge about this uranyl(V) carbonato complex is required because it plays an important role in natural redox processes. Furthermore, the uranyl carbonate species is one of the potential species for the migration study on nuclear waste repositories. This study intends to investigate the electrochemical and complexation properties of uranyl carbonate complex in aqueous Na_2CO_3 solution by cyclic voltammetry (CV) measurements, bulk electrolysis, and X-ray absorption fine structure (XAFS) spectroscopy.

Experimental

Materials

The starting material $Na_4[UO_2(CO_3)_3]$ was prepared from $UO_2(NO_3)_2 \cdot 6H_2O$ according to a previous paper [9]. This uranyl carbonate compound was dissolved in a desired concentration of aqueous Na_2CO_3 solution to give a concentration of 50 mM U, and used both for electrochemical experiments and XAFS spectroscopy. All the chemicals used in this study (except $UO_2(NO_3)_2 \cdot 6H_2O$) were reagent grade and supplied by Wako Pure Chemical Ind., Ltd., Japan and Merck KGaA, Germany.

Electrochemical Experiments

CV measurements and bulk electrolysis were performed with a BAS CV-50W voltammetric analyzer or a Meinsberger Potentiostat/Galvanostat PS6. Cyclic voltammograms were obtained under dry Ar atmosphere by using a three-electrode system: a Pt wire counter electrode, an Ag/AgCl reference electrode, and three different working electrodes (Pt, Au, and glassy carbon). Sample solutions for CV measurements were deoxygenated by bubbling dry Ar gas in the solutions for at least 3 hours in advance. For X-ray absorption measurements, bulk electrolysis of uranyl(VI) carbonate solution was performed under dry N_2 atmosphere with a Pt mesh working electrode (80 mesh, 35 × 25 mm, supplied by Bioanalytical System (BAS), Inc.), a Pt wire counter electrode, and a Ag/AgCl reference electrode. A Vycor glass diaphragm was used to separate counter- and reference electrodes from the sample solution. The applied reduction potential was –900 mV vs. Ag/AgCl. UV-vis absorption spectra of the samples were measured before and after the electrochemical reduction using a Varian UV-Vis-NIR spectrophotometer Cary 5G to identify the reduction product in the samples.

X-ray Absorption Measurements

XAFS measurements were carried out on the Rossendorf Beamline BL20 (ROBL) at the European Synchrotron Radiation Facility (ESRF) under dedicated ring operating condition (6.0 GeV, 200 mA). A Si(111) double-crystal monochromator was employed in channel-cut mode. Uranium L_{III}-edge spectra were collected in transmission mode using Ar-filled ionization chambers at ambient temperature. The obtained spectra were treated by using the data analysis program WinXAS (Ver. 3.1) [10]. Theoretical phases and amplitude functions were calculated from the program FEFF 8.20 [11]. The spectra were fit with four single scattering (SS) paths of axial oxygen atoms (O_{ax}), equatorial (O_{eq}) and distal (O_{dist}) oxygen atoms and carbon atoms of co-ordinated carbonate ions (*i.e.* U-O_{ax}, U-

$O_{eq}(CO_3^{2-})$, U-C, and U-$O_{dist}(CO_3^{2-})$), and two multiple scattering (MS) paths (*i.e.* U-O_{ax}- U-O_{ax} and U-C-O_{dist}-C), which were derived from the crystal structure of $Na_2Ca[UO_2(CO_3)_3]\bullet xH_2O$ [12].

Results and Discussion

Cyclic Voltammetry

Figure 1 shows the cyclic voltammograms of $U^{VI}O_2^{2+}$ in 1M-Na_2CO_3 solution at pH = 12.0 for three different working electrodes. The scan rate was varied from 10 to 100 mV/s. Each cyclic voltammogram shows a clear reduction peak (-950 to -900 mV for Pt and Au-electrodes, and -1700 to -1500 mV for glassy carbon electrode) and an oxidation peak (-700 to -400 mV for Pt and Au, and 0 to 250 mV for glassy carbon), corresponding to the reduction of $U^{VI}O_2^{2+}$ to $U^{V}O_2^{+}$ and the reoxidation of $U^{V}O_2^{+}$ to $U^{VI}O_2^{2+}$, respectively. The separation between the cathodic and anodic peaks (ΔE_p) obviously depended on the scan rate for all the cyclic voltammograms and is significantly larger than that expected for a reversible reaction. The kinetic parameters calculated from these cyclic voltammograms are listed in Table 1, suggesting that the present redox process of uranyl ions is classified as a quasireversible system [13] and is interpreted as an electron-transfer limited system [8]. The cyclic voltammogram using the Au working electrode seems to have two oxidation peaks. This may indicate that the redox process is followed by a successive reaction, such as the dissociation of uranyl complexes. On the other hand, only a single redox couple was observed in the cyclic voltammogram using Pt or glassy carbon electrode and no successive reaction occurred. Considering these facts, we conclude that either a Pt or a glassy carbon working electrode is appropriate for the bulk electrolysis.

Figure 1. Cyclic voltammograms for 50 mM UVIO22+ in 1M Na2CO3 solution (pH = 12.0)

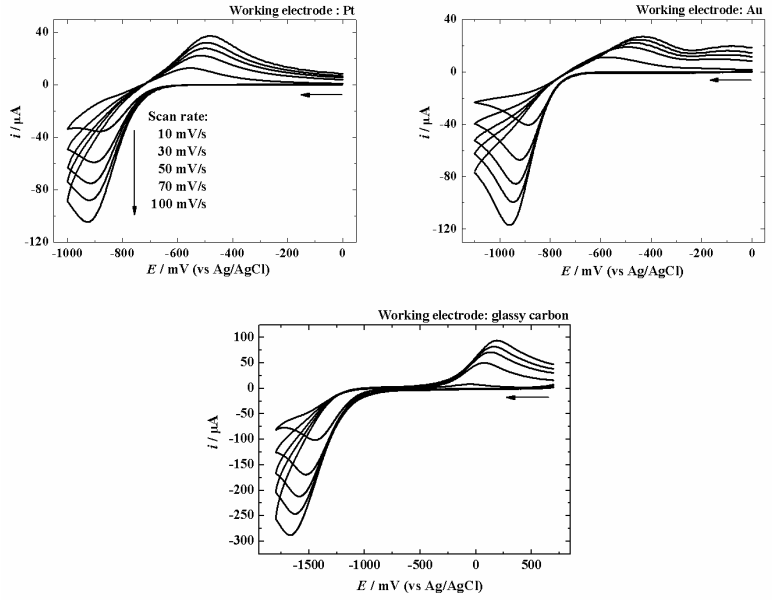

Table 1. $U^{VI}O_2^{2+}$/ $U^{V}O_2^{+}$ redox parameters calculated from the cyclic voltammograms in Figure 1

Working electrode	Diffusion coefficient for reduced species (D_R) / cm^2/s	Standard rate constant (k^0) / cm/s
Pt	2.48×10^{-6}	2.36×10^{-4} ($\pm 0.35 \times 10^{-4}$)
Au	2.81×10^{-6}	2.39×10^{-4} ($\pm 0.21 \times 10^{-4}$)
Glassy carbon	3.73×10^{-6}	6.01×10^{-5} ($\pm 0.97 \times 10^{-5}$)

Bulk Electrolysis

Bulk electrolysis experiments of $U^{VI}O_2^{2+}$ in Na_2CO_3 solution were carried out in various concentrations of Na_2CO_3 with different pH in order to determine the appropriate conditions for preparing a stable uranyl(V) carbonate sample for XAFS measurement. The uranyl(V) carbonate species could be stabilized with the Na_2CO_3 concentrations higher than 0.8 M. The electrolysis performed in less than 0.8 M-Na_2CO_3 solution resulted in the production of yellow-brown colored fine precipitation. Furthermore, the reduced uranyl(V) carbonate species was stable only in the limited pH range of 11.7 < pH < 12.0. Any deviation from this pH range gave brownish precipitation, probably due to the disproportionation reaction mentioned above. The stability limits of uranyl(V) carbonate species are summarized in Figure 2. Additionally, the stability of uranyl(V) carbonate species also depends on the concentration of U and it decreases with increasing U concentration. Accordingly, the uranyl(V) carbonate sample for XAFS measurement was prepared in 1.4 M- Na_2CO_3 solution with pH = 11.9. Figure 3 shows the UV-vis absorption spectra of uranyl carbonate solution before and after the electrolysis. Characteristic absorption bands for the uranyl(VI) carbonato complex [14] considerably decreased after the electrolysis, as previously reported [6], suggesting that $U^{VI}O_2^{2+}$ was successfully reduced to $U^{V}O_2^{+}$. The U(V)/U(VI) ratio in the sample after the electrolysis was estimated as 94.4/5.6 (M/M) from the spectra.

Figure 2. Na_2CO_3 concentration -pH diagram for stable uranyl(V) carbonate species in Na_2CO_3 solution ([U] = 50mM)

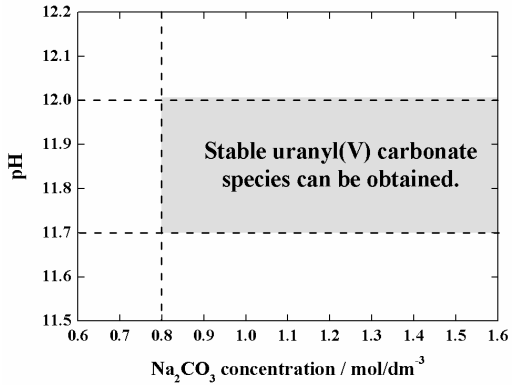

Figure 3. Variation in UV-Vis absorption spectra before and after the electrolysis of 50 mM $U^{VI}O_2^{2+}$ in 1.4 M Na_2CO_3 (pH = 11.9)

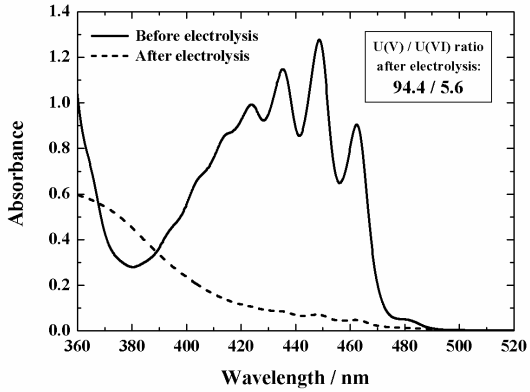

XAFS Measurements

The $U^{V}O_2^+$ species is extremely sensitive to O_2 and reoxidezes promptly. Therefore, the uranyl(V) carbonate sample obtained in the above-mentioned electrolysis was placed in a glass cuvette with a 1 cm optical path length under dry N_2 atmosphere in a glove box (O_2 concentration in the glove box was less than 1 ppm). The cuvette was then sealed up by hot melting. The sealed uranyl(V) carbonate sample was confirmed to be stable at least one month by successive UV-vis absorption measurements. A uranyl(VI) carbonate sample (*i.e.* the sample before the electrolysis) was transferred to a polyethylene container (optical path length = 1.3 cm) and sealed by melting.

The k^3-weighted U L_{III}-edge EXAFS spectra for the uranyl(VI)- and uranyl(V) carbonate species and their corresponding Fourier transforms (FTs) are shown in Figure 4. It is clear that the EXAFS oscillation pattern of the uranyl(V) species is different from that of the uranyl(VI) one. Additionally, the EXAFS spectrum of our uranyl(V) carbonate sample is dissimilar to the previously reported EXAFS spectrum for uranyl(V) tricarbonate species [15]. Their FTs exhibit some similarities, suggesting that the co-ordination geometry of the uranyl(V)- and uranyl(VI) species is comparable. However, every peak of the FT magnitude (solid line) of the uranyl(V) species shows approximately 0.1 Å higher *R* values than that of the uranyl(VI) one.

Figure 4. k^3-weighted U L_{III} of uranyl(VI) and uranyl(V) carbonate species in 1.4 M Na_2CO_3 (left) and their corresponding Fourier transforms (right) (solid line: experimental data, circled data: theoretical fit)

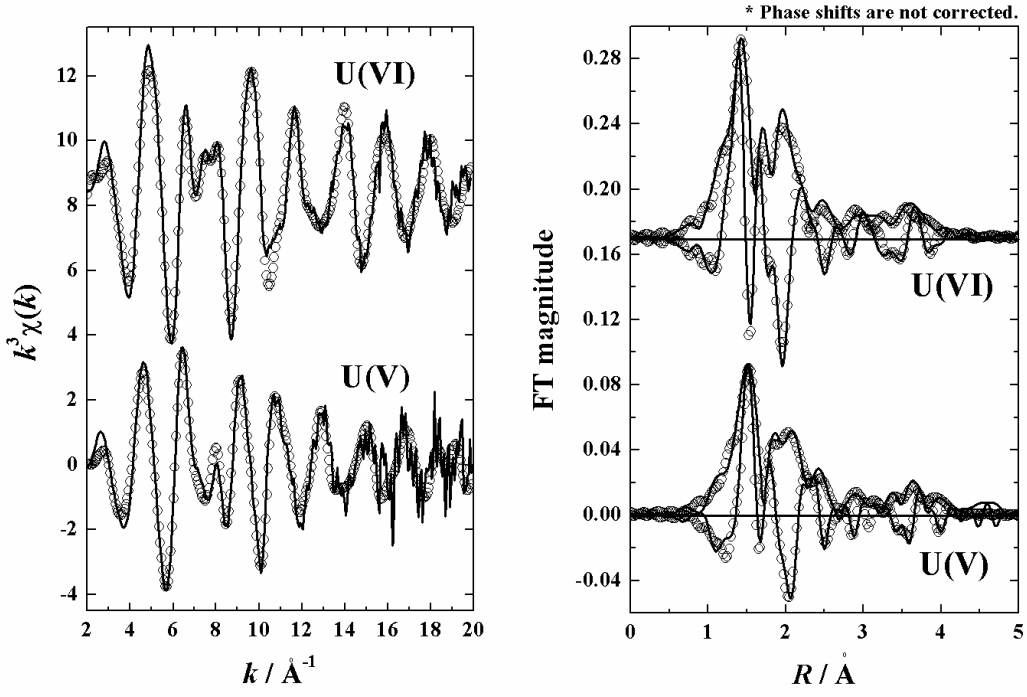

The structural parameters obtained from the curve fitting are listed in Table 2. Several studies have suggested that both uranyl(V)- and uranyl(VI) cations predominantly form a bidentate-co-ordinated tricarbonato complex, $[UO_2(CO_3)_3]^{n-}$, in basic Na_2CO_3 solutions [14-18]. Therefore, the co-ordination numbers (*N*) were fixed to the tricarbonato complexes values. Each interatomic distance (*R*) for the

uranyl(V) tricarbonato complex is longer than that for the uranyl(VI) tricarbonato complex due to the decrease in the charge density of uranyl center. The present results also reveal that the interatomic distance for U^{VI}-O_{dist} (a single scattering path) is longer than the effective distance for the multiple scattering along U^{VI}-C-O_{dist}-C. This may imply that U, C, and O_{dist} atoms are not arranged linearly and the bond between C and O_{dist} is slightly tilted relative to the U center. A similar tilting of the carbonate groups has also been observed in the solid structure of $Na_2Ca[UO_2(CO_3)_3]\bullet xH_2O$ [12]. The $[UO_2(CO_3)_3]^{n-}$ complexes have a high negative charge and this charge is assumed to be compensated by counter cations [19]. Therefore a fit including Na as countercation was performed. This fit yielded a U-Na distance of 3.87 Å for uranyl(VI) and 3.98 Å for uranly(V) and reduced the error of the fit, although this is not certain proof of their presence. The uranyl(V) complex shows larger Debye-Waller factors (σ^2) than the uranyl(VI) one. This is surely related with the increase in interatomic distances on the uranyl(V) complex and associated weaker chemical bonding between $U^{V}O_2^{+}$ and CO_3^{2-} compared to that between $U^{VI}O_2^{2+}$ and CO_3^{2-}. Consequently, the uranyl(V) carbonato complex is supposed to be less stable than the uranyl(VI) one. The electrochemical instability of uranyl(V) carbonato species might be caused by this weaker bond strength of $U^{V}O_2^{+}$.

Table 2. EXAFS structural parameters obtained from curve fitting

	Shell	Path	N (fixed)	R / Å	σ^2 / Å^2	ΔE_0 / eV	S_0^2 (fixed)	Fitting residual
U(VI)	Oax	SS	2	1.81	0.0015	5.26	0.9	14.8
	Oeq	SS	6	2.44	0.0059			
	C	SS	3	2.92	0.0030			
	Oax	MS(4)	2	3.60	0.0070			
	Odist	SS	3	4.17	0.0045			
	C-Odist-C	MS(4)	3	4.23	0.0039			
U(V)	Oax	SS	2	1.91	0.0023	4.86	0.9	16.4
	Oeq	SS	6	2.50	0.0070			
	C	SS	3	2.93	0.0030			
	Oax	MS(4)	2	3.83	0.0060			
	Odist	SS	3	4.23	0.0030			
	Odist-C	MS(4)	3	4.23	0.0067			
	Error			±0.005	±0.0005	±0.01		

Figure 5. Structure of uranyl tricarbonato complex $[UO_2(CO_3)_3]^{4-}$ in the single crystal of $Na_2Ca[UO_2(CO_3)_3]\bullet xH_2O$ [12]

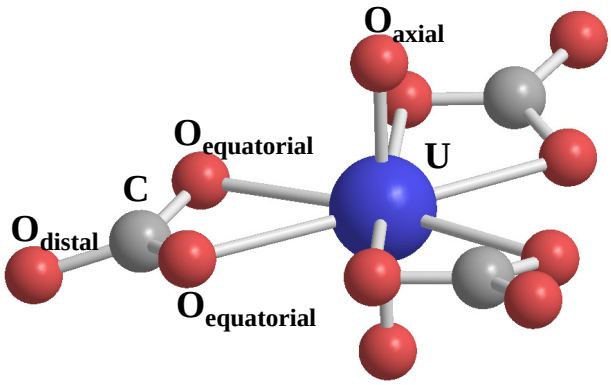

Summary

The electrochemical behavior and structure of uranyl carbonate species in aqueous carbonate solution were investigated. The redox reaction between $U^{VI}O_2^{2+}$ and $U^{V}O_2^{+}$ is quasireversible in 1.0 M Na_2CO_3 solution. High purity of uranyl(V) carbonate sample was obtained by a bulk electrolysis in the Na_2CO_3 concentration higher than 0.8 M, in the limited pH range of 11.7 < pH < 12.0. Both $U^{VI}O_2^{2+}$ and $U^{V}O_2^{+}$ formed the tricarbonate complex, $[UO_2(CO_3)_3]^{n-}$ (n = 4 for uranyl(VI), 5 for uranyl(V)), in aqueous carbonate solution. The U-O interatomic distances of the uranyl(V) carbonato complex are longer than those of the uranyl(VI) carbonato one.

References

1. D.M.H. Kern, E.F. Orlemann, *J. Am. Chem. Soc.*, **71**, 2102 (1949).
2. K. Mizuoka, S.-Y. Kim, M. Hasegawa, T. Hoshi, G. Uchiyama, Y. Ikeda, *Inorg. Chem.*, **42**, 1031 (2003).
3. K. Mizuoka, S. Tsushima, M. Hasegawa, T. Hoshi, Y. Ikeda, *Inorg. Chem.*, **44**, 6211 (2005).
4. S.-Y. Kim, K. Mizuoka, Y. Ikeda, *unpublished data*.
5. D. Cohen, *J. Inorg. Nucl. Chem.*, **32**, 3525 (1970).
6. D.W. Wester, J.C. Sullivan, *Inorg. Chem.*, **19**, 2838 (1980).
7. C. Madic, D.E. Hobart, G.M. Begun, *Inorg. Chem.*, **22**, 1494 (1983).
8. D.E. Morris, *Inorg. Chem.*, **41**, 3542 (2002).
9. "*Gmelins Handbuch der anorganischen Chemie*", 8. Auflage, System-Nummer 55, S. 193, Verlage Chemie, Berlin, 1936.
10. T. Ressler, *J. Synchrotron Rad.*, **5**, 118 (1998).
11. A.L. Ankudinov, B. Ravel, J.J. Rehr, S.D. Conradson, *Phys. Rev. B*, **58**, 7565 (1998).
12. A. Coda, A.D. Giusta, V. Tazzoli, *Acta Cryst.*, **B37**, 1496 (1981).
13. J. Heinze, *Angew. Chem. Int. Ed.*, **23**, 831 (1984).
14. K. Mizuguchi, Y.-Y. Park, H. Tomiyasu, Y. Ikeda, *J. Nucl. Sci. Technol.*, **30**, 542 (1993).
15. T.I. Docrat, J.F.W. Mosselmans, J.M. Charnock, M.W. Whiteley, D. Collison, F.R. Livens, C. Jones, M.J. Edmiston, *Inorg. Chem.*, **38**, 1879 (1999).
16. J.P. Scanlan, *J. Inorg. Nucl. Chem.*, **39**, 635 (1971).
17. S.Ó. Cinnéide, J.P. Scanlan, M.J. Hynes, *J. Inorg. Nucl. Chem.*, **37**, 1013 (1975).
18. P.G. Allen, J.J. Bucher, D.L. Clark, N.M. Edelstein, S.A. Ekberg, J.W. Gohdes, E.A. Hudson, N. Kaltsoyannis, W.W. Lukens, M.P. Neu, P.D. Palmer, T. Reich, D.K. Shuh, C.D. Tait, B.D. Zwick, *Inorg. Chem.*, **34**, 4797 (1995).
19. G. Bernhard, G. Geipel, T. Reich, V. Brendler, S. Amayri, H. Nitsche, *Radiochim. Acta*, **89**, 511 (2001).

RADIOCHEMICAL SYNTHESIS OF SODIUM FLUORIDE

J. Jankowski, K. Kasprzak, A. Dąbkowski, A. Kowalska, B, Kowal, B. Małkowski
Department of Nuclear Medicine, Center of Oncology, Bydgoszcz, Poland

Abstract

Fluoride ^{18}F is taken up in bone in proportion to blood flow and bone metabolism activity. The fluoride ion becomes incorporated into bone as a result of ion exchange. It was known that (^{18}F)NaF has the highest sensitivity in detecting bone metastases. In our department we have performed only FDG PET-CT studies so far. The aim of the study was to obtain the sodium fluoride (^{18}F)NaF suitable for PET-CT diagnostics.

ACTINIDES INTERACTION WITH BIOLOGICAL MOLECULES

A. Jeanson[1], C. Den Auwer[1], P. Moisy[1] and C. Vidaud[2]
[1]DEN/DRCP/SCPS, CEA Marcoule, 30207 Bagnols-sur-Cèze Cedex, France
[2]DSV/DIEP/SBTN, CEA Marcoule, 30207 Bagnols-sur-Cèze Cedex, France

Abstract

For toxicological purposes, general understanding needs to be deepened on intramolecular interactions in molecular actinide species. Metallobiomolecules are thus considered as elaborate inorganic complexes with well-designed metal active sites. Although the various interaction processes between essential biological cations and proteins are widely studied, focus on the actinides is more seldom.

Because of its major role on iron transport, our study focuses on the transferrin system. To cast light on the interaction between transferrin and actinides, this paper presents a brief review of related data in the literature. In this field, X ray Absorption Spectroscopy can be used as a structural and electronic metal cation probe. Combination with more traditional spectroscopic techniques such as spectrophotometry is ideal for the understanding of the chelation mechanism. Our recent results on holotransferrin are presented at the end of the paper. Fitting of the EXAFS data needs to take into account multiple scattering effects. The first low-Z (oxygen and/or nitrogen atoms) co-ordination shell has been found at 2.02 Å, in good agreement with literature structural data obtained with X-ray diffraction. Parallely, study of actinide complexation with transferrin has been undertaken with UV-vis-NIR spectroscopy and EXAFS.

Introduction

In the field of human technology, internal contamination with actinides can induce both radiological and chemical toxicity. Whatever the way of contamination (inhalation, ingestion or wound), the radionuclide is absorbed into, and then transported by blood before being deposited in its target organs in which it is stored and then slowly eliminated through urines and faeces.

Although there is a tremendous volume of data available on the interaction of plutonium with living organisms as plants, nearly all the studies are limited to macroscopic or physiological measurements with no specific information at the molecular level. Molecular approaches have been more seldom due to the combined intricacy of metallo biochemistry and actinide chemistry. However, such “molecular speciation” in actinide biomolecules is of considerable interest in order to understand the potential transport of radionuclide inside living organisms. It also has an important input in providing guidance on the structure, affinity and design of potential specific chelating agents synthesized and used for the elimination of an incorporated radionuclide.

According to Taylor, actinides, when in the blood serum, are mainly complexed to transferrin [1]. Transferrin is an abundant protein in mammalian serum. Like its homologues in egg white and milk (ovotransferrin and lactoferrin), serum transferrin regulates iron transport in cells. Transferrin is thus likely to be an essential vector for actinides in living organisms, and actinide-transferrin systems should be studied in order to better understand assimilation mechanisms of radioactive elements in living organisms. Several studies have shown that the conformation of transferrin depends on the complexed ion [2]. To be able to establish if transferrin is one possible way for actinides to enter human cells, it is essential to determine if the transferrin-actinide complex has the right conformation to be recognised by its receptors.

The chemical behaviour similarity between Pu(IV) and Fe(III) has been observed on several occasions, especially in the transferrin system. Indeed, Pu(IV) bound to transferrin has been reported to be located in the iron site [4,5]. A homology is also expected for Np(IV) and Th(IV) which are chemically similar to Pu(IV). Moreover, Study of U(VI) complexation with transferrin would be interesting as well, because of the structural difference between U(VI) ("rod-like") and "spherical-like" actinides (IV).

This paper reviews some of the literature data available on this field, and presents in the last paragraph our latest results on iron transferrin complex. Our preliminary results on actinide transferrin complexes are also reviewed and more detail analysis will be published elsewhere.

Macroscopic physiological studies

Since the fifties, impact of actinides on living organisms has been deeply studied. These studies show that actinides are chemical poisons as well as radiological hazards. Because of their strong tendency to hydrolyse at physiological pH, the free actinide ions in living organisms can only exist in complexed form or as hydrolysed species [1]. In a review of Taylor about actinide speciation in blood [1], it is shown that the majority of the total blood content of U and Th is associated with the blood cells, while 90 % of the Pu(IV), Am(III), Cm(III) and Cf(III) in blood are found in plasma. Moreover, actinides in plasma are mainly complexed to transferrin.

Thorium

The only stable oxidation state for thorium in aqueous solution is Th(IV): at physiological pH, thorium salts hydrolyse to form colloidal particles of $Th(OH)_4$. Th(IV) has been reported to be transported in the bloodstream bound to transferrin [6]. Th(IV) ion or its hydroxide colloids react *in vivo* with proteins, amino acids and nucleic acids to form stable complexes in tissues, principally in bone, liver, bone marrow, spleen, and kidneys [6-11].

Uranium

Uranium is a common trace element in the environment and some uranium intake and accumulation is natural. The most stable species in aqueous solution and *in vivo* is the uranyl ion UO_2^{2+}. Uranyl is nephrotoxic, chemically toxic, and carcinogenic in bone, the major long-term storage organ for soluble uranium. In humans, about 65% of uranium intake is excreted. 20% of the total uranium absorbed into the circulation is deposited in bone, and about 12% in kidney. The renal excretion pathway explains the tendency of U(VI) to concentrate in the kidneys [6,12-14]. Using a thermodynamic speciation code, Sutton *et al.* have predicted uranium solubility and speciation in several human biological fluids, taking into account pH, uranium concentration, fluid composition, and ionic strength of each system. They show that uranium solubility is several times higher inside a cell, controlled by the formation of potassium-autunite ($K_2(UO_2)_2(PO_4)_2.6H_2O$), than outside a cell, controlled by the formation of sodium-autunite ($Na_2(UO_2)_2(PO_4)_2.8H_2O$). Carbonate, hydroxide and phosphate complexes seem to be the dominant species in many of the biological fluids [15]. Generally, uranyl cation is partitioned in the serum into the uranyl bis- and tris-carbonate complexes and UO_2:protein:carbonate complexes with human serum albumin, transferrin or other protein. Of the two fractions, the uranyl-carbonate complexes are more diffusible into tissue, while the portion bound to protein is the portion cleared from the serum via transport to and elimination from the kidneys [16,17].

Neptunium

The chemical toxicity of NpO_2^+ is similar to that of UO_2^{2+}. Depending on redox conditions *in vivo*, Np exists as weakly complexing Np(V) or as Np(IV), which forms complexes as stable as those of Pu [6,18]. Distribution of neptunium 24h after absorption into blood of adult animals seems independent of species and mode of administration. About 50% of absorbed neptunium is excreted in urine in the first 24h, and 45% are accumulated in the skeleton, its main target tissue, the rest being mainly deposited in liver. The dominant neptunium species circulating and excreted in urine is Np(V), while that of bone and liver deposits is Np(IV) [19].

Plutonium

In biological systems, most Pu is in the (IV) oxidation state [20,21], and forms complexes with citrate, ascorbate, amino acids and proteins. The most important biological complex of Pu in plasma is that formed with transferrin [22,23]. Durbin *et al.* showed that the behaviour of Pu in mammals may depend on the form in which the radionuclide is administered, on the way of contamination, and on the contaminated subject age and species [20]. Both the amount and rates of Pu absorption decrease in the order: soluble complexes > hydrolysable salts > insoluble compounds. When introduced as a metabolizable complex or simple salt, Pu is transported in plasma mainly by transferrin. It is then deposited in liver, which is favoured when Pu is introduced directly by the parenteral way, or on the bone surface, which is favoured when Pu has been transported across barriers as in the case of injection or inhalation. Absorption of Pu from the gastrointestinal tract is greater in very young animals than in adults. Deposition of Pu in bone is greater in growing animals than in young adults [20].

Structural studies

In order to better understand the interaction mechanisms between actinides and transferrin, it is useful to study complexation processes with amino-acids and peptides that are molecular bricks of the transferrin complexation site. One should however keep in mind that cooperative effect from the protein tertiary structure might also be significant.

Actinide-amino acid and Actinide-peptide-like ligand complexes

Amino acids

Very few structural studies in aqueous media have been undertaken on actinide complexation with amino-acid, probably because of the difficulty of actinide hydrolysis at neutral pH.

The interactions of uranyl ion with aspartic and glutamic acid, both dicarboxylate amino acids, in NaCl aqueous solution have been reported by Gianguzza *et al.* [28]. In addition to the simple species $(UO_2)A$ (A^{2-}= aspartic or glutamic ligand), protonated $(UO_2)AH^+$ and hydroxo $(UO_2)_2A(OH)_2$ mixed species have also been found. $(UO_2)A(OH)^-$ was also hypothesised [28]. The generally low thermodynamic stability of the uranyl carboxylate interactions and propensity for uranyl hydrolysis appears to inhibit the structural determination of many amino-acid complexes. Of the twenty common amino acids, only uranyl structures with two of those, proline and glycine, are known. These structures are reviewed by Van Horn *et al*. [16] The structure with proline (complex formula: $[UO_2(Pro)_2(NO_3)_2]$) is hexaco-ordinate in the equatorial plane, exhibiting monodentate co-ordination from the prolyl carboxylate donor, with nitrate ligands completing the co-ordination sphere of the uranyl cation. Two different complexes are formed with glycine: a bis-glycinatodichloro uranyl complex, which exhibits distorted pentagonal bipyramidal geometry, with one monodentate carboxylate glycine, and one bidentate. (the chloride anions, which complete the co-ordination sphere of uranyl, are in cis) and a tetrakis-glycinato complex with a hexagonal bipyramidal co-ordination sphere with alternating bidentate and monodentate carboxylato donors in the equatorial plane of uranyl [16,29-31].

It must be kept in mind that all these structures do not truly mimic protein binding sites, since the amino acid ligands bind the actinide with their peptidic group. In metalloproteins, the peptidic bound defines the secondary structure of the edifice, while lateral group intervene in metal complexation.

Peptide-like ligands

Four types of thorium complexes have been determined by X-ray diffraction (Raymond *et al.* [32-35]), in order to explore ligand structures that would prove optimal for the design of actinides chelating agents. A tetrakis(catecholato)thorate(IV) complex, two tetrakis(N-alkylalkane-hydroxamato)-thorium(IV) complexes, hydroxypyridinone complexes and terephtalamide complexes are described in Gorden's review. It must be noted that, while hydroxypyridonate complexes with Ce(IV), used as model for the actinides, are eight co-ordinate, X-ray crystal structure of a Th(IV)-HOPO complex shows that thorium is nine co-ordinate [6, 32-36].

Uranyl has been shown to bind to synthesised polypeptides (Aspartate-Alanine-Histidine-Lysine (DAHK) and Glycine-Glycine-Histidine (GGH)) in presence of carbonate ions, and to form $[[UO_2(CO_3)_2(DAHK)]$ (log K = 3.1±0.4) and $[UO_2(CO_3)_2(GGH)]$ (log K = 2.2±0.4) complexes [37]. No structural study of these complexes has yet been undertaken.

Four uranyl tetradentate Me-3,2-HOPO ligands, the most promising sequestering agents yet studied, have been characterised [6,38]. All the complex structures are similar, composed of one uranyl, one tetradentate 3,2-HOPO ligand, and one co-ordinated solvent molecule. The structures demonstrate that uranyl is fully bond by those ligands in a nearly planar ring perpendicular to the axis occupied by the oxo oxygen atoms. In each case, the metal ion is co-ordinated by seven oxygen atoms in slightly distorted bipyramidal geometry.

A neptunyl diamide complex has been synthesised and characterised by Tian *et al.* [39]. The complex formula is $[Np(V)O_2(L^2)_2]ClO_4$, with L^2 = tetramethyl-3-oxa-glutaramide. The O=Np=O moiety is perfectly linear, with Np=O distances of 1.729 Å. The two L^2 ligands are tri-co-ordinated, coplanar in the equatorial plane, and mirror images of each other.

Ce(IV) and Hf(IV) complexes have often been used as models for the study of Pu(IV) co-ordination chemistry. Gorden *et al.* [6] have reported in their review several catecholato and hydroxypyridinone –Ce and –Hf structures. Hf(IV) has been found not as suitable as Ce(IV) to model actinide(IV), due to some ligand field difference.

Neu *et al.* [40, 41] have synthesised a plutonium complex with desferrioxamine E (DFOE), a cyclic hydroxamates siderophore containing 1-amino-5-hydroxyaminopentane as a building block. Siderophores are low-molecular weight chelating agents that are excreted by many microorganisms in order to obtain sufficient iron. Whatever the oxidation state of the reactant, a Pu(IV)-DFOE adduct is formed. The co-ordination sphere is a distorted tricapped-trigonal prism, with the DFOE in approximately one hemisphere and three water molecules in the other. To accommodate these water molecules, the hydroxamate groups are twisted by 20° relative to the [Fe(III)(DFOE)] structure were the six-co-ordinate cation is coplanar with the siderophore, thus fully encapsulated. These similarities between the crystal structures of Fe(III)-DFOE and Pu(IV)-DFOE may explain why the Pu(IV)-DFOB complex (DFOB is the linear analogue of cyclic DFOE) has been shown to be recognized by the bacteria, but not taken up as efficiently as Fe(III)-DFOB.

Gorden *et al.* have recently reported the first Pu(IV) hydroxypyridonate complex to be structurally characterised [42]. The asymmetric unit cell contains two unique eight-co-ordinate plutonium complexes. Each central Pu atom is co-ordinated by eight oxygen atoms, four from each 5LIO(Me-3,2-HOPO) ligands, forming a sandwich-like structure. There are two different types of coordinating oxygen bonds in each Pu molecule: phenolic and amid, with oxygen atoms coordinating the amide having a longer metal-oxygen bond length. Both of the Pu co-ordination spheres in [Pu(IV){5LIO(Me-3,2-HOPO)}] are distorted bicapped trigonal prisms.

Actinide-proteins complexes

A screening of uranyl-protein complexes of the Protein Data Bank (PDB) structures has been carried out by Van Horn *et al.* [16]. The co-ordination donors include aspartyl and glutamyl carboxylate, tyrosinate and amide oxygen donors. Acidic amino-acids (Asp and Glu) or free carboxylate terminus are indicated as binding uranium in most of the reported structures. However, those structures are rarely resolved enough to refine the oxo ligands of uranyl. Pible *et al.* have recently developed an *in silico* method in order to localize complexation sites of uranyl in 3D-structures of proteins [27].

Transferrin

Description of transferrins

Transferrins are monomeric glycoproteins of about 80 kDa with a single polypeptide chain of 670-700 amino acids, used for the solubilization, sequestration, and transport of ferric iron. Three main families of transferrins are known: serum transferrin, which represents 3% of plasmatic proteins, lactoferrin, present in secretory fluids, and ovotransferrin, the protein of avian egg white. The levels of sequence similarity between these transferrins are sufficient to imply that they share a common three-dimensional structure [43].

The global structure of transferrins is represented on Figure 1.A. The polypeptide chain is first of all folded into two globular lobes, representing the N-terminal and C-terminal halves of the molecule. Each lobe contains a single iron binding site, and each has essentially the same folding. The two lobes are joined by a short connecting polypeptide. Each lobe is composed of two separately folded domains, which confers the protein a great flexibility. When Fe(III) is complexed in a site of transferrin, the lobe is closed, as its two domains draw nearer. Target organs' cells of transferrin possess membrane receptors which selectively bind the diferric form of transferrin (holotransferrin), where both lobes are closed, to the detriment of its free form (apotransferrin), fully open. The

holotransferrin binds to specific cell receptor molecules, is internalized, released its iron inside the cell, and is then liberated and re-enters circulation as apoprotein [43,44].

Figure 1: A: Structure of differic porcine serum transferrin (from structure 1H76 of PDB [45]). B: scheme of the transferrin binding site (from ref. [43])

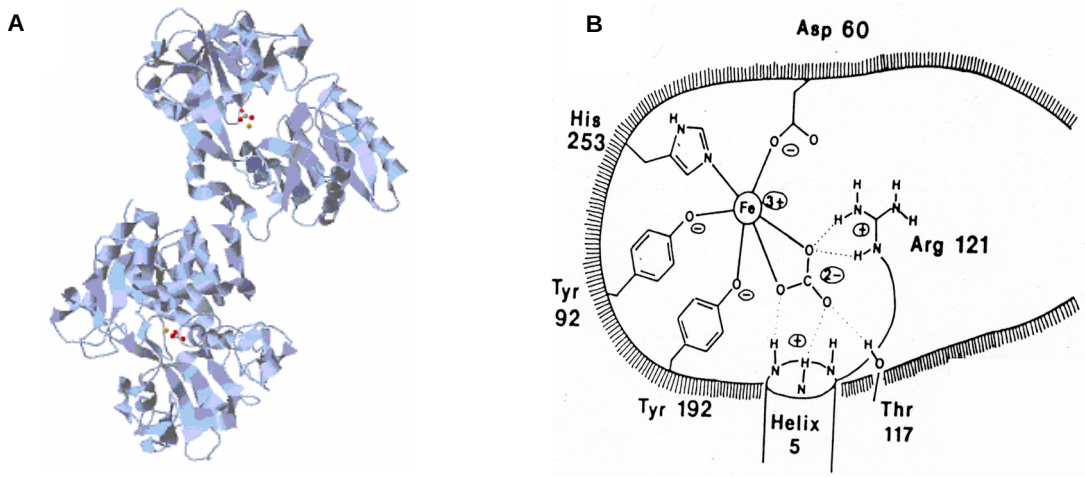

Holotransferrin structures have been determined by X-Ray diffraction. Both lobes of transferrin are quite similar, however iron affinity seems to be slightly more important for the C-terminal lobe than for the N-terminal one [3]. The C-lobe is indeed known to bind iron more strongly, release it more slowly, and to be conformationally less flexible [43,46,47]. The iron complexation site is represented schematically in Figure 1.B. In both lobes, iron's ligands are phenolate oxygens of two tyrosines (Tyr95, Tyr188), imidazole nitrogen of one histidine (His249) and carboxylic oxygen of an aspartate (Asp63). A synergistic anion is required for the complexation in its bidentate co-ordination mode. It forms a distorted octahedron co-ordination sphere. In physiological media, carbonate fills the role of the synergistic anion. However, some other organic anions, as oxalate, lactate, or nitrilotriacetate, can substitute in carbonate-free conditions [43,48]. A few Extended X-ray Absorption Fine Structure (EXAFS) studies of transferrins have already been carried out, mainly by Garrat *et al*. [49]. These studies, undertaken with ovotransferrin and serum transferrin, indicated the co-ordination of six low-Z ligands with bond distances of 1.9-2.1 Å, consistent with X ray crystallography studies.

In 1993, Lindley *et al.* [50] proposed a mechanism for iron uptake. The initial stages are the binding of the synergistic anion, followed by the metal ion which is first bound to the carbonate ion and the two tyrosines, all located in the same domain. Iron is then complexed by aspartate and histidine, situated on the other domain, which allows the lobe closure. Grossmann *et al.* showed that the domain closure is probably a two-step process [51]. However a single-domain binding, without domain closure, is possible, when the metal ion does not bind to aspartate and histidine. It should be kept in mind that the distinction between close and open state is critical, since without closure of the lobe, transferrin would not favour receptor binding and entry into cells [52].

Other metals

Transferrins are regarded primarily as iron-binding proteins. However, they can accommodate a wide variety of other metal ions, including most of the first row transition elements, several of the second and third rows, group 13 metal ions, lanthanides and actinides [43]. It should be noted that transferrins have a strong preference for cations with a high positive charge. Most of the non-transition

metal ions bound are tri- or tetravalent [43]. Several cations, as Cr(III), Mn(III), VO(II),…, have been shown to bind in the iron complexation site [43,53], but not necessarily with the same amino acids.

Garrat *et al.* [54] have shown, from an EXAFS study of chicken dicupric ovotransferrin, that in the case of Cu(II), the synergistic anion may be capable of behaving as a monodentate ligand. They proposed that only three protein donor groups bind to Cu(II), with the synergistic anion monodentate in one lobe, and bidentate in the other lobe. However, this difference with regards to holotransferrin does not seem to affect the domain closure. Indeed, small angle X-Ray scattering studies [43,55] have shown that Cu-Ovotransferrin complex is conformationally indistinguishable from the differic protein. Binding of In(III) and Al(III) also induces similar closure of the domain. In contrast, Hf(IV) did not lead to the same domain closure. It has been proposed that most of the smaller cations will favour a closed conformation, whereas most of the larger may not. However, a more recent study by Harris *et al.* [56] argues that the size of the Hf(IV) ion is not the critical factor. They suggested that the lack of domain closure in Hf-Tf may be related to the combination of a higher co-ordination number and the strong hydrolytic tendency of the Hf(IV) ion.

There have been a number of studies of lanthanide binding to transferrins. The four smaller lanthanides used (Eu(III), Tb(III), Ho(III), and Er(III)) were shown to bind at both sites of transferrin, whereas two larger ions (Pr(III) and Nd(III)) bound only at one site. It was suggested that one of the specific transferrin sites was too small to accommodate larger lanthanides [43,57]. However, the study of Harris *et al.* cited above showed that neither the C- nor the N-terminal binding site imposes a significant size restriction for metals with radii up to that of Cd(III), or 0.95 Å. Both sites seem to be able to bind large metal ions, but the study does not exclude a more subtle decrease in binding affinity due to steric restriction [56]. Baker *et al.* recently suggested that both metal sites were restricted to a maximum co-ordination number of six, and that even the insertion of additional water ligands into the co-ordination sphere could probably lead to domain opening [52]. Moreover, transferrin seems to stay in its open conformation when complexing lanthanides, the co-ordination sphere of the latter being completed by water molecule or other species [43,58].

Actinide-Transferrin complexes

Harris *et al.* [24] have studied thorium(IV) complexation with transferrin, with nitrilotriacetic acid (NTA) as a synergistic anion, using a difference ultraviolet spectroscopy method. They showed that at physiological pH, transferrin binds two thorium ions at non-equivalent sites. The C-terminal binding site of transferrin co-ordinates via two tyrosine residues and the N-terminal one via one tyrosine. The N-terminal site seems to be slightly smaller than the C-terminal site and cannot readily accommodate cations larger than Eu(III). This may explain why Th(IV) large ionic radius makes it difficult to fit into the N-terminal site. Based on this size criterion, Th(IV) may not be a good biological model for Pu(IV) in the case of transferrin. Influence of pH on the complexation was also studied. As pH decreases under neutral pH, the relative binding strength of NTA versus transferrin seems to increase, and only 0.3 thorium ions are bound to transferrin. Above pH 9, there is a conformational change in the protein which converts the C-terminal site in a second one tyrosine binding site [24].

Uranyl complexation with transferrin has been demonstrated by numerous methods, as UV difference spectroscopy [59], chromatography [60], electrophoresis and TRLIF (Time-Resolved Laser-Induced Fluorescence) [61]. The structure of the transferrin binding site of uranyl has been studied by Vidaud *et al.* by UV-visible spectroscopy and FTIR (Fourier Transform Infra-Red) experiments. A binding site has been proposed, involving some amino acids of the iron complexation site [25].

Complexation of neptunium (IV) with transferrin and NTA as a synergistic anion has already been investigated by Racine [62] and Llorens *et al.* [26]. Transferrin binds two Np(IV) ions in presence of a synergistic anion. The complex is less stable than the iron-transferrin complex. It is also unstable with time, presumably due to an oxydation of Np(IV) to Np(V), which binds very weakly to

transferrin [62]. Complexation of Np(IV) with transferrin is characterised in the visible region by the appearance of bands at 747, 732 and 727 nm while the band at 740 nm decreases and in the NIR region the band at 980 nm decreases and a new band appears at 995 nm. The absence of a band at 610 nm confirms that Np is in its (IV) oxidation state [26]. A preliminary EXAFS study of Np-transferrin complex has shown that the actinide is mostly bound to the protein *via* oxygen and/or nitrogen donor functions, with a co-ordination number of eight which may include water molecules [26,63].

Complexation of plutonium(IV) with transferrin has also been confirmed [4,5]. Although UV difference spectra are equivocal, it seems likely that two Pu(IV) are bound [43,64]. However, *in vitro* studies have shown that Pu(IV) apparently does not induce the closure of the transferrin lobes [65], and that $Pu(IV)_2$-Tf was not recognised by membrane receptors of transferrin of liver cells [62,66,67].

Our first results

Although the EXAFS spectrum of holotransferrin has been reported in the literature, no complete description of the environment has been provided in aqueous phase yet. Study of the complexation of actinides (IV) has also been undertaken and is reported by the authors in reference [26] and [63]. However, a detailed description of the actinide co-ordination sphere is still lacking. Further results will be published elsewhere. In our approach, actinides chelation with transferrin has first been monitored by UV-visible-NIR spectroscopy. Determination of the structure of the complexation site is being carried out with EXAFS measurements.

Holotransferrin

The first step of our study was to choose a reliable model to fit the experimental EXAFS spectrum of holotransferrin. A screening of transferrin structures published in the PDB has been carried out. All structures are in agreement with the iron site described in introduction, i.e. two tyrosine residues, one aspartate and one histidine. Table 1 summarises the distances within the iron complexation site of transferrin from some X-Ray diffraction structures of PDB. It illustrates that these structures vary significantly from each other. These variations must be due to the experimental methods used to obtain crystals as for 1GVC, obtained with an excess of NTA. Some structures are also poorly resolved, like 1A8E. We shall keep in mind that our EXAFS spectra were recorded in solution whereas PDB structures describe transferrin in the solid state.

Table 1. Iron-ligand bond distances for some X-ray diffraction structures of transferring (from PDB) [68,69,70,71].

1A8E [68] human Tf		N-term	**1GVC** [69] duck ovoTf			**1NNT** [70] hen ovoTf			**1LCT** [71] human lactoTf		N-term
a.a.	**at**	**distance**	**a.a.**	**at**	**distance**	**a.a.**	**at**	**distance**	**a.a.**	**at**	**distance**
FE	Fe	0.000	FE	Fe	0.000	FE	Fe	0.000	FE	Fe	0.000
TYR	O	1.796	NTA	O	1.744	TYR	O	1.774	TYR	O	1.917
TYR	O	1.972	TYR	O	1.861	ASP	O	1.914	ASP	O	1.992
BCO3	O	1.990	NTA	O	2.056	TYR	O	2.013	TYR	O	2.002
ASP	O	2.030	CO3	O	2.086	CO3	O	2.095	CO3	O	2.094
HIS	N	2.036	CO3	O	2.108	HIS	N	2.261	HIS	N	2.149
ACO3	O	2.055				CO3	O	2.270	CO3	O	2.234
ACO3	O	2.240									
BCO3	O	2.421									

EXAFS spectra of all the iron transferrin PDB structures were calculated with the feff8 code, and compared to the experimental spectrum of holotransferrin. From this comparison the 1LCT structure was qualitatively chosen as an acceptable model for the fit.

The Fe K-edge EXAFS spectrum and corresponding Fourier transform of holotransferrin are presented in Figure 2A and 2B. The Fourier transform clearly shows backscattering contributions from the closest neighbours of iron (I) and from a second shell (II). The presence of a contribution near 3.8 Å (III) will also be discussed. Note that the distinction between the co-ordination sites of each lobes of transferrin is impossible with EXAFS technique because of their structural similarity. Both iron ions were thus considered equivalent. Multiple scattering paths were included in order to obtain a good adjustment of the experimental spectrum (R factor = 0.03). The first contribution was fitted with a shell of 6 oxygen atoms at 2.02 Å (σ^2 = 0.019 Å²). In order to obtain a satisfactory adjustment of the second shell, two types of carbon were taken into account: 5 carbon atoms at 3.09 Å (σ^2 = 0.017 Å²) and 1 at 2.51 Å (σ^2 = 0.001 Å²) (from carbonate anion) as well as the corresponding 3-leg scattering paths. The contribution at 3.8 Å is due to the focusing effect which intensifies the multiple scattering contributions from the distal oxygen atom of the carbonate anion, as well as from diffusion paths between two oxygen atoms of amino-acids on each side of the Fe(III) ion. It is thus in good agreement with the pseudo-octahedral co-ordination polyhedron of Fe(III) in holotransferrin from X-ray diffraction database.

Figure 2. k^3 weighted EXAFS spectrum (A) and corresponding Fourier transform (B) of Fe(III) in the holotransferrin (solid line: experimental data; dots: best fit).

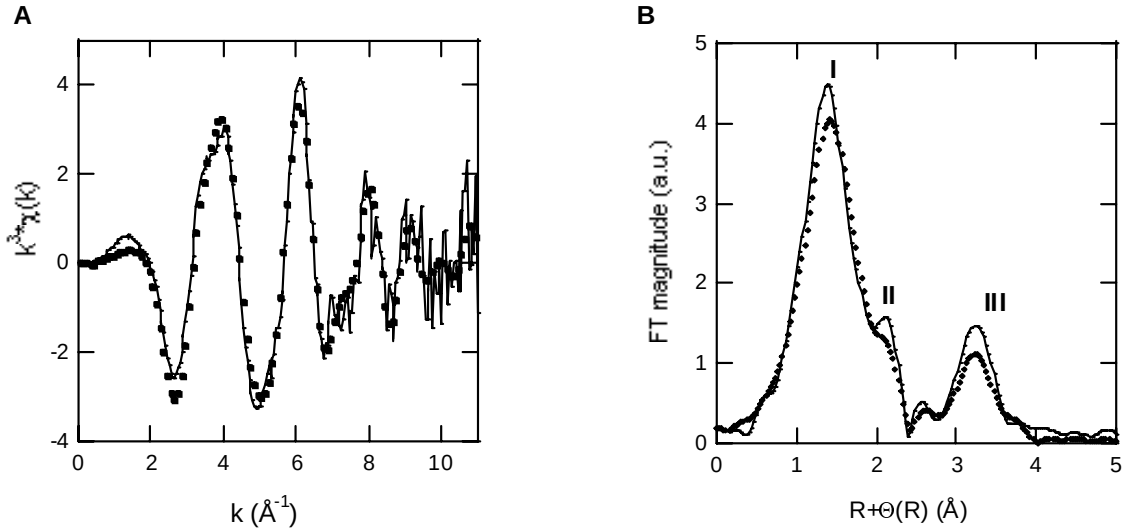

Table 2 shows the comparison between fitted distances, distances of the 1LCT model, and the mean distances of all transferrin structures reported in the PDB. Fitted Fe-C distances are in good agreement with Fe-C distances of DRX structures. On the other hand, the average Fe-O bound is found quite shorter. This may point out that holotransferrin in solution could be more relaxed than in the crystallized state.

Table 2. Comparison between best fit distances obtained from EXAFS data fitting, and the corresponding distance in 1LCT structure and all PDB structures of transferrin.

	Fitted distances	d 1LCT	d PDB
dFe-O (Å)	2.02	2.06	2.08
dFe-Ccarb (Å)	2.51	2.50	2.52
dFe-Caa (Å)	3.09	3.08	3.11

Actinides-Transferrin complexes

Further results on actinide-transferrin complexes will be published elsewhere.

A full interpretation of the EXAFS spectra of U(VI)(Tf), and Np(IV)(Tf) and Pu(IV)(Tf) with synergistic NTA anion is in progress. Those spectra are complicated by the complexity of the chelation site of transferrin. Owing to the higher number of co-ordination of actinides than that of iron, and to the presence of nitrilotriacetic acid as a synergistic anion instead of the carbonate anion, the co-ordination site is expected to be distorted, which may withdraw the focusing effect described above. Np(IV)(Tf) and Pu(IV)(Tf) spectra and their corresponding Fourier transforms are compared to those of Fe(III)(Tf) on Figure 3.

Figure 3. k^3 weighted EXAFS spectrum (A) and corresponding Fourier transform (B) of Fe(III)(Tf), Np(IV)(Tf) and Pu(IV)(Tf)

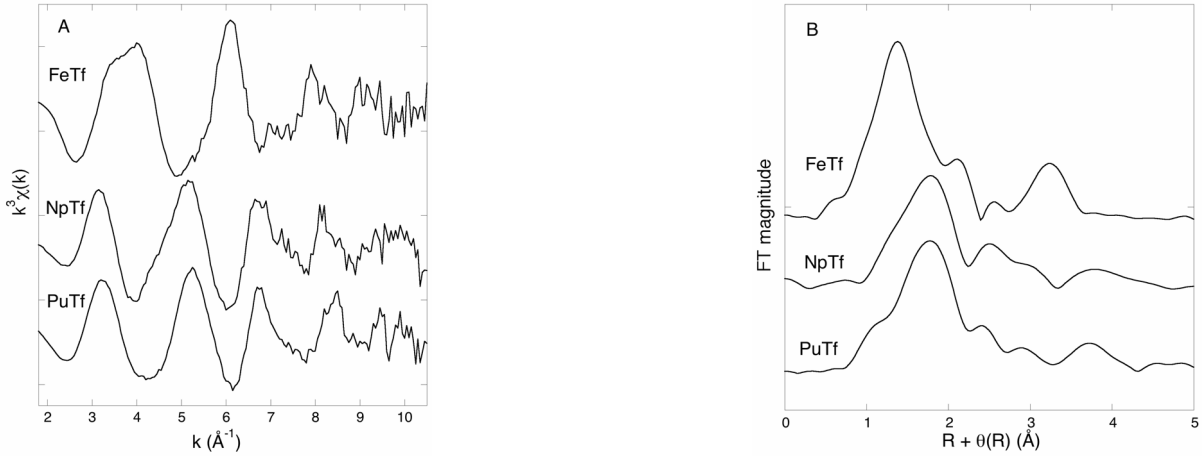

Parallely, studying actinides interaction with each amino-acid present in the iron site in transferrin should help us to better understand the structure of the chelation site. Among these, aspartate can be represented by acetate. Amino- and carboxylic groups of tyrosine and histidine must be protected in order to avoid complexation on the peptidic chain instead of on the lateral chain. Investigating pentapeptides mimicking parts of the iron site is also necessary in order to comprehend interaction mechanisms between actinides and amino-acids of this site. The AcAsp-Asp-Pro-Asp-AspNH_2, AcHis-Tyr-Pro-His-TyrNH_2 and AcTyr-Tyr-Pro-Tyr-TyrNH_2 pentapeptides, which have been synthesised, could be good models of parts of the iron site of transferrin. Both aspartate-modelling

ligands have been used to complex Np(IV). Interpretation of the spectroscopic data on these complexes is in progress.

Acknowledgements

We thank for financial support the CEA/DEN/MRTRA, and the French Nuclear-Toxicology program.

EXAFS spectra were recorded at the European Synchrotron Radiation Facility (Grenoble, France), Fe K-edge spectra at beamline BM29, and actinides L_{III}-edge at the Forschungszentrum Rossendorf beamline (BM20). The authors would like to thank Pier Lorenzo Solari, Andreas Scheinost and Christophe Hennig.

References

1. D.M. Taylor, *J. Alloys Compd* (1998), **271**, 6.
2. W.R. Harris, B. Yang, S. Abdollahi, Y. Hamada, *J. Inorg. Biochem* (1999), **76**, 231.
3. P. Aisen, A. Leibam, J. Zweier, *J. Biol. Chem* (1978), **253**, 1930.
4. H. Lee, P.J. Sadler, H. Sun, *Eur. J. Biochem.* (1996), **242**, 387.
5. W.R. Harris, *Structure Bonding* (1998), **92**, 121.
6. E. Gorden, J. Xu, K.N. Raymond, P. Durbin, *Chem. Rev.* (2003), **103**, 4207.
7. G.N. Stradling, S.A. Gray, M.J. Pearce, I. Wilson, J.C. Moody, R. Burgada, P.W. Durbin, K.N. Raymond, *Hum. Exp. Toxicol.* (1995), **14**, 165.
8. *Internationl Commission on radiological Protection. Ann. ICRP* (1995), **25**, 1.
9. G.N. Stradling, S.A. Hodgson, M. Pearce, *Radiat. Prot. Dosim.* (1998), **79**, 445.
10. D.M. Taylor, G.N. Stradling, M.-H. Nenge-Napoli, *Radiat. Prot. Dosim.* (2000), **87**, 11.
11. E. Peter, M. Lehmann, *Int. J. Radiat. Biol.* (1981), **40**, 443.
12. A. Tannenbaum, *Toxicology of Uranium*, McGraw-Hill Book Co.: New York (1951).
13. N.L. Spoor, J.B. Hursh, H.C. Hodge, J.N Stannard, J.B. Hursh, *Uranium, Plutonium, Transplutonic Elements*, Handbook of Experimental Pharmacology 36, Springer-Verlag: Berlin (1973).
14. C. Voegtlin, H.C. Hodge, *The Pharmacology and Toxicology of Uranium Compounds*, McGraw-Hill Book Co.: New York (1949).
15. M. Sutton, S.R. Burastero, *Chem. Res. Toxicol.* (2004), **17**, 1468.
16. J.D. Van Horn, H. Huang, *Coord. Chem. Rev.* (2006), **250**, 765.
17. H.C. Hodge, *AMA Arch. Indust. Health.* (1956), **14**, 43.
18. *The chemistry of the actinides elements*, 2nd ed., Chapman and Hall, London, U.K., 1986.
19. P.W. Durbin, B. Kullgren, J. Xu, K.N. Raymond, P.G. Allen, J.J. Bucher, N.M. Edelstein, D.K. Shuh, *Health Phys.* (1998), 75, 34.
20. P.W. Durbin, *Health Phys.* (1975), **29**, 495.
21. K.G. Scott, D.J. Axelrod, J.F. Crowley, J.G. Hamilton, *J. Biol. Chem.* (1948), **176**, 283.
22. W. Stevens, F.W. Bruenger, B.J. Stover, *Radiat. Res.* (1968), **33**, 490.

23. G.A. Turner, D.M. Tatlor, *Physics Med. Biol.* (1968), **13**, 535.

24. W.R. Harris, C.J. Carrano, V.L. Pecoraro, K.N. Raymond, *J. Am. Chem. Soc.* (1981), **103**, 2231.

25. C. Vidaud *et al.*, article in preparation.

26. I. Llorens, C. Den Auwer, P. Moisy, E. Ansoborlo, C. Vidaud, H. Funke, *FEBS J.*, 2005, **272**,1739.

27. O. Pible, P. Guilbaud, J.-L. Pellequer, C. Vidaud, E. Quéméneur, *Biochimie* (in press, accepted 17 may 2006).

28. A. Gianguzza, A. Pettigano, S. Sammartano, *J. Chem. Eng. Data* (2005), **50**, 1576.

29. R.N. Shchelokov, Y.N. Mikhailov, G.M. Loboanova, A.S. Kanishcheva, I.M. Orlova, N.B. Generalova, G.V. Podnebesnova, *Rus. J. Inorg. Chem.* (1982), **27**, 1324.

30. N.W. Alcock, D.J. Flanders, T.J. Kemp, M.A. Shand, *J. Chem. Soc. Dalton Trans.* (1985), 517.

31. A.D. Keramidas, M.P. Rikkou, C. Drouza, C.P. Raptopoulou, A. Terzis, I. Pashalidis, *Radiochim. Acta* (2002), **90**, 549.

32. S.R. Sofen, K. Abu-Dari, D.P. Freyberg, K.N. Raymond, *J. Am. Chem. Soc.* (1978), **100**, 7882.

33. W.L. Smith, K.N. Raymond, *J. Am. Chem. Soc.* (1981), **103**, 3341.

34. J. Xu, E. Radkov, M. Ziegler, K.N. Raymond, *Inorg. Chem.* (2000), **39**, 4156.

35. C.J. Gramer, K.N. Raymond, *Inorg. Chem.* (2004), **43**, 6397.

36. J. Xu, D.W. Whisenhunt Jr., A.C. Veeck, L.C. Uhlir, *Inorg Chem.* (2003), **42**, 2665.

37. H. Huang, S. Chaudhary, J.D. Van Horn, *Inorg. Chem.* (2005), **44**, 813.

38. J. Xu, K.N. Raymond, *Inorg. Chem.* (1999), **38**, 308.

39. G. Tian, J. Xu, L. Rao, *Angew. Chem. Int. Ed.* (2005), **44**, 6200.

40. M.P. Neu, J.H. Matonic, C.E. Ruggiero, B.L. Scott, *Angew. Chem. Int. Ed.* (2000), **39**, 1442.

41. S.G. John, C.E. Ruggiero, L.E. Hersman, C.-S. Tung, M.P. Neu, *Environ. Sci. Technol.* (2001), **35**, 2942.

42. A.E. Gordon, D.K. Shuh, B.E. Tiedemann, R.E. Wilson, J. Xu, K.N. Raymond, *Chem. Eur. J.* (2005), **11**, 2842.

43. E.N. Baker, *Advances in inorganic chemistry* (1994), **41**, 389.

44. J.N. Octave, Y.-J. Schneider, A. Trouet, R.R. Crichton, *Trends Biochem. Sci.* (1983), **8**, 217.

45. D.R. Hall, J.M. Hadden, G.A. Leonard, S. Bailey, M. Neu, M. Winn, P.F. Lindley, *Acta Crystallogr*. (2002), **58**, 70.

46. P. Aisen, A. Liebman, J. Zweier, *J. Biol. Chem.*(1978), **253**, 1930.

47. S.A. Kretchmar, K.N. Raymond, *J. Am. Chem. Soc.* (1986), **108**, 6212.

48. M.R. Schlabach, G.W. Bates, *J. Biol. Chem.* (1975), **250**, 2182.

49. R.C. Garratt, R.W. Evans, S.S. Hasnain, P.F. Lindley, *Biochem. J.* (1986), **233**, 479.

50. P.F. Lindley, M. Bajaj, R.W. Evans, R.C. Garrat, S.S. Hasnain, H. Jhoti, P. Kuser, M. Neu, K. Patel, R. Sarra, R. Strange, A. Walton, *Acta Cryst.* (1993), **D49**, 292.

51. J.G. Grossmann, J.B. Crawley, R.W. Strange, K.J. Patel, L.M. Murphy, M. Neu, R.W. Evans, S.S. Hasnain, *J. Mol. Biol.* (1998), **279**, 461.

52. H.M. Baker, C.J. Baker, C.A. Smith, E.N. Baker, *J. Biol. Inorg. Chem.* (2000), **5**, 692.

53. P. Aisen, *Iron in biochemistry and medicine*, Vol. II, Academic Press: London (1980), 87.

54. R.C. Garratt, R.W. Evans, S.S. Hasnain, P.F. Lindley, R. Sarra, *Biochem. J.* (1991), **280**, 151.

55. J.G. Grossmann, M. Neu, R.W. Evans, P.F. Lindley, H. Appel, S.S. Hasnain, *J. Mol. Biol.* (1993), **231**, 554.

56. W.R. Harris, B. Yang, S. Abdollahi, Y. Hamada, *J. Inorg. Biochem.* (1999), **76**, 231.

57. C.K. Luk, *Biochemistry* (1971), **10**, 2838.

58. B.F. Anderson, H.M. Baker, G.E. Norris, S.V. Rumball, E.N. Baker, *Nature* (1990), **344**, 784.

59. W. Stevens, F.W. Bruenger, D.R. Atherton, J.M. Smith, G.N. Taylor, *Actinides in Man and Animals –- Proceedings of the Snowbird Actinide Workshop* (1979), M.E. Wrenn Editor – RD Press, 457.

60. J.R. Cooper, G.N. Stradling, H. Smith, S.E. Ham, *Int. J. Radiat. Biol.* (1982), **41**, 421.

61. S. Scapolan, *Mise au point et évaluation de techniques de spéciation pour l'étude des espèces biologiques circulantes de l'uranium*, Université Paris XI Orsay, France, 1998.

62. R. Racine, *Etude des mécanismes de complexation du neptunium en milieu biologique en vue de la mise au point d'une thérapeutique applicable en cas d'incorporation accidentelle*, Université Paris XI Orsay, France, 2001.

63. C. Den Auwer, I. Llorens, P. Moisy, C. Vidaud, F. Goudard, C. Barbot, P.L. Solari, H. Funke, *Radiochim. Acta* (2005), **93**, 699.

64. J.R. Duffield, D.M. Taylor, *Inorg. Chim. Acta* (1987), **140**, 365.

65. J.G. Grossmann, M. Neu, E. Pantos, F.J. schwab, R.W. Evans, E. Townes-Andrews, P.F. Lindley, H. Appel, W.-D. Thies, S.S. Hasnain, *J. Mol. Biol*. (1992), **225**, 811.

66. D.M. Taylor, A. Seidel, F. Planas-Bohne, U. Schuppler, M. Neu-Müller, R. Wirth, *Inorg. Chim. Acta* (1987), **140**, 361.

67. W.R. Harris, *Struct. Bonding* (1998), **92**, 121.

68. R.T. MacGillivray, S.A. Moore, J. Chen, B.F. Anderson, H. Baker, Y. Luo, M. Bewley, C.A. Smith, M.E. Murphy, Y. Wang, A.B. Mason, R.C. Woodworth, G.D. Brayer, E.N. Baker, *Biochemistry* (1998), **37**, 7919.

69. P. Kuser, D.R. Hall, M.L. Haw, M. Neu, R.W. Evans, P.F. Lindley, *Acta Crystallogr. Sect. D* (2002), **58**, 777.

70. J.C. Dewan, B. Mikami, M. Hirose, J.C. Sacchettini, *Biochemistry* (1993), **32**, 11963.

71. C.L. Day, B.F. Anderson, J.W. Tweedie, E.N. Baker, *J. Mol. Biol.* (1993), **232**, 1084.

NEPTUNIUM SPECIATION IN HUMIC ACID – GOETHITE SYSTEM

Stepan Kalmykov[1], Thorsten Schäfer[2], Francis Claret[3], Yuri Teterin[4], Aigul Khasanova[1], Natalia Shcherbina[1], and Irina Perminova[1]

[1] Lomonosov Moscow State University, Moscow, Russia,
[2] Forschungszentrum Karlsruhe, Institut für Nukleare Entsorgung (INE), Karlsruhe, Germany
[3] CEA Saclay, CEA/DPC/SECR/LSRM, Gif sur Yvette, France
[4] Scientific centre "Kurchatovskiy Institute", Moscow, Russia

Abstract

Humic acids (HA) are known to have significant effect on metal ion speciation in the environment and may either enhance or depress their migration ability depending on geochemical conditions. This study deals with Np(V) behaviour in HA-goethite suspension at different pH values. The HA used in this study were enriched in hydroquinone group content that define their redox properties.

The sorption of Np(V) by goethite in the presence of HA was studied in batch mode at pHs from 2.5 to 9. It was established that at low pH values the sorption of Np agrees with the sorption of HA by goethite and was significantly higher than in binary Np-goethite system. The scanning transmission X-ray microscopic (STXM) study done at National Synchrotron Light Source (BNL, USA) was used to characterize humic surface coatings on goethite. According to STXM, organic matter "hot spots" were observed in the central region of goethite particles. These "hot spots" revealed high amounts of $C{=}C_{arom}$ and aliphatic structures, whereas edge regions of goethite particles or the cloudy regions around this particle contained lower amounts of these organic functionalities. The particle edge structures and the surrounding of the particle were enriched in oxygen-containing functional groups. The enhanced Np sorption at low pH values was explained by its reduction to tetravalent state with formation of stable Np(IV) humates that was established by Vis-NIR spectrophotometry for binary Np(V)-HA solutions and XPS for ternary Np-HA-goethite system.

At pH > 6 neptunium retention by HA-goethite suspension was slightly lower that in the absence of HA that is due to week Np(V) – humic complexation in solution. According to STXM no detection of organics on goethite minerals by carbon K-edge measurements was possible and the results might be interpreted as an absence of organic matter sorption on the mineral phases under the conditions of batch-type studies. The absence of Np(V) reduction in these pH interval was also established by Vis-NIR spectrophotometry.

LOCAL STRUCTURE OF SOME ACTINIDE OXIDES AND SOLUTIONS

Alexander Kostenko and Alexander Soldatov
Faculty of Physics, Rostov State University, Rostov on Don, Russia

Steven D. Conradson
Los Alamos National Laboratory, Chemistry Division, Materials Science and Technology Division and Nuclear Materials Technology Division, Los Alamos, NM 87545, USA

Abstract

Theoretical analysis of the L_3-edge XANES spectra of some actinide oxides was performed by the self-consistent full multiple scattering method. XANES simulations were made for the clusters of Pu oxides and colloid solutions. Density function theory was applied to generate possible models of Pu co-ordination in colloidal solutions. The reasons for variations of the actinide L_3-edge white lines intensities are discussed.

Introduction

At present the problem of the safe disposal of nuclear waste becomes issue of the day. Most of the radioactive materials are being disposed in very deep stable waterproof ground horizons. But unfortunately not all nuclear repositories are well protected from leaching. And even the most modern methods of disposal can't guarantee safety preservation of the nuclear waste for extremely long terms, such as half-life of Pu and U isotopes. In fact nuclear materials could react with various environmental compounds leaching from the repository.

By now numerous studies are dedicated to the research of structure, chemical activity, solubility and other properties of different actinide oxides and hydroxides (see for example ref.[1-3]). Many of the studies are based on the investigation of the EXAFS spectra (Extended X-ray Absorption Fine Structure). It is well known that the shape of XANES spectrum depends not only on bond length but also on the bonding angles. Considering these properties of XANES spectra it's possible to study full 3-dimentional local structure around absorbing atom. That means one can use XANES to improve radial distribution data obtained by investigating EXAFS or by other methods and to obtain angular distribution of atoms.

In the present study we analyse XANES (e.g. X-ray Absorption Near Edge Structure) spectra on the basis of theoretical simulations to investigate local structure of Pu crystalline oxides and colloids.

Theoretical approaches

Theoretical spectra of crystalline PuO_2 were calculated on the basis of a self consistent field (SCF) full multiple scattering method implemented in FEFF8.4 code [4]. The importance of the SCF approach to obtain a reasonable crystal potential for plutonium oxides and hydrides in XANES analysis has been shown before [4,5]. The algorithm for the FMS method has been described elsewhere [5]. Phase shifts of the photoelectron were calculated in the framework of the self-consistent crystal muffin-tin (MT) potential scheme with 15% overlapping MT spheres. For the experimental energy resolution, a value of 2.0 eV was used. These factors were treated as contributions to the imaginary part of the self-energy term. Self-consistent potentials and corresponding phase-shifts were calculated for the clusters of atoms having 5.0 Å radii.

The spectra have been simulated using several types of exchange potentials: non-local potential, Dirac-Fock potential, Hedin-Lundqvist potential and Dirac-Hara potential. Dependence of spectra on a relaxation of electrons in the presence of a core-hole has been studied as well.

The best agreement with experiment has been achieved for the spectra calculated with Hedin-Lundqvist potential in the presence of a core-hole. In the most cases using Hedin-Lundqvist potential one can obtain the best agreement in energy positions of spectra features at the cost of over-spreading of these features. For the PuO_2 case we can see that Hedin-Lundqvist potential calculations provides a good agreement for the energy positions of all XANES features as well as for their relative intensities. FMS calculations of the U L3-edge XANES were performed for different sizes of clusters, form only one absorbing atom to 295 atoms in the cluster. One can see that calculated L3-edge XANES spectra shows almost no dependence on the number of atoms used in simulation (for cluster of 21 atoms and more).

In the Figure 3 one can see the experimental L3-edge spectra of the crystalline PuO_2 in comparison with the spectra calculated for ideal structure of PuO_2 (unit cell dimensions are 1.35 x 1.35 x 1.35 angstrom), for the structure with unit cell stretched by 0.15 angstrom along one edge, and the spectra calculated for unit cell stretched along one edge by 0.15 angstrom and squeezed by 0.13 angstrom by another. Such transformations make notable displacements in B and C peak positions and the changes in peak A intensity.

Figure 1. Comparison of the theoretical and experimental XANES spectra of crystalline PuO_2 made for different types of exchange potentials.

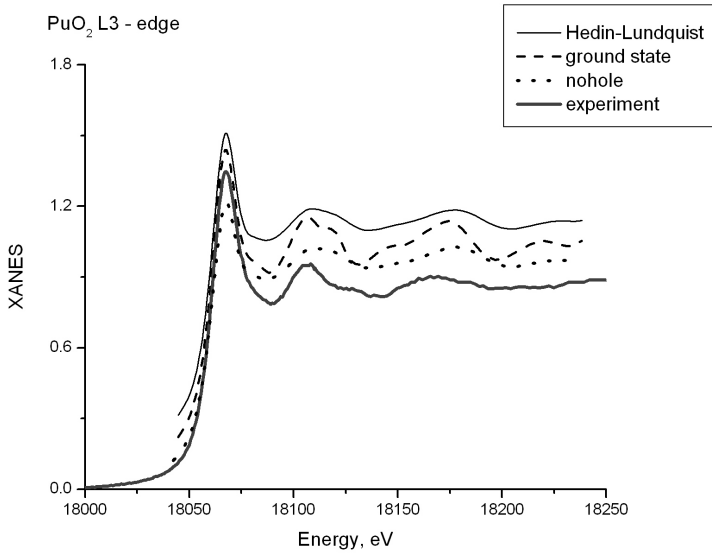

Figure 2. Comparison of the experimental XANES spectra of crystalline PuO_2 and the theoretical spectra made for different sizes of cluster (right plot) and a model view of PuO_2 cluster with 295 atoms.

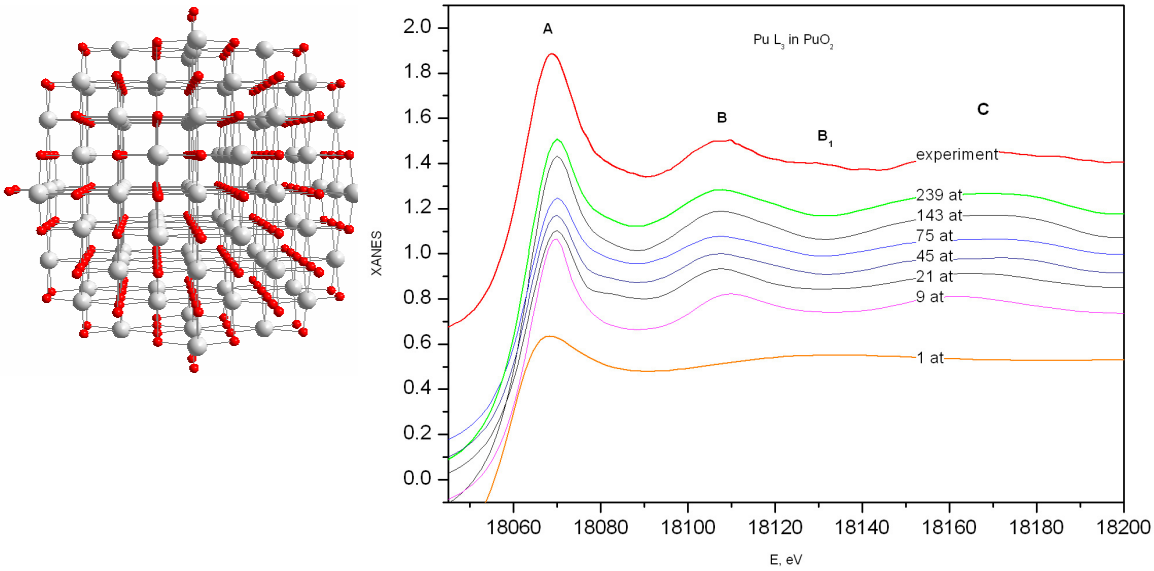

Figure 3. Variation of PuO_2 cell (on the left) and the corresponding XANES spectra (on the right).

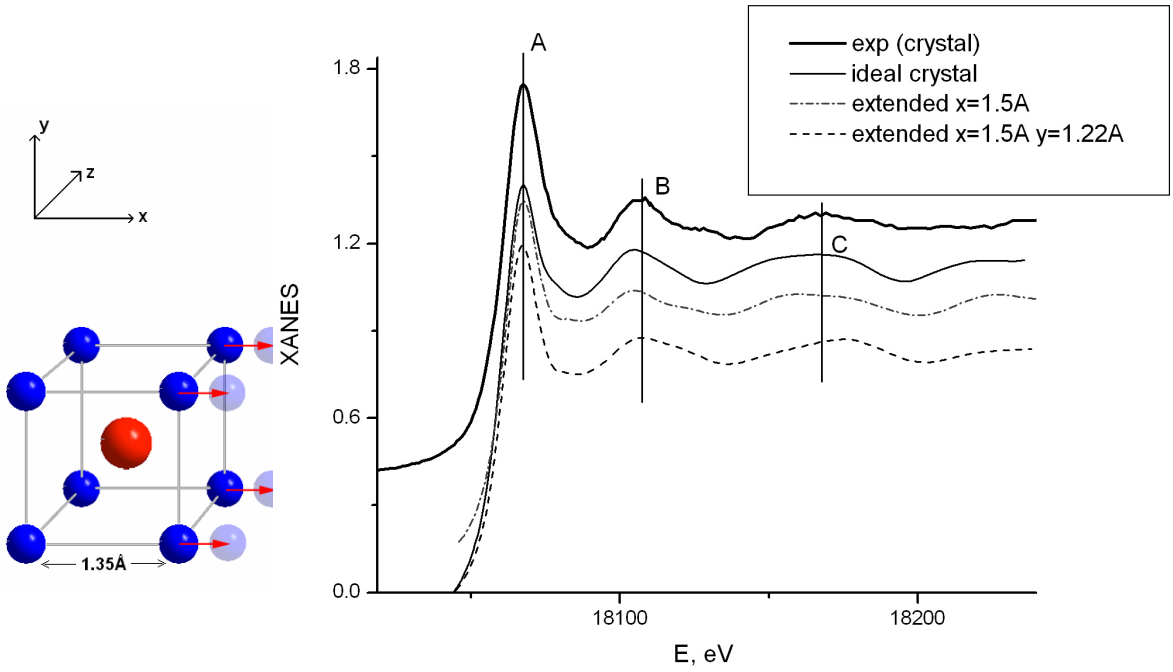

Theoretical XANES spectra of crystalline PuO_2 calculated using known structural data on the basis of FMS theory fits experimental spectra very good. High sensitivity of the U L3-edge XANES to the small variations in local structure of some actinide oxides has been demonstrated recently in [6]. That allows us to expect that XANES could be useful in investigations of colloidal actinide solutions as well.

Colloid solutions

Theoretical approach discussed above was applied to study a model structure of Pu colloid proposed in [3]. According to that model HO-groups, O atoms and H_2O molecules form sort of a cubic cage around Pu. Crystal structure of PuO_2 was taken as initial approximation of Pu hydroxide, and then hydrogen atoms were added. We have used DFT (density functional theory) approach [7] as it is implemented in ADF2006.1 code for geometry optimization to Pu hydroxide structure.

White line is one of the most remarkable features of the Pu L_3-edge XANES in colloid solution. But understanding of its behavior is far from complete. Experiments show that white line intensity of Pu L_3-edge goes up when crystallization factor of Pu solution goes down that is not a usual behavior for the solutions. Taking into account that XANES simulations made for PuO_2 seems to be independent from the cluster size one cannot bind such behavior only to the cluster size alteration. Most likely better conclusions could be made here analyzing some stereochemistry effects that should be discernible in XANES.

Sixteen hydrogen atoms were added into the cluster consisted of Pu central atom and eight oxygen atoms. Table 1 shows the shortest bond lengths in PuO8H16 cluster after optimization. Bonds between O and H atoms are close to bond lengths of H_2O molecules, so one can consider the optimized cluster to be a Pu atom surrounded by H_2O molecules at the distances about 2.5 angstrom.

In Figure 4 one can see that variation of the structure results in some variation of the white line relative intensity. The same changes take place in experimental spectra obtained for different crystallisation factor in colloids. In spite there was an agreement in while line intensity changes further simulations (optimization of the local structure) need to be done to reproduce the XANES features above 18100 eV.

Figure 4. Theoretical and experimental XANES spectra of PuO_2 made for different levels of optimization in the model structure [3].

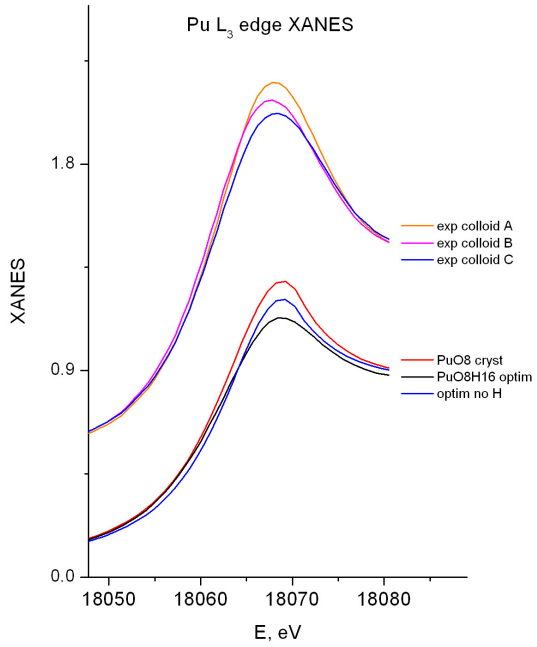

Table 1. The lengths of the shortest bonds in optimized PuO_8H_{16} cluster.

Bond type	Average bond length, Å	Minimal bond length, Å	Maximal bond length, Å
Pu – O	2.435	2.417	2.447
O – H	1.002	0.99	1.01
Pu – H	2.646	2.084	2.951

Conclusions

SCF FMS theory was found to be an adequate tool for the analysis of the Pu L_3-edge XANES of crystalline oxide and colloids. The calculated XANES spectra correspond well to the experimental

data. DFT geometry optimization can produce possible models for the local structure of plutonium hydroxide colloidal solutions.

Acknowledgments

We would like to express our gratitude to Melissa Denecke and Joerg Rothe for making available experimental data of the Pu L3-edge XANES of Pu colloidal species published in [3].

References

[1] S.D. Conradson *et al*., *J. Sol. State Chem*. 178 (2005) 521–535.

[2] M.A. Deneke, *Coord. Chem. Rev. 250* (2006) 730-754.

[3] J. Rothe, C. Walther, M.A. Denecke, and Th. Fanghanel, *Inorg Chem* 43 (2004) 4708-4718

[4] J.J. Rehr, A.L. Ankudinov, *Coord. Chem. Rev*. 249 (2005) 131–140.

[5] A.L. Ankudinov, S.D. Conradson, J. Mustre de Leon, J.J. Rehr, *Phys. Rev*. B 57 (1998) 7518-7525.

[6] A. Soldatov, D. Lamoen, M. Konstantinovic, S. Van den Berghe, A. Scheinost, M. Verwerft, *J. of Sol. State Chem.* (2006) corrected proofs published on the web.

[7] G. te Velde, F.M. Bickelhaupt, S.J.A. van Gisbergen, C. Fonseca Guerra, E.J. Baerends, J.G. Snijders, and T. Ziegler, *J. Comput Chem* 22, 931 (2001).

TOWARDS A MECHANISTIC UNDERSTANDING OF ACTINIDE RETENTION BY CEMENTITIOUS MATERIALS

P. Mandaliev, S. Churakov, R. Dähn, J. Tits, E. Wieland
Paul Scherrer Institut, CH-5232 Villigen-PSI, Switzerland

Abstract

Calcium silicate hydrate (C-S-H) are considered to be the most important constituent of hardened cement paste (HCP) with respect to their abundance and the diversity of structural sites exposed for cation and anion binding [1]. Furthermore, C-S-H phases may control the long term release of radionuclides due to their stability during the evolution of the cementitious near field.

The retention of Nd (III) by crystalline C-S-H phases has been studied by combined use of wet chemical methods, synchrotron – based spectroscopic, laboratory-based X-ray diffraction techniques and an appropriate theoretical approach. The investigations enable us to propose a mechanistic model for the immobilisation of trivalent lanthanides and actinides in crystalline C-S-H phases.

1. Atkins, M., Glasser, F. P.: Application of Portland cement-based materials to radioactive waste immobilisation, *Waste Manage*. 12, 105 (1992).

DATA VISUALISATION AND EVALUATION OF FLUORESCENCE YIELD XAFS SPECTRA

Stefan Mangold
Forschungszentrum Karlsruhe (FZK), Institute for Synchrotron Radiation, P.O. Box 3640, D-76021 Karlsruhe, Germany

Abstract

Fluorescence detection is often used to measure XAFS spectra of diluted or thick samples that cannot be measured in the normal transmission mode. For the last two decades mostly energy-dispersive semi-conductor detectors were used for this task. Because of the limited energy resolution of these detectors, nowadays also secondary monochromator systems are used to gain more energy resolution. The usage of this systems is limited because the number of beamlines for RIXS and similar techniques is restricted to a view insertion devise beamlines on mainly third generation sources and the needed intensity is so high that it could cause changes in the speciation of the sample. But even for the usage of semi-conductor detectors is nevertheless of utmost importance to separate the interesting fluorescence line as good as possible from neighbouring emission lines and from the peak caused by elastically scattered photons. Especially the scattering line can cause sever problems, because it changes it's position depending on the excitation energy. Modern fluorescence detector electronics therefore allow the user to store the complete fluorescence spectra for each energy of the monochromator during a XAFS scan. This enables to perform an elaborate peak fitting procedure and thus minimises the background contribution to the fluorescence yield-XAFS (fl-XAFS) spectra.

To enable the post processing of the acquired data a set of procedures in IgorPro 5 was developed. For a 3-dimensional graphical display of data the OpenGL-plotter of IgorPro is used. Additional to the fitting procedures it is also possible to set new SCA-windows. The fitting procedure uses a multiple Gauss peaks to a sub range of a set of spectra. Especially very diluted systems induces a lot of problems to the background subtraction in a standard data EXAFS data evaluation, because of a steadily decreasing overlap of the peak of interest with the elastic and inelastic scattering peaks. The two main advantages is the reduction of the background before the absorption edge and the correction a complex slope after the absorption edge.

XAS STUDY OF $(U_{1-Y}PU_Y)O_2$ SOLID SOLUTIONS

P. Martin[1,*], S. Grandjean[2], C. Valot[1], G. Carlot[1], M. Ripert[1], P. Blanc[2] and C. Hennig[3]
[1]CEA Cadarache, DEN/DEC/SESC, bât. 130, 13108 St Paul-lez-Durance cedex, France.
[2]CEA Marcoule, DEN/DRCP/SCPS, BP 171, 30270 Bagnols-sur-Cèze cedex, France
[3]Forschungszentrum Rossendorf, Institute of Radiochemistry, P.O. Box 510119, 01314 Dresden, Germany.

Abstract

A new procedure for $(U,Pu)O_2$ nuclear fuel manufacturing based on the oxalic co-precipitation of U(IV) and Pu(III) followed by the thermal conversion of the co-precipitate into oxide is under development. In order to fully investigate the ideality of solid solution with Pu content equal to 50, 30, 15 and 7 at.%, XRD and XAS characterisations at uranium and plutonium L_{III} edges have been undertaken. Using XRD, a face centred cubic structure was observed in each case, and the cell parameter deduced follows satisfactorily the Vegard's law. However, EXAFS measurements moderate these results; only the $(U_{0.5}Pu_{0.5})O_2$ sample leads to the same conclusion as XRD. For the lower plutonium concentration, a disordered hyperstoichiometric structure $(U_{1-y}Pu_y)O_{2+x}$ has been revealed. In those compounds, cuboctahedral oxygen defects are only located around uranium atoms and not in the Pu environment. A much more complex structure than that suggested by the XRD is thus observed with a non-random distribution of plutonium atoms within the uranium sites of the $(U_{1-y}Pu_y)O_{2+x}$ structure.

XPS STUDY OF Th, U, Np AND Pu CONTAINING MURATAITE CERAMICS

Konstantin Maslakov and Yury Teterin
RRC "Kurchatov Institute", Moscow, Russia

Anton Teterin
Institute of General and Inorganic Chemistry, Moscow, Russia

Sergey Yudintsev
Institute of Geology and Ore Depositions of RAS, Moscow, Russia

Sergey Stefanovsky
Moscow NPO "Radon", Moscow, Russia

Abstract

Immobilisation of the long-lived radioactive high-level wastes (HLW) requires high-stability and high-capacity matrixes. The synthesized analogues of the natural murataite are promising matrixes for the actinide-containing HLW disposal. To understand the chemical processes inside these matrixes it is necessary to know the physical and chemical states of the included radionuclides. X-Ray photoelectron spectroscopy proved to be the most adequate method for this purpose. The present work carried out an XPS study of the murataite titanate ceramic samples (Ti-Mn-Ca-An-Zr-Al-Fe-O, where An = Th, U, Np, Pu) containing 10 mass % of An. The X-ray diffraction data show that the studied ceramics was formed by the dominating murataite phase with thrice-, octo- and penta-repeated fluorite cell. The quantitative elemental and ionic analysis of the studied ceramics was done on the basis of the XPS parameters from the all available binding energy range 0 to 1000 eV. The oxidation states of the included metal ions were determined to be: Ca^{2+}, Ti^{4+}, Mn^{2+}, Fe^{3+}, Zr^{4+}, Al^{3+}, An^{4+}. Average metal-oxygen interatomic distances in the studied ceramics were evaluated on the basis of the oxygen binding energies. The XPS data were compared to the SEM–EDS results.

Introduction

The most dangerous long-lived radionuclides in the high-level radioactive wastes (HLW) are actinides. Their immobilisation requires the higher stability matrixes [1]. To understand chemical processes inside these matrixes it is necessary to know the physical and chemical states of the included radionuclides (elemental and ionic compositions, oxidation states, number of uncoupled electrons on the metal ions, coordination structure etc.).

The present work carried out the X-ray diffraction (XRD), electron microscopy (EM) with energy-dispersion spectrometer SEM-EDS and XPS analysis of murataite samples containing thorium, uranium, plutonium and neptunium as models of ceramic matrixes for immobilisation of actinides in order to determine their structure and oxidation states of included metal ions.

Experimental

The samples of murataite ceramic were obtained from the mixtures of simple oxides by melting in a platinum ampoule at 1 450°C within 30 minutes and after that cooled to 1 300°C at the rate of 2°C per minute, after that – cooled to 20°C at the rate of 10°C per minute. The ampoules were cut and the samples were studied with the XRD, SEM-EDS and XPS. The calculated compositions of the samples are shown in Table 1. This ratio of the components provided the highest murataite yield in the ceramics (up to 90%).

Table 1. Calculated composition of murataite ceramics.

Sample	Calculated composition, oxides weight %									
	ThO_2	UO_2	NpO_2	PuO_2	TiO_2	MnO	CaO	ZrO_2	Al_2O_3	Fe_2O_3
M-Th	10	–	–	–	55	10	10	5	5	5
M-U	–	10	–	–	55	10	10	5	5	5
M-Np	–	–	5	–	56	12	12	5	5	5
M-Pu	–	–	–	10	55	10	10	5	5	5

XPS spectra of the studied samples were measured with electrostatic spectrometers MK II VG Scientific using non-monochromatized Al $K\alpha_{1,2}$ radiation under 1.3 10^{-7} Pa at room temperature. The device resolutions measured as full width on the half-maximum (FWHM) of the Au $4f_{7/2}$ line on the standard rectangular golden plate was 1.2 eV. Electron binding energies E_b(eV) for the studied samples were calibrated using the binding energy of the C 1s electrons of adventitious carbon accepted to be equal to 285.0 eV. The FWHMs are given relatively to the width of the C1s peak of hydrocarbons accepted to be equal to 1.3 eV for comparison with the data of other studies. The studied samples were prepared from finely dispersed powders milled in the agate mortar as thick flat layers glued on scotch tape.

Results and discussion

Synthetic murataite is titanium, calcium, manganese, aluminum, iron, zirconium, actinide and rare-earth based complex oxide with the fluorite-like structure. There have been found several different murataite-like structures with thrice-, octo- and penta-repeated basic fluorite cell of the following parameters 14.8, 24.6 and 39.4 Å respectively. The murataite-like lattice can have different exchange types, including ones with triple- and tetravalent rare-earth and actinide elements. Murataite composition is suggested to be described by the following formula $A_4B_2C_7O_{22}$, where position “A” is

occupied by cations Ca, Mn, and An, "B" – by Mn, Ti, Zr and An, "C' – by Ti, Al, Fe. According to the XRD and SEM data, M-Th, M-U, M-Np and M-Pu samples consist of the dominating murataite phase with thrice-, octo- and penta-repeated fluorite cell and small amount of crichtonite-like titanate.

XPS elemental and ionic quantitative analysis employs usually the most intense peaks from the included elements. However, the fine XPS structure parameters are also very important for determination of oxidation states of the M 3d and An 5f transition elements (M – metal, An – actinide). For example, the Ti 3s, Mn 3s, Fe 3s multiplet splitting is proportional to the number of the uncoupled 3d electrons in titanium, manganese and iron ions, which allows unambiguous determination of the oxidation states. The shake up satellite structure in the An 4f spectra allows the determination of lanthanide and actinide oxidation states and ionic type of chemical bond [2-4].

Table 2. Binding energies E_b(eV) and FWHMs $\Gamma^{a)}$(eV) of the outer (MO) and core electrons for murataite ceramics and metal oxides.

Sample	MO	An $4f_{7/2}$	Ca $2p_{3/2}$	Ti $2p_{1/2}$	Mn $2p_{3/2}$	Fe $2p_{3/2}$	Zr $3d_{5/2}$	Al 2p	O 1s
M-Th	4.4; 6.2; 17.4; 22.2; 30.5; 37.1; 43.7;	334.2 (1.5) 6.7 sat	346.8 (1.5)	458.4 (1.3)	641.3 (2.5)	709.9 (2.6)	182.4 (1.1)	74.1 (1.4)	530.1 (1.5) 532.2 (1.5)
M-U	1.8; 5.6; 17.5; 22.2; 30.5; 37.1; 43.7	380.2 (2.1) 6.5sat	346.7 (1.6)	458.2 (1.1)	641.0 (2.1)	710.0 (2.6)	182.2 (1.1)	74.1 (1.4)	530.0 (1.4) 532.0 (1.3)
M-Np	4.0; 21.6; 24.5; 30.5; 36.8; 42.6; 48.1	403.0 (1.7) 6.2 sat	346.7 (1.8)	458.6 (1.1)	641.0 (2.1)	709.9 (2.6)	182.5 (1.1)	73.7 (1.1)	530.1 (1.4) 532.2 (1.3)
M-Pu	4.4; 22.0; 24.7; 30.5; 36.9; 43.5; 48.3	426.1 (1.7) 7.4 sat	346.7 (1.6)	458.5 (1.2)	641.0 (2.4)	710.3 (2.9)	182.2 (1.2)	74.0 (1.4)	530.0 (1.3) 532.1 (1.3)
CaO	4.3; 20.1; 24.3; 42.9		346.0 (1.7)						528.9 (1.4)
TiO_2	5.9; 7.6; 22.4; 27.4			458.9					530.5
MnO					641.4 (3.6)				530.3
Mn_2O_3					642.2 (3.3)				530.6
MnO_2					642.9 (3.1)				530.4
Fe_2O_3	5.4; 7.1; 21.9					711.1			530.0
ZrO_2	5.6; 21.3; 30.6						182.5		530.1
Al_2O_3								74.3	532.2

[a)]FWHMs are given in parentheses relative to the FWHM of the C1s peak accepted to be Γ(C 1s) = 1.3 eV.

For the studied ceramics the following peaks were chosen: Ca 2p, Ti 2p,3s, Mn 2p, Fe 2p, An 4f, Zr 3p,3d, Al 2p and O 1s (Table 2). Unfortunately, other peaks (such as Ca 3s, Fe 3s, Mn 3s and An 5d) because of their low intensity were difficult to reliably measure. In case of an overlap between different peaks like Ca 2p – Zr $3p_{1/2}$, other peaks that can be observed more individual can be used, for example, the Zr 3d peak. The Ca 2p and Zr 3p spectra for the studied samples are observed as spin-orbit split doublets with the splitting (ΔE_{sl}) of 3.5 eV for the Ca 2p and 13.7 eV for the Zr 3p. The Ti 2p spectra were observed as an intense doublet at 458.2–458.6 eV and split by ΔE_{sl} = 5.7 eV (Table 2),

and the Ti 3s spectra – as a single peak at E_b(Ti 3s)=62.3 eV and Γ(Ti 3s)=2.3 eV. It agrees with the fact of the absence of the extra electron density on titanium ions, which does not lead to the Ti 3s peak widening due to the induced charge. Titanium oxidation state is Ti^{4+}. The Mn 2p spectra from murataites were observed as a low intense spin-orbit split doublet with ΔE_{sl}(Mn 2p)=11.2 eV and Γ(Mn $2p_{3/2}$)=2.1 eV. On the higher binding energy side from the basic Mn $2p_{3/2}$ peak a shake up satellite with ΔE_{sat}(Mn 2p) ~ 6 eV was observed. Despite the low intensity, these spectra yield a suggestion that manganese oxidation state in murataite is Mn^{2+}. The Al 2p spectra were observed as a single asymmetric peak with Γ(Al 2p)=1.1–1.4 eV, which corresponds to Al^{3+} ion (Table 2). The Fe 2p spectra from murataite samples are very low intense, which enables only to evaluate the Fe $2p_{3/2}$ binding energy to be ~ 710 eV. It indicates that iron oxidation state in murataite must be Fe^{3+} (Table 2).

Figure 1. XPS spectra for murataite ceramics: a – Th 4f from M-Th sample; b – U 4f from M-U sample; c – Np 4f from M-Np sample; d – Pu 4f from M-Pu sample.

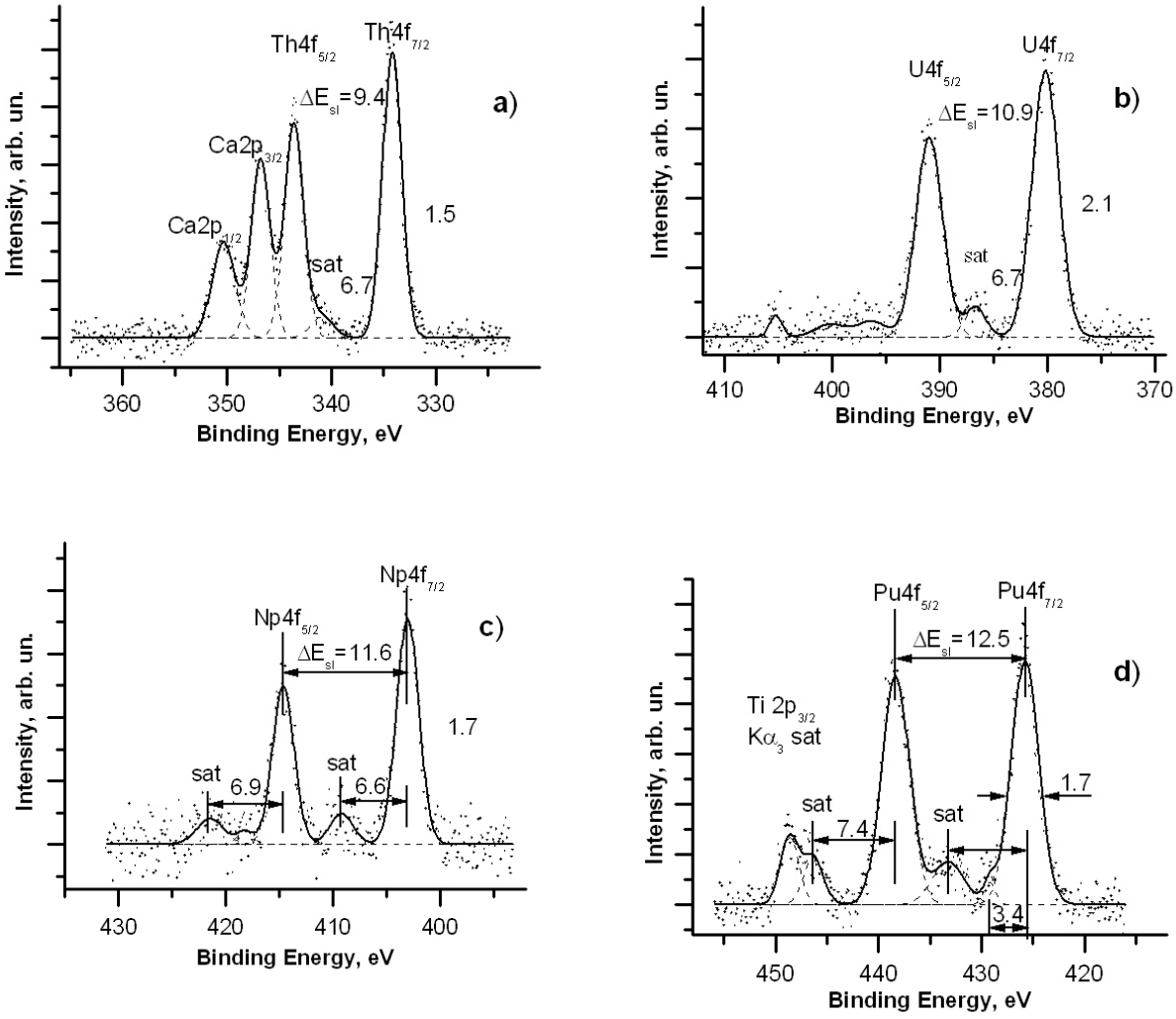

The An 4f spectra for all studied samples exhibit the fine structure typical for the An^{4+} ions. Thus Th 4f spectrum for the M-Th sample reveals the doublet split at ΔE_{sl} = 9.4 eV with the typical for Th^{4+} ions shake up satellite at $\Delta E_{sat} \approx 6.7$ eV from the Th $4f_{7/2}$ peak (Figure 1a). The satellite structure for the Th $4f_{5/2}$ peak is superposed with the $Ca2p_{1/2}$ peak. The U 4f peak from M-U sample exhibit the doublets split at ΔE_{sl} = 10.9 eV with the typical for U^{4+} ions shake up satellite at $\Delta E_{sat} \approx 6.7$ eV from U $4f_{7/2}$ peak (Figure 1b). The position of the same satellite for U $4f_{5/2}$ peak is difficult to evaluate because of low intensity of the spectrum. The Np 4f spectrum (Figure 1c) from the M-Np sample exhibits the fine structure typical for the Np^{4+} ions. Indeed, this spectrum displays the doublets split at ΔE_{sl} = 11.6 eV. On the higher binding energy side from the basic peaks at $\Delta E_{sat} \approx 6.8$ eV the typical shake up satellites of about 15% intensity were observed. The Pu 4f spectrum from the Sample M-Pu exhibits the fine structure typical for the Pu^{4+} ions (Figure 1d). This spectrum reveals the doublet split at ΔE_{sl} = 12.5 eV. On the higher binding energy side from the basic peaks at ΔE_{sat} =7.4 eV the typical shake up satellite of about 19% intensity was observed. Additional line in Pu 4f spectrum at about 449 eV (Figure 1d) is originated from $K\alpha_3$ X-ray satellite for the intensive Ti $2p_{3/2}$ peak. Another peak in Pu 4f spectrum at ΔE = 3.4 eV from Pu $4f_{7/2}$ peak is difficult to unambiguously identify. It may results, for example, from Zr 3s line.

The low binding energy XPS from murataite samples exhibits the structure attributed to the outer electrons. Unfortunately, this XPS structure allows only limited qualitative elemental analysis since it consists of systems of molecular orbitals (MO) attributed lines, but not single atomic peaks. The sharpest peaks in the low binding energy region are indicated in Table 2.

On the basis of the intensities (areas under the peaks) taking into account the experimental sensitivity coefficients the relative atomic compositions of the studied samples were determined and compared with calculated compositions of these samples:

$Ti_{1.00}Mn_{0.30}Ca_{0.33}Th_{0.07}Zr_{0.09}Al_{0.35}Fe_{0.19}O^{I}_{3.78}O^{II}_{1.76}$ (M-Th, XPS)

$Ti_{1.00}Mn_{0.20}Ca_{0.26}Th_{0.06}Zr_{0.06}Al_{0.14}Fe_{0.09}O^{I}_{3.04}$ (M-Th, Calculated)

$Ti_{1.00}Mn_{0.22}Ca_{0.33}U_{0.05}Zr_{0.08}Al_{0.27}Fe_{0.16}O^{I}_{3.89}O^{II}_{1.54}$ (M-U, XPS)

$Ti_{1.00}Mn_{0.20}Ca_{0.26}U_{0.05}Zr_{0.06}Al_{0.14}Fe_{0.09}O^{I}_{3.04}$ (M-U, Calculated)

$Ti_{1.00}Mn_{0.23}Ca_{0.32}Np_{0.03}Zr_{0.09}Al_{0.15}Fe_{0.01}O^{I}_{3.58}O^{II}_{0.57}$ (M-Np, XPS)

$Ti_{1.00}Mn_{0.24}Ca_{0.31}Np_{0.03}Zr_{0.06}Al_{0.14}Fe_{0.09}O^{I}_{3.06}$ (M-Np, Calculated)

$Ti_{1.00}Mn_{0.20}Ca_{0.32}Pu_{0.03}Zr_{0.09}Al_{0.26}Fe_{0.08}O^{I}_{3.70}O^{II}_{0.98}$ (M-Pu, XPS)

$Ti_{1.00}Mn_{0.20}Ca_{0.26}Pu_{0.05}Zr_{0.06}Al_{0.14}Fe_{0.09}O^{I}_{3.04}$ (M-Pu, Calculated)

Two values for oxygen content (O^{I} and O^{II}) correspond to portions of the O 1s spectra at different binding energies (Table 2), with O^{I} being the oxygen from ceramics and O^{II} being the oxygen from the oxygen-contained groups adsorbed on the surface. Murataite surface composition determined on the basis of the XPS parameters, except for zirconium, aluminium and iron, does not differ from the calculated data with the accuracy to within the measurement error. Significant difference between calculated and measured concentrations of zirconium, aluminium and iron can be explained by fact that XPS peaks for these elements are low intense which makes difficult to correctly measure their areas.

Average metal–oxygen interatomic distances for studied murataite samples were evaluated using O 1s spectra. These spectra consist of two peaks at ~ 530 and ~532 eV. Taking into account eq. (1, 2):

$$E_b(eV)=2.27\ R_{M\text{-}O}^{-1}(nm) + 519.4, \quad (1)$$

derived in [5], wherefrom

$$R_{M–O}(nm)=2.27\ (E_b - 519.4)^{-1}, \quad (2)$$

on the basis of the O 1s binding energy one can evaluate the average metal–oxygen ($R_{M–O}$ (nm)) interatomic distance in the studied samples. Thus, they are 0.212 nm (M-Th, M-Np) and 0.214 nm (M-U, M-Pu) for the first peak in the O 1s spectrum and ~0.180 nm for the second one. The difference between the values 0.212 nm and 0.214 nm is insignificant in this case since the measurement error is equal to 0.002 nm. We would like to note that though eq. (1, 2) are not directly applicable for mixed oxides we use them here to estimate the average metal–oxygen interatomic distance on the basis of the O 1s binding energy.

As it follows from eq. (1) the O 1s binding energy decrease as the interatomic distance ($R_{M–O}$) increases. Therefore, one can conclude that the value 0.180 nm is too low for ceramics and must be attributed to the hydroxide groups on the surface. It agrees with the elemental analysis data indicating that the O 1s binding energy for the studied samples is the same.

Conclusions

1. According to the XRD and SEM-EDS analysis, the titanate ceramics is formed by the dominating murataite phase with thrice-, octo- and penta-repeated basic fluorite cell.

2. On the basis of the XPS spectra structure in the binding energy range 0–1000 eV the quantitative elemental and ionic analysis was carried out. The oxidation states of the included metal ions in all samples was determined to correspond to the following ions, as it was predicted: Ca^{2+}, Ti^{4+}, Mn^{2+}, Fe^{3+}, Zr^{4+}, Al^{3+}, Np^{4+}, Pu^{4+}, Th^{4+}, U^{4+}.

3. On the basis of the oxygen binding energies in the studied ceramics samples the average interatomic distances metal–oxygen were evaluated to be 0.212±0.002 nm for M-Th and M-Np samples, 0.214±0.002 nm for M-U and M-Pu samples and ~0.180 nm for the impurity hydroxyl groups on the sample surface.

Acknowledgement

The work was supported by the RFBR grant 04-03-32892, grant of the Foundation for support of the Russian science 2006, grant of the president of Russia on the federal support of the leading scientific schools (NSh–284.2006.3) and the grant of the initiative projects on basic researches of RRC "Kurchatov Institute" 2006-2007.

References

1. N.P. Laverov, S.V. Yudintsev, S.V. Stefanovsky, Y.N. Jang, *Doklady Earth Science* **381**(9) (2001) 1053.
2. Yu.A. Teterin, A.S. Baev, X-Ray photoelectron spectroscopy of light actinide compounds, Moscow: *TsNIIAtominform*, 1986. (in Russian).
3. Yu.A. Teterin, A.Yu. Teterin, *Russian Chemical Reviews* **73**(6) (2004) 541.
4. Yu.A. Teterin, A.Yu. Teterin, *Russian Chemical Reviews* **71**(5) (2002) 347.
5. M.I. Sosulnikov, Yu.A. Teterin, DAN SSSR **317**(2) (1991) 418. (in Russian)

UMo NUCLEAR FUELS BEHAVIOUR UNDER HEAVY ION IRRADIATION: A µ-XAS STUDY

H. Palancher[1,2], P. Martin[1], V. Nassif[2], O. Proux[2], J.L. Hazemann[2], S. Dubois[1], C. Valot[1], N. Wieschalla[3], C. Sabathier[1], W. Petry[3], C. Jarousse[4]

[1]Commissariat à l'Énergie Atomique, Cadarache, F-13108 St Paul-Lez-Durance Cedex, France

[2]BM30B, ESRF, 6, rue J. Horowitz, 38500 Grenoble Cedex, France

[3]Forschungsneutronenquelle Heinz Maier-Leibnitz (FRM II), Technische Universität München, D-85747 Garching bei München, Germany

[4]CERCA (a subsidiary of AREVA NP), Les Berauds, B.P. 1114, 26104 Romans Cedex – France

Abstract

A worldwide program encourages the use of low enriched uranium (LEU, $^{235}U<20$ wt. %) in the fuels for research and material test reactors, which uses currently high enriched uranium (^{235}U concentration up to 93 wt. %). Due to the decrease in ^{235}U enrichment for the conversion to LEU, the total density of uranium atoms in the fuel must be increased accordingly. To preserve the neutron flux, metallic uranium alloys could be the best fuel material. The fuel, which consists of UMo alloy spherical particles surrounded by an Al matrix (cf. Figure 1-A), is rolled between two aluminium claddings.

Post-irradiation examinations of U-7wt%Mo [1,2,3] demonstrated its strong potentialities as fuel but they also pointed out its interaction with aluminium (cf. Figure 1-B). In certain cases this interaction can cause a break-away swelling of the plate. The aim of this project is the understanding of:

- the phenomena driving the growth of the interaction layer.
- the influence on interaction layer composition of limited adjunction of elements (silicon…) to the Al matrix.

To overcome the difficulties inherent to the in-pile irradiated samples, an out-of-pile methodology (collaboration between CEA, FRM II and CERCA) has been developed based on heavy ion irradiation. This methodology enables to simulate the fission fragment damages using a 80MeV iodine beam at the Maier Leibnitz laboratory (Garching, Germany) [4,5]. After irradiation, samples are characterised at micrometer scale by microscopy (SEM coupled with EDX) and X-Ray techniques (XRD and XAS).

The irradiation (final dose: $2 \cdot 10^{17}$ at/cm^2) of undoped U-7wt%Mo fuel plates leads to the formation of an interaction layer surrounding each fuel particles (cf. Figure 1-C). µ-XRD analysis performed at the ESRF (ID18f) showed only the presence of UAl_3 phase in the interaction layer [5]. Same results have been obtained on in-pile irradiated fuel by Sears *et al* [6] using neutron diffraction confirming the interest of the developed methodology. However the behaviour of the Mo atoms in the interaction layer could not be defined on the basis of µ-XRD measurements.

Thus we performed a µ-EXAFS study at the Mo K edge on BM30B at the ESRF using two Rh-coated mirrors installed in the Kirkpatrik-Baez geometry. The size of the spot was lower than 20×10 µm^2. This poster will be focused on the results of these measurements.

Figure 1: Comparison between SEM pictures of fresh, in-pile and heavy ion irradiated UMo dispersed fuels.

A- fresh UMo7/Al fuel

B- neutron irradiated UMo7/Al fuel [7]

C- heavy ion irradiated UMo7/Al fuel

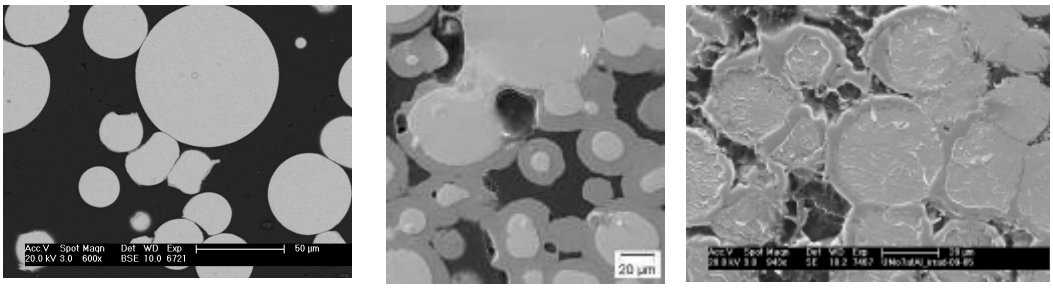

References

[1] M.K. Meyer *et al*, Journal of Nuclear Materials 304, 221 (2002).

[2] F. Huet *et al*, Proceedings of the 25th International Meeting on RERTR, Chicago (USA) (2003).

[3] A. Leenaers *et al*, Journal of Nuclear Materials 335, 39 (2004).

[4] N. Wieschalla *et al* , Proceedings of the 27th International Meeting RERTR, Boston (USA) (2005)

[5] H. Palancher *et al*, Proceedings of the 10th International Meeting RRFM, Sofia (Bulgaria) (2006).

[6] D.F. Sears *et al*, Proceedings of the 10th International Meeting RRFM, Sofia (Bulgaria) (2006).

[7] J. Noirot *et al*., Private communication (2006).

STXM/NEXAFS INVESTIGATION OF THE HUMIC ACID/METAL ION INTERACTION

Markus Plaschke, Jörg Rothe, Melissa A. Denecke
Institut für Nukleare Entsorgung, Forschungszentrum Karlsruhe, Postfach 3640,
D-76021 Karlsruhe, Germany, e-mail: plaschke@ine.fzk.de

Abstract

Humic acids (HA) are known to play an important role in modifying the transport and bioavailability of trace elements in the geosphere. This aspect has to be considered in the safety assessment of nuclear waste disposal. HA/actinide ion interaction is investigated by STXM (Scanning Transmission X-ray Microscopy) / NEXAFS (Near Edge X-ray Absorption Fine Structure) spectromicroscopy at the carbon K-edge performed at the NSLS-STXM endstation (National Synchrotron Light Source, Brookhaven, NY). This technique provides high spatial resolution and spectroscopic information on a 100 nm scale which is highly desired for the characterization of chemically heterogeneous HA. Measurements are performed *in situ* on hydrated colloidal species enclosed in a thin film of water between two silicon nitride membranes. STXM/NEXAFS allows to directly probe the chemical functional groups involved in HA reactions. To understand spectral features of HA C 1s-NEXAFS with and without metal ion complexation, a set of model compounds is investigated. Substituted benzoic acids are examined to demonstrate the effects of functional groups on the C 1s-NEXAFS spectra of complex organic acids, including HA. The peak positions for aromatic and carboxylic groups in these spectra are in agreement with common assignments. The spectral position of the peak for substituted aromatic carbon shifts with increasing withdrawing effect of the substituent to higher photon energies. Polyacrylic acid (PAA) and different PAA metal ion complexes are investigated as model substances for metal ion complexation by HA. Tb(III)-, Zr(IV)- and U(VI)-PAA exhibit general spectral signatures previously observed for the PAA/Eu(III)-PAA system. For these different metal cations, similar spectral changes and distinct variations in peak intensities are observed going from the uncomplexed to the metal-loaded macromolecules. From the comparison of spectral signatures in natural and model systems we can identify HA fractions with strongly differing affinity to metal ions.

References

M. Plaschke, J. Rothe, M.A. Denecke, Th. Fanghänel, *J. Electron Spectrosc. Relat. Phenom.* 135 (2004) 53.

M. Plaschke, J. Rothe, M. Altmaier, M.A. Denecke, Th. Fanghänel, *J. Electron Spectrosc. Relat. Phenom.* 148 (2005) 151.

EXAFS STUDY OF PLUTONIUM SORPTION ONTO KAOLINITE

T.Ye. Reich[1], N.L. Banik[1], R.A. Buda[1], S. Amayri[1], J. Drebert[1], J.V. Kratz[1], N. Trautmann[1], A.L. Ageev[2], M.E. Korshunov[2], T. Reich[1]

[1] Institute of Nuclear Chemistry, Johannes Gutenberg-University Mainz, Mainz, Germany

[2] Institute of Mathematics and Mechanics, Ural Branch of Russian Academy of Sciences, Ekaterinburg, Russia

Abstract

The uptake mechanism of plutonium by kaolinite was investigated by applying X-ray absorption spectroscopy to batch sorption samples (total Pu concentrations 1 and 10 μM; 4 g kaolinite/L in 0.1 M $NaClO_4$; $1 \leq pH \leq 9$; presence and absence of ambient CO_2). For XAFS measurements, one sample was prepared from a Pu(III) solution at pH 6 under argon atmosphere. Three samples were obtained by sorption of Pu(IV) at pH 1, 4, and 9 in an air-equilibrated system. The Pu L_{III}-edge XANES spectra indicated that in all samples, including the Pu(III) sample, plutonium is sorbed at the kaolinite surface as Pu(IV). The Pu L_{III}-edge k^3-weighted EXAFS spectra showed eight oxygen atoms at an average Pu-O distance of 2.3 Å. Two Pu atoms were detected at ~3.7 Å in all spectra, indicating the formation of polynuclear Pu(IV) species at the kaolinite surface. For the sample prepared from Pu(III) solution, an additional Pu-O shell at 3.2 Å was observed. The spectra of samples prepared from Pu(IV) included a Pu-Al/Si co-ordination shell at approximately 3.6 Å, indicating formation of inner-sphere sorption complexes. The structural models used in the least-squares fits were confirmed by an alternative EXAFS data analysis approach based on a modified Tikhonov regularization method.

Introduction

For the safety assessment and design of nuclear waste repositories, detailed studies of the migration behaviour of plutonium are necessary. Its migration behaviour in a potential rock formation of a repository and in the aquifer after a possible radionuclide release from the repository must be known. Besides salt and granite, clay might be a relevant host rock for which the kinetics, thermodynamics, redox behavior, and speciation of plutonium must be investigated. Since clays are an important component of many soils, the sorption of plutonium onto clay surfaces is an important factor influencing the migration of this element. Plutonium has a strong tendency to co-exist in different oxidation states, where each of them can interact differently with the clay. In this study, batch experiments of Pu(III) and Pu(IV) sorption on the reference clay mineral kaolinite have been combined with Pu L_{III}-edge EXAFS spectroscopy to obtain molecular-level information that is fundamental for understanding the interaction of plutonium with the water-kaolinite interface.

Experimental

Batch experiments

Before preparing samples for the EXAFS measurements, the sorption of tri- and tetravalent plutonium onto kaolinite was investigated over the pH range 0-11 by batch-type experiments at Pu concentrations relevant for XAFS [1, 2]. The sorption experiments were carried out at room temperature and in the presence of light using 15 mL polypropylene screw cap centrifuge tubes. Kaolinite KGa-1b (Source Clays Repository) was suspended in de-ionized water (4 g/L). The suspension was preconditioned in 0.1 M $NaClO_4$ and shaken for 48-64 h. The pH was adjusted using 0.1 M $HClO_4$ or 0.1 M NaOH solutions. Then, ^{239}Pu was added to give a total concentration of 1-10 µM with immediate readjustment of the pH. After a contact time of 48-120 h, the solid and liquid phases were separated by centrifugation (2500 rpm for 1 h). The plutonium uptake by kaolinite was determined by measuring the content of free Pu ions in the liquid phase using liquid scintillation counting. The sorption studies have been performed both under aerobic and anaerobic conditions.

Figure 1 shows the sorption of Pu(III) and Pu(IV) as a function of pH under ambient air conditions. Pu(IV) is strongly sorbed over the entire pH range with the sorption edge (50 % sorption) occurring at very acidic conditions of pH ~1. The sorption edge for Pu(III) is observed at a higher pH of ~5.5, and maximum sorption was at pH ~10. In summary, the interaction of tetravalent plutonium with kaolinite is stronger, i.e., sorption extends over a larger pH range than for Pu(III).

Figure 1. Comparison of the sorption of tri- and tetravalent plutonium onto kaoliniteas a function of pH; $p(CO_2) = 10^{-3.5}$ atm, 4 g/L, contact time 120 h.

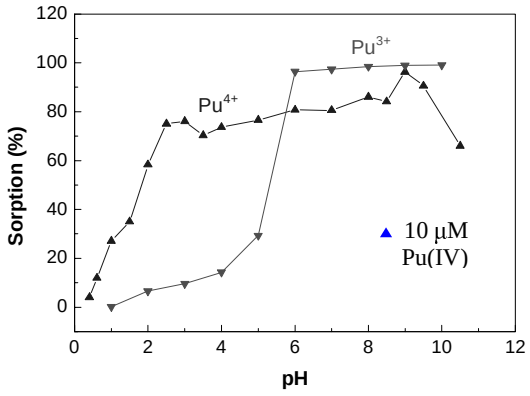

EXAFS experiments and data treatment

Four samples A-D (see Table 1) were prepared with a total concentration of 10 μM ^{244}Pu following the same procedure as for the batch experiments. The Pu(IV) samples A, C, and D were air equilibrated. Sample B was prepared with Pu(III) in a glove box under argon atmosphere.

Table 1: Summary of samples examined by XAFS.

Sample	Pu	pH	Atmosphere	Pu loading (ppm)
A	IV	1	air	94
B	III	6	argon	243
C	IV	4	air	370
D	IV	9	air	412

All samples were measured as wet pastes at the Angströmquelle Karlsruhe (ANKA) at the INE beamline. Plutonium L_{III}-edge XAFS data were collected in fluorescence mode at room temperature. Theoretical scattering phases and amplitudes were obtained with FEFF 8.20 [3]. An atomic cluster of 252 atoms based on the crystal structure of soddyite [4] was used to define the Hedin-Lundqvist self-energy potentials for the FEFF calculations. The automatic overlap of the self-consistent muffin-tin potentials was 1.3. Least-squares refinement of the near-neighbour surrounding of plutonium sorbed onto kaolinite was done with the EXAFSPAK program [5] over the *k*-ranges 2.1-7.5 Å^{-1} for the sample A and 2.3-9.7 Å^{-1} for samples B, C, and D, respectively.

Since it was difficult to find a unique structural model for modelling the experimental data using EXAFSPAK, the raw spectra were analysed in addition by an alternative approach, i.e., a modified Tikhonov regularization method [6] that does not require a structural model as input. Briefly, the relative positions of different pairs of atoms, e.g., Pu-O, Pu-Si, and Pu-Pu, can be described by three partial radial distribution functions (RDFs) $g_j(r)$. The relationship between the experimental EXAFS spectrum $\chi(k)$ and g_j is given by the equation:

$$Ag \equiv \sum_{j=1}^{3} A_j g_j = \frac{4\pi\rho_0}{k} S_0^2(k) \sum_{j=1}^{3} c_j \int_{a_j}^{b_j} f_j(k,r) e^{\frac{-2r}{\lambda(k)}} \times \sin\left(2kr + \varphi_j(k,r)\right) g_j(r) dr = \chi(k), \qquad (1)$$

where the wave vector $k \in [c,d]$, $f_j(k,r)$ is the backscattering amplitude, $\varphi_j(k,r)$ is the backscattering phase shift, $\lambda(k)$ is the electron inelastic mean free path, S_0^2 is the amplitude reduction factor, and ρ_0 is the atomic density. To determine the solutions g_j, j = 1, 2, 3, the system of Fredholm integral equations (1) must be solved [6]. This is a typical example of an ill-posed problem. The three solutions of (1) are determined using *a priori* information about the structure of the near-neighbour surrounding of plutonium, i.e., each RDF g_j consists of a small number of narrow peaks that are separated in distance by intervals Δr. The algorithm for the determination of g_j is described in [6-9] and consists of the following steps: variation Tikhonov method [6], application of separating functionals [7] to find the intervals Δr where true peaks are absent, and iteration method with filtration in real space [8].

Results and discussion

The plutonium oxidation state in samples A-D was identified by the corresponding Pu L_{III}-edge XANES spectra (Figure 2, left). In all XANES spectra neither a shift in the absorption-edge energy nor a significant structural difference at the high energy side of XANES was observed, indicating that

the plutonium in all samples is sorbed at the surface of kaolinite as Pu(IV). It can be concluded that the initial Pu(III) in sample B was oxidized to Pu(IV).

The k^3-weighted experimental EXAFS data and least-squares fits for samples A-D are shown in Figure 2 (middle). All but one (sample A) of them shows a good signal-to-noise ratio out to a *k*-value of ~10 $Å^{-1}$. All spectra are dominated by a low-frequency oscillation due to the backscattering from the nearest oxygen atoms. The EXAFS spectra of samples A, C, and D are very similar. Sample B shows a different EXAFS pattern, in particular in the *k*-range 6-8 $Å^{-1}$. The Fourier transform (FT) of the EXAFS spectra (Figure 2, right) represents a pseudo radial distribution function of the plutonium near-neighbor surrounding. The most prominent peak in all spectra is at ~1.8 Å (uncorrected for phase shift) and arises from the backscattering caused by eight oxygen atoms coordinated to Pu(IV). A Pu-Pu interaction at ~3.7 Å with two plutonium atoms is observed in all spectra, indicating the formation of polynuclear plutonium species at the kaolinite surface. In addition to the Pu-O and Pu-Pu coordination shells, a third shell at an intermediate distance had to be included in all fits. The best fit to the data of samples A, C, and D, which were prepared with $1x10^{-5}$ M Pu(IV), was obtained with a Pu-Al/Si co-ordination shell at 3.6–3.7 Å. In case of sample B, a second Pu-O shell at 3.25±0.02 Å had to be included in the shell fit. The metrical parameters for samples A-D are given in Table 2.

Figure 2: Pu L_{III}-edge XANES (left) and k^3-weighted EXAFS spectra (middle) with corresponding Fourier transform magnitudes (right). Calculations were performed by non-linear least-squares fits using EXAFSPAK.

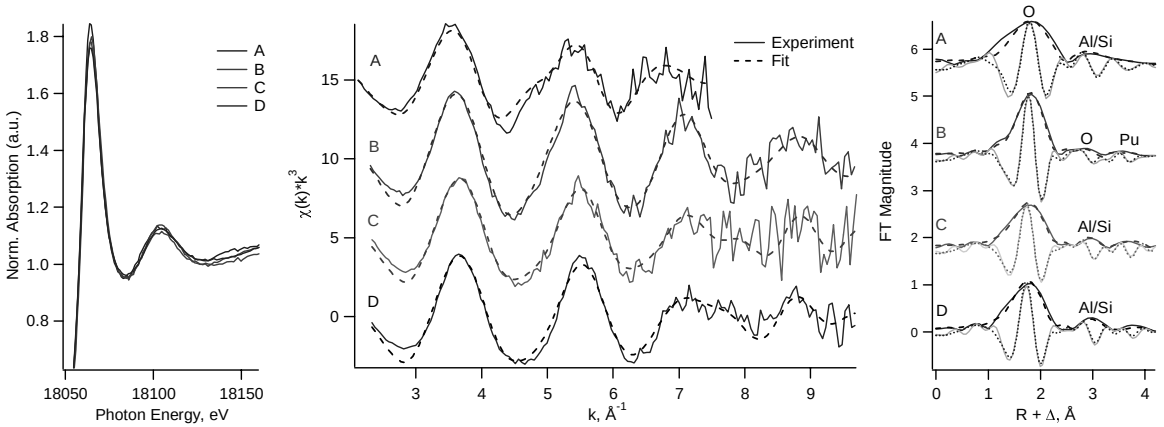

Table 2. Results of least-squares refinement. The coordination numbers were fixed. Distances *r* to Pu neighbors are in Å (± 0.02 Å). Debye-Waller factors σ^2 are in $Å^2$ (± 0.004 $Å^2$).

	8 x O_1		2 x O_2		2 x Al/Si		2 x Pu	
	r	σ^2	*r*	σ^2	*r*	σ^2	*r*	σ^2
A	2.34	0.0212	-	-	3.66	0.0054	3.70	0.0080
B	2.31	0.0110	3.25	0.0070	-	-	3.70	0.0150
C	2.28	0.0169	-	-	3.62	0.0091	3.69	0.0076
D	2.27	0.0154	-	-	3.62	0.0050	3.68	0.0145

To increase the reliability of the structural analysis by least-squares fitting, the EXAFS analysis of samples B and C was repeated using the modified regularisation method described before. Inter-atomic distances and corresponding co-ordination numbers were derived from the position of the maximum and the area, respectively, of the RDF peaks displayed in Figs. 3 and 4. The following results were obtained: The RDF *g*(Pu-O) for sample B has one peak corresponding to ~8 oxygen atoms centered at 2.32 Å followed by a broad peak ranging from 2.6-3.5 Å with ~9 oxygen atoms (Figure 3, left). The RDF *g*(Pu–Pu) exhibits a single peak originating from one plutonium atom at 3.69 Å (Figure 3, right). No Pu-Al/Si interaction was detected for sample B. Sample C is similar to sample B in that the RDFs in Figure 4 show a peak of ~8 oxygen atoms at 2.28 Å and a peak of ~2 plutonium atoms at 3.65 Å, respectively. However, instead of a second oxygen peak as observed for sample B, *g*(Pu-Al/Si) of sample C has one peak of ~2 Al/Si atoms centered at 3.60 Å.

Figure 3: Partial radial distribution functions *g(r)* for sample B. *g*(Pu-Si) is not shown since no Pu-Al/Si interaction was detected by the method of separating functionals.

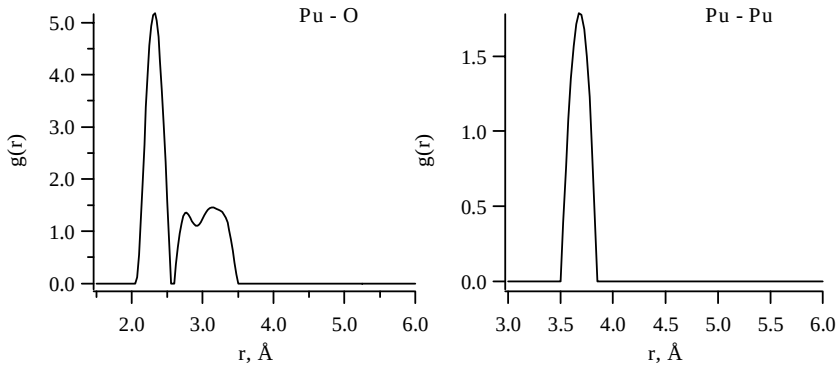

Figure 4: Partial radial distribution functions *g(r)* for sample C.

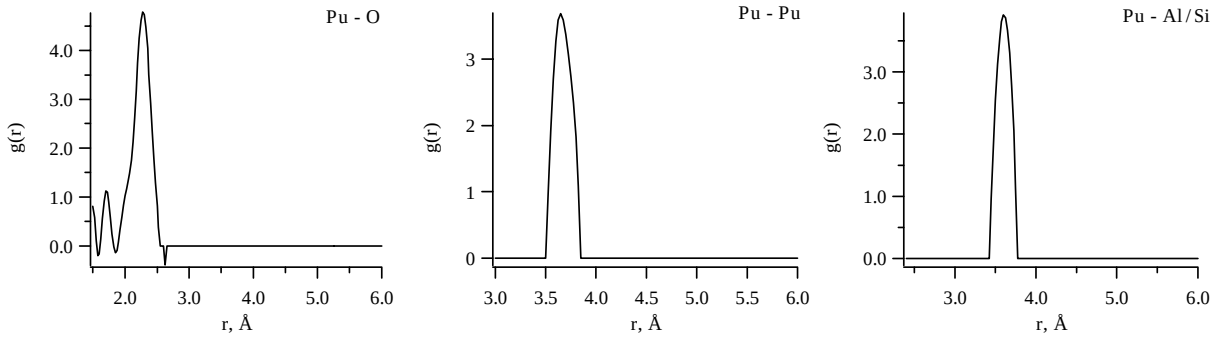

Table 3. EXAFS structural parameters of Pu sorbed onto kaolinite. Method 1: least-squares refinement; method 2: modified Tikhonov regularisation. (*r* - distance in Å, *N* - coordination number, * - fixed values).

Sample	Method	Pu-O_1		Pu-O_2		Pu-Si		Pu-Pu	
		r	*N*	*r*	*N*	*r*	*N*	*r*	*N*
B	1	2.31	8*	3.25	2*	-	-	3.70	2*
	2	2.32	7.8	2.6 ÷ 3.5	9.2	-	-	3.69	0.8
C	1	2.28	8*	-	-	3.62	2*	3.69	2*
	2	2.28	7.5	-	-	3.60	1.7	3.65	1.6

The results of the two alternative EXAFS analysis methods for samples B and C are given in Table 3. This comparison shows that the corresponding $g_j(r)$, which were calculated by the modified Tikhonov regularisation method without assuming any structural model, agree within the experimental errors with the results from the least-squares refinement. The only significant difference is the coordination number for the second oxygen shell of sample B. The least-squares refinement assuming a Gaussian distribution resulted in two oxygen atoms at 3.25 Å (Table 3). In contrast, the modified Tikhonov regularisation gave a broad distribution in the range of 2.6-3.5 Å (Figure 3, left) with a peak area corresponding to nine atoms. Such a distribution cannot be modelled by a single Gaussian peak. Therefore, the difference in the Pu-O co-ordination number could be caused by the limitation imposed by the structural model used for the least-squares refinement.

In summary, the sorption mechanism for samples A, C, and D can be rationalized by an inner-sphere sorption of polynuclear Pu(IV) species at the kaolinite surface. The EXAFS spectrum of sample B prepared from Pu(III) under argon atmosphere resulted in Pu(IV) at the kaolinite surface, but did not show indication of inner-sphere sorption since no Pu-Al/Si interaction was observed. The Pu(IV) in sample B has a Pu-O interaction at 3.25 Å instead. Similar Pu-O distances were observed for Pu(IV) colloids [10]. The cause of the detected structural differences of sample B compared to samples A, C, and D, and the reason for the oxidation of Pu(III) to Pu(IV) are the subject of ongoing studies.

Acknowledgement

We gratefully acknowledge ANKA for the provision of beam time, B. Brendebach, K. Dardenne, M.A. Denecke, and J. Rothe for their support at the INE-Beamline, and Bundesministerium für Wirtschaft und Technologie for financial support (project No. 02E9653). R.A. Buda was supported by a fellowship of the DFG Graduiertenkolleg No. 826. A.L. Ageev and M.E. Korshunov were supported by the Russian Basic Research Foundation (grant No. 06.01.00116).

References

[1] N.L. Banik, R.A. Buda, S. Bürger, J.V. Kratz, N. Trautmann *Radiochim. Acta* (submitted).

[2] R.A. Buda, N.L. Banik, J.V. Kratz, N. Trautmann *Radiochim. Acta* (in preparation).

[3] A.L. Ankudinov, C.E. Bouldin, J.J. Rehr, J. Sims, H. Hung *Phys. Rev. B* 65 104107/1 (2002).

[4] F. Demartin, C.M. Gramaccioli, T. Pilati *Acta Cryst. C* 48 1 (1992).

[5] G.N. George, I.J. Pickering: EXAFSPAK – A Suite of Computer Programs for Analysis of X-ray Absorption Spectra, Stanford (2000).

[6] Yu.A. Babanov, V.V. Vasin, A.L. Ageev, N.V. Ershov *Phys. Stat. Sol. B* 105 747 (1981).

[7] A.L. Ageev, T.V. Antonova, T.Ye. Reich, T. Reich, C. Hennig *Mathematic Modelling* 16 81 (2004).

[8] A.L. Ageev, M.E. Korshunov, T.Ye. Reich, T. Reich, H. Moll *J. Inverse and Ill-posed Problems* (submitted).

[9] T.Ye. Reich, Ph.D. Thesis, Johannes Gutenberg-Universität Mainz (in preparation).

[10] S.D. Conradson *Appl. Spectrosc.* 52 252A, (1998).

THE MOLECULAR TOPOLOGY OF URANIUM(VI) BONDING TO IRON AND ALUMINIUM OXYHYDROXIDE NANOCLUSTERS REVISITED BY EXAFS SPECTROSCOPY

André Rossberg[1,2], Kai-Uwe Ulrich[3] and Andreas C. Scheinost[1,2]
[1]Forschungszentrum Rossendorf, Institute of Radiochemistry,
P.O. Box 510119, D-01314 Dresden, Germany
[2]The Rossendorf Beamline at ESRF, B.O. Box 220, F-38043 Grenoble, France
[3]Washington University in St. Louis, Environmental Engineering Science,
Campus Box 1180, St. Louis MO 63130, U.S.A.

Abstract

Applying a novel approach to the spectral analysis of Extended X-ray Absorption Fine Structure (EXAFS) we were able to derive an advanced 3-D structural model of the uranyl sorption complex on hydrated carbonate-free surfaces of aluminum(III) and iron(III) oxyhydroxide nanoclusters. The calculated molecular model fits the EXAFS data consistently up to a radial sphere of 4.5 Å around the uranium absorber. Being unaware of the physicochemical reasons for the specific complex topology characterized by a slightly tilted and distorted geometry, alternative ideas of EXAFS interpretation are discussed.

X-RAY ABSORPTION FINE STRUCTURE SPECTROSCOPY OF Eu(III) AND UO_2^{2+} COMPLEXATION WITH POLYACRYLIC ACID

Jörg Rothe, Markus Plaschke, Bernd Schimmelpfennig, Melissa A. Denecke
Forschungszentrum Karlsruhe, Institut für Nukleare Entsorgung, Postfach 3640, D-76021 Karlsruhe, Germany

Abstract

Scanning Transmission X-ray Microscopy (STXM), C 1s-Near Edge X-ray Absorption Fine Structure (NEXAFS) spectroscopy, Extended X-ray Absorption Fine Structure (EXAFS) and quantum-chemical calculations are applied to investigate the electronic and structural effects of metal ion complexation with polyacrylic acid (PAA). PAA is chosen as simple model ligand for polyfunctional humic acids. C 1s-NEXAFS spectral changes observed for the PAA/Eu(III)-PAA and PAA/UO_2^{2+}-PAA systems indicate a stronger interaction between the metal cation and the ligand molecule for uranyl (greater decrease in C 1s (COOH) $\rightarrow \pi^*_{C=O}$ transition intensity and an increase in the broad absorption feature above 286.5 eV). This is in agreement with UO_2^{2+}-PAA having a complex formation constant orders of magnitude higher than Eu(III)-PAA. EXAFS analysis and *ab initio* energy minimization calculations reveal associated differences in the molecular structure of the two complexes. Eu(III) is co-ordinated by around four water molecules and four carboxylate groups in a monodentate fashion in the aqueous Eu(III)-PAA complex. There are only three bidentate coordinated carboxylate groups in the equatorial plane of the dioxo cation in the aqueous UO_2^{2+}-PAA complex, resulting in a molecular structure similar to that in crystalline $UO_2(C_2H_3O_2)_3$.

Introduction

Transport and bioavailability of trace metal elements in the environment are determined to a large extent by sorption processes. Binding to inorganic or organic carrier colloids like clays or humic substances may strongly enhance trace element mobility in aquatic environments. Humic acids (HA) comprise a class of natural water-soluble polyelectrolytes with dimensions in the nm range and an inherent chemical poly-functionality [1]. HA may play a significant role in the far-field transport of actinide ions potentially released from a future underground nuclear waste repository [2]. It is well known from previous EXAFS studies that carboxylate functionalities are likely to act as primary metal ion complexing sites in HA [3, 4]. Polyacrylic acid (PAA: $[-CH_2-CH(COOH)-]_n$) has a high content of carboxyl functional groups attached to a simple backbone of variable chain length and therefore finds application to mimic HA in metal cation polyelectrolyte sorption studies. The advantage PAA has as a HA model is that one can circumvent the structural uncertainties intrinsic to HA. Numerous publications utilising such a strategy to study the interaction between metal cations and HA have been reported. For example, Lis and co-workers [5] investigate the change of spectroscopic properties of Eu(III) bound to PAA with varying molecular weight. They report a predominance of rapid, strong binding of the lanthanide cation in a 1:3 Eu(III):[COO-] molar ratio, with retention of three hydration water molecules. Montavon *et al*. [6] oberserve a rearrangement of PAA chains to form inner-sphere complexation sites, where Eu(III) is coordinated with three carboxylate groups. Martínez *et al*. [7] characterize Eu(III) binding in various mixtures of PAA and polyvinylsulfonic acid (PVS). These authors emphasize the need for detailed knowledge about the number and type of binding environments, as well as their relative contributions to the overall sorption, in order to describe metal complexation by polyelectrolytes. Gerstmann and co-workers [8] use optical absorption spectroscopy to assess Pu(IV)/Pu(VI)-PAA interaction, proposing a chelation effect to describe formation constants that are greater than those from corresponding complexes with low-molecular carboxylic acids. Kubota and Tochiyama determine complex formation constants for Eu(III) [9] and Np(V) [10] with PAA in comparison to HA by solvent extraction studies. Striking similarities have been recently observed for spectral trends for C 1s-NEXAFS signatures before and following complexation with Eu(III) in the PAA/Eu(III)-PAA and HA/Eu(III)-HA systems [11, 12]. Why changes in the PAA C 1s-NEXAFS associated with metal ion complexation significantly vary with the type of metal cation (Me^{n+}) is unknown. In this study we investigate the Eu(III)-PAA and the UO_2^{2+}-PAA complexation by comparing the C 1s-NEXAFS obtained from the PAA ligand with the L3-edge EXAFS obtained from the metal cations. Based on the molecular structure of the lanthanide and actinyl ion complexes derived from EXAFS we suggest that different Me^{n+}-PAA binding mechanisms might be responsible for varying C 1s-NEXAFS spectral signatures. C 1s-NEXAFS are extracted from stacks of STXM images from selected sample regions, recorded as a function of incident photon energy E. The EXAFS results are compared to quantum chemical calculations.

Materials and Methods

Sample preparation

All chemicals are of analytical grade (purchased from Sigma-Aldrich, Deisenhofen, Germany) unless specified otherwise. For the investigation of Eu(III)-PAA, acidic solutions (pH~2) of the europium nitrate salt (diluted ICP-MS standard) are added to acidic PAA solutions (background electrolyte 0.1 M NaCl, Merck suprapur, Darmstadt, Germany). A pH around 5 is adjusted by adding small portions of 0.1 M NaOH. The UO_2^{2+}-PAA samples are prepared similarly, using a 1E-2 M stock solution of uranyl nitrate hexahydrate (Merck, Darmstadt, Germany) in 0.1 M NaCl (pH 4). The final total PAA (c PAA) and Me^{n+} concentrations (c Me^{n+}) and the corresponding pH values of the sample solutions for both spectroscopy methods are summarised in Table 1. Sample solutions for EXAFS experiments contain excess PAA ligand concentrations and are enclosed in capped 400 µl polyethylene vials. Metal-to-ligand ratios for samples to be investigated by STXM/NEXAFS

spectromicroscopy are chosen to saturate the loading capacity of the polyelectrolyte. In this case complete precipitation of PAA is induced. The sample preparation technique for STXM measurements using wet cells has been described elsewhere [13]. The Me^{n+}-PAA aqueous suspensions are investigated as thin films enclosed between two silicon nitride membrane windows of a wet cell. Na(I)-PAA is measured in the dried state.

Table 1: List of samples investigated in this study.

Sample	method	c PAA (g/L)	c Me^{n+} (mol/L)	pH
Eu(III)-PAA	STXM	1.9	3.1E-2	4.9
	EXAFS	0.44	1.0E-3	5.0
U(IV)-PAA	STXM	0.03	6.0E-4	4.6
	EXAFS	0.95	2.1E-3	4.5

STXM and C 1s-NEXAFS spectroscopy

STXM investigations are performed at the STXM endstation (X-1A outboard-STXM) at the National Synchrotron Light Source, Brookhaven, NY [14]. The experimental setup is schematically depicted in Figure 1. A Fresnel zone plate is used to focus the soft X-ray undulator beam into a spot of nominal 55 nm width (Rayleigh resolution criterion [15]). The STXM endstation provides a flux of about 10^7 photons/sec, with an energy bandwidth of about 0.1 eV at the C 1s-energy (see, e.g., [16] and references therein). For extracting NEXAFS spectra, stacks of images are recorded as a function of the photon energy E. For a review of the procedure for image stack data analysis, see [17]. E is varied for recording images in 1 eV steps in the range 280-285 eV, in 0.1 eV steps for 283-292 eV, in 0.5 eV steps at energies 292-300 eV and in 1 eV steps at energies 300-305 eV. C 1s-NEXAFS spectra are extracted through the analysis of the absorption signal, $\mu(E)*d = \ln(I_0(E)/I(E))$, of vertical projections onto aligned image stacks. Image regions free of particles supply information on the incoming intensity (I_0). The transmitted intensity (I) is derived from image regions containing carbonaceous structures. NEXAFS spectra are displayed after subtracting a linear pre-edge background (280-283 eV), followed by normalization ($\mu*d = 1$) at 300 eV.

Figure 1: Experimental setup of STXM; ZP: zone plate; OSA: order-sorting aperture (image taken from [13] with kind permission from the publisher *http://journals.iucr.org***)**

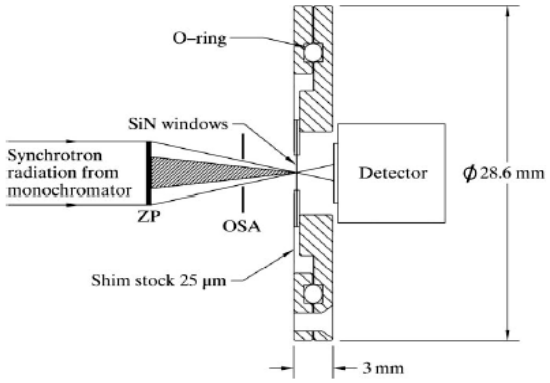

EXAFS spectroscopy

Eu L3- (6977 eV) and U L3- (17166 eV) EXAFS measurements are performed at the ANKA INE-Beamline for actinide research [18], Forschungszentrum Karlsruhe, Germany, using pairs of Ge(220) (2d=4.0Å) and Ge(422) crystals (2d=3.412Å) in the double crystal monochromator, respectively. The INE-Beamline is equipped with a collimating first and a focusing second mirror. The beam spot used is 6×1.5 mm^2. Higher harmonic radiation in the incident beam is suppressed by detuning the parallel alignment of the DCM crystals to 70% of photon flux peak intensity. The spectra are calibrated against the first derivative X-ray absorption near edge structure (XANES) spectrum of an Fe foil (7112 eV) for the Eu L3- and a Zr foil (17998 eV) for the U L3-edge. EXAFS spectra are recorded in fluorescence detection mode by normalizing the energy dependent Eu $L\alpha_{1,2}$ and U $L\alpha_{1,2}$ fluorescence intensity to I_0. Fluorescence radiation is registered using a 5-pixel energy dispersive solid state Ge detector (Canberra LEGe) and I_0 measured using N_2 (Eu) or Ar (U) filled ionization chambers at ambient pressure. Up to six scans are collected and averaged for each sample.

EXAFS data analysis is based on standard least square fit techniques [20] using the WinXAS [21] (v3.0) and the UWXAFS [22] program packages. The region up to about 600 eV above the Eu L3 edge (k~11 $Å^{-1}$) and up to about 800 eV above the U L3 edge (k~14.5 $Å^{-1}$) is investigated. EXAFS data is recorded in equidistant k-steps (0.03 Å-1) beginning ~40 eV above the ionization energy (E_0). Atomic background functions $\mu_0(E)$ are optimized with respect to spurious contributions below ~1.1 Å (for Eu) and ~0.9 Å (for U, i.e., about half of the nearest neighbour distance) in the Fourier transform (FT) of the data using WinXAS. For E_0 of both edges, the origin for calculation of the $\chi(k)$-function, is fixed at the maximum of the most intense absorption feature the white line (WL). Metrical parameters (neighboring atomic distances R_i, mean square displacements or EXAFS Debye-Waller factors σ^2_i, and co-ordination numbers N_i for the different co-ordination shells i) are determined using the *feffit* code (v2.98). For the analysis of the Eu(III)-PAA sample, backscattering amplitude and phase shift functions for single scattering paths are obtained from FEFF (v8.2) [23, 24] calculations. For the U(VI)-PAA sample, the amplitude and phase shift functions are calculated using an 11-atom cluster having atomic positions derived from the tris(acetato)dioxouranate $UO_2(C_2H_3O_2)_3$ crystal structure [19]. This cluster is also used to simulate the $UO_2(C_2H_3O_2)_3$ U L3-EXAFS. Scattering paths up to an effective length of 3.631 Å are used in the simulation, including double scattering within the equatorial shell and triple scattering along the uranyl axis. Prior to analysis, the k^2-weighted Eu and k^3-weighted U L3-EXAFS spectra are Fourier-transformed using symmetric square windows with δk=0.2 $Å^{-1}$ 'Hanning sills'. All fit operations are performed on the FT data in R-space over the radial distance range given in Table 2. The amplitude reduction factor S_0^2 is set to 0.8 for both edges.

Quantum chemical calculations

Quantum chemical calculations are performed to obtain structural data to be compared with EXAFS results. Calculations are carried out at the Density Functional Theory (DFT) level for the UO_2^{2+}-PAA complex. We apply the B3-LYP functional, using a pseudo potential for uranium to parameterize the core electrons and their interaction with the valence electrons as well as relativistic effects. The light atoms are described by small basis sets of SV(P)-quality as provided by the TURBOMOLE package [25]. C_{3h} symmetry is imposed and the optimized structure is confirmed to be a local minimum by calculating the harmonic frequencies. Eu(III)-PAA is investigated at the DFT-level using more flexible basis sets.

Table 2: Data range and metric parameters extracted by least-square fit analysis of Eu and U L3-EXAFS spectra. Values in parentheses are statistical uncertainties of the last digit. Values in italics are derived from TURBOMOLE calculations. Values in square brackets are for $UO_2(C_2H_3O_2)_3$ reported in [19]. A fixed value is denoted by [f] and a global parameter in the fit by [c].

Sample	fit range R-Δ (Å)	shell	R (Å)	N	σ^2 (Å^2)	ΔE (eV)	*R*-factor
Eu(III)-PAA	1.04-3.37	O	2.43(3) *2.42$_{COO}$/2.46$_{H2O}$*	8.3(8)	0.0057(8)	4.02	0.0025
		C	3.62(3) *3.47*	3.7(4)	0.0055(8)	0.70	
Uranyl-PAA	1.01-2.39	O_{ax}	1.77(2) [1.76] *1.78*	2.0[f] [2.0]	0.0017(6)	11.0[c]	0.021
		O_{eq}	2.46(2) [2.46] *2.50*	6.5(8) [6.0]	0.0080(9)	11.0[c]	
		C	2.89(3) [2.85] *2.88*	3.3(4) [3.0]	0.0080(9)	11.0[c]	

Results and Discussion

C 1s-NEXAFS spectra and STXM images of Me^{n+}-PAA complexes

The STXM image of the UO_2^{2+}-PAA aggregates (Figure 2) exhibits a somewhat different morphology compared to that reported in [11] for Eu(III)-PAA. We observe uniform aggregates with a few regions of embedded dense material in UO_2^{2+}-PAA, while Eu^{3+}-PAA is characterised by a more fractal morphology. However, in both cases the signature of the NEXAFS spectra extracted from these aggregates is independent of the location within the specimen, pointing to their chemical homogeneity. The normalized C 1s-NEXAFS spectra of Na(I)-, Eu(III)- and UO_2^{2+}-PAA are displayed in Figure 3. The Na(I)-PAA C 1s-NEXAFS is dominated by the C 1s (COOH) $\rightarrow \pi^*_{C=O}$ transition resonance at ~288.4 eV (carboxylic peak). As described previously [11, 12], Me^{n+}-PAA samples exhibit a strong C 1s (COOH) $\rightarrow \pi^*_{C=O}$ transition intensity decrease compared to that of Na(I)-PAA. This decrease is accompanied by the appearance of a broad absorption feature above 286.5 eV, adjacent to the carboxyl resonance. The C 1s (COOH) $\rightarrow \pi^*_{C=O}$ intensity decrease is larger for UO_2^{2+}-PAA compared to Eu(III)-PAA; the corresponding intensity increase of the new transition feature is in the same order. Because no optical density loss is observed in Me^{n+}-PAA sample STXM images taken at the beginning and at the end of each stack, we exclude the possibility of radiation damage being responsible for the observed spectral changes [11]. Hence, the C 1s (COOH) $\rightarrow \pi^*_{C=O}$ transition intensity decrease and the appearance of the feature near 286.5 eV must result from electronic and/or structural rearrangements in the PAA carboxylic groups induced by metal cation complexation. It is interesting to note that the UO_2^{2+}-PAA complex formation constant is reported to be orders of magnitude higher than for Eu(III)-PAA [26, 27]. This difference likely lies in different bonding mechanisms for the linear dioxo cation and the spherical lanthanide cation (*cf.* below).

Figure 2: STXM image (288.4 eV) of PAA aggregates induced by uranyl complexation (c PAA: 0.03 g/L, c UO_2^{2+}: $6 \cdot 10^{-4}$ mol/L, pH 4.6)

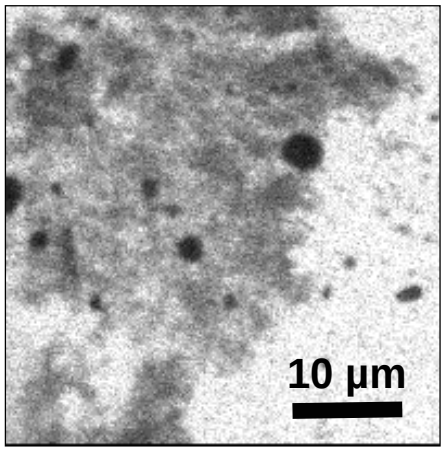

Figure 3: Normalized C 1s-NEXAFS spectra of Na^+, Eu^{3+} and $(UO_2)^{2+}$-PAA

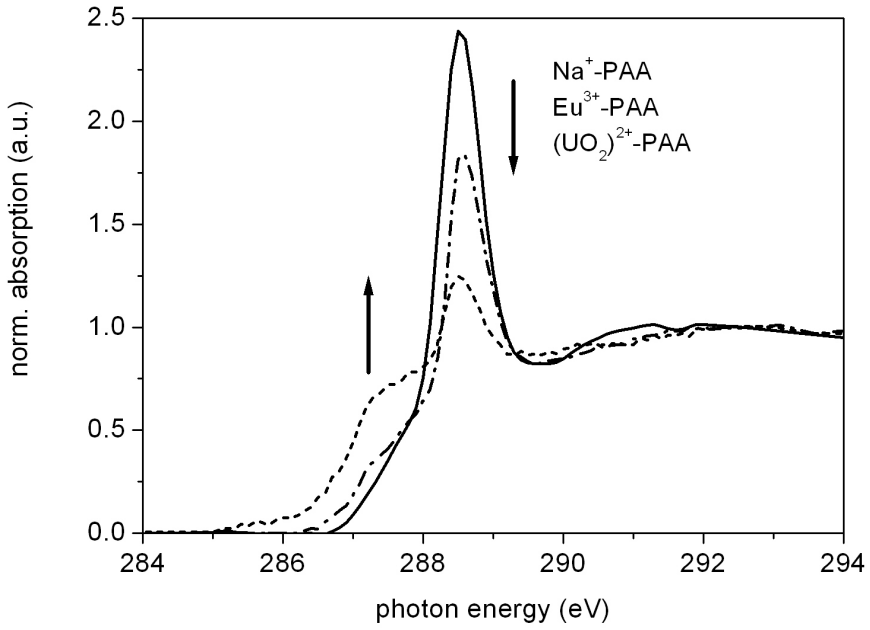

EXAFS and energy optimized molecular structures of Me^{n+}-PAA complexes

The coordination environment of the Eu(III)-PAA and UO_2^{2+}-PAA complexes are determined by EXAFS spectroscopy. Figure 4a shows the k^2-weighted Eu L3-edge Eu(III)-PAA data, together with R-space fit results; Figure 4b shows k^3-weighted U L3-edge UO_2^{2+}-PAA data. Metrical parameters obtained by the least-square fit procedure are summarized in Table 2. Figure 4c depicts results for the $UO_2(C_2H_3O_2)_3$ FEFF EXAFS simulation. Eu L3-EXAFS indicates the presence of four second shell

carbon atoms at a 3.62 Å distance, in addition to 8-9 first shell oxygen atoms at 2.43 Å. This points to formation of predominantly a Eu(III)-PAA complex, where 4 of the 8-9 water molecules originally present in the Eu^{3+} aquo ion [28] are replaced by the same number of monodendate bound carboxyl ligands. This corroborates TRLFS results reported in [11], where fluorescence lifetime changes associated with complex formation are interpreted to indicate a reduction of the number of coordinating water molecules from 8-9 in the aquo ion to 4 in the complex.

Figure 4: (a) Eu L3-EXAFS and R-space fit results for Eu(III)-PAA; (b) U L3-EXAFS and R-space fit results for Uranyl-PAA; (c) FEFF8 U L3-EXAFS simulation for tris(acetato)dioxouranate. Left panel: FT magnitude of EXAFS data (solid line), fit magnitude (open circles), FT imaginary part (thin solid line) and fit imaginary part (open triangles); right panel: k^2 or k^3-weighted raw data (thin solid line), back-transformed fit (open circles) and corresponding Fourier-filtered data (solid line)

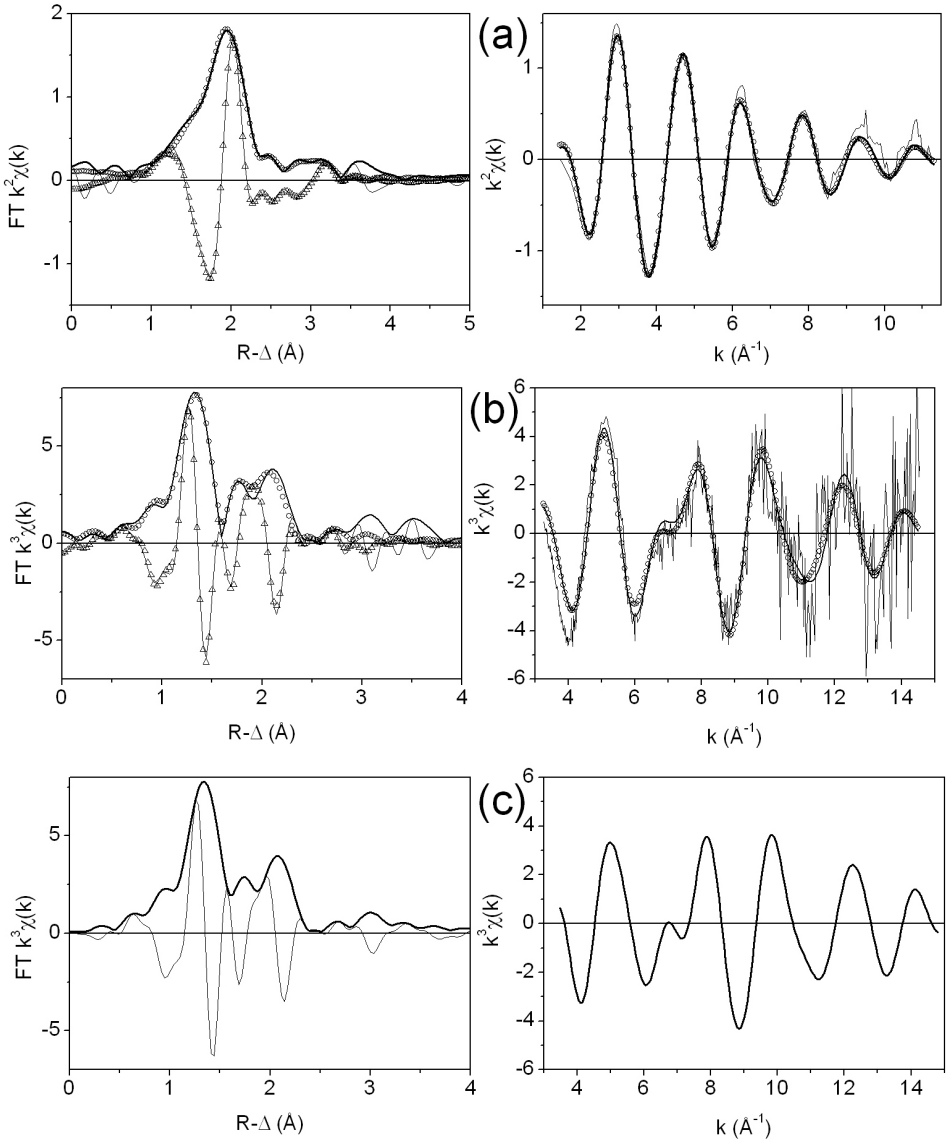

The energy optimized structure in Figure 5a obtained by TURBOMOLE calculations shows Eu(III) to bind 4 carboxylate groups (two neighbouring carboxylate groups from two PAA chains) in a monodentate fashion. Several hydration water molecules are required to complete the first coordination sphere. Hydrogen-bond between the COO^--groups and the hydration water molecules are indicated by dashed lines. Applying simple geometric assumptions to the EXAFS fit results allows estimation of the C-O-Eu angle to be about 151° (assuming a C-O distance of 1.34 Å [29], *cf.* triangle in Figure 5a). In the case of EXAFS results for UO_2^{2+}-PAA, the U-O_{eq} co-ordination number and bond distance value (about 6 O atoms at 2.46 Å) and the clear presence of second next neighbour shell of carbon atoms (about 3 C atoms at 2.89 Å) are in agreement with predominant bidentate co-ordination of uranyl cations by three carboxylate groups in the equatorial plane. This same carboxylate complexation mode was reported by Denecke *et al*. [30] and Moll *et al*. [31] for simple, non polymeric organic acids. Comparison of our fit results to the molecular structure in $UO_2(C_2H_3O_2)_3$ [19] indicates the aqueous UO_2^{2+}-PAA complex to have a similar local uranium structure as the crystalline solid; the simulated $UO_2(C_2H_3O_2)_3$ EXAFS generally reproduces the three FT magnitude peaks and FT imaginary part of the UO_2^{2+}-PAA EXAFS very well. The additional feature visible above 3 Å (R-Δ) in the experimental data and the simulation is due to multiple scattering along the linear uranyl axis [32]. The quantum chemical calculations support the presence of three bidentate bound ligands in the equatorial plane of the dioxo cation (U-O bond length ~2.50 Å). A possible structure based on these calculations is shown in Figure 5b.

Figure 5: Molecular structure of (a) Eu(III)-PAA and (b) UO_2^{2+}-PAA derived from TURBO-MOLE energy minimisation calculations. Hydrogen bonding in Eu(III)-PAA is indicated by dashed lines. The triangle shows the C-O-Eu bonding angle estimated from EXAFS results

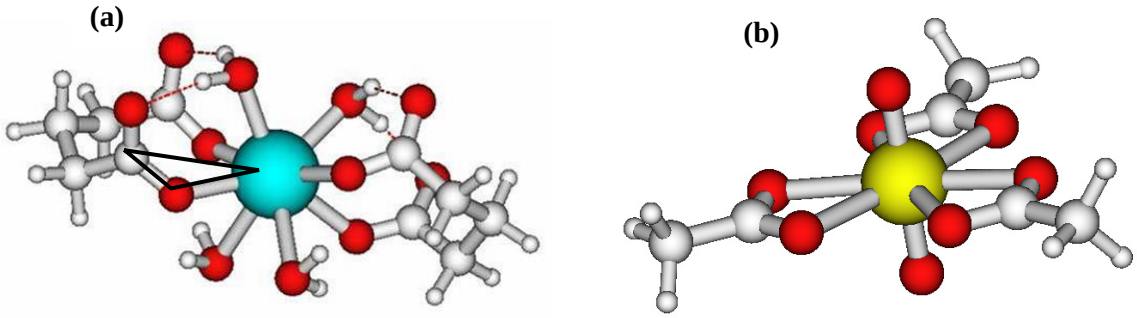

Conclusions

We observe a distinct metal ion complexation effect in the C 1s-NEXAFS of different Me^{n+}-PAA complexes. The extent of the spectral changes varies with the type (or charge) of the metal cation. EXAFS results show that the carboxylate bonding mode (monodentate in Eu(III)-PAA and bidentate in UO_2^{2+}-PAA) differs for the different cations. Energy-minimized coordination structures for the two complexes obtained from quantum-chemical calculations give the same differing binding modes. The difference in molecular structures is likely the source of the difference in complex formation constants (or strength of the chemical bonds) reported for the two systems investigated. These results combined show that the different observed NEXAFS signatures are associated with different binding modes. This means that differences in metal cation-ligand interaction such as binding mode and bond strength may be directly discerned from NEXAFS spectral signatures. Our quantum-chemical activities are

presently being extended to enable reproduction of the PAA/Me^{n+}-PAA C 1s-NEXAFS spectral changes by DFT based *ab initio* calculations.

Acknowledgements

We are grateful for beam-time allotment by BNL/NSLS. STXM data was collected at the X-1A station developed by the group of Janos Kirz and Chris Jacobsen at SUNY Stony Brook, with support from the Office of Biological and Environmental Research, U.S. DoE under contract DE-FG02-89ER60858, and the NSF under grant DBI-9605045. We acknowledge Sue Wirick for technical assistance with the STXM measurements. This work receives financial support from the Helmholtz Association of National Research Centres, Bonn, Germany, within the Virtual Institute of Functional Properties of Aquatic Interfaces.

References

1. M.H.B. Hayes, in: P. Mac Carthy, R.L. Malcolm, R.S. Swift (Eds.), Humic Substances II, John Wiley, New York, 1989.
2. J.I. Kim, MRS Bulletin 19(12) (1994) 47.
3. M.A. Denecke, D. Bublitz, J.I. Kim, H. Moll, I.J. Farkes, J. Synchrotron Rad. 6 (1999) 394.
4. M.A. Denecke, T. Reich, S. Pompe, M. Bubner, K.-H. Heise, H. Nitsche, P.G. Allen, J.J. Bucher, N.M. Edelstein, D.K. Shuh, K.R. Czerwinski, Radiochim. Acta 82 (1998) 103.
5. S. Lis, Z. Wang, G.R. Choppin, Inorg. Chim. Acta 239 (1995) 139.
6. G. Montavon, B. Grambow, New J. Chem. 27 (2003) 1344.
7. G.A. Martínez, S.J. Traina, T.J. Logan, J. Coll. Interf. Sci. 204 (1998) 33.
8. U.C. Gerstmann, C. Lierse, K.E. Geckeler, Radiochim. Acta 89 (2001) 377.
9. T. Kubota, O. Tochiyama, K. Tanaka, Y. Niibori, Radiochim. Acta 90 (2002) 569.
10. O. Tochiyama, H. Yoshino, T. Kubota, M. Sato, K. Tanaka, Y. Niibori, T. Mitsugashira, Radiochim. Acta 88 (2000) 547.
11. M. Plaschke, J. Rothe, M.A. Denecke, Th. Fanghänel, J. Electron Spectrosc. Relat. Phenom. 135 (2004) 53.
12. M. Plaschke, J. Rothe, M. Altmaier, M.A. Denecke, Th. Fanghänel, J. Electron Spectrosc. Relat. Phenom. 148 (2005) 151.
13. U. Neuhäusler, C. Jacobsen, D. Schulze, D. Stott, S. Abend, J. Synchrotron Rad. 7 (2000) 110.
14. C. Jacobsen, S. Williams, E. Anderson, M. T. Browne, C. J. Buckley, D. Kern, J. Kirz, M. Rivers, X. Zhang, Opt. Commun. 86 (1991) 351.
15. S. Spector, C. Jacobsen, D. Tennant, in: J. Thieme, G. Schmahl, E. Umbach, D. Rudolph (Eds.), X-ray microscopy and spectromicroscopy, Springer: Berlin, Heidelberg, 1998.
16. U. Neuhäusler, S. Abend, C. Jacobsen, G. Lagaly, Colloid Polym. Sci. 277 (1999) 719.
17. C. Jacobsen, G. Flynn, S. Wirick, C. Zimba, J. Microsc. 197(2) (2000) 173.
18. M.A. Denecke, J. Rothe, K. Dardenne, H. Blank, J. Hormes, Physika Scripta T115 (2005) 1001.
19. A. Navaza, P. Charpin, D. Vigner, Acta Cryst. C47 (1991) 1842.
20. D.E. Sayers, B.A. Bunker, in: D.C. Koningsberger, R. Prins (Eds.), X-ray Absorption: Techniques of EXAFS, SEXAFS and XANES, J. Wiley & Sons: New York, 1988.

21. T. Ressler, J. Physique IV 7-C2 (1997) 269.
22. E.A. Stern, M. Newville, B. Ravel, Y. Yacoby, D. Haskel, Physica B 208&209 (1995) 117.
23. A.L. Ankudinov, B. Ravel, J.J. Rehr, S.D. Conradson, Phys. Rev. B 58 (1998) 7565.
24. A.L. Ankudinov, J.J. Rehr, Phys. Rev. B 56 (1997) 1712.
25. R. Ahlrichs, M. Bär, M. Häser, H. Horn, C. Kölmel, Chem. Phys. Lett. 162 (1989) 165.
26. T. Kukota, O. Tochiyama, K. Tanaka, Y. Niibori, Radiochim. Acta 90 (2002) 569.
27. D. Leroy, L. Martinot, C. Jérôme, R. Jérôme, Polymer 42 (2001) 4589.
28. W.D.J. Horrocks, D.R. Sudnick, J. Am. Chem. Soc. 101 (1979) 334.
29. A. Streitwieser, Jr., C.H. Heathcock, Organische Chemie, Verlag Chemie: Weinheim, 1980 (p. 507).
30. M.A. Denecke, T. Reich, M. Bubner, S. Pompe, K.-H. Heise, H. Nitsche, P.G. Allen, J.J. Bucher, N.M. Edelstein, D.K. Shuh, J. Alloy Comp. 271-273 (1998) 123.
31. H. Moll, G. Geipel, T. Reich, G. Bernhard. T. Fanghänel, I. Grenthe, Radiochim. Acta 91 (2003) 11.
32. E.A. Hudson, P.G. Allen, J. Terminello, M.A. Denecke, T. Reich, Phys. Rev. B 54 (1996) 156.

EXAFS AND UV-VIS INVESTIGATION OF THE FIRST CO-ORDINATION SPHERE OF THE URANYL ION IN $UO_2(NO_3)_2(TBP)_2$

Kelly Servaes[a], Christoph Hennig[b], and Christiane Görller-Walrand[a]

[a] Katholieke Universiteit Leuven, Department of Chemistry, Molecular Design and Synthesis, B-3001 Leuven, Belgium; [b] Forschungszentrum Rossendorf, Institute of Radiochemistry, D-01314 Dresden, Germany

Abstract

The co-ordination behaviour of the uranyl ion UO_2^{2+} has regained interest due to the problem of nuclear waste management and environmental issues. At the end of the nuclear fuel cycle, reprocessing of the spent nuclear fuel mainly occurs by means of liquid-liquid extraction. During the PUREX process, the spent fuel is dissolved in a nitric acid solution. Uranium is extracted from the aqueous nitric acid fuel solution with an organic phase containing tri-n-butylphosphate (TBP; extracting agent). However, little is known about the structure of the chemical species involved in the liquid-liquid extraction process. The first co-ordination sphere of the uranyl ion UO_2^{2+} in $UO_2(NO_3)_2(TBP)_2$ was studied using UV-Vis absorption spectroscopy and EXAFS spectroscopy. The characteristic vibrational fine structure in the UV-Vis absorption spectrum points at a high symmetrical complex (D_{2h} co-ordination symmetry). The uranium polyhedron is composed of two axial oxygens located at 1.77 ± 0.01 Å, four nitrate (bidentate) oxygens at 2.52 ± 0.01 Å and two phosphate oxygens (TBP) located at 2.38 ± 0.01 Å.

Introduction

The determination of the structure of uranyl complexes in solution is rather complicated. In the past, symmetry effects could only be revealed by means of spectroscopic techniques like UV-Vis absorption spectroscopy, luminescence and magnetic circular dichroism (MCD). Nowadays, a modern technique is available to determine some limited structural parameters in solution: Extended X-ray Absorption Fine Structure (EXAFS). The combination of UV-Vis absorption spectroscopy and EXAFS seems to be an excellent tool to elucidate the structure of uranyl species in solution. In a previous paper, we demonstrated the existence of a $[UO_2Cl_4]^{2-}$ complex with D_{4h} co-ordination symmetry in acetonitrile solution by this combination of UV-Vis and U L_{III} EXAFS spectroscopy [1].

$UO_2(NO_3)_2(TBP)_2$ is one of the extracted solvates in the PUREX process. In the PUREX (*plutonium and uranium recovery by extraction*) process, uranium and plutonium are extracted from the aqueous nitric acid solution with an organic phase (mostly kerosene) which contains tri-n-butylphosphate (TBP). The following reaction takes place [2]:

$$UO_2^{2+}{}_{(aq)} + 2NO_3^-{}_{(aq)} + 2TBP_{(org)} \Leftrightarrow UO_2\left(NO_3\right)_2\left(TBP\right)_{2(org)}$$

The crystal structures of analoguous organophosphate compounds of uranium(VI) are already known for a long time [3, 4]. However, a crystal structure determination of $UO_2(NO_3)_2(TBP)_2$ is not possible, because the complex formed with the most frequently used neutral extractant, tri-n-butylphosphate (TBP), is a liquid at room temperature. The analog with tri-isobutylphosphate (TiBP) crystallizes readily and its structure provides the same chemical information [3].

These days, the co-ordination behaviour of the uranyl ion has raising interest due to the problem of nuclear waste management and environmental issues. The design of new, more selective extracting agents in the reprocessing of spent nuclear fuel demands an insight in the structure of the uranyl complexes present in the extracting process. A lot of research is going on concerning the liquid-liquid extraction process of uranium and plutonium as well as to elucidate the structure of the extraction species formed [5 - 9]. Den Auwer *et al*. demonstrated that there is no structural difference between $UO_2(NO_3)_2(TiBP)_2$ in the solid state and liquid $UO_2(NO_3)_2(TBP)_2$ in TBP solution at 295 K by XAS spectroscopy and IR spectroscopy [5]. Furthermore, the influence of the steric effect of the alkyl groups in $[UO_2(NO_3)_2(OPO_3R_3)_2]$ (where R is an alkyl group) on the U-O bond lengths was studied by EXAFS spectroscopy [6]. Knowlegde of the geometry of the complex can reveal a relation with the extracting abitility of the organophosphate compounds. In this paper, we investigated the first co-ordination sphere of the uranyl ion UO_2^{2+} in $UO_2(NO_3)_2(TBP)_2$ using UV-Vis absorption spectroscopy and U L_{III} EXAFS spectroscopy.

Experimental details

$UO_2(NO_3)_2(TBP)_2$: The solvate was prepared in an excess of TBP by dissolving $UO_2(NO_3)_2{\cdot}6H_2O$ in pure TBP [2, 5].

UV-Vis absorption spectra were recorded at room temperature on a Varian Cary 5000 spectrophotometer in the wavelength interval between 600 nm and 300 nm.

EXAFS measurements. For the EXAFS measurements, we used a solution that contains 50 mM $UO_2(NO_3)_2{\cdot}6H_2O$ in TBP. Uranium L_{III}-edge EXAFS spectra were collected at the Rossendorf Beamline at the European Synchrotron Radiation Facility (ESRF, Grenoble, France) [10]. The measurements were carried out in transmission mode using argon-filled ionization chambers at ambient temperature and pressure. Higher harmonics were rejected by two Pt-coated mirrors. The measurements were performed using a double crystal Si(111) monochromator in equidistant k-steps of 0.05 $Å^{-1}$ across the EXAFS region. Two scans were recorded and then averaged. An Y metal foil (first

inflection point at 17038 eV) was used for energy calibration. The U L_{III} threshold energy, $E_{k=0}$, was defined at 17185 eV. EXAFS data were extracted from the raw absorption spectra by standard methods including a spline approximation for the atomic background with the program EXAFSPAK [11]. Theoretical phase and amplitude functions were calculated with FEFF 8.2. [12]. The scattering phase and amplitude functions were calculated using the crystal structure of $UO_2(NO_3)_2(TiBP)_2$ [3]. The amplitude reduction factor, S_0^2, was defined as 0.9 in the FEFF calculation and fixed to that value in the data fits. In all fits, the co-ordination number of the uranyl oxygen atoms (O_{ax}) was held constant at two. The main multiple scattering paths, with their relative importance, are defined according to the notation in Figure 1 and shown in Table 1.

Hudson *et al*. indicated that the scattering contributions from paths U-O_{ax1}-O_{ax2} and U-O_{ax1}-U-O_{ax1} tend to cancel each other [13]. Therefore, the twofold degenerated 4-legged multiple scattering path U-O_{ax1}-U-O_{ax2} (abbreviated as MS U-O_{ax}) was included in the curve fit by constraining its Debye-Waller factor, σ^2, and its effective path length to twice the values of the corresponding, freely fitted U-O_{ax} single scattering path. Scattering contributions with less than 5 % were not considered in the fit procedure.

Figure 1. First co-ordination sphere of $UO_2(NO_3)_2(TiBP)_2$ [3]. The alkyl groups are left out for clarity.

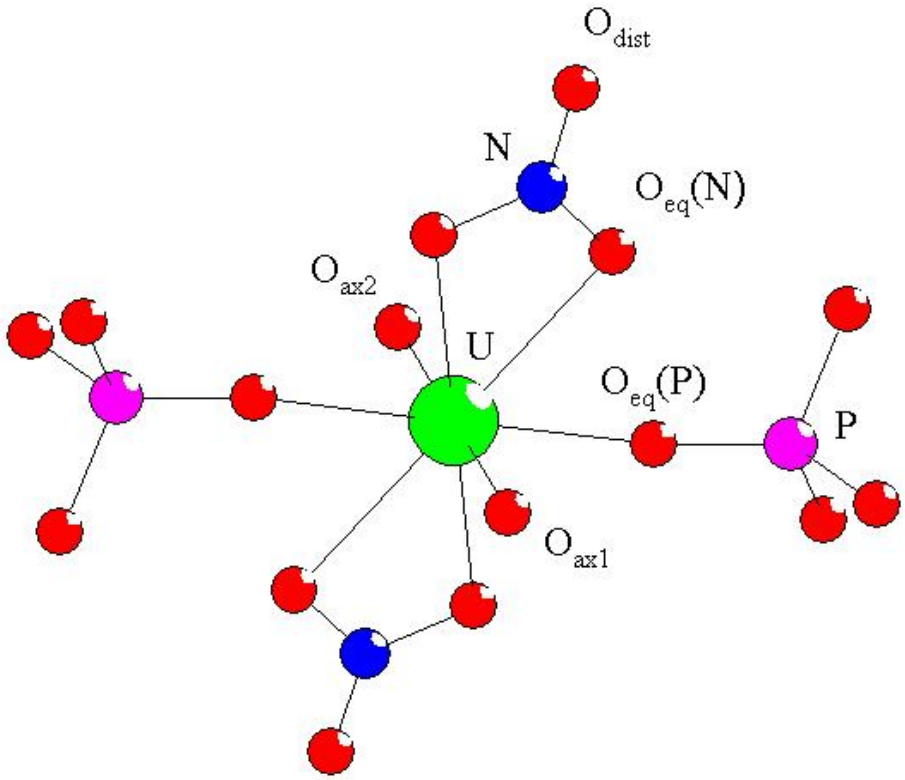

Table 1. Principal scattering pathways, taken from $UO_2(NO_3)_2(TiBP)_2$

Pathway	Scattering length [Å]	Intensity
U-O_{ax}	1.757	100
U-O_{ax1}-O_{ax2}	3.514	10.9
U-O_{ax1}-U-O_{ax2}	3.514	19
U-O_{ax1}-U-O_{ax1}	3.514	12.8
U-O_{eq}(P)	2.372	47.6
U-P	3.816	15.4
U-P-O_{eq}(P)	3.833	37.7
U-O_{eq}(P)-P-O_{eq}(P)	3.849	24
U-O_{eq}(N)	2.509	40.9
U-N	2.960	24.1
U-N-O_{eq}	3.374	6.4
U-O_{dist}	4.167	8.8
U-O_{dist}-N	4.167	23
U-N-O_{dist}-N	4.168	14.8

Results and discussion

The UV-Vis absorption spectrum of $UO_2(NO_3)_2(TBP)_2$ in TBP at room temperature shows a remarkable fine structure (Figure 2). The absorption bands of $UO_2(NO_3)_2(TBP)_2$ exhibit a small shift to higher energies compared to the free uranyl ion UO_2^{2+}, which is typical for the co-ordination by nitrate ions [14]. A change in the value of the symmetrical stretching vibration of uranyl (ν_s) is observed as well: ~760 cm^{-1} for $UO_2(NO_3)_2(TBP)_2$. This value is in accordance with literature data [14, 15].

The symmetry of the first co-ordination sphere of the uranyl ion has a great influence on the vibrational fine structure in the absorption spectrum. Based on the typical fine structure in the UV-Vis absorption spectrum, we propose a uranyl complex with D_{2h} co-ordination symmetry. The group of Görller-Walrand has studied the UV-Vis absorption spectrum of $UO_2(NO_3)_2{\cdot}6H_2O$ in the solid state [16]. From the crystal structure of $UO_2(NO_3)_2{\cdot}6H_2O$ it is clear that two bidentate nitrate groups and two water molecules are coordinated to the uranyl ion (D_{2h} co-ordination symmetry). However, the spectrum of liquid $UO_2(NO_3)_2(TBP)_2$ in TBP solution exhibits the same vibrational fine structure as $UO_2(NO_3)_2{\cdot}6H_2O$ [16]. Moreover, the calculated single-component spectrum of $UO_2(NO_3)_2$ in solution (D_{2h} symmetry) shows the same structural features as the spectra of $UO_2(NO_3)_2{\cdot}6H_2O$ and liquid $UO_2(NO_3)_2(TBP)_2$ [17]. Therefore, comparison with literature data confirms our statement that the $UO_2(NO_3)_2(TBP)_2$ species has a D_{2h} co-ordination symmetry with two bidentate nitrate groups and two phosphate groups in trans positions in the equatorial plane of the uranyl ion. Also in the crystal structure, there are discrete centrosymmetric molecules of $UO_2(NO_3)_2(TiBP)_2$ [3]. The same structure is observed for $UO_2(NO_3)_2(H_2O)_2$ where water molecules occupy the sites of the phosphate groups [3].

Figure 2. The UV-Vis absorption spectrum of $UO_2(NO_3)_2(TBP)_2$ in TBP at room temperature.

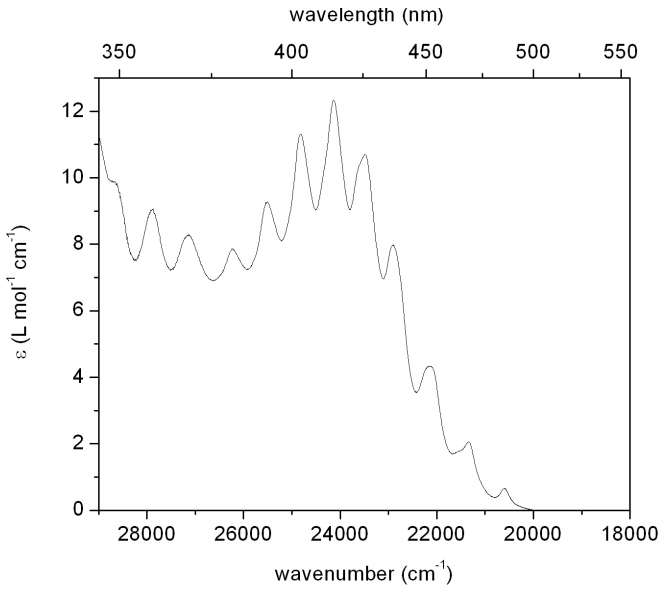

The U L_{III}-edge EXAFS measurements confirm the existence of a $UO_2(NO_3)_2(TBP)_2$ species in TBP. The raw k^3-weighted EXAFS data of $UO_2(NO_3)_2(TBP)_2$ in TBP are given in Figure 3. The 3-legged multiple scattering paths U-P-O_{eq}(P) and U-N-O_{dist} are abbreviated respectively as MS P and MS O_{dist} in Figure 3. Complex multiple scattering features are the result of the linear arrangement of the nitrogen and the distal oxygen in nitrate respectively the equatorial oxygen and phosphorus in tri-n-butylphosphate. Indeed, the bond angle U-O_{eq}(P)-P in the crystal structure of $UO_2(NO_3)_2(TiBP)_2$ is 164° (nearly linear) [3]. In the case of linear arrangement, the scattering amplitude is greatly enhanced in the forward scattering direction due to focusing of the electron wave to the next neighbour. This effect is therefore called "focusing effect" [18]. Not all multiple scattering paths of the N and P atoms with intensity > 5% were included in the shell fitting procedure because of the large quantity of parameters. The co-ordination numbers were fixed to the values of the crystal structure determinations in order to avoid correlation problems between N and σ^2. The largest peak in the Fourier transform represents the scattering contribution from the two axial oxygen (O_{ax}) atoms. The double peak at $R + \Delta = 2$ Å arises from two equatorial oxygen (O_{eq}) shells: a O_{eq}(N) shell from the nitrate groups and a O_{eq}(P) shell from the phosphate groups. Indeed, the peak at $R + \Delta = 2$ Å can not be completely covered by including one single shell of equatorial oxygen atoms in the fitting procedure. The structural parameters of the shell fitting including phase correction are summarised in Table 2.

Figure 3. U L_{III}-edge k^3-weighted EXAFS data and corresponding Fourier transform, taken over k=3.1-18 $Å^{-1}$. Experimental data as line and theoretical curve fit as dots.

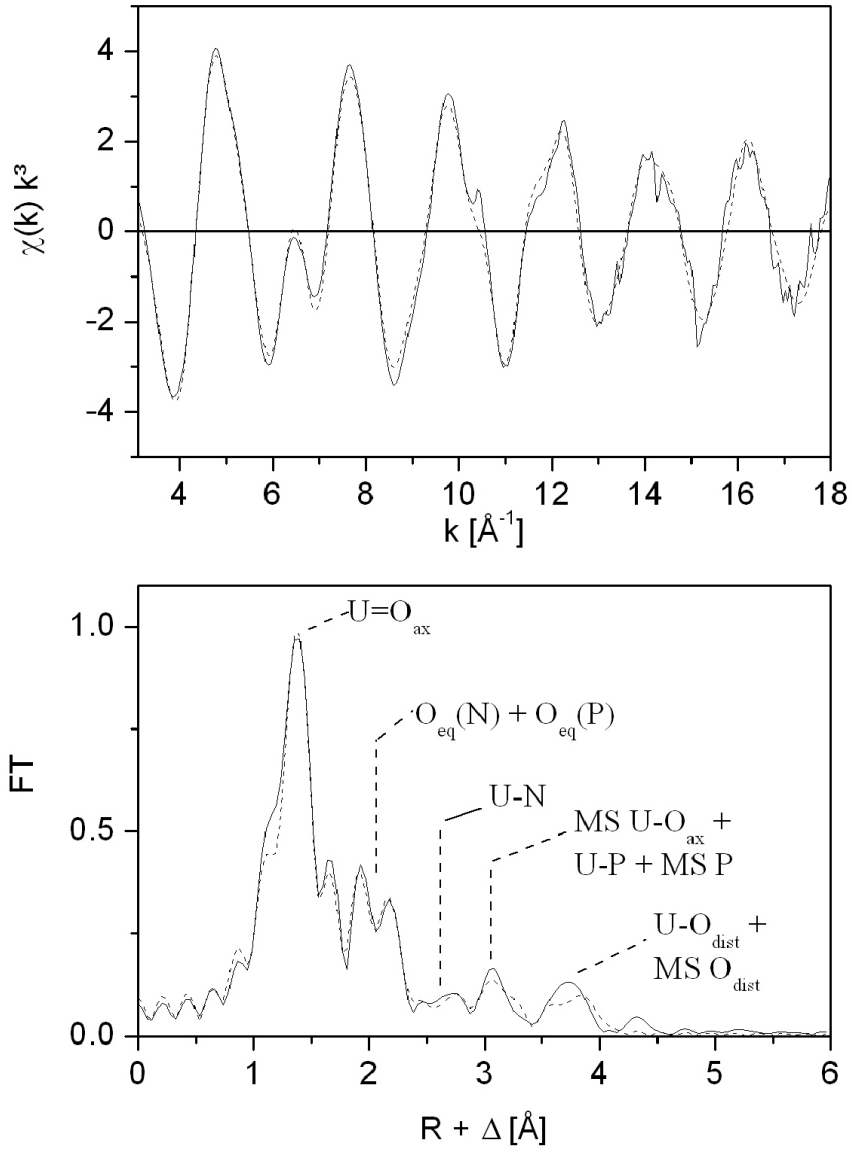

Table 2. EXAFS structural parameters.

	R [Å]	N	σ^2 [Å^2]
U-O_{ax}	1.77	2*	0.0013
MS O_{ax}	3.54	2*	0.0027
U-O_{eq}(P)	2.38	2*	0.0041
U-P	3.62	2*	0.0054
MS P	3.76	4*	0.0188
U-O_{eq}(N)	2.52	4*	0.0052
U-N	2.97	2*	0.0042
U-O_{dist}	4.25	2*	0.0026
MS O_{dist}	4.25	4*	0.0056

Errors in distances are ± 0.01 Å, * value fixed during the shell fit procedure, ΔE = 6.2 eV, σ Debye-Waller factor

The uranium polyhedron is composed of two axial oxygens located at 1.77 ± 0.01 Å, four nitrate (bidentate) oxygens at 2.52 ± 0.01 Å and two phosphate oxygens (TBP) located at 2.38 ± 0.01 Å. The possibility of a monodentate coordinated nitrate group has been rejected because of the presence of the two characteristic stretching frequencies of bidentate NO_3^- in the IR spectrum of liquid $UO_2(NO_3)_2(TBP)_2$ [5]. Furthermore, the U-N distance of 2.97 ± 0.01 Å indicates a bidentate co-ordination mode of the nitrate groups [19]. The focusing effect makes the distal oxygen atoms (O_{dist}) and P atoms in a large distance of 4.25 Å respectively 3.62 Å visible. These values agree well with the crystal structure determination of $UO_2(NO_3)_2(TiBP)_2$ [3] and structural parameters previously obtained for $UO_2(NO_3)_2(TBP)_2$ [5, 6]. As already observed for the $[UO_2(NO_3)_3]^-$ species, the U-O_{dist} distance is slightly longer in solution than in the solid [19].

Conclusion

In conclusion, we have shown that UV-Vis absorption spectroscopy as well as U L_{III}-edge EXAFS spectroscopy point unambiguously to the existence of a $UO_2(NO_3)_2(TBP)_2$ species in TBP solution. A D_{2h} co-ordination symmetry with two bidentate coordinated nitrate groups and two monodentate phosphate groups in the equatorial plane around the uranyl ion is proposed. The vibrational fine structure in the UV-Vis absorption spectrum is comparable with the features in the UV-Vis spectrum of solid $UO_2(NO_3)_2{\cdot}6H_2O$ (D_{2h}). The $UO_2(NO_3)_2(TBP)_2$ co-ordination polyhedron consists of two O_{ax} atoms at 1.77 ± 0.01 Å, four O_{eq} atoms of two bidentate nitrate groups at 2.52 ± 0.01 Å and two O_{eq} atoms of two phosphate groups at 2.38 ± 0.01 Å.

Acknowledgments

The EXAFS measurements were performed at the Rossendorf Beamline at the ESRF. KS is a research assistant of the Fund for Scientific Research, Flanders (Belgium) (F.W.O.-Vlaanderen).

References

[1] K. Servaes;C. Hennig; R. Van Deun; C. Görller-Walrand, *Inorg. Chem*. **2005**, *44*, 7705-7707.

[2] J.J. Katz; G.T. Seaborg; L.R. Morss, *The Chemistry of the Actinide Elements*, **1986**, Chapman and Hall, London.

[3] J.H. Burns; G.M. Brown; R.R. Ryan, *Acta Cryst.* **1985**, *C41*, 1446-1448 and ref. therein.

[4] G. Agostini; G. Giacometti; D.A. Clemente; M. Vicentini, *Inorg. Chim. Acta* **1982**, *62*, 237-240.

[5] C. Den Auwer; C. Lecouteux; M.C. Charbonnel; C. Madic; R. Guillaumont, *Polyhedron*, **1997**, *16*, 2233-2238.

[6] C. Den Auwer; M.C. Charbonnel; M.T. Presson; C. Madic; R. Guillaumont, *Polyhedron* **1998**, *17*, 4507-4517.

[7] M. Baaden; R. Shurhammer; G. Wipff, *J. Phys. Chem. B* **2002**, *106*, 434-441.

[8] R. Schurhammer; G. Wipff, *J. Phys. Chem. A* **2005**, *109*, 5208-5216.

[9] S.K. Sahu; M.L:P. Reddy; T.R. Ramamohan; V. Chakravortty, *Radiochim. Acta* **2000**, *88*, 33-37.

[10] W. Matz; N. Schell; G. Bernhard; F. Prokert; T. Reich; J. Claußner; W. Oehme; R. Schlenk; S. Dienel; H. Funke; F. Eichhorn; M. Betzl; D. Pröhl; U. Strauch; G. Hüttig; H. Krug; W. Neumann; V. Brendler; P. Reichel; M.A. Denecke; H. Nitsche, *J. Synchrotron Rad*. **1999**, *6*, 1076-1085.

[11] G.N. George; I.J. Pickering, EXAFSPAK, *a suite of computer programs for analysis of X-ray absorption spectra*, **2000**, Stanford Synchrotron Radiation Laboratory, Stanford.

[12] A.L. Ankudinov; B. Ravel; J.J. Rehr; S.D. Conradson, *Phys. Rev.* **1998**, *B58*, 7565-7576.

[13] E.A. Hudson; P.G. Allen; L.J. Terminello; M.A. Denecke; T. Reich, *Phys. Rev*. **1996**, *B54*, 156-165.

[14] R.G. Denning; D.N.P. Foster; T.R. Snellgrove; D.R. Woodwark, *Mol. Phys.* **1979**, *37*, 1089.

[15] C. Görller-Walrand; S. De Houwer; L. Fluyt; K. Binnemans, *Phys. Chem. Chem. Phys*. **2004**, *6*, 3292-3298 and ref. Therein.

[16] C. Görller-Walrand; S. De Jaegere, *J. Chim. Phys.* **1972**, *4*, 726-736 and ref. therein.

[17] S. De Houwer; C. Görller-Walrand, *J. Alloys Compd.* **2001**, *323-324*, 683-687.

[18] B.K. Teo, *EXAFS: Basic Principles and Data Analysis*, **1986**, Springer, Berlin, Heidelberg, New York, p. 183.

[19] K. Servaes; C. Hennig; I. Billard; C. Gaillard; R. Van Deun; C. Görller-Walrand, submitted to *Inorg. Chem*.

XAFS STUDIES ON ACTINIDE-PYRIDINE-DIAMIDE COMPLEXES FOR DEVELOPMENT OF AN INNOVATIVE SEPARATION PROCESS

Hideaki Shiwaku[1], Tsuyoshi Yaita[1, 2], Tohru Kobayashi[1], Masahiko Numakura[1], Shinichi Suzuki[2] and Yoshihiro Okamoto[2]

[1] Japan Atomic Energy Agency, Kouto, Sayo, Sayo, Hyogo 679-5148, JAPAN

[2] Japan Atomic Energy Agency, Tokai, Naka, Ibaraki 319-1195, JAPAN

Abstract

We have been studying the bond properties and the structures of actinide (An) and lanthanide (Ln) complexes in detail using several kinds of X-ray analyses by synchrotron radiation in order to elucidate the ionic recognition mechanism of organic ligands. Generally, an oxygen donor type ligand separates both An and Ln from solutions of spent fuel or high level radioactive waste. Separation ability of this type of ligand for An and Ln follows the order of the surface charge density of an ion, i.e., $An^{4+} > AnO_2^{2+} > An^{3+} = Ln^{3+} > AnO_2^{+}$ and/or a few structural factors. Therefore, this type of ligand is ineffective for the separation of An^{3+} and Ln^{3+} due to their similar chemical properties. Recently, new extractants like aromatic N-donor ligands have been developed using the preference of soft-donors to achieve the An^{3+}/Ln^{3+} separation. However, aromatic N-donor ligands often show a few problems such as protonation. In this developing process, we synthesized a new type of ligand, N,N'-dimethyl-N,N'-diphenylpyridine-2,6-carboxyamide (DMDPh-PDA). The PDA is hybrid type ligand having oxygen and nitrogen as donor atoms and follows a unique separation order, i.e., $An^{4+} > An^{3+} > AnO_2^{2+} > Ln^{3+} > AnO_2^{+}$, probably arising from the combined effects of covalent bonding and steric hindrance. Hence, clarification of any ionic recognition mechanism of the PDA is very interesting from the view point of structural analysis. In this presentation, we will show XAFS results of An and Ln complexes with PDA in solution and discuss separation mechanism of An and Ln by PDA. Various kinds of complexes between Ln/An and PDA were prepared for XAFS analysis. The Ln complexes were measured in transmission mode at the K absorption edge on the BL11XU at SPring-8. On the other hand, the U complexes were measured in fluorescence mode at the L_{III} absorption edge on the BL-27B at Photon Factory, High-energy Accelerator Research Organization (KEK).

Introduction

Conventional extraction separation processes, exploit the differences in the actinides' surface charge densities. That is, the extractability follows the order given in Figure 1, which follows in the order of an ionic interaction between the metal ion and extractants. Because of the differences in the extractability of various actinides, the separation process must be deployed in multi-stage steps, which increases the cost of using this method. To reduce the number of separation stages, we introduced a new separation concept from the former. Using the concepts of covalent bonding character and spatial-configuration control together as a new concept for extraction separation, we performed the molecular design and synthesis of a new type of ligand, *N,N'*-dimethyl-*N,N'*-diphenylpyridine-2,6-carboxyamide (DMDPh-PDA), shown in Figure 2.

Figure 1. The order of surface charge density of ions.

$$\mathbf{Pu^{4+} > UO_2^{2+} >> Am^{3+} > NpO_2^{+}}$$
$$\mathbf{(+4)\quad (+6)\qquad (+3)\quad (+5)}$$

Figure 2. Structure of *N, N'*-dimethyl-*N, N'*-diphenylpyridine-2,6-carboxyamide (DMDPh-PDA)

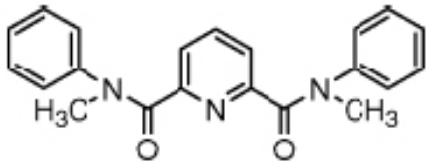

The order of the actinide affinity of DMDPh-PDA is shown in Figure 3. By using the DMDPh-PDA ligand, it became possible to separate actinides in an order different from the surface charge density. That is, the extraction of Am^{3+} and UO_2^{2+} is reversed, and it becomes possible to separate Pu^{4+}, Am^{3+}, and Cm^{3+} together directly from solutions containing UO_2^{2+}.

Figure 3. Separation order actinides using DMDPh-PDA, which has oxygen and nitrogen donors.

$$\mathbf{Pu^{4+} > Am^{3+} > UO_2^{2+} > NpO_2^{+}}$$
$$\mathbf{(+4)\quad (+3)\qquad (+6)\qquad (+5)}$$

The separation process designed around the DMDPh-PDA ligand is shown in Figure 4. If a PDA-based separation method is used, a simplification of the prior multi-step separation process is realized. At the same time, the separated Pu is more proliferation resistant, since the Pu is separated together with the highly radioactive Am and Cm. Furthermore, since the PDA extractant consists only of the

light element of C, H, O, N, it can be gasified through combustion, reducing secondary waste volumes. These three features present a clear economic, environmental, and safety advantages over existing processes. First, DMDPh-PDA complex is described and the advancement of a PDA ligand is described below.

Figure 4. Separation Processes by using PDA type ligand.

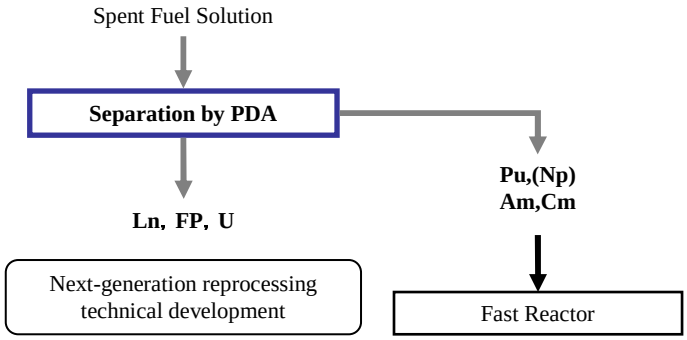

Experimental

We synthesized *N, N'*-dimethyl-*N, N'*-diphenylpyridine-2,6-carboxyamide (DMDPh-PDA) [1] and its derivatives. All of the ligands studied have both a nitrogen donor and two oxygen donors in one molecule.

The lanthanide complexes were measured in the transmission mode at the K absorption edge on BL11XU at SPring-8 [2]. The U complexes were measured in the fluorescence mode at the L_{III} absorption edge on the BL-27B at Photon Factory, High-energy Accelerator Research Organization (KEK) [3]. The solutions for analysis were sealed in a polyethylene cells having 3 cm path length in case of transmission mode on the BL11XU at SPring-8. Repeated XAFS scans were normalized and averaged. The data reduction and curve fitting were carried out using the program WinXAS version 3.1 [4]. The theoretical calculations were performed using FEFF8 [5].

Results and Discussions

XAFS measurements were carried out on various lanthanide complexes with DMDPh-PDA ligands. Figure 5 shows the radial structural function (|FT|) of La(III)-DMDPh-PDA in methanol. As compared with the case of a hydrate complex, $La(H_2O)_9$, the oxygen-lanthanum and nitrogen-lanthanum distances shift to lower R(Å) values. Other Ln-DMDPh-PDA complexes show the same tendency to shift lower R(Å) values. Since the multiple-scattering peak observed for a single crystal of La-DMDPh-PDA complex, [6] which is characteristic of bidentate coordinated nitrate anions, is not seen in the solution sample, nitrate anions, are not coordinated in the inner co-ordination sphere of the complex. The total co-ordination number of La in the solution phase La-DMDPh-PDA complex is found to be nine, just like the hydrated complex. Consequently, it is thought that this complex consists of a La ion, two tridentate DMDPh-PDA ligands and three H_2O or methanol molecules coordinated in the inner co-ordination sphere.

Figure 5. The radial structure function of La(III)-DMDPh-PDA in methanol and $La(H_2O)_9$.

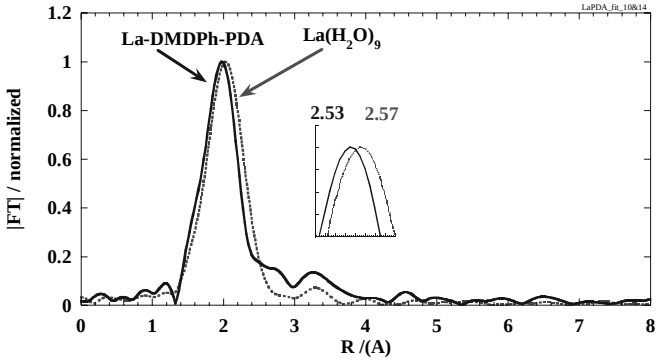

Figure 6 (a) shows the radial structural function of the UO_2-DMDPh-PDA complex formed in these solutions, and the identity of each peak. A peak corresponding to a U-U distance of XX Å is seen. Because a U-U distance is measurable, it is thought that the UO_2-DMDPh-PDA complex is dinuclear, a likely structural model is depicted in Fig 6(b). Two DMDPh-DPA ligands complex two uranyl ions, with other oxygen bearing ligands (water or methanol) bridging the two U centers and completing the co-ordination sphere. The steric bulk of the ligand appears to inhibit the co-ordination of two DMDPh-PDA ligands to a single UO_2^{2+} ion, which would promote the formation of the dinuclear species. Generally, the more ligands that enclose a metal ion, the greater the extractability of the resulting metal-ligand complex. Since only two DMDPh-PDA ligands coordinate *two* uranyl ions, DMDPh-PDA would appear to weaken extractability of UO_2^{2+} relative to the other actinides. This is the reason DMDPh-PDA ligand shows an affinity for the actinides that differs from the surface charge density order shown in Figure 3. It seems that the spatial configuration of the C=O ~ pyridine nitrogen ~ C=O donors of the DMDPh-PDA ligand "recognises" the spherical (non-actinyl) trivalent and tetravalent Ln/An ions.

Figure 6. The radial structure function of UO_2-DMDPh-PDA complex and its structural model.

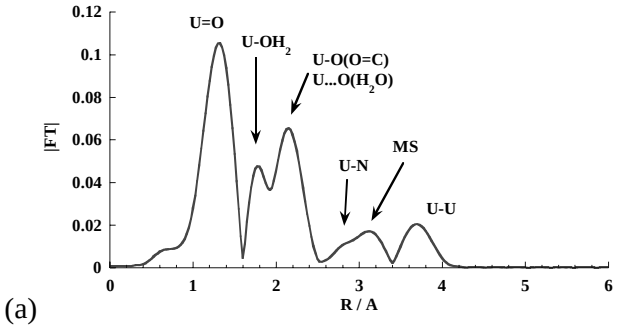

(a)

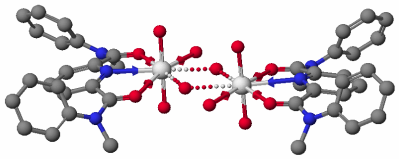

(b)

Although the DMDPh-PDA ligand is amply soluble in polar solvents well, it is less soluble in the paraffinic solvents that are strongly preferred in nuclear separations (for example, dodecane). Therefore, we improved the DPA molecule by increasing its solubility in paraffinic solvents. First, new ligands where the methyl group was replaced were synthesized. We synthesized the ligands *N*,*N*'-dioctyl-*N*,*N*'-diphenylpyridine-2,6-carboxyamide (DODPh-PDA) and *N*,*N*'-didodecyl-*N*,*N*'-diphenylpyridine-2,6-carboxyamide (DDoDPh-PDA).

Figure 7. The radial structure function of La-PDA and Eu-PDA in methanol.

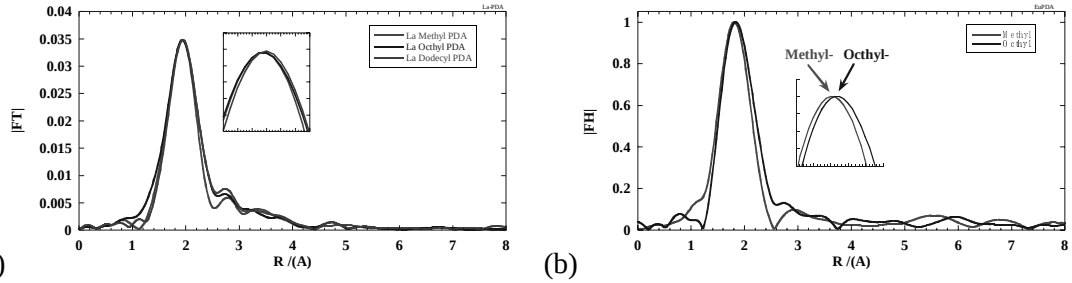

(a) (b)

The radial distribution function of a La-PDA complexes with varying alkyl substituents is shown in Figure 7 (a). Even if the methyl substituent on the amide nitrogen is replaced by an octyl group or a dodecyl group, the main peak of the radial structure function is in the same place and the distances of La-oxygen and La-nitrogen did not change. On the other hand, the distance of Eu-oxygen and Eu-nitrogen of the Eu-DODPh-PDA complex is slightly longer than that of Eu-DMDPh-PDA complex as shown in Figure 7 (b). Since the size of La^{3+} ion is larger than Eu^{3+} ion, we believe that when the ionic radius of a central metal is large, complex formation is not affected even if the length of an alkyl group changes. However, when the ionic radius is small, Eu^{3+} ion is more closely bound to the ligand. In this case, it appears that the ligands with long alkyl chains at the nitrogen of amide interfere with each other. This hypothesis is supported by model calculation, which show that the substituents exist on the same side of the molecule, so two ligands may interfere with each other as shown in Figure 8 (a).

Figure 8. The calculated structure of DODPh-PDA and DMpODPh-PDA

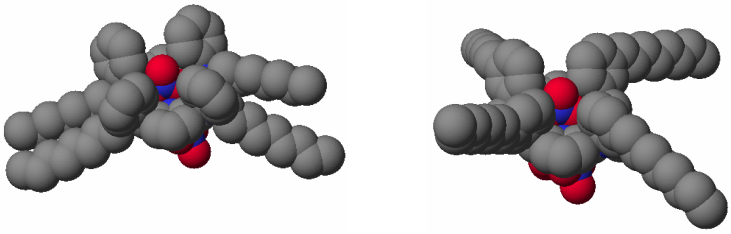

(a) (b)

We also synthesized a new ligand which placed long alkyl side chains on the phenyl groups, DMpODPh-PDA. According to model calculation, these side chains are more spatially dispersed, spreading as shown in Figure 8 (b). Therefore, when two ligands make a complex, the side chains will not interfere. This ligand is soluble in paraffinic solvents. It turns out that the separation factor is equivalent to the DMDPh-PDA ligand measured in another experiment.

Conclusions

We studied Ln- and U-pyridine-diamide complexes using XAFS to develop an innovative separation process. This hybrid hard-soft ligand has two oxygen donor and an aromatic nitrogen donor in one molecule. We showed that the PDA ligands possess a unique separation order, probably arising from the combination of the more covalent bond nature of the metal-nitrogen bonds and inter-ligand and metal-ligand steric hindrance. We are going to synthesize ligands with still higher separation factors that are soluble in paraffinic solvents from now on. Furthermore, we are going to pursue an ion recognition mechanism.

References

[1] T.Yaita, H.Shiwaku, S.Suzuki, Y.Okamoto, A.Shimada, Z.Assefa, and R.G.Haire, Physica Scripta. T115, 302 (2005)

[2] H.Shiwaku, T.Mitsui, K.Tozawa, K.Kiriyama, T.Harami, T.Mochizuki, 8th International Conference on Synchrotron Radiation Instrumentation, AIP Conference Proceedings, 705, 659 (2004)

[3] H.Konishi, A.Yokoya, H.Shiwaku, H.Motohashi, T.Makita, Y.Kashihara, S.Hashimoto, T.Harami, T.A. Sasaki, H.Maeta, H.Ohno, H.Maezawa, S.Asaoka, N.Kanaya, K.Itoh, N.Usami and K.Kobayashi, Nucl. Instr. Method Phys. Res. A, 372, 322 (1996)

[4] T.Ressler, J. Synchrotron Rad. 5, 118 (1998)

[5] S.I.Zabinsky, J.J.Rehr, A.Aukudionov, R.C.Albers and M.J.Eller, Phys. Rev. B 52, 2995 (1995)

[6] A.Shimada, “Development of Extractant for Trivalent Actinide and Clarification of its Extraction Mechanism”, Doctoral dissertation, 77 (2004)

STRUCTURAL ANALYSIS OF URANIUM(VI) AND NEPTUNIUM(VI) – N,N-DIALKYL MONOAMIDE COMPLEXES BY EXAFS

Shinichi Suzuki[1], Tsuyoshi Yaita[1,2], Yoshihiro Okamoto[2], Hideaki Shiwaku[2]
[1]Japan Atomic Energy Agency, Tokai-mura, Ibaraki, 319-1195 JAPAN
[2]Japan Atomic Energy Agency, Sayo-tyou, Hyogo, 679-5148 JAPAN

Abstract

N,N-dialkyl monoamides are noted as one of the alternative extractants of tri-butyl phosphate (TBP) in the field of nuclear fuel reprocessing. Extraction behavior of U(VI) and Pu(IV) with N,N-dialkyl monoamides is almost similar to those with TBP. N,N-dialkyl monoamides have some advantages against TBP, namely, their complete incinerability (CHON principle) and high stability for hydrolysis and radiolysis. Their main degradation products are carboxylic acids and secondary amines which hardly affect the separation of U(VI) and Pu(IV) from fission products(FP). Further, the synthesis of N,N-dialkyl monoamides is relatively easy.

In our group, an innovative chemical separation process is proposed for the treatment of spent nuclear fuel. One of the main purposes of this process is selective isolation of uranium with branched alkyl type N,N-dialkyl-monoamide(BAMA)[1]. Since BAMA has the steric hindrance on the complexation with metal cations, BAMA can be used to separate An(VI) from An(IV). One of BAMA, N,N-di-(2-ethyl)hexyl-(2,2-dimethyl)propanamide (D2EHDMPA), can recover U(VI) selectively without accumulating Pu(IV) in uranium isolation process. From the results of uranium extraction in the presence of neptunium, D2EHDMPA can extract and separate U(VI) from Np(VI) without reduction from Np(VI) to Np(V) or Np(IV). Furthermore, D2EHDMPA do not extract fission products like technetium in the presence of macro amount of uranium.

The structural parameters of uranium(VI)-BAMA and neptunium(VI)-BAMA were determined by EXAFS to elucidate the mechanism of selective separation of uranium(VI). EXAFS measurements of uranium(VI) and neptunium(VI)-BAMA complexes were performed at the BL-27B of KEK-PF. Uranium(VI) and neptunium(VI)-BAMA complexes were measured by transmission and/or fluorescence mode. BAMA used structural analysis were D2EHDMPA, N,N-di-(2-ethyl)hexyl-(2-methyl) propanamide (D2EHMPA), N,N-di-(2-ethyl)hexyl-(2-ethyl)butanamide (D2EH2EBA), N,N-di-(2ethyl)-hexanamide (D2EHHA), and N,N-di-octyl-hexanamide (DOHA) for uranium, and D2EHDMPA for neptunium(VI). Uranium(VI) and neptunium(VI)-BAMA samples for EXAFS measurement were prepared by solvent extraction method using n-dodecane as diluent. The obtained bond distance between uranium(VI) and oxygen of N,N-dialkyl monoamide are 2.39 Å for DOHA; 2.34 Å for D2EHHA, 2.34 Å for D2EHDMBA, and 2.26 Å for D2EH2EBA, respectively. Bond distances of U-O (O=C; BAMA) were changed dependence on amides structure, especially carbonyl alkyl branching on α-position.

[1] S.Suzuki, Y.Sasaki, T.Yaita, T.Kimura, International Conference of ATALANTE 2004, Nimes France, P1-63 (2004).

PHOTOEMISSION OF THE VALENCE ELECTRONS (0-40 EV) FROM ThO_2, UO_2, UO_{3-X} AND U_3O_8 AT THE Th(U)5d RESONANT EXCITATION EDGE WITH SYNCHROTRON RADIATION

Anton Teterin
Institute of General and Inorganic Chemistry, Moscow, Russia
Yury Teterin and Igor Utkin
RRC "Kurchatov Institute", Moscow, Russia
Tobias Reich
Johannes Gutenberg-Universität Mainz, Mainz, Germany
F.U. Hillebrecht
Institut für Festkörperforschung IFF-6 Forschungszentrum Jülich 52425 Jülich, Germany
S. Molodtsov
Technical University Dresden, Dresden, Germany
A. Varyahalov and V. Gudat
BESSY GmbH, Berlin, Germany

Abstract

Total electron yield and photoemission spectra of the outer electrons (0-40 eV binding energy) have been measured for UO_2, ThO_2, UO_{3-x} and U_3O_8. Spectra were taken at the Th(U)*5d* resonant absorption edge ($70 < h\nu < 140$ eV), using synchrotron radiation at the Russian-German Beamline BESSY II. For all studied oxides the photoemission spectra at the resonance edge exhibit pronounced intensity variations in the valence electrons energy range (0-40 eV). The spectral fine structure reflects the excitation-decay processes (inner photoeffect) involving the *An5d*, outer valence molecular orbitals (OVMO 0-13 eV binding energy) and inner valence molecular orbitals (IVMO 13-40 eV). Together with this process, regular photoemission takes place. The spectra reflect qualitatively the partial An*6p* and An*5f* electronic state densities. The structure of the spectra in the range of ~13-40 eV is attributed to the IVMO formation. The obtained data lead to four important conclusions. First – the peak at 1.9 eV was attributed to the localised weakly bound U *5f* electrons participating in the chemical bond. Second – the Th(U)*5f* filled electronic states appear during the chemical bond formation and are delocalised within the OVMO range, thus leading to the intensity growth at resonance. Third – the Th(U)*6p* electrons participate effectively in the IVMO and probably OVMO formation. This results in the intense structure in the IVMO range at the resonance. The structure reflects the partial density of the Th(U)*6p* electronic states. Fourth – correct calculation of the photoemission cross-sections (which is important for the quantitative ionic analysis) requires taking into account the significant contribution of the resonance effects.

Introduction

Overlap between the partially and completely filled orbitals of actinide (An) and ligand (L) ions, in the range from 0 to 50 eV binding energy (BE), leads to formation of the outer valence molecular orbitals (OVMO) between 0 – ~13 eV for the An*6p,6d,7s,5f* and O*2p* atomic orbitals (AOs), and inner valence molecular orbital (IVMO) between 15–50 eV for the An6s,6p and O*2p,2s* AOs in compounds [1]. As a result, X-ray photoelectron spectra (XPS) of actinide compounds exhibit a complex fine structure in the binding energy range of 0–50 eV. Interpretation of this structure enables to understand the role of the An*6p,5f* electrons in the chemical bonding and to establish a correlation of the spectral fine structure parameters with physical and chemical properties of actinide compounds [2]. This work studied the resonant photoemission of the valence electrons of UO_2, ThO_2, UO_{3-x} and U_3O_8 near the Th(U)*5d* absorption edge using SR in the excitation energy range $70 < h\nu < 140$ eV.

Experimental

Total electron yield (TEY) and resonant photoelectron (RPES) spectra were measured at the Russian-German Beamline BESSY II in Berlin. This work studied resonant electron photoemission from UO_2 and ThO_2 oxide overlayers on metal surfaces, as well as UO_{3-x} and U_3O_8 powders pressed in In on a Cu substrate [3]. Due to oxygen loss, substoichiometric UO_{3-x} formed on the surface of the UO_3 sample. Spectral intensity was normalised by the SR current. The scale factor was: 5 000 imp/50 scans (43 min) for ThO_2 and 2000 imp/50 scans (43 min) for UO_2. The C1s binding energy of surface carbon was accepted to be 285.0 eV.

Results and discussion

The present work examines the electron photoemission from thin films of UO_2 and ThO_2 deposited on metal surfaces, as well as from UO_{3-x} and U_3O_8 embedded in indium on copper substrates at the Th(U) *5d–5f* excitation threshold (Figure 2). The samples were not extra cleaned in the preparation chamber of the spectrometer. Substoichiometric UO_{3-x} oxide formed on the surface of the UO_3 sample due to the loss of oxygen in the spectrometer chamber. As a result, increased 5f intensity was observed around the resonance energy (Figure 2c). In UO_3 this 5f signal is missing, because all 5f electrons participate in the bonding. Earlier [4] a similar behavior was observed for the OVMO electrons (0–~13 eV BE) in UO_2 single crystals. Paper [3] considered electron photoemission at the $O_{4,5}$(U) edge from a UO_2 formed on the surface of uranium foil (Figure 2b). The resonance was expected to occur between 100-113 eV excitation energy (Figure 1b). Indeed, the more intense peaks appear in the spectrum excited at $h\nu$=110 eV. The authors of [3] for the first time observed the resonance in UO_2 and ThO_2, as well as in UO_{3-x} and U_3O_8 (Figure 2) for the OVMO and IVMO electrons in the binding energy range 0–40 eV. In this case, to a first approximation, this structure for the actinide (An) compounds can be described by the following excitation and decay processes:

$$\mathrm{An}5d^{10}(\mathrm{IVMO})^{k}(\mathrm{OVMO})^{m}5f^{n} + h\nu \rightarrow \mathrm{An}5d^{9}(\mathrm{IVMO})^{k}(\mathrm{OVMO})^{m}5f^{n+1}, \quad (1)$$

$$\mathrm{An}5d^{9}(\mathrm{IVMO})^{k}(\mathrm{OVMO})^{m}5f^{n+1} + (e^2/r) \rightarrow \mathrm{An}5d^{10}(\mathrm{IVMO})^{k}(\mathrm{OVMO})^{m}5f^{n-1} + e, \quad (2)$$

$$\mathrm{An}5d^{9}(\mathrm{IVMO})^{k}(\mathrm{OVMO})^{m}5f^{n+1} + (e^2/r) \rightarrow \mathrm{An}5d^{10}(\mathrm{IVMO})^{k}(\mathrm{OVMO})^{m-1}5f^{n} + e, \quad (3)$$

$$\mathrm{An}5d^{9}(\mathrm{IVMO})^{k}(\mathrm{OVMO})^{m}5f^{n+1} + (e^2/r) \rightarrow \mathrm{An}5d^{10}(\mathrm{IVMO})^{k-1}(\mathrm{OVMO})^{m}5f^{n} + e. \quad (4)$$

Figure 1. Total electron yield spectra from: a – ThO_2 on the surface of thorium plate, b – UO_2. The spectra were normalised to the photon flux. Electron BEs for the $An4d_{5/2,3/2}$ electrons in ThO_2 (a) and UO_2 (b) embedded in indium on titanium substrates are given [2].

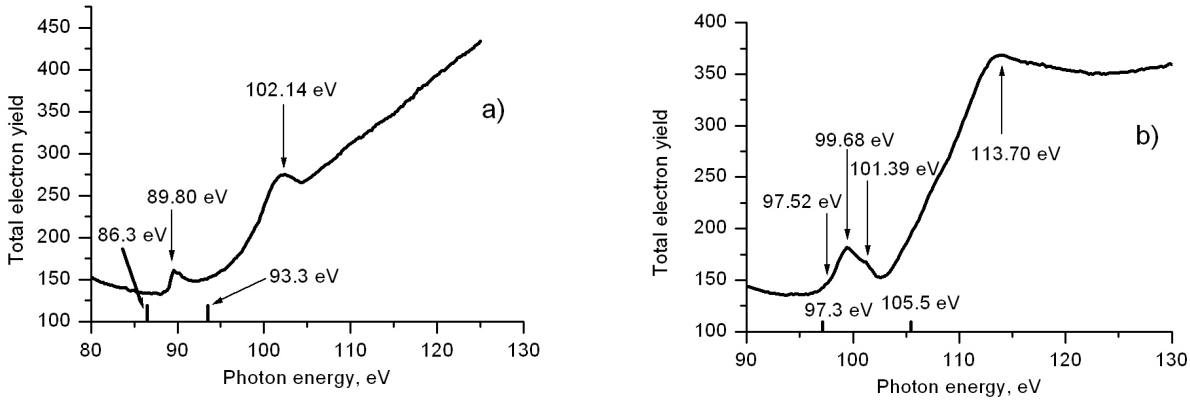

Figure 2. Photoemission from: a – ThO_2, b – UO_2, c – UO_{3-x}, d – U_3O_8 taken with different excitation energies $h\nu$. The spectral intensities were normalised to the ring current. The C*1s* binding energy from hydrocarbons on the sample surfaces was assumed to be 285.0 eV [3].

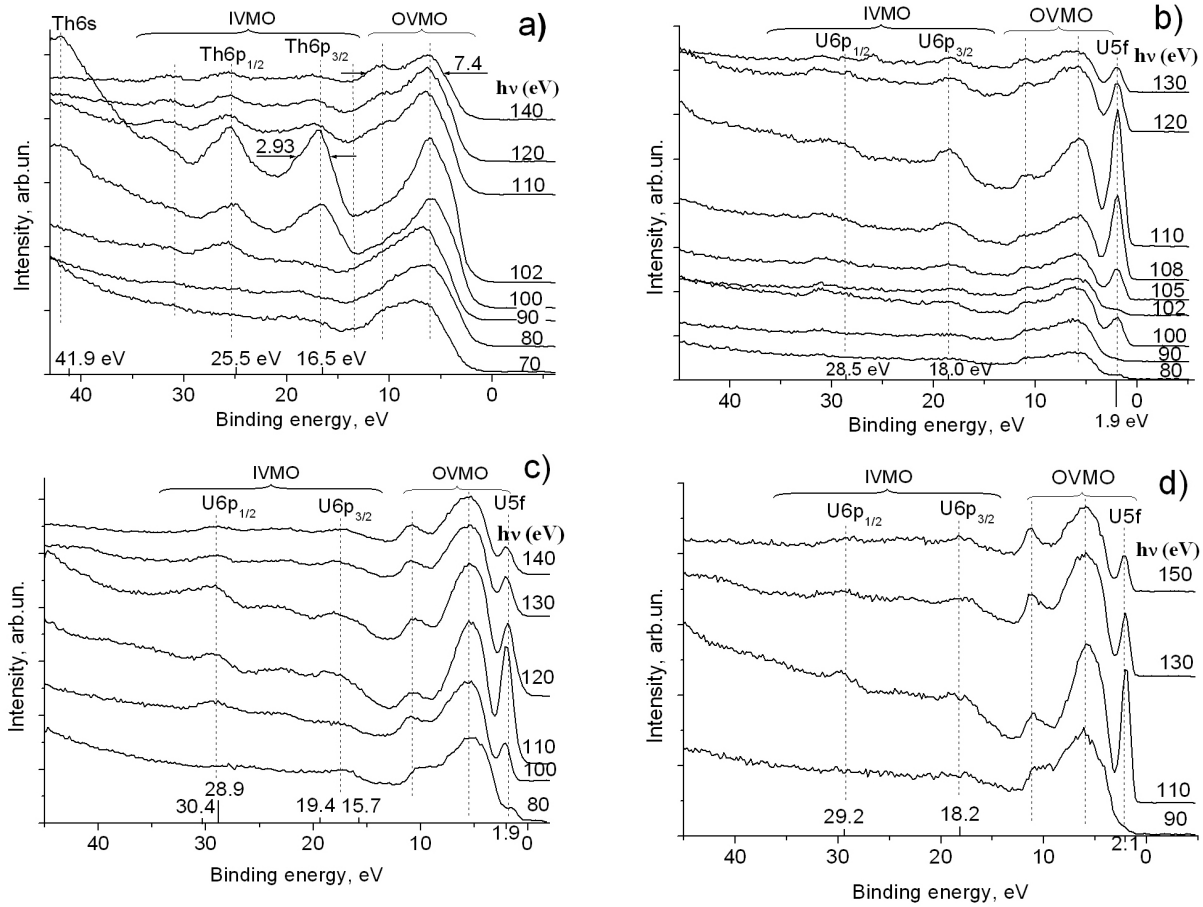

The three possible decay processes occur after the initial photoexcitation (1). They involve either transfer from the 5f (2), the OVMO (3) or the IVMO (4) into the 5d state. 5f electron emission in all three cases interferes with regular photoemission, and leads to resonance at the *5d–5f* excitation threshold. Since the considered resonant spectra are mostly due to the Auger electrons rather than to the photoemission, they reflect mostly the An*np* and An*5f* partial state densities. The observed complication of the structure in the ~15–40 eV energy range was explained by the IVMO formation. Since during the resonance the strongest intensity changes are expected for the U*5f,6p* related peaks, the obtained data allow the four important conclusions. First – the peak at 1.9 eV is attributed to the localized weakly bound U*5f* electrons. Second – the U*5f* electrons participating directly in the chemical bond are delocalized and this results in the OVMO intensity variation. Third – the U*6p* electrons participate effectively in the IVMO and probably OVMO formation, which results in the intense resonant structure in the IVMO energy range. This structure reflects the partial U*6p* electronic density in this spectral region. Fourth – correct calculation of the photoemission cross-sections (which is important for quantitative analysis) requires taking into account the significant contribution of the resonance effects.

Conclusions

1. Resonant photoemission of the valence electrons from UO_2, ThO_2, UO_{3-x} and U_3O_8 near the Th(U)*5d* absorption edge in the SR excitation energy range $70 < h\nu < 140$ eV was studied. For all studied samples a jump of intensity near the resonance edge was observed, which was not observed before for the energy range 0-40 eV.
2. The intense resonant structure (at 102 eV excitation for ThO_2 and 110 eV excitation for uranium oxides) was found to reflect the excitation and decay processes (inner photoeffect) involving the An5d and outer (OVMO – 0-13 eV) and inner (IVMO – 13-40 eV) valence molecular orbitals. The observed complication of the structure in the ~15-40 eV energy range was explained by the IVMO formation.
3. The An5f electrons were shown to participate directly in the chemical bond.

Acknowledgements

The work was supported by the RFBR grant 04-03-32892, the grant of the initiative projects on basic researches of the RRC “Kurchatov Institute” 2006-2007, the grant of the Foundation for support of the Russian science 2006 and the grant of the president of Russia on the federal support of the leading scientific schools (NSh–284.2006.3).

References

1. Yu.A. Teterin, S.G. Gagarin, Russian Chemical Review, **69, 10** (1996) 825.
2. Yu.A. Teterin, A.Yu. Teterin, Russian Chemical Review, **73, 6** (2004), 588.
3. Yu.A. Teterin, I.O. Utkin, A.Yu. Teterin, T. Reich, F.U. Hillebrecht, S.L. Molodtsov, A.Yu. Varykhalov, W. Gudat; BESSY GmbH, 12489, Berlin, Germany. Annual Report. 2004.
4. L. Cox, W.P. Ellis, R. Cowan, J.W. Allen, S.-J. Oh, I. Lindau, B.B. Pate, A.J. Arko, Phys.Rev. B., **35** (1987) 5761.

HYDRATION OF U(VI,V) AND Np(VI) IONS REVISITED

Satoru Tsushima, Andreas C. Scheinost
Institut für Radiochemie, Forschungszentrum Rossendorf (FZR), Dresden, Germany

Abstract

Hydration of uranyl(VI) ion has been a subject of both theoretical and experimental interests for many years. Most of the recent publications from both theory and experimental sides agree that the uranyl(VI) ion in aqueous solution exists as 5-fold $UO_2(H_2O)_5^{2+}$. In this work, we studied the hydration of uranyl(VI, V) and neptunyl(VI) ions in a further accurate way by optimising structures of $AnO_2(H_2O)_n^{2+/+}$ (n = 4, 5, 6) clusters at the DFT level in aqueous solution using polarizable continuum model (PCM). For uranyl(VI), we pay special focus on conformation of coordinating water molecules. A stable energy minimum with no imaginary vibrational frequency was found for $UO_2(H_2O)_5^{2+}$ having U-O_{ax} distance of 1.756 and 1.757 Å, and U-O_{eq} distance of 2.428, 2.436, 2.441, 2.441, and 2.443 Å. Three water planes stay perpendicular to the equatorial plane, while two water planes stay parallel to the equatorial plane. Structures and energies of 4-, and 5-fold uranyl(VI,V) and neptunyl(VI) aquo ions were studied and compared with recent experimental data some of which suggest presence of 4-fold actinyl hydrates.

Introduction

Hydration of actinyl(VI,V) ion has been a subject of study for many years. The most primitive information concerning actinyl(VI,V) ion hydration is “how many water molecules exist in primary hydration sphere”. The hydration number affects various properties of actinyl ions, such as complexation constant, spectroscopic and photochemical properties, mobility, and reactivity. The determination of hydration numbers is very important for quantum chemical calculations of actinyl complexes that have to be performed with assumed co-ordination numbers. With different co-ordination numbers, one can get properties which differ by several orders of magnitude. So the accurate determination of the hydration number is very essential. This is the motivation of the present study.

It is also very important to choose a proper model for quantum chemical calculations. Just by changing the position of second shell water molecules, one can easily get an energy difference of tens of kJ/mol. If the assumed model is wrong, one will get a Gibbs energy that is much higher than the real energy minimum. Therefore, stable intermediates have been searched for with special care not to get the wrong energy minimum.

Calculations

All quantum chemical calculations have been performed in aqueous phase (using PCM model) at the B3LYP level using Gaussian 03 package of programs [1]. As in previous computational studies, the energy-consistent small-core ECP and the corresponding basis set suggested by Küchle *et al.* [2] were used for uranium, neptunium, and oxygen. For the hydrogen, we used the Huzinaga [3] 5s functions contracted to 3s. The most diffuse basis functions on uranium and neptunium with the exponent 0.005 (all s, p, d, and f type functions) were omitted from the basis set, which had very small effect on energy (less than 1 kJ/mol) but made the convergence of the electronic wave function much easier.

Results and Discussions

Uranyl(VI) aquo ion

We first optimized the structures of 5-fold uranyl(VI) aquo ion, $UO_2(H_2O)_5^{2+}$. Several stationary points of the potential energy surface were found and confirmed to be the energy minima through vibrational frequency analysis with no imaginary vibrational frequency present. The structure with minimal Gibbs energy at 298.15 K is given in Figure 1. This structure has two different orientations of water molecules; three waters staying perpendicular to the equatorial plane and two waters staying parallel to the equatorial plane, having $U\text{-}O_{eq}$ distance between 2.428 Å and 2.443 Å. The minimum in electronic energy is not the same as the Gibbs energy minimum. It has similar structure with Figure 1 but has more disordered distribution of $U\text{-}O_{eq}$ distances between 2.415 Å and 2.478 Å. There are several energy minima that lie within several kJ/mol above the global energy minimum, and they have wide distribution of $U\text{-}O_{eq}$ distances. The entropy plays a determining factor in geometry conformation. The temperature plays a significant role in the structure as the entropy term *ST* in the Gibbs energy, and also by changing the dielectric constant of the solvent.

We also studied stability of 4-fold uranyl(VI) aquo ion in solution. When comparing the complex with different hydration number, "*n*+1" models have been used like in previous studies [4,5]. Figure 2 shows 4-fold uranyl(VI) aquo ion having one additional water in the second hydration sphere. Second shell water in complex (a) in Figure 2 has one hydrogen bond to the first shell water, while that in complex (b) has two hydrogen bonds. DFT calculations prevail that complex (a) is 24.4 kJ/mol lower in Gibbs energy compared to complex (b), clearly showing that the model with one hydrogen bond is more reasonable. The large difference in energy between (a) and (b) in Figure 2 originates from

entropy term (*ST*) and solvation energy. We also compared the Gibbs energy of Figure 1 (5-fold) and Fig2.(a) (4-fold) complexes. The 5-fold complex was favored by 29.9 kJ/mol compared to the 4-fold complex. The result is summarized in Table 1.

Figure 1 The structure of $UO_2(H_2O)_5^{2+}$ optimized in aqueous phase. Two waters stay parallel to the equatorial plane while three waters stay perpendicular to the equatorial plane.

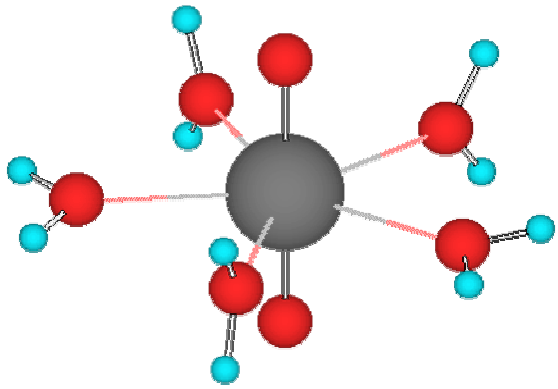

Figure 2 The structure of $UO_2(H_2O)_4(H_2O)^{2+}$ optimized in aqueous phase. The second shell water in complex (a) has only one hydrogen bonding to the first shell water, while that in complex (b) has two hydrogen bonds. DFT calculation shows that (a) is 24.4 kJ/mol more stable than (b).

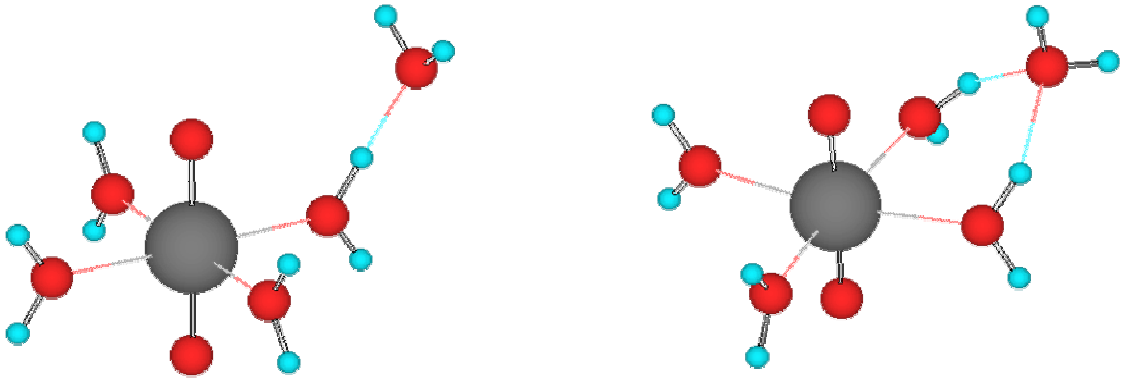

(a) **(b)**

Six-fold complexes were also tested against the 5-fold complex. The results are given in Figure 3. Second shell water in complex (a) in Figure 3 has one hydrogen bond to the first shell water, while that in complex (b) has two hydrogen bonds. The energy difference between (a) and (b) is very similar to the 4-fold case in Figure 2; complex (a) is 22.5 kJ/mol lower in Gibbs energy compared to complex (b). The result is also summarised in Table 1.

Figure 3 The structures of $UO_2(H_2O)_5(H_2O)^{2+}$ and $UO_2(H_2O)_6^{2+}$ optimized in aqueous phase. The second shell water in complex (a) has one hydrogen bond to the first shell water, while that in complex (b) has two hydrogen bonds. DFT calculations show that (a) is 22.5kJ/mol more stable than (b), and 42.9kJ/mol more stable than the 6-fold complex.

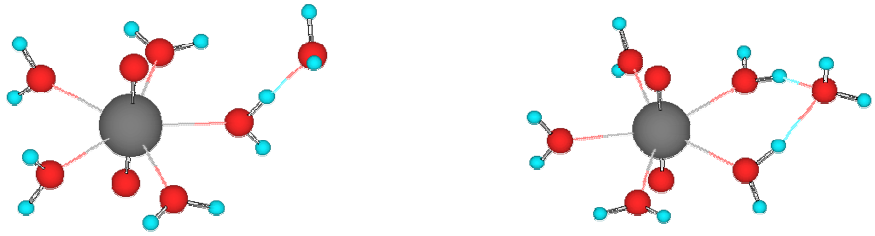

(a) **(b)**

Table 1. Relative Gibbs energy of $UO_2^{2+}(H_2O)_n^{2+}$ clusters (kJ/mol)

	Gibbs energy
UO_2^{2+}•$5H_2O$	0.0
UO_2^{2+}•$4H_2O$•H_2O *	+29.9
UO_2^{2+}•$4H_2O$•H_2O **	+54.3
UO_2^{2+}•$6H_2O$	+42.9
UO_2^{2+}•$5H_2O$•H_2O *	0.0
UO_2^{2+}•$5H_2O$•H_2O **	+22.5

*2nd shell water having one H bond

From the results presented here, we conclude that the 4-fold uranyl(VI) hydrate is much more stable than the 6-fold uranyl(VI). However, this does not rule out the possibility that the water exchange reaction proceeds through the associative (*A*-) mechanism. For the water exchange mechanism, the activation barrier is the determinative factor and not the energy of the intermediates. Further calculations for search of transition states both on *A*- and *D*- mechanisms are worthwhile and will be studied in the future.

Uranyl(V) and neptunyl(VI) aquo ions

Similar calculations have been performed for uranyl(V) and neptunyl(VI) aquo ions. Unlike uranyl(VI) case which has closed-shell f^0 configuration, both uranyl(V) and neptunyl(VI) are open-shell system with f^1 electronic configuration in which spin-orbit effect becomes important. However, it was found in recent studies [6,7] that the spin-orbit effects in a bare UO_2^+ ion and in the hydrated one, $UO_2(H_2O)_5^+$, are very similar, which suggests that they are also very similar among 4-, 5-, and 6-fold UO_2^+ hydrates. We consider the spin-orbit effect to cancel among the UO_2^+ and NpO_2^{2+} complexes having different co-ordination number, and therefore it was not taken into account here.

Two intermediates were identified for both uranyl(V) and neptunyl(VI). 5-fold complex and 4-fold complex with additional water molecule in a second hydration shell having two hydrogen bonds to the first shell water were identified. The Gibbs energy difference between 5-fold and 4-fold complex is 34.4 kJ/mol for UO_2^+ and 43.2 kJ/mol for NpO_2^{2+}. This number is much smaller than the analogous case for UO_2^{2+} where the difference in energy is 54.3 kJ/mol. There is no comparative experimental data for UO_2^+ hydrate as it easily goes through disproportionation. Concerning neptunyl(VI), short Np-O_{eq} distance of 2.36Å observed by Antonio *et al.* [8] by EXAFS agrees well with calculated distance for 4-fold NpO_2^{2+} (2.38-2.39 Å) rather than with 5-fold one (2.42-2.47 Å), and might suggest the dominancy of 4-fold species in the sample solution of Antonio *et al.*. This point should be further studied both experimentally and theoretically.

Conclusions

DFT calculations have shown that the 4-fold uranyl(VI) hydrate stays 24.4 kJ/mol above the 5-fold species, and is, therefore, much more stable than the 6-fold complex which stays 42.9 kJ/mol above the 5-fold species. This result is basically in line with a recent study by Soderholm *et al.* [9] in which they found 4-fold complex to stay very close to 5-fold species but at much closer level; only 5.0 kJ/mol energy difference.

DFT calculations show that uranyl(V) and neptunyl(VI) hydrates have even more close lying 4-fold and 5-fold hydrates. The Np-O_{eq} distance of 4-fold NpO_2^{2+} in our calculations agrees well with one of previous EXAFS measurements and might suggest an experimental evidence of 4-fold Np(VI) hydrate. This point should be studied further with special care both from theory and experimental sides.

Acknowledgements

S.Tsushima was supported by a contract with Institut für Radiochemie, Forschungszentrum Rossendorf (FZR) as a guest scientist, and also as a research fellow of Alexander-von-Humboldt (AvH) foundation. The generous allocation of computer time at Technische Universität Dresden is also gratefully acknowledged.

References

[1] Gaussian 03, Revision D.01, M.J. Frisch, *et al*. Gaussian, Inc., Pittsburgh PA, 2003.

[2] W. Küchle; M. Dolg; H. Stoll; H. Preuss, *J. Chem. Phys.* **1994**,100, 7535.

[3] S. Huzinaga, *J.Chem.Phys.*, **1965**, *42*, 1293.

[4] V. Vallet; U. Wahlgren; B. Schimmelpfennig; Z. Szabo; I. Grenthe, *J.Am.Chem.Soc*. **2001**, 123, 11999.

[5] S. Tsushima; T.X. Yang; A. Suzuki, *Chem.Phys.Lett*. **2001**, 334, 365.

[6] P.J. Hay; R.L. Martin; G. Schreckenbach, *J.Phys.Chem.A* **2001**, 104, 6259.

[7] S. Tsushima; U. Wahlgren; I. Grenthe, *J.Phys.Chem.A* **2006**, 110, 9175.

[8] M.R. Antonio; L. Soderholm; C.W. Williams; J.-P. Blaudeau; B.E. Bursten, *Radiochim.Acta* **2001**, 89, 17.

[9] L. Soderholm; S. Skanthakumar; J. Neuefeind, *Anal.Bioanal.Chem*. **2005**, 383, 48.

UPTAKE MECHANISMS OF Ni(II)/Co(II) BY CEMENT – A COMBINED MICROSCOPIC AND SPECTROSCOPIC APPROACH

M. Vespa, E. Wieland, R. Dähn, D. Grolimund, A.M. Scheidegger
Paul Scherrer Institut, 5303 Villigen, Switzerland

Abstract

Cement-based materials play an important role in multi-barrier concepts developed worldwide for the safe disposal of industrial and radioactive wastes in underground repositories. Cement is used to condition the waste materials and to construct the engineered barrier systems. Therefore, a mechanistic understanding of the processes governing the binding of heavy metals in cement systems is essential for long-term predictions of the environmental impact of cement-stabilized waste forms. Co and Ni isotopes are among important contaminants in waste materials resulting from electricity production in nuclear power plants.

In this study, Co and Ni uptake by Hardened Cement Paste (HCP) has been investigated with the aim of improving our understanding of the immobilization process of heavy metals in cement at the molecular level. To address the influence of the inherent heterogeneity of HCP on the uptake processes of heavy metals, micro X-ray fluorescence (XRF) and micro X-ray absorption spectroscopic (XAS) experiments were conducted on Ni(II) and Co(II) doped HCP. Although both Ni and Co are divalent metal ions, their behaviour in cementitious systems appear to be different. For example, the micro-spectroscopic study showed that Ni(II) is predominantly retained in layered double hydroxide (LDH) phases. For Co(II), the micro-spectroscopic investigations reveal a highly heterogeneous Co distribution with respect to concentration as well as Co speciation. At some Co-rich spots, Co(II) was found to be oxidized to Co(III) during the hydration period of HCP. XAS data analysis suggests that Co(II) is predominately incorporated into newly formed Co(II) hydroxide-like phases ($Co(OH)_2$), Co-LDH or Co-phyllosilicates.

The findings from the micro-spectroscopic study indicate that Co(II) and Ni(II) react differently during the hydration of cement and that both became immobilized in specific cement minerals. These immobilization processes are expected to reduce the mobility of Co(II) and Ni(II) in the cement matrix. Furthermore, it proves that the immobilization potential of cement on a micro-scale is element-specific.

X-RAY ABSORPTION SPECTROSCOPY INVESTIGATION OF LITHIUM NIOBATE IRRADIATED WITH HELIUM IONS ($^{+3}$He:$LiNbO_3$)

T. Vitova[1], M. – R. Zamani – Meymian[2], K. Maier[2], K. Peithmann[2], J. Hormes[1]
[1] Institute of Physics, Bonn University, Nussallee 12, 53115 Bonn, Germany
[2] Helmholtz – Institute for Radiation and Nuclear Physics, Bonn University, Nussallee 14 - 16, 53115 Bonn, Germany

Abstract

Significant changes of spectra taken at the Nb K and LIII – edges are observed after irradiating $LiNbO_3$ with $^{+3}$He ions (energy 40 MeV). Our XAFS study provides some insights into the structural changes that take place during the irradiation process. The measurements at the Nb LIII-edge support the assumption that there are changes in the geometrical structure. This result together with the performed FEFF8 calculations, done to simulate the Nb-K-XANES spectra, and the Extended X-ray Absorption Fine Structure (EXAFS) analysis suggest presence of Li vacancies and/or displacement of Li atoms.

Introduction

The electro-optic, photorefractive, and ferroelectric properties, as well as the robustness and uncomplicated fabrication of Lithium Niobate (LN) have been drawing the interest of research and industry for several decades. Improved properties of the crystals are achieved, for example, while doping the material with different metals or implanting or irradiating it with high or low energy ions. Significant changes (Delta n) in the refractive index \n are obtained, while irradiating $LiNbO_3$ with ^{+3}He ions (energy 40 MeV). Thus modified materials were successfully used for fabricating of a novel type of waveguide [1]. The goal of the here presented X-ray absorption spectroscopy (XAS) study is to investigate the structural changes that are responsible for the changes in the refractive index.

$LiNbO_3$ is a ferroelectric material, which exhibits spontaneous polarization at room temperature. As a result, the centrosymmetric positions of the Li and Nb atoms, octahedrally coordinated by six oxygen atoms, are destroyed and they are shifted along the z axis. At temperatures higher than the Curie temperature: 1471 K, the Li and Nb cations return to the central positions. One third of the octahedral interstices of Lithium Niobate are filled with Nb atoms, one-third with Li atoms and one-third vacant. In the case of congruently – melting $LiNbO_3$ (used in the present work) ~ 6 % of the Li positions are vacant. Some of the missing Li^+ ions are replaced by Nb^{5+} ions with compensating vacancies on the Nb site, maintaining charge neutrality [2].

Investigated Samples and Experimental Details

A commercially available $LiNbO_3$ crystal was cut into 5x6x0.5 mm^3 pieces, polished, and irradiated with ^{+3}He ions, at an energy of 40 MeV, at the isochron cyclontron of the Helmholtz-Insitute for Radiation and Nuclear Physics, University of Bonn. The relaxation process of the activated Nb is as follows:

1. $^{93}Nb(^{3}He,^{4}He)^{92}Nb$,
2. ^{92}Nb does an electron capture and transforms into ^{92}Zr, the half-life is 10 days,
3. ^{92}Zr relaxes by emitting a gamma particle, energy 934 keV.

One of those single crystals ($^{+3}He:LiNbO_3$), with a ~1 mm^2 irradiated spot and about 40 microns thickness was measured at the Nb K-edge (18.986 keV). From other crystals (160 and 190 minutes $^{+3}He:LiNbO_3$ irradiated samples), the irradiated spots were cracked and milled to fine powder. The powder irradiated samples were measured at the Nb LIII edge (2.371 keV). All spectra were recorded in transmission mode using ionization chambers for measuring the incoming flux I0 and the transmitted intensity I1.

The XAS experiment was carried out at the ANKA storage ring at the INE-Beamline. For details about the instrumentation at this beamline, see [3]. For energy monochromatization, a Lemonnier-type [4] double crystal monochromator equipped with Ge(422) (Nb K-edge) and Si(111) (Nb LIII-edge) crystals was used, leading to a minimum energy step width of 0.2 eV and 0.03 eV, respectively.

The theoretical calculations were performed with the FEFF8.2 [5] code. The structural information for the $LiNbO_3$, needed to create the list with atomic coordinates, was obtained from reference [6]. The calculations were done for a cluster of 200 atoms around Nb.

ARTEMIS [7] was used for the EXAFS analysis. The XAFS signal $\chi(k)$ was Fourier-transformed to R space, utilizing the following parameters: k range: 2-12 $Å^{-1}$, k weight: 2, Kaiser-Bessel Window: dk = 4, R range: 1-2 Å. A fit for O as nearest neighbor was performed in R space with a fixed amplitude reduction factor of 1 and fixed co-ordination numbers, while the distances, Debye-Waller factor, and E_0 were varied.

Results and Discussion

Figure 1 presents an absorption map (sample absorption at 19 keV as a function of the beam position) of the ~ 40 microns (one absorption length at 19 keV), single crystal irradiated sample.

Figure 1: Absorption map of the He:$LiNbO_3$ sample.

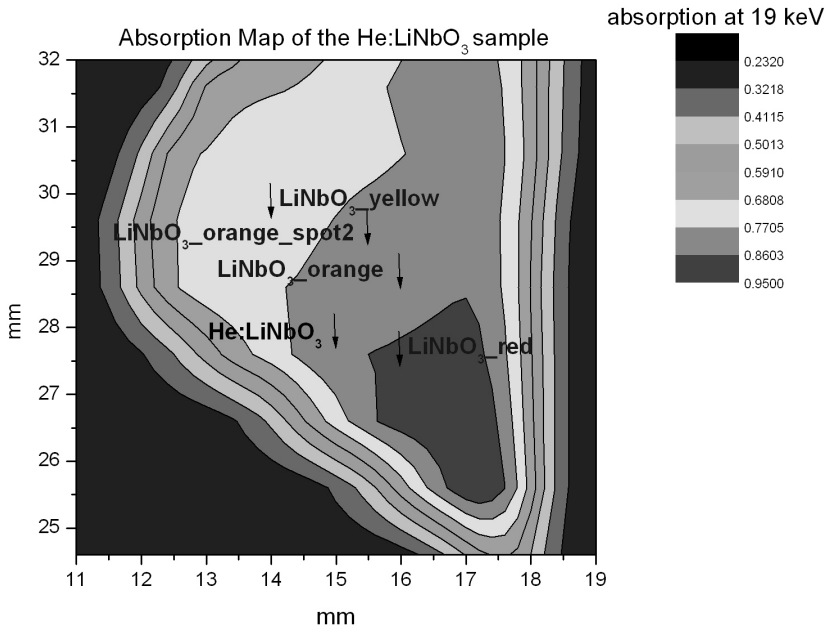

The enclosed areas present spots from the sample with different thicknesses. Figure 2 shows $LiNbO_3$ spectra (measured at the Nb K-edge) measured at different sample spots: A, 1.7 eV energy step and repeated measurements with 0.6 eV energy step: B. In Figure 2 C are compared spectra from Figure 2 A and B. In Figure 2 D is plotted a He:$LiNbO_3$ spectrum along with a $LiNbO_3$ spectrum. The small amplitude changes in the White Line (WL) region of the XANES spectrum of the irradiated lithium niobate (He:$LiNbO_3$) (Figure 2 D: b and c, Figure 3: b and c), compared to lithium niobate ($LiNbO_3$) (Figure 2 D: b and c, Figure 3: b and c), are within the experimental uncertainties and thus they are not regarded as significant. However, the increased intensity of the pre-edge shoulder of the He:$LiNbO_3$ spectrum (Figure 3 a) is reproducible and significant, and it certainly reflects structural changes occurring during the irradiation process.

We have carried out FEFF8 calculations, based on two different models, in order to explain the origin of the differences in the $LiNbO_3$ Nb K-XANES before and after irradiation. The first model is motivated from literature study [8], which also report effect “a” (Figure 3) (i.e., an increase in intensity of the pre-edge feature) and correlate this finding, in the case of octahedrally-coordinated transition metal oxides with displacement of the absorbing atom from the center of the octahedron. Figure 4 a and b show some of the calculated spectra based on a systematic variation of atomic coordinates, i.e., the Nb atoms are shifted 0.01, 0.02, or 0.03 Å along x, y, or z axis, in negative (along z axis, Figure 4 a) or positive (along z axis, Figure 4 b) directions. Going from biggest negative displacement across the z zero-position to positive displacements increases the pre-edge shoulder. These changes in oscillatory strength are compensated by the features b and c in the WL region. The results, in case of shifting along x and y axis (both directions), are similar, thus they are not shown.

Figure 2: Nb K-XANES spectra of $LiNbO_3$ measured at different spots (A), energy steps (A, B, C), and in comparison with a He:$LiNbO_3$ spectrum (D).

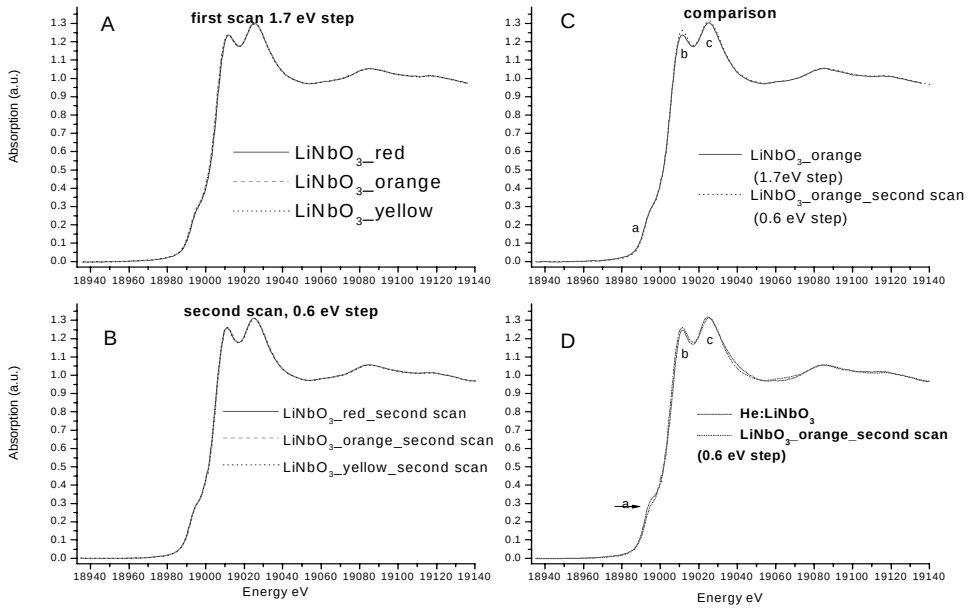

Figure 3: Nb K-XANES spectrum of $LiNbO_3$ in comparison with He:$LiNbO_3$.

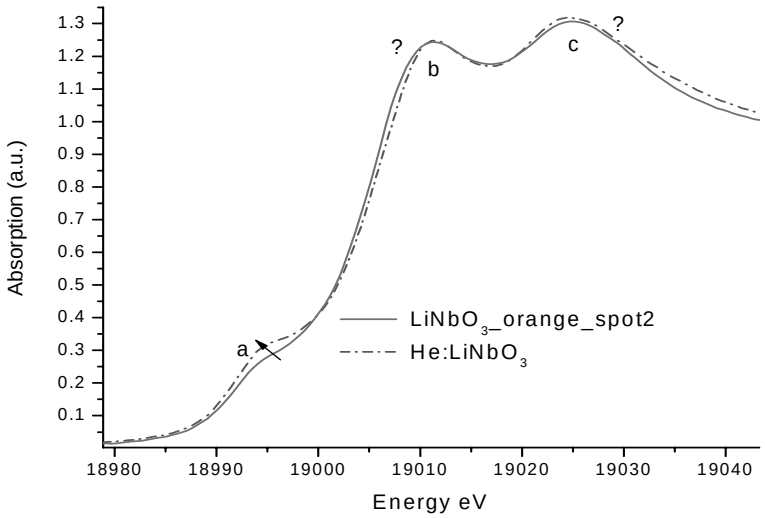

Figure 4 a: Calculated $LiNbO_3$ Nb-K-XANES spectra based on modified list of atomic co-ordinates, i.e., the Nb atoms are shifted 0.01, 0.02, or 0.03 Å along z axis, negative direction.

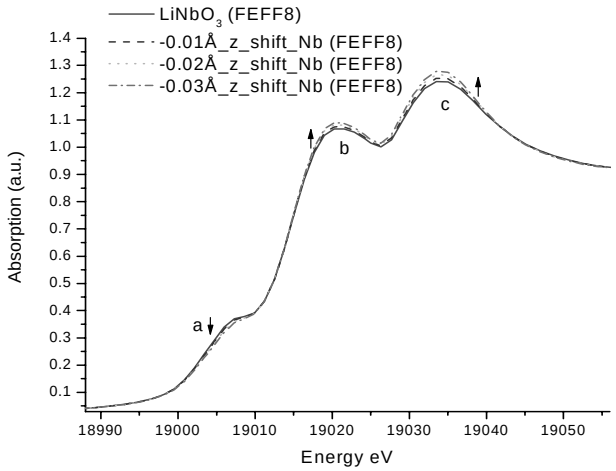

Figure 4 b: Calculated $LiNbO_3$ Nb-K-XANES spectra based on modified list of atomic co-ordinates, i.e., the Nb atoms are shifted 0.01, 0.02, or 0.03 Å along z axis, positive direction.

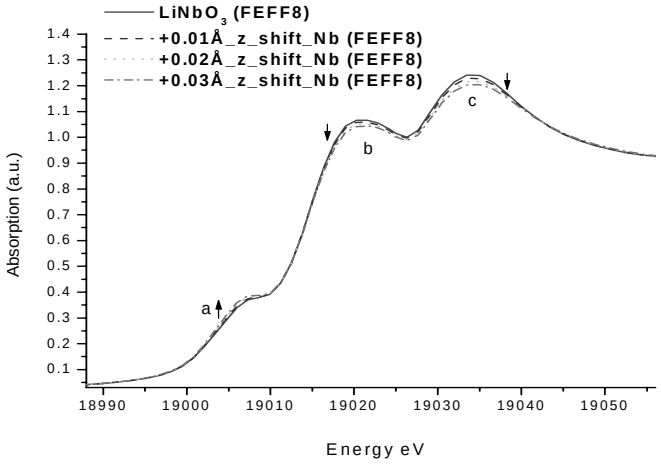

The second model implies the presence of Li and O vacancies in the structure. The vacancies are simulated by random removing of O and Li atoms from the list with atomic coordinates. The required spectrum converges after averaging of around 15 calculated spectra. Figure 5 a presents calculated spectra with dominating lithium vacancies. The case of dominating O vacancies is not shown as the resulted spectra are similar: raising pre-edge feature and redistribution of intensities in the WL region.

Figure 5 a: Calculated $LiNbO_3$ Nb-K-XANES spectra based on modified list of atomic co-ordinates, i.e., simulated Li vacancies and O vacancies, Li vacancies are dominating.

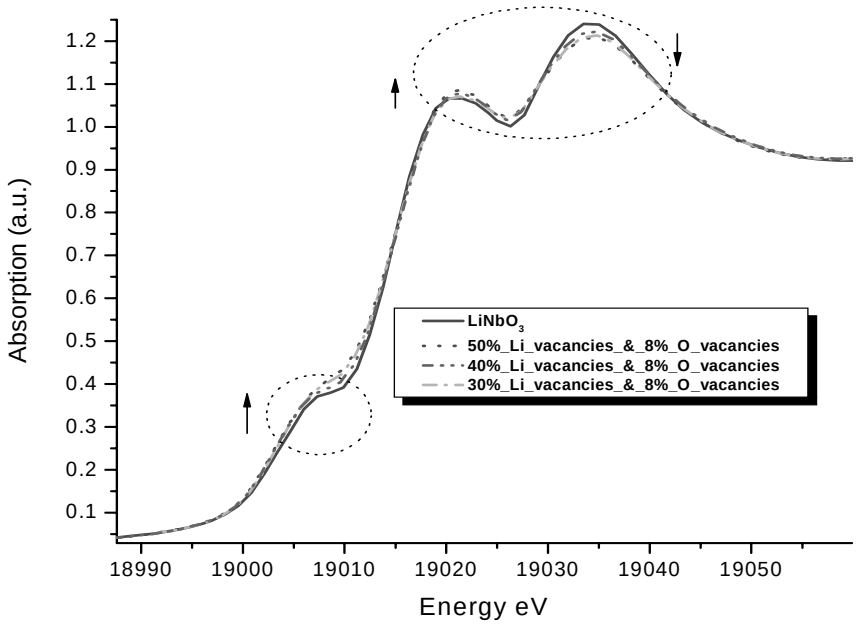

Only in one of the simulations, Figure 4 a, the amplitude of the pre-edge shoulder decreases. It is an expected effect, as the Nb atoms move towards the centrosymmetric position. In the remaining simulated XANES spectra the pre-edge shoulder is raising, which prevents a decision between the vacancies and distorted-octahedron models. Additional insights into the structural changes are provided by the EXAFS analysis. Figure 6 shows the Fourier transformed EXAFS of He:$LiNbO_3$ and $LiNbO_3$ samples. The best fit values for the first co-ordination shell of the He:$LiNbO_3$ sample are: 4 ± 1.2 oxygen atoms at 1.88 ± 0.02 Å and 2.6 ± 1.1 oxygen atoms at 2.12 ± 0.01 Å. The literature [6] values for $LiNbO_3$ are 3 oxygen atoms at 1.879 Å and 3 oxygen atoms at 2.125 Å. Evidently, the best-fit values for the first co-ordination shell of the He:$LiNbO_3$ sample do not support the distorted-octahedron-model (Table 1). The fit values also, clearly exclude major contribution of oxygen vacancies. Nb vacancies do not dominate as well, as, after irradiation, the amplitude of the peak corresponding to the Nb – Nb single scattering path remains the same (Figure 6, C). However, at the vicinity of the second co-ordination shell (Nb-Li) (Figure 6, circled area) changes are present, suggesting lithium vacancies and/or redistribution of Li atoms.

Figure 6: Fourier transformed EXAFS and first co-ordination shell fit of He.$LiNbO_3$ and $LiNbO_3$ Nb-EXAFS spectra.

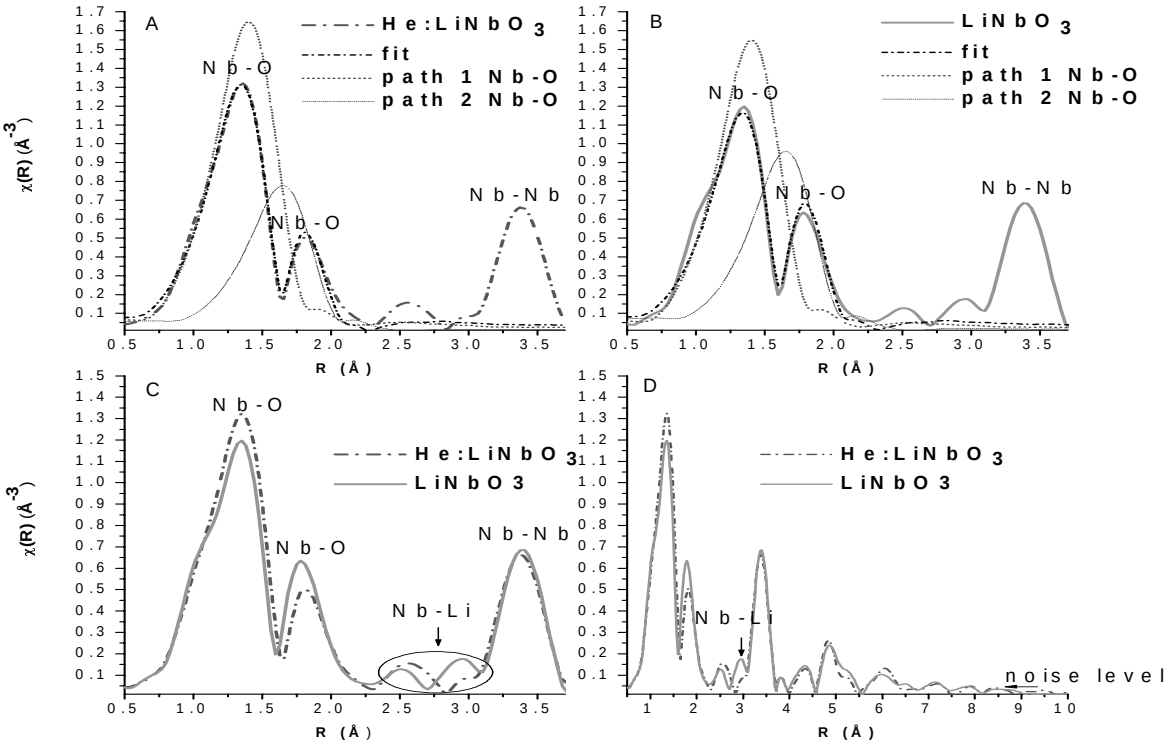

Table 1: Results from the EXAFS analysis of the Nb-O shells.

Coordination number N	$LiNbO_3$	3.6 ± 0.5	3.2 ± 0.5
	He:$LiNbO_3$	4 ± 1.2	2.6 ± 1.1
Distance R (Å)	$LiNbO_3$	1.89 ± 0.01	2.13 ± 0.01
	He:$LiNbO_3$	1.88 ± 0.02	2.12 ± 0.01

Figure 7 presents the XANES spectra of $LiNbO_3$ samples before and after irradiation measured at the Nb LIII edge. The plateau like shape resonances (Figure 7 A and B) of the $LiNbO_3$ spectrum has acquired an asymmetric shape with additional small shoulders (Figure 7 a, b, and A, B), demonstrating the altered structure of the irradiated material. The stronger effects in the spectrum of 160 minutes irradiated lithium niobate as compared to the spectrum of 190 minutes irradiated lithium niobate might be due to the uncontrolled mixing of irradiated and non-irradiated material used for preparing the powdered samples.

Figure 7: The Nb LIII-XANES spectra of $LiNbO_3$ samples before and after irradiation.

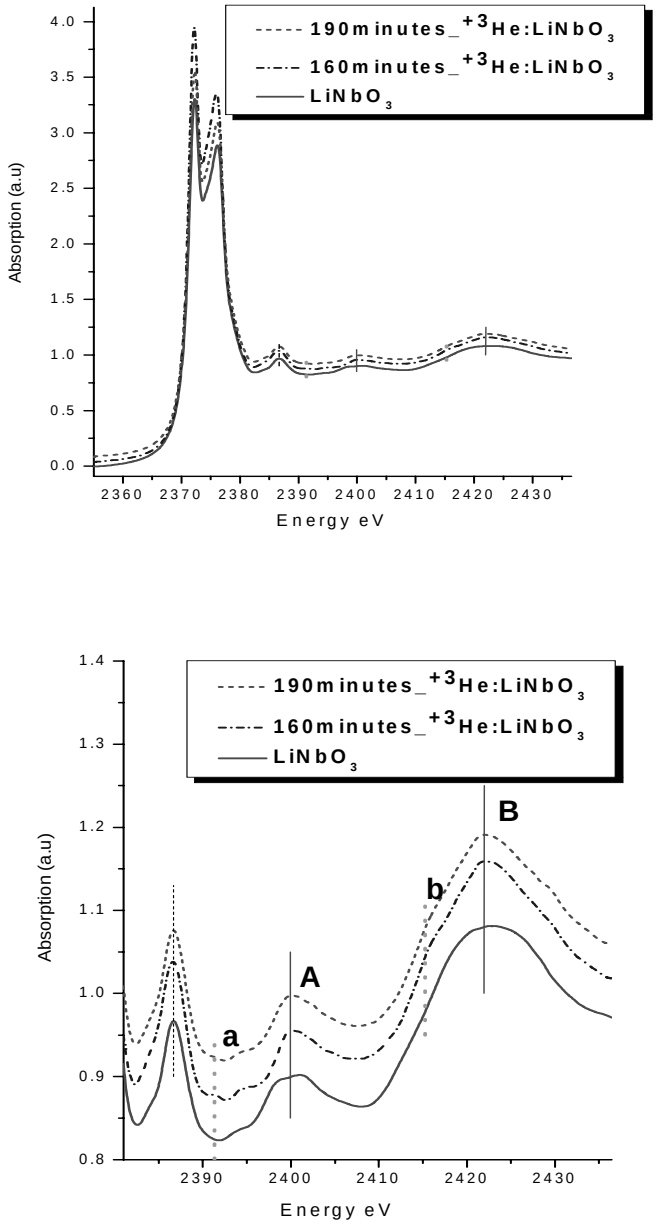

Conclusion

The EXAFS analysis shows that displacement of the Nb atoms as well as a dominating contribution from oxygen/niobium vacancies are unlikely explanations for the structural changes caused by the irradiation that cause the changes in Delta n. However the structural changes in the vicinity of the Nb-Li co-ordination shell in the Fourier transformed He:$LiNbO_3$ EXAFS spectrum, together with the XANES spectra measured at the Nb K- and LIII-edges and the corresponding Nb K-XANES simulated spectra strongly suggest changes in the geometrical structure, i.e., presence of Li vacancies and/or displacement of Li atoms.

Acknowledgement

Technical support of the cyclotron team of the Helmholtz-Institute, Universität Bonn, and the team of the INE-Beamline at ANKA is highly appreciated. We gratefully acknowledge ANKA for providing the beamtime. Financial support of the DFG (Forschergruppe 557) is as well gratefully acknowledged.

Reference

1. K. Peithmann; M.-R. Zamani-Meymian; M. Haaks; K. Maier; B. Andreas; K. Buse; H. Modrow, *Appl.Phys.***B 82**, 419-422 (2006).
2. D.P. Birnie, *Journal of Materials Science* **28**, 302-315 (1993).
3. M.A. Denecke; J. Rothe; K. Dardenne, H. Blank; J. Hormes, *Phys. Scr.* **T115**, 1001 (2005).
4. M. Lemmonier; O. Coller; C. Depautex; J.M. Esteva; D. Raoux, *Nucl. Instr. Meth.* **A 152**, 109 (1978).
5. A.L. Ankudinov; B. Ravel; J.J. Rehr; S.D. Conradson, *Phys. Rev.* **B 58**, 7565 (1998).
6. B.E. Etschmann; N. Ishizawa; V. Streltsov; S. Oishi, *Zeitschrift für Kristallographie* **216**, 455-461 (2001).
7. B. Ravel; M. Newville, J. Synchrotron Rad. **12**, 537-541 (2005).
8. V.A. Shuvaeva; K. Yanagi; K. Yagi; K. Sakaue; H. Terauchi, *J.Synchrotron Rad.* **6**, 367-369 (1999).

INVESTIGATION OF Zr(IV)-OLIGOMERS AND COLLOIDS BY ESI-TOF MASS SPECTROMETRY AND Zr K-XAFS

C. Walther, J. Rothe, S. Büchner, H.-R. Cho, M. Fuss
Forschungszentrum Karlsruhe, Institut für Nukleare Entsorgung, P.O. Box 3640, D-76021 Karlsruhe, Germany

Abstract

After the decay of the short lived fission-products, long lived fission products and actinides with half lifes exceeding 1000 years represent the dominant radioactive inventory in a future nuclear waste underground repository. Over time the radioactive waste might be exposed to ground water and corrode, allowing migration of the highly toxic inventory to the biosphere. Effective barriers must be designed to reduce this migration and, hence, restrict the radioactive exposure of the biosphere to a level below the natural radioactivity background. Mobilizing effects like solution of radionuclides and colloid mediated transport have to be counteracted by demobilizing reactions like surface sorption or incorporation into host matrices. However, the purely phenomenological description of these reactions is not sufficient. A detailed understanding of the molecular processes is required, in particular knowledge of the radionuclide speciation in solution depending on various chemical parameters. In this context, one element of high relevance is zirconium. Zr is a major fission product (^{93}Zr: $T_{1/2}$=1.5 million a). In its tetravalent state Zr also serves as chemical homologue for Pu(IV) (^{239}Pu: $T_{1/2}$=24000 a). Both tetravalent metal cations exhibit a strong tendency towards hydrolysis and subsequent formation of polynuclear species. Depending on the chemical conditions, even micrometer sized particles are found in solution, which might be highly mobile in the aquifer. Using a high resolution electrospray mass-spectrometer (BME-Albatros) the formation process of Zr(IV) oxide/hydroxide species is followed by investigation of the different steps from the “free” hydrated aquo-ion at very acidic conditions via hydrolysis complexes and oligomers towards nm sized colloids. We observe that highly charged Zr(IV)-tetramer and pentamer units are neutralized via hydrolysis with increasing pH, finally forming larger units close to the classical solubility limit. This finding is in accordance with earlier EXAFS investigations [1]. Detailed speciation information depending on metal ion concentration and pH obtained from ESI-TOF MS is compared to Zr K-XAFS spectroscopy results obtained for these samples.

[1] H.-R. Cho, C. Walther, J. Rothe, V. Neck, M.A. Denecke, K. Dardenne and Th. Fanghänel, *Anal. Bioanal. Chem.* **383**, 28 (2005).

Annex A

LIST OF PARTICIPANTS

Belgium

Christiane	Görrler-Walrand	Katholieke Universiteit Leuven
Koen	Janssens	University of Antwerp
Kelly	Servaes	Katholieke Universiteit Leuven
Rik	Van Deun	K.U.Leuven - Department of Chemistry

France

Fabien	Burdet	CEA Grenoble
Christophe	Den Auwer	CEA Marcoule
Clotilde	Gaillard	IPHC
Aurélie	Jeanson	CEA Marcoule
Stéphane	Lequien	CEA-CNRS
Philippe	Martin	CEA-Direction de l'énergie nucléaire (DEN)
Hervé	Palancher	CEA-Cadarache
Philippe	Raison	European Commission - CEA Cadarache
Eric	Simoni	Paris XI university
Bruno	Sitaud	Synchrotron SOLEIL
Valérie	Vallet	CNRS - University of Sciences and Tech. of Lille

Germany

Samer	Amayri	Johannes Gutenberg University of Mainz
Boris	Brendebach	Forschungszentrum Karlsruhe
Roberto	Caciuffo	European Commission, ITU Joint Research Center
Kathy	Dardenne	Forschungszentrum Karlsruhe
Melissa A.	Denecke	Forschungszentrum Karlsruhe
Sonja	Dierking	Johannes Gutenberg-Universität Mainz
Asuncion	Fernandez-Carretero	European Commission, ITU Joint Research Center
Harald	Funke	Forschungszentrum Rossendorf
Frank	Heberling	Forschungszentrum Karlsruhe
Christophe	Hennig	Forschungszentrum Rossendorf
Atsushi	Ikeda	Forschungszentrum Rossendorf e.V.
Reinhardt	Klenze	Forschungszentrum Karlsruhe
Stefan	Mangold	Forschungszentrum Karlsruhe
Petra	Panak	Forschungszentrum Karlsruhe
Markus	Plaschke	Forschungszentrum Karlsruhe
Tanja	Reich	Johannes Gutenberg-Universität Mainz
Tobias	Reich	Johannes Gutenberg-Universität Mainz
André	Rossberg	Forschungszentrum Rossendorf
Jörg	Rothe	Forschungszentrum Karlsruhe
Andreas	Scheinost	Forschungszentrum Rossendorf
Holger	Seher	Forschungszentrum Karlsruhe
Joe	Somers	European Commission, ITU Joint Research Center
Satoru	Tsushima	Forschungszentrum Rossendorf e.V.
Víctor Vicente	Vilas	Johannes Gutenberg University of Mainz

Tonya	Vitova	University of Bonn
Marcus	Walter	European Commission, ITU Joint Research Center
Clemens	Walther	Forschungszentrum Karlsruhe

Japan

Yoshihiro	Okamoto	Japan Atomic Energy Agency
Hideaki	Shiwaku	Japan Atomic Energy Agency
Shinichi	Suzuki	Japan Atomic Energy Agency
Tsuyoshi	Yaita	Japan Atomic Energy Agency (JAEA)

Poland

Jarosław	Jankowski	Center of Oncology

Russia

Grigory	Andreev	Inst. of physical chemistry of Russian Academy of Sciences
Olga	Batuk	Lomonosov Moscow State University
Stepan	Kalmykov	Lomonosov Moscow State University
Aleksander	Kostenko	Rostov State University
Konstantin I.	Maslakov	Russian Research Center “Kurchatov Institute”
Alexander	Soldatov	Rostov State University
Anton Yu	Teterin	Russian Research Center “Kurchatov Institute”
Yury A.	Teterin	Russian Research Center “Kurchatov Institute”

Sweden

Sergei	Butorin	Uppsala University
Lars	Werme	Svensk Kärnbränslehantering AB (SKB)

Switzerland

Rainer	Daehn	Paul Scherrer Institute
Daniel	Grolimund	Paul Scherrer Institute
Peter	Mandaliev	Paul Scherrer Institute
Marika	Vespa	Paul Scherrer Institute

United Kingdom

Andrew	Connelly	University of Sheffield
Francis	Livens	University of Manchester
Katherine	Morris	University of Leeds
Clint	Sharrad	University of Manchester
Jennifer	Waring	University of Manchester

United States

Maxim	Boyanov	Argonne National Laboratory
Steve	Conradson	Los Alamos National Laboratory
David	Shuh	Lawrence Berkeley National Laboratory

Annex B

COMMITTEES AND SUPPORT ORGANISATIONS

Local Organising Committee

Boris Brendebach (FZK-INE)
Kathy Dardenne (FZK-INE)
Melissa A. Denecke (FZK-INE)
Asuncion Fernandez-Carretero (ITU)
Stefan Mangold (FZK-ISS)
Tobias Reich (Uni Mainz)
Jörg Rothe (FZK-INE)
Holger Seher (FZK-INE)

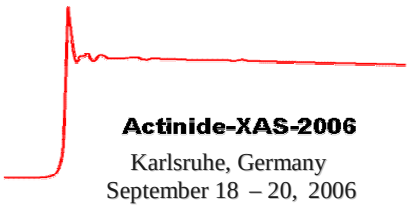

International Scientific Advisory Committee

Christophe Den Auwer	France
Stéphane Lequien	France
Eric Simoni	France
Bruno Sitaud	France
Melissa A. Denecke	Germany
Günter Kaindl	Germany
Tobias Reich	Germany
Andreas Scheinost	Germany
Thomas Fanghänel	ITU
Asuncion Fernandez-Carretero	ITU
Joseph Somers	ITU
Federico J. Mompean	OECD Nuclear Energy Agency
Stepan N. Kalmykov	Russia
André Scheidegger	Switzerland
Francis Livens	UK
Corwin Booth	USA
Steve Conradson	USA
Kenneth Kemner	USA
David K. Shuh	USA
Jim Tobin	USA

Supported by:

ACTINET – Network of Excellence for Actinide Sciences

FZK Program Nuclear

IA-SFS

EC Joint Research Centre - Institute for Transuranium Elements

OECD Nuclear Energy Agency

OECD PUBLICATIONS, 2 rue André-Pascal, 75775 PARIS CEDEX 16
Printed in France.